

BULLETIN OF RUSSIAN STATE MEDICAL UNIVERSITY

BIOMEDICAL JOURNAL OF PIROGOV RUSSIAN NATIONAL
RESEARCH MEDICAL UNIVERSITY

EDITOR-IN-CHIEF Denis Rebrikov, DSc, professor

DEPUTY EDITOR-IN-CHIEF Alexander Oettinger, DSc, professor

EDITORS Valentina Geidebrekht, Nadezda Tikhomirova

TECHNICAL EDITOR Evgeny Lukyanov

TRANSLATORS Ekaterina Tretiyakova, Vyacheslav Vityuk

DESIGN AND LAYOUT Marina Doronina

EDITORIAL BOARD

Averin VI, DSc, professor (Minsk, Belarus)
Alipov NN, DSc, professor (Moscow, Russia)
Belousov VV, DSc, professor (Moscow, Russia)
Bogomilskiy MR, corr. member of RAS, DSc, professor (Moscow, Russia)
Bozhenko VK, DSc, CSc, professor (Moscow, Russia)
Bylova NA, CSc, docent (Moscow, Russia)
Gainetdinov RR, CSc (Saint-Petersburg, Russia)
Gendlin GYe, DSc, professor (Moscow, Russia)
Ginter EK, member of RAS, DSc (Moscow, Russia)
Gorbacheva LR, DSc, professor (Moscow, Russia)
Gordeev IG, DSc, professor (Moscow, Russia)
Gudkov AV, PhD, DSc (Buffalo, USA)
Gulyaeva NV, DSc, professor (Moscow, Russia)
Gusev EI, member of RAS, DSc, professor (Moscow, Russia)
Danilenko VN, DSc, professor (Moscow, Russia)
Zarubina TV, DSc, professor (Moscow, Russia)
Zatevakhin II, member of RAS, DSc, professor (Moscow, Russia)
Kagan VE, professor (Pittsburgh, USA)
Kzyshkowska YuG, DSc, professor (Heidelberg, Germany)
Kobriniskii BA, DSc, professor (Moscow, Russia)
Kozlov AV, MD PhD (Vienna, Austria)
Kotelevtsev YuV, CSc (Moscow, Russia)
Lebedev MA, PhD (Darem, USA)
Manturova NE, DSc (Moscow, Russia)
Milushkina OYu, DSc, professor (Moscow, Russia)
Mitupov ZB, DSc, professor (Moscow, Russia)
Moshkovskii SA, DSc, professor (Moscow, Russia)
Munblit DB, MSc, PhD (London, Great Britain)

Negrebetsky VV, DSc, professor (Moscow, Russia)
Novikov AA, DSc (Moscow, Russia)
Pivovarov YuP, member of RAS, DSc, professor (Moscow, Russia)
Platonova AG, DSc (Kiev, Ukraine)
Polunina NV, corr. member of RAS, DSc, professor (Moscow, Russia)
Poryadin GV, corr. member of RAS, DSc, professor (Moscow, Russia)
Razumovskii AYU, corr. member of RAS, DSc, professor (Moscow, Russia)
Rebrova OYu, DSc (Moscow, Russia)
Rudoy AS, DSc, professor (Minsk, Belarus)
Rylova AK, DSc, professor (Moscow, Russia)
Savelieva GM, member of RAS, DSc, professor (Moscow, Russia)
Semiglazov VF, corr. member of RAS, DSc, professor (Saint-Petersburg, Russia)
Skobolina NA, DSc, professor (Moscow, Russia)
Slavyanskaya TA, DSc, professor (Moscow, Russia)
Smirnov VM, DSc, professor (Moscow, Russia)
Spallone A, DSc, professor (Rome, Italy)
Starodubov VI, member of RAS, DSc, professor (Moscow, Russia)
Stepanov VA, corr. member of RAS, DSc, professor (Tomsk, Russia)
Suchkov SV, DSc, professor (Moscow, Russia)
Takhchidi KhP, member of RAS, DSc, professor (Moscow, Russia)
Trufanov GE, DSc, professor (Saint-Petersburg, Russia)
Favorova OO, DSc, professor (Moscow, Russia)
Filipenko ML, CSc, leading researcher (Novosibirsk, Russia)
Khazipov RN, DSc (Marsel, France)
Chundukova MA, DSc, professor (Moscow, Russia)
Shimanovskii NL, corr. member of RAS, DSc, professor (Moscow, Russia)
Shishkina LN, DSc, senior researcher (Novosibirsk, Russia)
Yakovovskaya RI, DSc, professor (Moscow, Russia)

SUBMISSION <http://vestnikrgmu.ru/login?lang=en>

CORRESPONDENCE editor@vestnikrgmu.ru

COLLABORATION manager@vestnikrgmu.ru

ADDRESS ul. Ostrovityanova, d. 1, Moscow, Russia, 117997

Indexed in Scopus. CiteScore 2020: 0.4

Scopus[®]

Indexed in RSCI. IF 2018: 0,5

**НАУЧНАЯ ЭЛЕКТРОННАЯ
БИБЛИОТЕКА
LIBRARY.RU**

Indexed in WoS. JCR 2020: 0.4

WEB OF SCIENCE[™]

Listed in HAC 31.01.2020 (№ 507)



**ВЫСШАЯ
АТТЕСТАЦИОННАЯ
КОМИССИЯ (ВАК)**

Five-year h-index is 6

**Google
scholar**

Open access to archive

CYBERLENINKA

Issue DOI: 10.24075/brsmu.2021-05

The mass media registration certificate № 012769 issued on July 29, 1994

Founder and publisher is Pirogov Russian National Research Medical University (Moscow, Russia)

The journal is distributed under the terms of Creative Commons Attribution 4.0 International License www.creativecommons.org



Approved for print 31.10.2021
Circulation: 100 copies. Printed by Print.Formula
www.print-formula.ru

ВЕСТНИК РОССИЙСКОГО ГОСУДАРСТВЕННОГО МЕДИЦИНСКОГО УНИВЕРСИТЕТА

НАУЧНЫЙ МЕДИЦИНСКИЙ ЖУРНАЛ РНИМУ ИМ. Н. И. ПИРОГОВА

ГЛАВНЫЙ РЕДАКТОР Денис Ребриков, д. б. н., профессор

ЗАМЕСТИТЕЛЬ ГЛАВНОГО РЕДАКТОРА Александр Эттингер, д. м. н., профессор

РЕДАКТОРЫ Валентина Гейдебрехт, Надежда Тихомирова

ТЕХНИЧЕСКИЙ РЕДАКТОР Евгений Лукьянов

ПЕРЕВОДЧИКИ Екатерина Третьякова, Вячеслав Витюк

ДИЗАЙН И ВЕРСТКА Марины Дорониной

РЕДАКЦИОННАЯ КОЛЛЕГИЯ

В. И. Аверин, д. м. н., профессор (Минск, Белоруссия)
Н. Н. Алипов, д. м. н., профессор (Москва, Россия)
В. В. Белоусов, д. б. н., профессор (Москва, Россия)
М. Р. Богомилский, член-корр. РАН, д. м. н., профессор (Москва, Россия)
В. К. Боженко, д. м. н., к. б. н., профессор (Москва, Россия)
Н. А. Былова, к. м. н., доцент (Москва, Россия)
Р. Р. Гайнетдинов, к. м. н. (Санкт-Петербург, Россия)
Г. Е. Гендлин, д. м. н., профессор (Москва, Россия)
Е. К. Гинтер, академик РАН, д. б. н. (Москва, Россия)
Л. Р. Горбачева, д. б. н., профессор (Москва, Россия)
И. Г. Гордеев, д. м. н., профессор (Москва, Россия)
А. В. Гудков, PhD, DSc (Буффало, США)
Н. В. Гуляева, д. б. н., профессор (Москва, Россия)
Е. И. Гусев, академик РАН, д. м. н., профессор (Москва, Россия)
В. Н. Даниленко, д. б. н., профессор (Москва, Россия)
Т. В. Зарубина, д. м. н., профессор (Москва, Россия)
И. И. Затевахин, академик РАН, д. м. н., профессор (Москва, Россия)
В. Е. Каган, профессор (Питтсбург, США)
Ю. Г. Кжышковска, д. б. н., профессор (Гейдельберг, Германия)
Б. А. Кобринский, д. м. н., профессор (Москва, Россия)
А. В. Козлов, MD PhD (Вена, Австрия)
Ю. В. Котелевцев, к. х. н. (Москва, Россия)
М. А. Лебедев, PhD (Дарем, США)
Н. Е. Мантурова, д. м. н. (Москва, Россия)
О. Ю. Милушкина, д. м. н., доцент (Москва, Россия)
З. Б. Митупов, д. м. н., профессор (Москва, Россия)
С. А. Мошковский, д. б. н., профессор (Москва, Россия)
Д. Б. Мунблит, MSc, PhD (Лондон, Великобритания)

В. В. Негребский, д. х. н., профессор (Москва, Россия)
А. А. Новиков, д. б. н. (Москва, Россия)
Ю. П. Пивоваров, д. м. н., академик РАН, профессор (Москва, Россия)
А. Г. Платонова, д. м. н. (Киев, Украина)
Н. В. Полунина, член-корр. РАН, д. м. н., профессор (Москва, Россия)
Г. В. Порядин, член-корр. РАН, д. м. н., профессор (Москва, Россия)
А. Ю. Разумовский, член-корр., профессор (Москва, Россия)
О. Ю. Реброва, д. м. н. (Москва, Россия)
А. С. Рудой, д. м. н., профессор (Минск, Белоруссия)
А. К. Рылова, д. м. н., профессор (Москва, Россия)
Г. М. Савельева, академик РАН, д. м. н., профессор (Москва, Россия)
В. Ф. Семиглазов, член-корр. РАН, д. м. н., профессор (Санкт-Петербург, Россия)
Н. А. Скоблина, д. м. н., профессор (Москва, Россия)
Т. А. Славянская, д. м. н., профессор (Москва, Россия)
В. М. Смирнов, д. б. н., профессор (Москва, Россия)
А. Спаллоне, д. м. н., профессор (Рим, Италия)
В. И. Стародубов, академик РАН, д. м. н., профессор (Москва, Россия)
В. А. Степанов, член-корр. РАН, д. б. н., профессор (Томск, Россия)
С. В. Сучков, д. м. н., профессор (Москва, Россия)
Х. П. Тахчиди, академик РАН, д. м. н., профессор (Москва, Россия)
Г. Е. Труфанов, д. м. н., профессор (Санкт-Петербург, Россия)
О. О. Фаворова, д. б. н., профессор (Москва, Россия)
М. Л. Филипенко, к. б. н. (Новосибирск, Россия)
Р. Н. Хазипов, д. м. н. (Марсель, Франция)
М. А. Чундокова, д. м. н., профессор (Москва, Россия)
Н. Л. Шимановский, член-корр. РАН, д. м. н., профессор (Москва, Россия)
Л. Н. Шишкина, д. б. н. (Новосибирск, Россия)
Р. И. Якубовская, д. б. н., профессор (Москва, Россия)

ПОДАЧА РУКОПИСЕЙ <http://vestnikrgmu.ru/login>

ПЕРЕПИСКА С РЕДАКЦИЕЙ editor@vestnikrgmu.ru

СОТРУДНИЧЕСТВО manager@vestnikrgmu.ru

АДРЕС РЕДАКЦИИ ул. Островитянова, д. 1, г. Москва, 117997

Журнал включен в Scopus. CiteScore 2020: 0,4

Журнал включен в WoS. JCR 2020: 0,4

Индекс Хирша (h²) журнала по оценке Google Scholar: 6

Scopus[®]

WEB OF SCIENCE™

Google
scholar

Журнал включен в РИНЦ. IF 2018: 0,5

Журнал включен в Перечень 31.01.2020 (№ 507)

Здесь находится открытый архив журнала

**НАУЧНАЯ ЭЛЕКТРОННАЯ
БИБЛИОТЕКА
LIBRARY.RU**



**ВЫСШАЯ
АТТЕСТАЦИОННАЯ
КОМИССИЯ (ВАК)**

CYBERLENINKA

DOI выпуска: 10.24075/vrgmu.2021-05

Свидетельство о регистрации средства массовой информации № 012769 от 29 июля 1994 г.

Учредитель и издатель — Российский национальный исследовательский медицинский университет имени Н. И. Пирогова (Москва, Россия)

Журнал распространяется по лицензии Creative Commons Attribution 4.0 International www.creativecommons.org



Подписано в печать 31.10.2021

Тираж 100 экз. Отпечатано в типографии Print.Formula
www.print-formula.ru

REVIEW	5
Recombinant adeno-associated viruses as a gene delivery vehicle for the use in molecular medicine Usman NYu, Rebrikov DV Рекомбинантные аденоассоциированные вирусы как средство доставки генов для использования в молекулярной медицине Н. Ю. Усман, Д. В. Ребриков	
ORIGINAL RESEARCH	11
Alterations in tancytes and related cell populations of arcuate nucleus in streptozotocin-induced Alzheimer disease model Voronkov DN, Stavrovskaya AV, Gushchina AS, Olshanskiy AS Изменения таницитов и ассоциированных с ними клеточных популяций аркуатного ядра в стрептозоциновой модели болезни Альцгеймера Д. Н. Воронков, А. В. Ставровская, А. С. Гущина, А. С. Ольшанский	
CLINICAL CASE	20
Moyamoya disease as a possible cause of ischemic stroke in adult patients Vishnyakova AYU, Rostovtseva TM, Kovrazhkina EA, Golovin DA, Gubsky IL, Lelyuk SE, Lelyuk VG Болезнь моямая как возможная причина ишемического инсульта у взрослых А. Ю. Вишнякова, Т. М. Ростовцева, Е. А. Ковражкина, Д. А. Головин, И. Л. Губский, С. Э. Лелюк, В. Г. Лелюк	
ORIGINAL RESEARCH	28
Activation of sensorimotor integration processes with a brain-computer interface Rubakova AA, Ivanova GE, Bulatova MA Активация процессов сенсомоторной интеграции с помощью интерфейса «мозг-компьютер» А. А. Рубакова, Г. Е. Иванова, М. А. Булатова	
ORIGINAL RESEARCH	34
Antitumor effect of radiation therapy on orthotopic PDX models of human esophageal adenocarcinoma Kiblitckaya AA, Goncharova AS, Anisimov AE, Snezhko AV Dimitriadi SN, Maslov AA, Gevorkyan YA, Kolesnikov EN Противоопухолевое влияние лучевой терапии на ортотопическую PDX-модель аденокарциномы пищевода человека А. А. Киблицкая, А. С. Гончарова, А. Е. Анисимов, А. В. Снежко, С. Н. Дмитриади, А. А. Маслов, Ю. А. Геворкян, Е. Н. Колесников	
ORIGINAL RESEARCH	41
Similarities and differences between the <i>Chaetopterus variopedatus</i> polychaete luciferases depending on the type of habitat Purtov KV, Petushkov VN, Rodionova NS, Chepurnykh TV, Kozhemyako VB, Zagitova RI, Shcheglov AS, Ziganshin RH, Tsarkova AS Сходство и различия люцифераз полихет <i>Chaetopterus variopedatus</i> в зависимости от места их обитания К. В. Пуртов, В. Н. Петушков, Н. С. Родионова, Т. В. Челурных, В. Б. Кожемяко, Р. И. Загитова, А. С. Щеглов, Р. Х. Зиганшин, А. С. Царькова	
ORIGINAL RESEARCH	47
Predictive potential of macrophage population phenotyping in malignization of <i>H. pylori</i>-associated chronic gastritis Golubinskaya EP, Sataieva TP, Fomochkina II, Kubyshkin AV, Makalish TP, Shkolyar NA, Galyshevskaya AA, Varghese DV Предиктивный потенциал фенотипирования макрофагальной популяции в малигнизации <i>H. pylori</i>-ассоциированного хронического гастрита Е. П. Голубинская, Т. П. Сатаева, И. И. Фомочкина, А. В. Кубышкин, Т. П. Макалиш, Н. А. Школяр, А. А. Галышевская, Д. В. Варгхесе	

ORIGINAL RESEARCH

54

Microbiota of semen samples with normozoospermia: analysis of real-time PCR data

Voroshilina ES, Zornikov DL, Ivanov AV, Pochernikov DG, Panacheva EA

Микробиота эякулята у пациентов с нормозооспермией по результатам исследования методом ПЦР в реальном времени

Е. С. Ворошилина, Д. Л. Зорников, А. В. Иванов, Д. Г. Почерников, Е. А. Паначева

ORIGINAL RESEARCH

62

Assessment of COVID-19 clinical course in patients vaccinated with Sputnik V, SARS-CoV-2 S protein RBD domain variation and serum virus neutralizing activity

Kolobukhina LV, Burgasova OA, Kruzhkova IS, Bakalin VV, Generalova LV, Shagaev AV, Ogarkova DA, Nikiforova MA, Vasina DV, Gushchin VA, Smetanina SV

Оценка клинического течения COVID-19 у пациентов, вакцинированных «Спутник V», изменчивости RBD-домена S-белка SARS-CoV-2 и вируснейтрализующих свойств сыворотки

Л. В. Колобухина, О. А. Бургасова, И. С. Кружкова, В. В. Бакалин, Л. В. Генералова, А. В. Шагаев, Д. А. Огаркова, М. А. Никифорова, Д. В. Васина, В. А. Гуцин, С. В. Сметанина

ORIGINAL RESEARCH

71

Analysis of causes of early neonatal mortality during COVID-19 pandemic in 2020 in Russia

Tumanova UN, Shchegolev AI, Chausov AA, Shuvalova MP

Анализ причин ранней неонатальной смертности в Российской Федерации в 2020 г. (год пандемии COVID-19)

У. Н. Туманова, А. И. Щеголев, А. А. Чаусов, М. П. Шувалова

RECOMBINANT ADENO-ASSOCIATED VIRUSES AS A GENE DELIVERY VEHICLE FOR THE USE IN MOLECULAR MEDICINE

Usman NYu¹✉, Rebrikov DV^{1,2}

¹ Kulakov National Medical Research Center for Obstetrics, Gynecology and Perinatology, Moscow, Russia

² Center for Precision Genome Editing and Genetic Technologies for Biomedicine, Pirogov Russian National Research Medical University, Moscow, Russia

Viral mechanisms for the delivery of genetic material are widely used in molecular medicine. Recombinant adeno-associated viruses (rAAV) represent a promising tool for *in vivo* gene delivery. The review considers nosological spectrum, molecular mechanisms, the choice of drug administration route depending on target structures, the choice of serotype, and the methods of active ingredient manufacturing for rAAV-mediated gene therapy.

Keywords: adeno-associated viruses, AAV, rAAV, gene therapy

Author contribution: Usman NYu — preparation of the manuscript; Rebrikov DV — editing of the manuscript.

✉ **Correspondence should be addressed:** Natalia Usman
Oparina, 4, Moscow, 117997, Russia; natalia.usman@yandex.ru

Received: 19.10.2021 **Accepted:** 29.10.2021 **Published online:** 31.10.2021

DOI: 10.24075/brsmu.2021.051

РЕКОМБИНАНТНЫЕ АДЕНОАССОЦИИРОВАННЫЕ ВИРУСЫ КАК СРЕДСТВО ДОСТАВКИ ГЕНОВ ДЛЯ ИСПОЛЬЗОВАНИЯ В МОЛЕКУЛЯРНОЙ МЕДИЦИНЕ

Н. Ю. Усман¹✉, Д. В. Ребриков^{1,2}

¹ Национальный медицинский исследовательский центр акушерства, гинекологии и перинатологии имени В. И. Кулакова, Москва, Россия

² Центр высокоточного редактирования и генетических технологий для биомедицины, Российский национальный исследовательский медицинский университет имени Н. И. Пирогова, Москва, Россия

Вирусные механизмы доставки генетического материала широко используются в молекулярной медицине. Рекombинантные аденоассоциированные вирусы (rAAV) представляют собой перспективный инструмент для доставки генов *in vivo*. В обзоре представлены нозологический спектр, молекулярные механизмы, выбор способа введения препарата в зависимости от структур-мишеней, выбор серотипа, а также методы производства активных ингредиентов для rAAV-опосредованной генной терапии.

Ключевые слова: аденоассоциированные вирусы, AAV, rAAV, генотерапия

Вклад авторов: Н. Ю. Усман — подготовка рукописи; Д. В. Ребриков — редактирование рукописи.

✉ **Для корреспонденции:** Наталья Юрьевна Усман
Опарина, д. 4, г. Москва, 117997, Россия; natalia.usman@yandex.ru

Статья получена: 19.10.2021 **Статья принята к печати:** 29.10.2021 **Опубликована онлайн:** 31.10.2021

DOI: 10.24075/vrgmu.2021.051

Biological basis for the recombinant adeno-associated virus-mediated gene delivery

Adeno-associated viruses (AAV, *Dependoparvovirus*, Parvoviridae) were discovered as impurities in laboratory preparations of adenoviruses. The interest in AAV, which had long been purely scientific, moved into a practical plane in connection with the development of gene therapy.

AAV infectious particles are icosahedral. The capsid is assembled of three types of protein subunits, variants of which determine the specificity of viral particles in relation to the recipient's immune system (serotype). The genome is flanked with inverted terminal repeats (ITR) of T-shaped secondary structure, which prime the complementary DNA synthesis in the infected cell nucleus. In addition, ITR serve as recombinogenic sequences for the formation of transcribed concatemeric molecules of viral DNA; they also provide a replication origin and a packaging signal. The AAV genome contains two coding genes, *rep* and *cap*, with multiple reading frames — *rep* for the factors of replication and particle assembly and *cap* for capsid proteins. It is important to emphasize that AAV life cycle can only be maintained upon coinfection of the host cell with other viruses.

Viral mechanisms for the delivery of genetic material are widely used in molecular medicine. For their implementation, a prototype viral genome sequences are distributed over

different carrier (vector) DNA molecules. Structuring and regulatory elements of the virus are cloned into one vector, with a therapeutic module (cargo) subsequently incorporated to obtain a composite (recombinant) unit intended for the packaging and delivery. Coding sequences of own genes of the virus are cloned into another vector. The use of vectorized DNA fragments that complement one another functionally while being physically disconnected is called *trans*-complementation. This is a 'kill two birds with one stone' solution, as (1) the extraction of viral coding sequences makes room for the cargo; (2) the delivery is safe for the target cell, as certain genes essential for self-maintenance of the virus have been removed from the recombinant version of its genome intended for the delivery. Production of viral particles proceeds in a living eukaryotic cell. Having received both vectors, this cell begins to produce infectious particles containing the recombinant viral DNA.

Recombinant AAVs (rAAVs) represent a promising platform for *in vivo* gene delivery. Compared with alternative systems, rAAVs have a number of advantages:

1) the absence of human pathogens among known AAV strains offsets the risks associated with sporadic transgression of the virus to the wild type;

2) rAAV sequences do not integrate in the target cell genomes, which is a principal safety factor for *in vivo* applications (in humans, wild-type AAVs are capable of integration into

genomic locus AAVS1, which results in latency. The integration is based on structural similarity between ITR and AAVS1 and requires participation of viral proteins Rep. Recombinant AAVs are devoid of *rep* coding sequences and do not integrate);

3) small infectious particles of AAV (20–26 nm) have higher penetrating capacity compared to retro- and lentiviruses (100–200 nm), certain AAV serotypes can cross the blood-brain barrier.

At the same time, rAAV gene therapy platforms have a number of drawbacks, first of all, the expensive complex production and the need of using genetic elements of other viruses (adeno-, herpes simplex, or baculo-) as a potential source of biological contamination. Other disadvantages of rAAV platforms include the risk of excessive immune response to the therapy and tight restrictions on the size of the cargo [1–3].

Indications for the rAAV-mediated gene delivery

Despite its historical focus on monogenic autosomal-recessive disorders, the scope of indications for the use of gene therapy with rAAV delivery is much wider. The possibility of using rAAV is being actively investigated for conditions with complex etiology, including not only genetic, but also environmental factors: heart failure [4, 5], joint inflammatory diseases [6], neurological and neurodegenerative diseases [7–9], malignant tumors [10, 11], and morbid viral infections [12].

Therapeutic goals of the rAAV-mediated gene delivery

Therapeutic goal of nucleic acid delivery refers to molecular mechanisms of the compensatory effect. For monogenic diseases, a default option is functional replacement of the mutant gene copies with properly operating transcriptional units. As an alternative to gene replacement, the therapy may be aimed at correction of signaling pathways by adding active genes (gene addition), specific shutdown of target genes by transgene expression products at the level of transcription, translation, or protein (gene silencing), as well as delivery of DNA templates for genome editing e.g. CRISPR-based (gene editing) [2].

The choice of administration route depending on target structures

Local administration of the drug is a proper choice for pathological processes localized in accessible anatomical compartments (eyeball, joint). For pathologies of the central nervous system (CNS), the drug can be injected into a specific area of the brain or cerebrospinal fluid; however, both procedures are highly invasive. The feasibility of minimally invasive systemic administration of viral particles depends on clinical situation.

For local administration of rAAV, the choice of serotype is non-critical. By contrast, when the drug is administered systemically, the success of therapy largely depends on the choice of serotype for the most selective transduction of target organs and tissues. The liver and the muscles are targeted more effectively than other organs.

The liver can be targeted with almost any known human AAV serotype. This is consistent with the fact that the majority of natural AAV strains in humans and primates infect hepatic and splenic tissues. Hepatocytes represent the primary target for a number of monogenic metabolic disorders, including familial hypercholesterolemia (*LDLR*), ornithine transcarbamylase

deficiency (*OTC*), Crigler-Najjar syndrome (*UGT1A1*), hemophilia A (*F8*), hemophilia B (*F9*), glycogen storage disease type Ia (*G6PC*), and mucopolysaccharidosis type I, II, IIIA or VI (respectively, *IDUA*, *IDS*, *SGSH* or *ARSB*).

The muscles can be targeted with AAV8 and AAV9 serotypes. Nosological scope for primary targeting of muscle tissues includes Duchenne muscular dystrophy (*DMD*), Pompe disease (*GAA*), and X-linked myotubular myopathy (*MTM1*). It is important to note that the transduced muscle tissue can serve as a secreted polypeptide factory for the treatment of non-muscle diseases.

Transduction of CNS neurons and glial cells requires either highly invasive injection techniques or the use of AAV serotypes capable of crossing the blood-brain barrier (AAV9, AAVrh.10). Monogenic CNS disorders, for which the use of rAAV platforms is considered relevant, include spinal muscular atrophy (*SMN1*), aromatic L-amino acid decarboxylase deficiency (*DDC*), Canavan disease (*ASPA*), GM1 gangliosidosis (*GLB1*), mucopolysaccharidosis type III (*GNS*, *HGSNAT*, *NAGLU*, *SGSH*), Rett syndrome (*MECP2*), and Batten disease (*CLN2*, *CLN6*) [2].

The importance of serotype

Design of rAAV serotypes produced an entire area of applied research. At the systemic level, the serotype must ensure effective drug targeting with minimal immunogenicity (the immune response can be directed towards transgene expression product if it is foreign). At the subcellular level, the serotype must ensure (1) particle integrity during endosomal transport (endosomal escape) and (2) particle resistance to proteasomal degradation in cytosol before transportation to the nucleus, where viral DNA exits the capsid. Serotype design is based on modifying the structure of AAV capsid proteins encoded by cap gene. Contemporary approaches for obtaining capsids with enhanced properties include directed evolution, rational design, and natural discovery.

Directed evolution stands for artificial selection of successful variants after random modification of the template by using polymerase chain reaction of low fidelity (error-prone PCR) or multiple fragment swapping between different variants of the same sequence (capsid shuffling). Rational design means targeted optimization of a serotype using protein engineering methods. Alterations in polypeptide structure are introduced at the level of the coding templates. Site-directed mutagenesis allows single substitutions at antigenically relevant amino acid positions in a polypeptide. For example, substitutions of tyrosine residues exposed at the particle surface can significantly increase the efficacy of endosomal transport after particle internalization and their resistance to proteasomal degradation in the cytosol; a corresponding enhancement of transduction efficiency has been demonstrated in a mouse model [13]. Modification of epitopes in the already assembled capsids can be carried out by chemical methods [14]. Another area of rational capsid design for rAAV is creation of cap chimeric genes. The selectivity of targeting can be enhanced by introducing integrin-binding motifs or immunoglobulin-like ScFv domains with high affinity to surface markers of target cells.

Finally, new relevant AAV serotypes can be discovered by analyzing high-throughput data produced by 'omics' technologies. Competent borrowing from nature should always involve comprehensive examination of the available options. The majority of natural AAV strains are species-specific: some infect humans, other infect mice, etc. The prevalence of AAV-specific antibodies in human populations may reach 80% [15].

If we 'dress' our therapeutic construct in the capsid of one of the human AAV strains, the immune system may quickly attack the drug, the titer will decrease rapidly, and the transduction will be ineffective. On the other hand, if we take a capsid (serotype) very distant from human serotypes (e.g. murine), then, firstly, we risk an excessive immune response with the most severe consequences. Secondly, the affinity of the particles to the receptors at the surface of target cells may not be strong enough, since murine AAV serotypes have been adapted to murine receptors by the evolution, and the transduction will fail as well. The problem has two solutions.

1. When borrowing serotypes from closely related species, the risk of excessive immune response is moderate. At the same time, the patient lacks high-affinity prêt-à-porter antibodies, while receptors at the surface of target cells may recognize such particles satisfactorily thus promoting efficient transduction. This is not just an idea; for example, in the designation of the serotype AAVrh.10, already established in clinical studies, 'rh' is derived from 'rhesus monkeys' (*Macaca mulatta*).

2. It is also possible to use serotypes once present in the human virome but already dismissed by evolution. Such ancestral serotypes, to which we harbor no antibodies, are found by computational methods of evolutionary genetics *in silico*.

In the practical aspect, it is important to understand that serotype design is a formidable task, which requires comprehensive functional testing. To generate options is easy enough, but their proper evaluation is methodologically challenging. Today, only about a dozen different rAAV serotypes have been promoted to clinical applications, including trials, with AAV2 being the most favored. The list includes several relatively new serotypes with enhanced targeting properties, most notably AAV8, AAV9, and AAVrh.10 [2].

Design of therapeutic modules

Design of cargoes for rAAV-mediated gene delivery is tricky. ITR are the only sequences left from the prototype viral genome, with the rest space reserved for a therapeutic module. A minimal cassette comprises a promoter, a coding sequence, and a 3' noncoding region with polyadenylation and transcription termination signals. The packaging size limit is 4,700 nucleotides, including ITR. Experimental attempts of packaging for constructs larger than 5,200 nucleotides produced particles containing fragments of variable length with truncated (chopped off) 5' termini. Such defective particles were capable of delivering reporter genes *in vitro* only at a high multiplicity of infection, which is completely unacceptable for *in vivo* applications [3]. The principles and pitfalls of the therapeutic module engineering are given in Table.

Manufacturing options

Production of recombinant viruses harnesses eukaryotic cells as biological factories. The most convenient solutions involve special cell lines genetically modified for the task — the so-called packaging cell lines with certain (but not all) genes required for the production of recombinant viral particles built into their own chromosomes.

The first packaging cell lines for rAAV were HeLa cells stably transfected with (i. e. they are having built-in copies of) *rep-cap* genes and the rAAV genome *per se* — a therapeutic module flanked with ITR. Production of rAAV particles in this system is triggered by infection of the cells with adenovirus (AdV). A serious drawback of this system is the presence of adventitious AdV (inactivated by heating the isolates at 56 °C for 30–60 minutes, to

which rAAV is resistant.) Another disadvantage of this system is nonversatility, as a new line of genetically modified HeLa cells had to be obtained for each new construct-serotype combination [22]. More recent systems for rAAV manufacturing used replication-deficient herpes simplex virus (HSV) as a helper [23].

The majority of currently established protocols for rAAV manufacturing employ a line of HEK293 cells with two built-in AdV genes, *E1a* and *E1b*. Other necessary AdV genes reside in the helper plasmid fed into the system only at the start of the production cycle. The separation of AdV genes into different vehicle molecules is due to safety concerns: co-existence of significant portion of the AdV genetic material in a cell can lead to recombination restoring a replication-competent AdV, contagious and potentially hazardous. Another plasmid, called *cis*-plasmid, carries the replication template — a therapeutic module flanked by ITR. Yet another vehicle molecule required for the production, called *trans*-plasmid, contains coding sequences of *rep* and *cap* — these are AAV genes, expression of which is indispensable for the replication of rAAV DNA and the packaging of viral particles. All three plasmids involved in the production (helper, *cis*-, and *trans*-) are genetically engineered molecules with structures thoroughly verified by sequencing. The plasmids are amplified in *E. coli* to amounts required for the transfection.

Transfection is a gentle non-viral method of delivering genetic material to eukaryotic cells. In transfection, genetic material enters the cell by means of phagocytosis (in contrast with transduction, which involves the use of viral delivery mechanisms). DNA is incorporated into colloidal particles of some suitable physiologically neutral substance (calcium phosphate, lipofectamine, polyethyleneimine) and these particles are fed to the cells. Most transfection protocols use the same scheme: plasmid DNA is diluted with a small volume of serum-free medium or saline, so is the filler substance; the aliquots are combined, incubated to form phagocytatable complexes, and added to the cells. It is important to note that the HEK293^{F1ab} cell line has been adapted for suspension growth in order to enhance the yields [2, 24].

Replication of rAAV in living cells may be accompanied by capturing small fragments of cellular genetic material by the virus. Considering that both HeLa and HEK293 cell lines are derived from humans, the safety of such capturing events is questionable. Contamination of therapeutic constructs with cellular sequences can facilitate their integration into the patient's genome, causing genotoxic effects. To circumvent this problem, it was proposed to use insect Sf9 cells in combination with compatible baculovirus helper sequences; the concept seems to work out [25].

Regardless of a particular protocol used for rAAV production, not only the culture medium (supernatant) but also the cells must be collected at the end of the production cycle, since a significant portion of the particles remain trapped. (In retro- and lentivirus manufacturing, it is usually sufficient to collect the supernatant.) A huge amount of free viral and non-viral DNA in the cell lysates makes a DNase treatment mandatory. In addition, there is always an admixture of empty and underassembled particles, which must be eliminated by centrifugation in a CsCl or iodixanol density gradient followed by several rounds of chromatography. Purification of rAAV particles by ultracentrifugation is possible for research applications only and cannot be scaled up for manufacturing purposes [26].

Conclusion

The global clinical experience with rAAV is actively expanding, and the interest in this research area remains very high. The first rAAV-based drug fully approved for clinical use was Glybera® (a.k.a. Alipogene tiparovec, uniQure; the Netherlands)

Table. Design of cargo sequences for rAAV-mediated gene therapy

Basic requirements	Problems	Possible solutions	Examples and comments
The therapeutic effect should be maximized	Transgene expression level may be insufficient	Use strong promoters	e. g. cytomegalovirus (CMV) promoter
		Use additional regulatory elements facilitating transgene expression	e. g. introns-enhancers, the woodchuck hepatitis virus posttranscriptional regulatory element (WPRE)
		Add the Kozak consensus sequence	CCACCATG or CCACCATGG, where ATG is the translation initiation codon
		Optimize codon usage and GC content	
	Eliminate inhibitory motives	including cryptic splice sites and terminators, as well as secondary structures that undermine stability of the transcript	
	Supraphysiological expression levels of transgene in target and off-target tissues may be toxic		The effect was described for transgenes of <i>MECP2</i> (hepatotoxicity) in a mouse model of Rett syndrome [16] and <i>HexA/HexB</i> (neurotoxicity) in a primate model of GM2 gangliosidosis [17]
Transgene expression must be specific	Transgene expression in off-target structures may significantly enhance the immune response to the product	Use tissue-specific promoters	
		Add binding sites for microRNA species highly expressed in antigen-presenting cells to the 3' noncoding region of the transgene	Professional antigen-presenting cells express microRNA miR-142-3p. Addition of miR-142-3p binding sites to the construct reduces transgene expression in macrophages and dendritic cells, thus suppressing immune response to the product [18]
Accommodation of large transgenes	Coding sequences of certain genes are lengthy	Save space by creating mini- and microgens encoding incomplete polypeptides with (partially) preserved functionalities	Clinical potential of this approach is being investigated for Duchenne disease (<i>DMD</i>), <i>CEP290</i> - associated form of Leber congenital amaurosis, and dysferlinopathy (<i>DYSF</i>) [2]
		Deliver coding sequences in portions	The engineering strategy is as follows: divide the open reading frame at a boundary between protein domains and clone the fragments into two different vectors for packaging into separate viral particles, while complementing each construct with recombinogenic sequences flanked by splice sites for the excision from pre-mRNA. Alternatively, use post-translational reunification of the protein by the intein-mediated protein trans-splicing; this route is feasible for some clinically significant polypeptides (dystrophin, Cas9). Given the low efficiency of polypeptide integrity reconstitution in experimental systems, discussion of clinical applications for such approaches would be premature. Since the success depends on probability of simultaneous infection of the same target cell with two different particle types, it may require an increase in the viral load compared with the standards [2,19]
Enhancement of the transgene presence in target cells	The transgene exists in the form of non-replicated concatemeric molecules (episomes) inevitably diluted in mitotically active cell populations	Stimulate integration with due regard to genotoxicity risks	Recombinant AAV-based platforms are the method of choice for <i>in vivo</i> gene delivery largely because of their safety compared to retro- and lentiviruses, which become incorporated into the host cell genome upon the transduction. Extremely rare events of spontaneous partial integration of rAAV material into human genome are clinically irrelevant [20]. Site-specific integration of rAAV transgenes can be achieved by genome editing; however, such interventions are associated with increased risks of genotoxicity. Undesirable side effects on chromosomal environment in the case of transgene integration can be reduced by adding insulator elements [21]

designed to treat the autosomal-recessive lipoprotein lipase (LPL) deficiency. The enzyme, produced predominantly by adipose and muscle tissues which release it into the blood, is functioning at the inner surface of endothelial lining of the capillaries in extrahepatic tissues. Patients with LPL deficiency experience severe impairment of triglyceride metabolism. The active ingredient of Glybera® is constituted by viral particles with AAV1 serotype, containing a copy of the LPL gene with expression-enhancing elements. Glybera® is administered intramuscularly by multiple injections once in every 10 years. The drug was approved for clinical use in Europe in 2012, but withdrawn from the European Community Register of Orphan Medicinal Products in 2017 due to commercial failure; as of 2018, the treatment was received by 31 patients [27, 28].

Another rAAV-based drug, Luxturna® (a.k.a. Voretigene neparvovec, Spark Therapeutics; USA), is known as the

first rAAV-based gene therapy approved by the U.S. Food and Drug Administration agency (FDA) in 2017. Luxturna® is used to treat the RPE65-dependent congenital Leber amaurosis, a severe autosomal recessive oculopathy that manifests from birth. The active ingredient of Luxturna® is constituted by viral particles with AAV2 serotype, containing a copy of the RPE65 gene with expression-enhancing elements. The drug is administered by subretinal injection [29].

In 2019, another rAAV-based drug, Zolgensma®, for the treatment of autosomal-recessive spinal muscular atrophy, received FDA approval [30]. The query "adeno-associated virus" currently yields a list of 159 studies at ClinicalTrials.gov [31]. The clinical trials are in progress, and since there are still more questions than answers in this area, we can expect them to gain momentum.

References

- Chen W, Yao S, Wan J, Tian Y, Huang L, Wang S, et al. BBB-crossing adeno-associated virus vector: An excellent gene delivery tool for CNS disease treatment. *J Control Release*. 2021; 333: 129–38. DOI: 10.1016/j.jconrel.2021.03.029. PubMed PMID: 33775685.
- Wang D, Tai PWL, Gao G. Adeno-associated virus vector as a platform for gene therapy delivery. *Nat Rev Drug Discov*. 2019; 18 (5): 358–78. DOI: 10.1038/s41573-019-0012-9. PubMed PMID: 30710128.
- Wu Z, Yang H, Colosi P. Effect of genome size on AAV vector packaging. *Mol Ther*. 2010; 18 (1): 80–6. DOI: 10.1038/mt.2009.255. Epub 2009 Nov 10. PubMed PMID: 19904234.
- Bass-Stringer S, Bernardo BC, May CN, Thomas CJ, Weeks KL, McMullen JR. Adeno-Associated Virus Gene Therapy: Translational Progress and Future Prospects in the Treatment of Heart Failure. *Heart Lung Circ*. 2018; 27 (11): 1285–300. DOI: 10.1016/j.hlc.2018.03.005. PubMed PMID: 29703647.
- Greenberg B, Butler J, Felker GM, Ponikowski P, Voors AA, Desai AS, Barnard D, Bouchard A, Jaski B, Lyon AR, Pogoda JM, Rudy JJ, Zsebo KM. Calcium upregulation by percutaneous administration of gene therapy in patients with cardiac disease (CUPID 2): a randomised, multinational, double-blind, placebo-controlled, phase 2b trial. *Lancet*. 2016; 387 (10024): 1178–86. DOI: 10.1016/S0140-6736(16)00082-9. PubMed PMID: 26803443.
- Evans CH, Ghivizzani SC, Robbins PD. Gene Delivery to Joints by Intra-Articular Injection. *Hum Gene Ther*. 2018; 29 (1): 2–14. DOI: 10.1089/hum.2017.181. PubMed PMID: 29160173.
- Huang L, Wan J, Wu Y, Tian Y, Yao Y, Yao S, et al. Challenges in adeno-associated virus-based treatment of central nervous system diseases through systemic injection. *Life Sci*. 2021; 270: 119142. DOI: 10.1016/j.lfs.2021.119142. PubMed PMID: 33524419.
- Mijanović O, Branković A, Borovjagin A, Butnaru DV, Bezrukov EA, Sukhanov RB, Shpichka A, Timashev P, Ulasov I. Battling Neurodegenerative Diseases with Adeno-Associated Virus-Based Approaches. *Viruses*. 2020; 12 (4): 460. DOI: 10.3390/v12040460. PubMed PMID: 32325732.
- Privolizzi R, Chu WS, Tijani M, Ng J. Viral gene therapy for paediatric neurological diseases: progress to clinical reality. *Dev Med Child Neurol*. 2021; 63 (9): 1019–29. DOI: 10.1111/dmcn.14885. PubMed PMID: 33834479.
- Nawaz W, Huang B, Xu S, Li Y, Zhu L, Yiqiao H, et al. AAV-mediated in vivo CAR gene therapy for targeting human T-cell leukemia. *Blood Cancer J*. 2021; 11 (6): 119. DOI: 10.1038/s41408-021-00508-1. PubMed PMID: 34162832.
- Bower JJ, Song L, Bastola P, Hirsch ML. Harnessing the Natural Biology of Adeno-Associated Virus to Enhance the Efficacy of Cancer Gene Therapy. *Viruses*. 2021; 13 (7): 1205. DOI: 10.3390/v13071205. PubMed PMID: 34201599.
- Colón-Thillet R, Jerome KR, Stone D. Optimization of AAV vectors to target persistent viral reservoirs. *Virol J*. 2021; 18 (1): 85. DOI: 10.1186/s12985-021-01555-7. PubMed PMID: 33892762.
- Zhong L, Li B, Mah CS, Govindasamy L, Agbandje-McKenna M, Cooper M, et al. Next generation of adeno-associated virus 2 vectors: point mutations in tyrosines lead to high-efficiency transduction at lower doses. *Proc Natl Acad Sci U S A*. 2008; 105 (22): 7827–32. DOI: 10.1073/pnas.0802866105. PubMed PMID: 18511559.
- Kelemen RE, Mukherjee R, Cao X, Erickson SB, Zheng Y, Chatterjee A. A Precise Chemical Strategy To Alter the Receptor Specificity of the Adeno-Associated Virus. *Angew Chem Int Ed Engl*. 2016; 55 (36): 10645–9. DOI: 10.1002/anie.201604067. PubMed PMID: 27483453.
- Calcedo R, Morizono H, Wang L, McCarter R, He J, Jones D, et al. Adeno-associated virus antibody profiles in newborns, children, and adolescents. *Clin Vaccine Immunol*. 2011; 18 (9): 1586–8. DOI: 10.1128/CVI.05107-11. PubMed PMID: 21775517.
- Gadalla KKE, Vudhironarit T, Hector RD, Sিনnett S, Bahey NG, Bailey MES, et al. Development of a Novel AAV Gene Therapy Cassette with Improved Safety Features and Efficacy in a Mouse Model of Rett Syndrome. *Mol Ther Methods Clin Dev*. 2017; 5: 180–90. DOI: 10.1016/j.omtm.2017.04.007. PubMed PMID: 28497075.
- Golebiowski D, van der Bom IMJ, Kwon CS, Miller AD, Petrosky K, Bradbury AM, et al. Direct Intracranial Injection of AAVrh8 Encoding Monkey β -N-Acetylhexosaminidase Causes Neurotoxicity in the Primate Brain. *Hum Gene Ther*. 2017; 28 (6): 510–22. DOI: 10.1089/hum.2016.109. PubMed PMID: 28132521.
- Majowicz A, Maczuga P, Kwikkers KL, van der Marel S, van Logtenstein R, Petry H, et al. Mir-142-3p target sequences reduce transgene-directed immunogenicity following intramuscular adeno-associated virus 1 vector-mediated gene delivery. *J Gene Med*. 2013; 15 (6–7): 219–32. DOI: 10.1002/jgm.2712. PubMed PMID: 23658149.
- Chamberlain K, Riyadh JM, Weber T. Expressing Transgenes That Exceed the Packaging Capacity of Adeno-Associated Virus Capsids. *Hum Gene Ther Methods*. 2016; 27 (1): 1–12. DOI: 10.1089/hgtb.2015.140. PubMed PMID: 26757051.
- Kaepfel C, Beattie SG, Fronza R, van Logtenstein R, Salmon F, Schmidt S, et al. A largely random AAV integration profile after LPLD gene therapy. *Nat Med*. 2013; 19 (7): 889–91. DOI: 10.1038/nm.3230. PubMed PMID: 23770691.
- Liu M, Maurano MT, Wang H, Qi H, Song CZ, Navas PA, et al. Genomic discovery of potent chromatin insulators for human gene therapy. *Nat Biotechnol*. 2015; 33 (2): 198–203. DOI: 10.1038/nbt.3062. PubMed PMID: 25580597.
- Clark KR, Voulgaropoulou F, Fraley DM, Johnson PR. Cell lines for the production of recombinant adeno-associated virus. *Hum Gene Ther*. 1995; 6 (10): 1329–41. DOI: 10.1089/hum.1995.6.10-1329. PubMed PMID: 8590738.
- Clément N, Knop DR, Byrne BJ. Large-scale adeno-associated viral vector production using a herpesvirus-based system enables manufacturing for clinical studies. *Hum Gene Ther*. 2009; 20 (8): 796–806. DOI: 10.1089/hum.2009.094. PubMed PMID: 19569968.
- Grieger JC, Soltys SM, Samulski RJ. Production of Recombinant Adeno-associated Virus Vectors Using Suspension HEK293 Cells and Continuous Harvest of Vector From the Culture Media for GMP FIX and FLT1 Clinical Vector. *Mol Ther*. 2016; 24 (2): 287–97. DOI: 10.1038/mt.2015.187. PubMed PMID: 26437810.
- Kondratov O, Marsic D, Crosson SM, Mendez-Gomez HR, Moskalenko O, Mietzsch M, et al. Direct Head-to-Head Evaluation of Recombinant Adeno-associated Viral Vectors Manufactured in Human versus Insect Cells. *Mol Ther*. 2017; 25 (12): 2661–75. DOI: 10.1016/j.ymthe.2017.08.003. PubMed PMID: 28890324.
- Nass SA, Mattingly MA, Woodcock DA, Burnham BL, Ardinger JA, Osmond SE, et al. Universal Method for the Purification of Recombinant AAV Vectors of Differing Serotypes. *Mol Ther Methods Clin Dev*. 2017; 9: 33–46. DOI: 10.1016/j.omtm.2017.12.004. PubMed PMID: 29349097.
- Available from: https://en.wikipedia.org/wiki/Alipogene_tiparovec.
- Balasubramanian S, Aggarwal P, Sharma S. Lipoprotein Lipase Deficiency. In: *StatPearls Treasure Island (FL): StatPearls Publishing; 2021. PubMed PMID: 32809630*.
- Available from: https://en.wikipedia.org/wiki/Voretigene_neparovec.
- Available from: <https://www.askbio.com/newly-approved-spinal-muscular-atrophy-gene-therapy-zolgensma-validates-askbio-gene-therapy-platform/>.
- Available from: <https://clinicaltrials.gov/ct2/results?cond=&term=adeno-associated+virus&cntry=&state=&city=&dist=> retrieved on 2021-10-26.

Литература

- Chen W, Yao S, Wan J, Tian Y, Huang L, Wang S, et al. BBB-crossing adeno-associated virus vector: An excellent gene delivery tool for CNS disease treatment. *J Control Release*. 2021; 333: 129–38. DOI: 10.1016/j.jconrel.2021.03.029. PubMed PMID: 33775685.
- Wang D, Tai PWL, Gao G. Adeno-associated virus vector as a platform for gene therapy delivery. *Nat Rev Drug Discov*. 2019; 18 (5): 358–78. DOI: 10.1038/s41573-019-0012-9. PubMed PMID: 30710128.
- Wu Z, Yang H, Colosi P. Effect of genome size on AAV vector packaging. *Mol Ther*. 2010; 18 (1): 80–6. DOI: 10.1038/mt.2009.255. Epub 2009 Nov 10. PubMed PMID: 19904234.
- Bass-Stringer S, Bernardo BC, May CN, Thomas CJ, Weeks KL, McMullen JR. Adeno-Associated Virus Gene Therapy: Translational Progress and Future Prospects in the Treatment of Heart Failure. *Heart Lung Circ*. 2018; 27 (11): 1285–300. DOI: 10.1016/j.hlc.2018.03.005. PubMed PMID: 29703647.
- Greenberg B, Butler J, Felker GM, Ponikowski P, Voors AA, Desai AS, Barnard D, Bouchard A, Jaski B, Lyon AR, Pogoda JM, Rudy JJ, Zsebo KM. Calcium upregulation by percutaneous administration of gene therapy in patients with cardiac disease (CUPID 2): a randomised, multinational, double-blind, placebo-controlled, phase 2b trial. *Lancet*. 2016; 387 (10024): 1178–86. DOI: 10.1016/S0140-6736(16)00082-9. PubMed PMID: 26803443.
- Evans CH, Ghivizzani SC, Robbins PD. Gene Delivery to Joints by Intra-Articular Injection. *Hum Gene Ther*. 2018; 29 (1): 2–14. DOI: 10.1089/hum.2017.181. PubMed PMID: 29160173.
- Huang L, Wan J, Wu Y, Tian Y, Yao Y, Yao S, et al. Challenges in adeno-associated virus-based treatment of central nervous system diseases through systemic injection. *Life Sci*. 2021; 270: 119142. DOI: 10.1016/j.lfs.2021.119142. PubMed PMID: 33524419.
- Mijanović O, Branković A, Borovjagin A, Butnaru DV, Bezrukov EA, Sukhanov RB, Shpichka A, Timashev P, Ulasov I. Battling Neurodegenerative Diseases with Adeno-Associated Virus-Based Approaches. *Viruses*. 2020; 12 (4): 460. DOI: 10.3390/v12040460. PubMed PMID: 32325732.
- Privolizzi R, Chu WS, Tijani M, Ng J. Viral gene therapy for paediatric neurological diseases: progress to clinical reality. *Dev Med Child Neurol*. 2021; 63 (9): 1019–29. DOI: 10.1111/dmcn.14885. PubMed PMID: 33834479.
- Nawaz W, Huang B, Xu S, Li Y, Zhu L, Yiqiao H, et al. AAV-mediated in vivo CAR gene therapy for targeting human T-cell leukemia. *Blood Cancer J*. 2021; 11 (6): 119. DOI: 10.1038/s41408-021-00508-1. PubMed PMID: 34162832.
- Bower JJ, Song L, Bastola P, Hirsch ML. Harnessing the Natural Biology of Adeno-Associated Virus to Enhance the Efficacy of Cancer Gene Therapy. *Viruses*. 2021; 13 (7): 1205. DOI: 10.3390/v13071205. PubMed PMID: 34201599.
- Colón-Thillet R, Jerome KR, Stone D. Optimization of AAV vectors to target persistent viral reservoirs. *Virology*. 2021; 18 (1): 85. DOI: 10.1186/s12985-021-01555-7. PubMed PMID: 33892762.
- Zhong L, Li B, Mah CS, Govindasamy L, Agbandje-McKenna M, Cooper M, et al. Next generation of adeno-associated virus 2 vectors: point mutations in tyrosines lead to high-efficiency transduction at lower doses. *Proc Natl Acad Sci U S A*. 2008; 105 (22): 7827–32. DOI: 10.1073/pnas.0802866105. PubMed PMID: 18511559.
- Kelemen RE, Mukherjee R, Cao X, Erickson SB, Zheng Y, Chatterjee A. A Precise Chemical Strategy To Alter the Receptor Specificity of the Adeno-Associated Virus. *Angew Chem Int Ed Engl*. 2016; 55 (36): 10645–9. DOI: 10.1002/anie.201604067. PubMed PMID: 27483453.
- Calcedo R, Morizono H, Wang L, McCarter R, He J, Jones D, et al. Adeno-associated virus antibody profiles in newborns, children, and adolescents. *Clin Vaccine Immunol*. 2011; 18 (9): 1586–8. DOI: 10.1128/CVI.05107-11. PubMed PMID: 21775517.
- Gadalla KKE, Vudhironarit T, Hector RD, Sinnott S, Bahey NG, Bailey MES, et al. Development of a Novel AAV Gene Therapy Cassette with Improved Safety Features and Efficacy in a Mouse Model of Rett Syndrome. *Mol Ther Methods Clin Dev*. 2017; 5: 180–90. DOI: 10.1016/j.omtm.2017.04.007. PubMed PMID: 28497075.
- Golebiowski D, van der Bom IMJ, Kwon CS, Miller AD, Petrosky K, Bradbury AM, et al. Direct Intracranial Injection of AAVrh8 Encoding Monkey β -N-Acetylhexosaminidase Causes Neurotoxicity in the Primate Brain. *Hum Gene Ther*. 2017; 28 (6): 510–22. DOI: 10.1089/hum.2016.109. PubMed PMID: 28132521.
- Majowicz A, Maczuga P, Kwikkers KL, van der Marel S, van Logtenstein R, Petry H, et al. Mir-142-3p target sequences reduce transgene-directed immunogenicity following intramuscular adeno-associated virus 1 vector-mediated gene delivery. *J Gene Med*. 2013; 15 (6–7): 219–32. DOI: 10.1002/jgm.2712. PubMed PMID: 23658149.
- Chamberlain K, Riyad JM, Weber T. Expressing Transgenes That Exceed the Packaging Capacity of Adeno-Associated Virus Capsids. *Hum Gene Ther Methods*. 2016; 27 (1): 1–12. DOI: 10.1089/hgtb.2015.140. PubMed PMID: 26757051.
- Kaeppl C, Beattie SG, Fronza R, van Logtenstein R, Salmon F, Schmidt S, et al. A largely random AAV integration profile after LPLD gene therapy. *Nat Med*. 2013; 19 (7): 889–91. DOI: 10.1038/nm.3230. PubMed PMID: 23770691.
- Liu M, Maurano MT, Wang H, Qi H, Song CZ, Navas PA, et al. Genomic discovery of potent chromatin insulators for human gene therapy. *Nat Biotechnol*. 2015; 33 (2): 198–203. DOI: 10.1038/nbt.3062. PubMed PMID: 25580597.
- Clark KR, Voulgaropoulou F, Fraley DM, Johnson PR. Cell lines for the production of recombinant adeno-associated virus. *Hum Gene Ther*. 1995; 6 (10): 1329–41. DOI: 10.1089/hum.1995.6.10-1329. PubMed PMID: 8590738.
- Clément N, Knop DR, Byrne BJ. Large-scale adeno-associated viral vector production using a herpesvirus-based system enables manufacturing for clinical studies. *Hum Gene Ther*. 2009; 20 (8): 796–806. DOI: 10.1089/hum.2009.094. PubMed PMID: 19569968.
- Grieger JC, Soltys SM, Samulski RJ. Production of Recombinant Adeno-associated Virus Vectors Using Suspension HEK293 Cells and Continuous Harvest of Vector From the Culture Media for GMP FIX and FLT1 Clinical Vector. *Mol Ther*. 2016; 24 (2): 287–97. DOI: 10.1038/mt.2015.187. PubMed PMID: 26437810.
- Kondratov O, Marsic D, Crosson SM, Mendez-Gomez HR, Moskalenko O, Mietzsch M, et al. Direct Head-to-Head Evaluation of Recombinant Adeno-associated Viral Vectors Manufactured in Human versus Insect Cells. *Mol Ther*. 2017; 25 (12): 2661–75. DOI: 10.1016/j.yth.2017.08.003. PubMed PMID: 28890324.
- Nass SA, Mattingly MA, Woodcock DA, Burnham BL, Ardinger JA, Osmond SE, et al. Universal Method for the Purification of Recombinant AAV Vectors of Differing Serotypes. *Mol Ther Methods Clin Dev*. 2017; 9: 33–46. DOI: 10.1016/j.omtm.2017.12.004. PubMed PMID: 29349097.
- Available from: https://en.wikipedia.org/wiki/Alipogene_tiparovvec.
- Balasubramanian S, Aggarwal P, Sharma S. Lipoprotein Lipase Deficiency. In: *StatPearls Treasure Island (FL): StatPearls Publishing; 2021*. PubMed PMID: 32809630.
- Available from: https://en.wikipedia.org/wiki/Voretigene_neparovvec.
- Available from: <https://www.askbio.com/newly-approved-spinal-muscular-atrophy-gene-therapy-zolgensma-validates-askbio-gene-therapy-platform/>.
- Available from: <https://clinicaltrials.gov/ct2/results?cond=&term=adeno-associated+virus&cntry=&state=&city=&dist=> retrieved on 2021-10-26.

ALTERATIONS IN TANYCYTES AND RELATED CELL POPULATIONS OF ARCUATE NUCLEUS IN STREPTOZOTOCIN-INDUCED ALZHEIMER DISEASE MODEL

Voronkov DN , Stavrovskaya AV, Gushchina AS, Olshanskiy AS

Research Center of Neurology, Moscow, Russia

It is assumed that dysfunction of tanyocytes could be one of the components of pathogenesis of both Alzheimer disease and type 2 diabetes mellitus. The study was aimed to assess alterations in the tanyocyte morphology in the Alzheimer disease model. The 3 mg/kg streptozotocin dose was injected in the lateral ventricles of Wistar rats in order to model the Alzheimer disease. Alterations in hypothalamic tanyocytes were assessed 2 weeks, 4 weeks, 3 months and 6 months after administration of the toxin. Immunohistochemistry was used to identify the protein markers of tanyocytes (vimentin, nestin), astrocytes (GFAP, glutamine synthetase) and neurons (HuC/D), as well as to assess cell proliferation (with the use of Ki67 protein) and mitochondrial alterations (mitochondrial complex IV, PGC1a). Administration of streptozotocin lead to β -amyloid accumulation in hypothalamus and ventricular enlargement ($p < 0.001$). Streptozotocin damaged both $\alpha 1/\alpha 2$ tanyocytes and $\beta 1$ tanyocytes. The intensity of vimentin staining in $\alpha 1/\alpha 2$ tanyocytes decreased by week 4 ($p = 0.003$), and in $\beta 1$ tanyocytes it decreased in three months ($p < 0.001$). The same trend was observed for nestin. The number of Ki67+ nuclei decreased ($p < 0.05$), and the expression of proteins associated with mitochondria changed. The density of hypothalamic tanyocytes decreased by week 4 after administration of the toxin. Moreover, astrocyte activation was revealed. However, no prominent damage to both astrocytes and neurons was observed within four weeks after administration of streptozotocin. The revealed high tanyocyte vulnerability to streptozotocin is in line with the hypothesis of the role of damage to hypothalamic structures in both local and systemic metabolic disorders occurring in the Alzheimer disease models.

Keywords: hypothalamus, tanyocytes, streptozocine, Alzheimer disease

Author contribution: Voronkov DN — immunohistochemical study, morphometric study, data analysis and interpretation, manuscript writing; Stavrovskaya AV — study planning, stereotactic surgery, data analysis and interpretation, manuscript writing and editing; Gushchina AS, Olshanskiy AS — stereotactic surgery, specimens preparation for morphological study.

Compliance with ethical standards: the study was approved by the local Ethics Committee (protocol № 2–5/19 dated February 20, 2019). The animals were manipulated in accordance with the requirements of the European Convention for the Protection of Vertebral Animals Used for Experimental and Other Scientific Purposes (CETS № 170) and the Council of the European Communities Directive 2010/63/EU, order of the Ministry of Health of the Russian Federation № 119H "On Approval of Rules of Good Laboratory Practice" dated April 1, and GOST 33216-2014 "Rules for Working with Laboratory Rodents and Rabbits".

 **Correspondence should be addressed:** Dmitry N. Voronkov
per. Obukha, 5, Moscow, 105064, Russia; voronkov@neurology.ru

Received: 07.10.2021 **Accepted:** 21.10.2021 **Published online:** 29.10.2021

DOI: 10.24075/brsmu.2021.050

ИЗМЕНЕНИЯ ТАНИЦИТОВ И АССОЦИИРОВАННЫХ С НИМИ КЛЕТОЧНЫХ ПОПУЛЯЦИЙ АРКУАТНОГО ЯДРА В СТРЕПТОЗОЦИНОВОЙ МОДЕЛИ БОЛЕЗНИ АЛЬЦГЕЙМЕРА

Д. Н. Воронков , А. В. Ставровская, А. С. Гущина, А. С. Ольшанский

Научный центр неврологии, Москва, Россия

Предполагается, что дисфункция таницитов может быть одним из звеньев патогенеза как болезни Альцгеймера, так и диабета 2-го типа. Целью работы было охарактеризовать морфологические изменения таницитов при моделировании болезни Альцгеймера. Крысам линии Вистар вводили стрептозоцин в дозе 3 мг/кг в латеральные желудочки мозга для моделирования болезни Альцгеймера. Оценивали изменения таницитов гипоталамуса через 2, 4 недели, 3 и 6 месяцев после введения токсина. Иммуногистохимическим методом выявляли маркерные белки таницитов (виментин, нестин), астроглии (GFAP, глутаминсинтетазы) и нейронов (HuC/D), а также оценивали пролиферацию клеток (по белку Ki67) и митохондриальные изменения (митохондриальный комплекс IV, PGC1a). Введение стрептозоцина привело к накоплению β -амилоидного пептида в гипоталамусе и увеличению размеров желудочков ($p < 0,001$). Стрептозоцин повреждал как $\alpha 1/\alpha 2$, так и $\beta 1$ -танициты. Интенсивность окрашивания на виментин $\alpha 1/\alpha 2$ таницитов снижалась к 4-й неделе ($p = 0,003$), а $\beta 1$ -таницитов — через три месяца ($p < 0,001$). Ту же направленность изменений наблюдали и для нестина. Снижалось число Ki67+ ядер ($p < 0,05$) и менялась экспрессия белков, связанных с митохондриями. К 4-й неделе после введения токсина плотность таницитов гипоталамуса снижалась. Кроме того, выявили активацию астроглии, однако выраженного повреждения как астроцитов, так и нейронов до четырех недель после введения стрептозоцина не наблюдали. Выявленная повышенная уязвимость таницитов к действию стрептозоцина согласуется с предположением о роли повреждения структур гипоталамуса в развитии как локальных, так и системных метаболических нарушений при моделировании болезни Альцгеймера.

Ключевые слова: гипоталамус, танициты, стрептозоцин, болезнь Альцгеймера

Вклад авторов: Д. Н. Воронков — иммуногистохимическое исследование, морфометрический анализ, анализ и интерпретация данных, написание рукописи; А. В. Ставровская — планирование исследования, стереотаксические операции, анализ и интерпретация данных, написание и редактирование рукописи; А. С. Гущина, А. С. Ольшанский — стереотаксические операции, подготовка материала для морфологического исследования.

Соблюдение этических стандартов: исследование одобрено локальным этическим комитетом (решение № 2-5/19 от 20 февраля 2019 г.). Манипуляции с животными проводили в соответствии с требованиями European Convention for the Protection of Vertebral Animals Used for Experimental and Other Scientific Purposes (CETS № 170) и директивой Совета европейских сообществ 2010/63/ЕС, Приказом МЗ РФ № 119Н от 1 апреля 2016 г. «Об утверждении Правил лабораторной практики», а также «Правилами работы с лабораторными грызунами и кроликами» (ГОСТ 33216-2014).

 **Для корреспонденции:** Дмитрий Николаевич Воронков
пер. Обуха, д. 5, г. Москва, 105064, Россия; voronkov@neurology.ru

Статья получена: 07.10.2021 **Статья принята к печати:** 21.10.2021 **Опубликована онлайн:** 29.10.2021

DOI: 10.24075/vrgmu.2021.050

Streptozotocin (STZ), the glucosamine-nitrosourea derivative, is an alkylating agent, which causes DNA damage resulting in reduced proliferative activity and cell death. By virtue of chemical similarity with glucose, STZ has a high affinity for glucose transporter (GLUT2). It is selectively captured by pancreatic islet β -cells, which is used for pancreatic cancer therapy and, in case of systemic administration, to model diabetes mellitus in experimental animals [1]. The study, involving the use of pancreatic islet cells, showed that streptozotocin caused DNA breaks and activation of poly(ADP-ribose) polymerases (PARP), which in turn resulted in decreased levels of NAD (being the substrate for PARP) and cell death [2].

Single intracerebral injection of STZ causes neurodegeneration. It is assumed that STZ reduces local glucose metabolism and brain energy metabolism [3–5]. Intracerebroventricular injection of STZ results in progressive death of neurons in hippocampus and neocortex, white matter damage, and cholinergic system dysfunction, causing cognitive impairment in animals [3]. STZ-induced neurochemical changes are as follows: β -amyloid accumulation, tau hyperphosphorylation, and dysfunction of insulin receptors [6–8]. These effects of intracerebral STZ injection reproduce the features of sporadic Alzheimer disease (AD) and are in line with the “type 3 diabetes” hypothesis, which links neurodegeneration in AD and local insulin resistance [9–11]. However, the precise mechanisms of STZ effects on the brain have not yet been well explored, and the hypothesis of STZ-induced direct irreversible insulin receptor desensitization is criticized by some researchers [5].

It is assumed that dysregulation of hypothalamic systems, involved in maintaining energy homeostasis, is one of the causes of AD. Neuroimaging studies have revealed changes in hypothalamic nuclei of patients with AD. According to some sources, insulin resistance and diabetes increase the risk of AD [12]. However, pathologic changes in hypothalamic cell populations in the streptozotocin-induced AD model have not been thoroughly explored. In particular, alterations in tanycytes of the wall of the third ventricle are of interest. Tanycytes are chemosensitive glial ependymal cells. There are several tanycyte subtypes, $\alpha 1$, $\alpha 2$, $\beta 1$, $\beta 2$ [13], varying in neurochemical profiles, localization in the wall of the third ventricle, and connections with hypothalamic nuclei. Tanycytes are involved in homeostatic regulation, and serve as sensors of glucose, fatty acids and other nutrients, as well as of the hormones leptin, ghrelin and insulin, involved in regulation of metabolic processes [14, 15]. The effects of targeted tanycyte injury on obesity have been described, the role of tanycytes in the control of eating behavior and association of those with orexigenic neurons of the arcuate nucleus have been demonstrated [16, 17]. Tanycyte involvement in systemic regulation of energy metabolism suggests that dysfunction of tanycytes could be one of the components of pathogenesis of both AD and type 2 diabetes mellitus [15, 18]. There is no detailed description of the tanycyte response to intracerebroventricular injection of STZ. Specification of changes in hypothalamic structures in this popular AD model would help us to move towards understanding the contribution of damage to hypothalamic cell populations to the pathogenetic processes in AD and type 2 diabetes mellitus.

The study was aimed to assess the dynamic changes in the of hypothalamic tanycytes in the streptozotocin-induced Alzheimer disease model.

METHODS

Animals

The study involved 20 Wistar rats (males, 320–350 g, age 3 months by the beginning of the experiment) kept in the vivarium with constant access to food and water. The animals ($n = 16$) received intracerebroventricular (ICV) injections of STZ (Abcam; UK), and the control group ($n = 4$) received 0.9% NaCl solution. After administration of the toxin, the animals, which received STZ, were randomly divided into four groups (four animals per group) and withdrawn from the experiment by decapitation using the guillotine (OpenScience; Russia) 2 weeks, 4 weeks, 3 months and 6 months after injection.

Stereotactic surgery

STZ was dissolved in 0.9% NaCl in a dose of 3 mg/kg, 5 μ L of the solution were injected into each lateral ventricle using the stereotaxic manipulator (Stoelting; USA). The following coordinates were used for injection: AP = -0.8 ; L = 1.5; V = 3.5 (in accordance with Paxinos G, Watson C, “The Rat Brain in Stereotaxic Coordinates”). The combination of tiletamine/zolazepam in a dose of 3 mg/100 g, and intramuscular injection of the 3 mg/kg xylazine dose were used for anesthesia; the animals were premedicated with 0.04 mg/kg dose atropine administered by subcutaneous injection 10–15 min before xylazine hydrochloride administration.

Immunohistochemical analysis

For immunohistochemical study, brain specimens were fixed for 24 h in 4% formalin, and impregnated with 30% sucrose. Then the frozen frontal sections of the hypothalamus, 10 μ m thick, were prepared. Antigen unmasking was performed by heating the sections with citrate buffer (antigen retrieval buffer, pH = 6.0; Sigma; Germany) in the steamer for 20 min. The study involved the use of mouse monoclonal antibodies (Abcam; UK) against tanycyte markers, nestin (Nes) and vimentin (Vim), and rabbit polyclonal antibodies (Sigma; Germany) against astroglial proteins, glial fibrillary acidic protein (GFAP) and glutamine synthetase (GS). Neurons were identified using mouse antibodies (Invitrogen; USA) against the RNA-binding protein HuC/D. Mitochondrial alterations were assessed using the rabbit antibodies (Invitrogen; USA) against PGC1 α (transcriptional coactivator, regulator of mitochondrial biogenesis) and MT-CO1 (cytochrome C oxidase subunit I, mitochondrial respiratory chain complex IV). Cell proliferation was evaluated using the rabbit anti-Ki67 antibody (Dako; Denmark), and β -amyloid deposits were identified using the rabbit anti- β -amyloid 1–42 antibody (Sigma; Germany). The sections were incubated with primary antibodies for 24 h at room temperature; antibodies were diluted in accordance with the manufacturer's guidelines. Binding was visualized with the use of appropriate pairs of anti-mouse or anti-rabbit IgG secondary antibodies, conjugated with Alexa 488 or Alexa 555 fluorochromes (Invitrogen; USA). The slides were mounted with FluoroShield mounting medium (Abcam; UK), containing diamidino phenylindole (DAPI) for cell nuclei labeling.

Morphometric study and statistical data processing

The slides were examined using the Nikon Eclipse NiU fluorescence microscope (Nikon; Japan) with installed Nikon DS-Qi camera (Nikon; Japan) and NIS Elements software

(Nikon; Japan). The measurements were performed on the 12-bit images acquired using the same settings of the microscope illumination system with the 20x or 40x lens magnification. Areas of interest (lumen of the ventricle, cell nucleus or soma) were manually selected on the images using the graphic tablet (Wacom; Japan). Cell density and immunofluorescent stain intensity in the areas of interest were assessed in at least 25 fields of view in a series of 6–8 frontal slices acquired at various levels of hypothalamus (the results were presented as % of maximum brightness level — 4096 shades of gray). A total of 150–300 cells per animal were selected in the images in order to assess the intensity of MT-CO1 and PGC1 α immunofluorescent staining. The data acquired for one animal were averaged. The data acquired for the group were presented as median and interquartile range (Me [LQ; HQ]). Statistical analysis was carried out using the Statistica 12.0 (StatSoft; USA) and GraphPad Prism (GraphPad Software; USA) software. The differences between groups were evaluated with the nonparametric Kruskal Wallis test and subsequent Dunn's test for paired intergroup comparisons. The differences were considered significant when $p < 0.05$.

RESULTS

Intracerebroventricular injection of STZ resulted in the increasing damage to the wall of the third ventricle and hypothalamic structures. Macroanatomical study revealed the dilated third ventricle (Fig. 1A, D): in the second week after STZ administration the area of the third ventricle on the slice was significantly ($p < 0.001$) larger compared to controls (more than twice larger), and continued to further increase. By month 6 after administration, the area of the third

ventricle on the slice increased by more than 20 times, and necrosis was revealed in the adjacent hypothalamic nuclei. Simulation of pathomorphological findings, characteristic of Alzheimer disease, upon STZ administration was confirmed by accumulation of β -amyloid peptide 1–42 in hypothalamic structures (Fig. 1B).

When detecting vimentin, damage to gliopendymal elements of the wall of the third ventricle was observed (Fig. 1A). By week 4 after STZ administration, staining intensity in the zone of $\alpha 1$ and $\alpha 2$ tanyocyte (forming connections with dorsomedial and ventromedial hypothalamic nuclei respectively) localization significantly decreased ($p = 0.003$) compared to controls. The decrease in vimentin staining intensity in the zone of $\beta 1$ tanyocyte (projections to the arcuate nucleus) localization was less prominent, and significant changes ($p < 0.001$) were detected only three months after STZ administration. Ependymocytes of the dorsal region of the wall of the third ventricle remained intact until week 4 after administration of STZ. Distinct Vim+ tanyocytes of the hypothalamic median eminence persisted after three months, while there were found no Vim+ ependymal cells in other regions of the wall of the third ventricle by month 6. Our study was focused mostly on assessing the changes in the wall of the third ventricle 2 and 4 weeks after STZ administration due to rapidly increasing damage to tanyocytes.

Identification of both nestin and vimentin made it possible to demonstrate changes in the morphology of tanyocytes. Visually, during week 2 after STZ administration, there were thickened Vim+ processes and deformation of the ventricular wall ependymal layer in the zone of $\beta 1$ tanyocyte localization and the transition zone ($\beta 1/\alpha 2$ tanyocytes) (Fig. 2A). Similar changes were found when detecting nestin (Fig. 2A). The nestin staining intensity decreased by week 4 after STZ administration

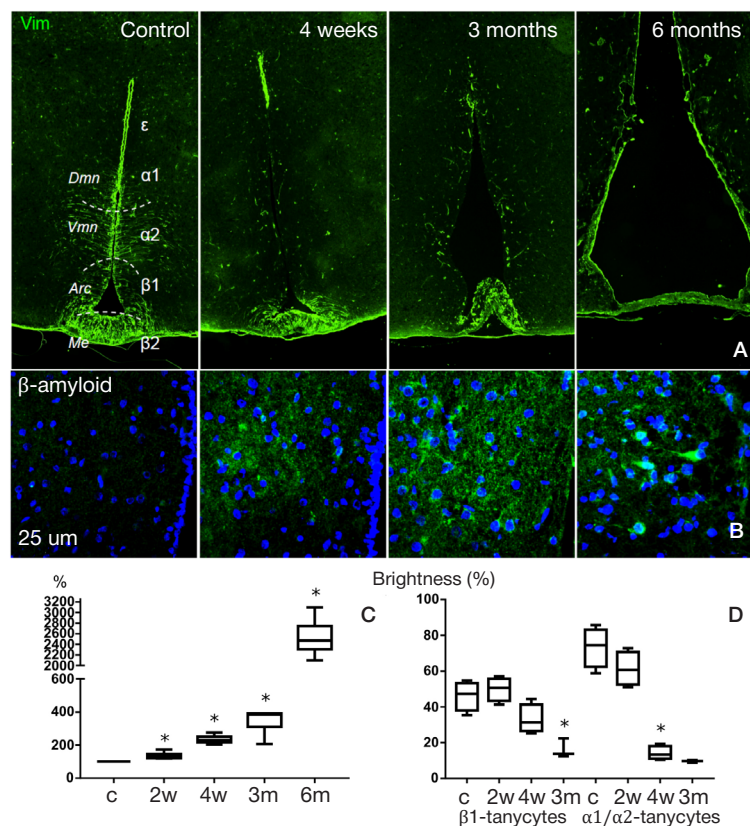


Fig. 1. Streptozotocin-induced changes in the third ventricle and adjacent structures. **A.** Identification of vimentin (Vim). **B.** Identification of β -amyloid in hypothalamic arcuate nucleus. **C.** Changes in the area of the third ventricle, % of the value of control (c). **D.** Changes in vimentin staining intensity (brightness, % of maximum levels) in the zone of $\beta 1$ tanyocyte and $\alpha 1/\alpha 2$ tanyocyte localization. c — control; 2w, 4w, 3m, 6m — groups 2 and 4 weeks, 3 and 6 months after administration of streptozotocin; * — $p < 0.05$; populations of tanyocytes ($\alpha 1$, $\alpha 2$, $\beta 1$, $\beta 2$) and ependymocytes (ϵ) are denoted by Greek letters; Dmn — dorsomedial hypothalamic nucleus; Vmn — ventromedial hypothalamic nucleus; Arc — hypothalamic arcuate nucleus; Me — hypothalamic median eminence

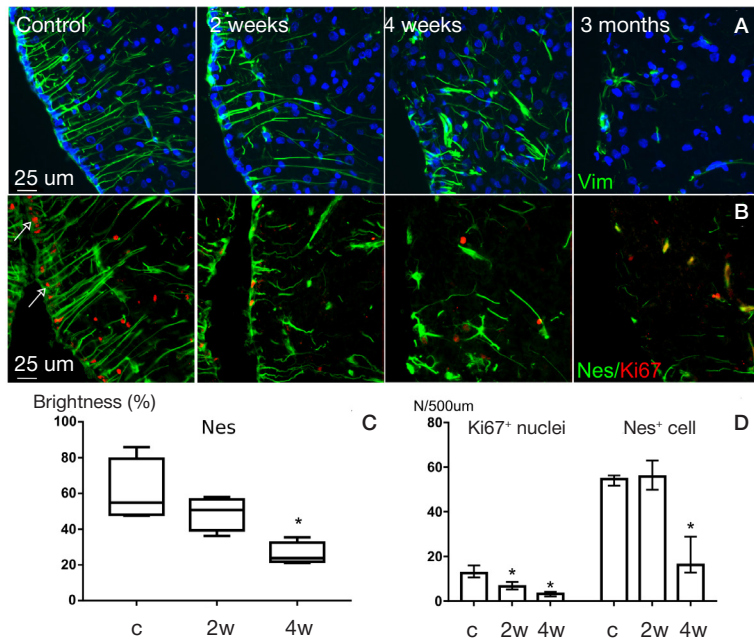


Fig. 2. Streptozotocin-induced changes in the morphology of tanycytes. **A.** Identification of vimentin (shown in green), DAPI staining of nuclei (blue). **B.** Identification of nestin (green) and Ki67 (red; arrows point to Ki67-positive nuclei). **C.** Changes in nestin staining intensity (brightness, % of maximum levels). **D.** Changes in the number of Nes⁺ and Ki67⁺ glial ependymal cells (number per unit of ventricular wall length). For notation see Fig. 1

compared to controls ($p = 0.024$), along with the Nes⁺ $\beta 1$ tanycyte density ($p < 0.001$) (Fig. 2C, D). However, the number of Ki-67-positive nuclei in tanycytes significantly decreased ($p = 0.049$; Fig. 2D) by week 2, which confirmed the effects of STZ on the proliferative activity of cells.

The damage to tanycytes was preceded by altered expression of proteins, associated with mitochondrial functions. Reduced intensity of tanycyte cytoplasm staining with anti-MTCO1 (mitochondrial respiratory chain complex IV) antibody

compared to controls ($p = 0.013$) was observed starting from week 2 after STZ administration, earlier than the reduction of tanycyte density and the decrease in nestin expression (Fig. 3A, B). Furthermore, MT-CO1 staining in cell bodies of the adjacent arcuate nucleus persisted, and counting neurons of the arcuate nucleus during weeks 2 and 4 after STZ administration revealed no significant decrease in the neuronal density compared to controls. Detection of transcriptional coactivator PGC1 α (involved in regulation of a number of mitochondrial functions)

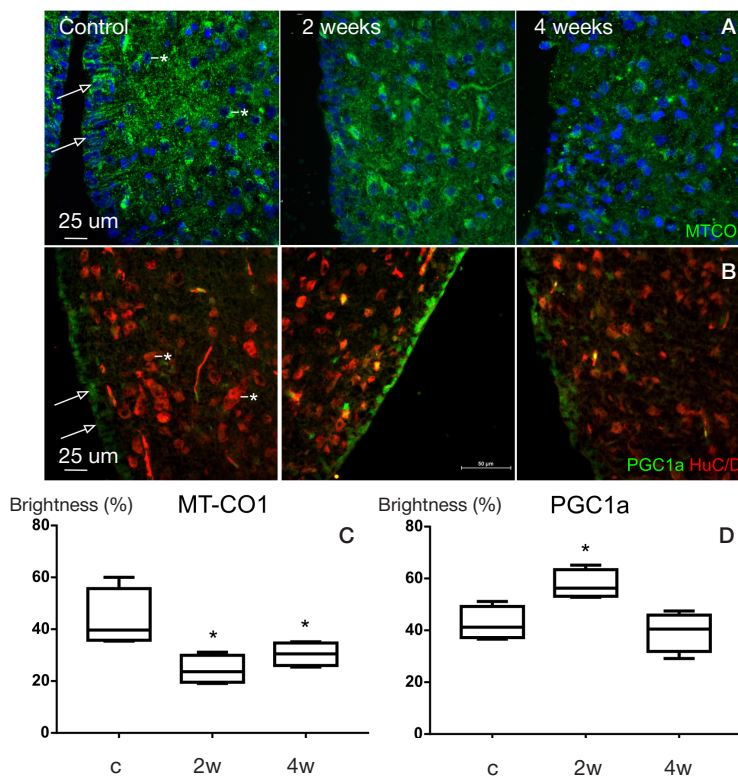


Fig. 3. Identification of tanycyte proteins associated with mitochondrial functions. **A.** Identification of MT-CO1 (mitochondrial respiratory chain complex IV); DAPI staining of nuclei (shown in blue). **B.** Identification of PGC1 α (green); neurons (red) were identified using the anti-HuC/D antibodies. **C.** Changes in tanycyte cell body MT-CO1 staining intensity (brightness, % of maximum levels). **D.** Changes in tanycyte cell nuclei PGC1 α staining intensity (brightness, % of maximum levels). Arrows point to tanycytes, neurons are marked with asterisks. For notation see Fig. 1

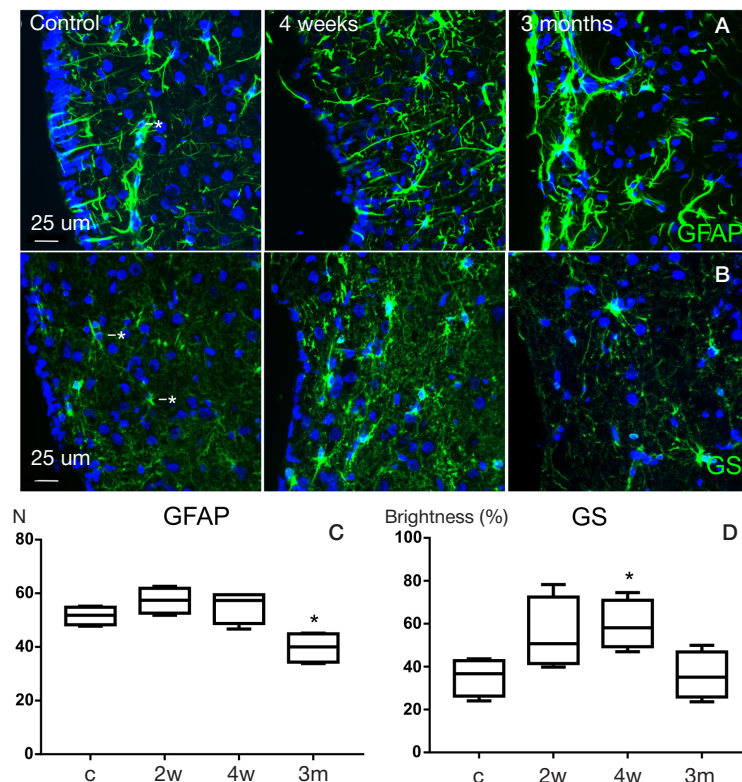


Fig. 4. Streptozotocin-induced changes in astroglia in the zone of hypothalamic arcuate nucleus (in the vicinity of the wall of the third ventricle). **A.** Identification of GFAP (shown in green); DAPI staining of nuclei (blue). **B.** Identification of glutamine synthetase (GS, green); DAPI staining of nuclei (blue). **C.** Changes in the number of GFAP-positive cells in the field of view. **D.** Changes in glutamine synthetase staining intensity (brightness, % of maximum levels). Astrocytes are marked with asterisks. For notation see Fig. 1

revealed the significantly ($p = 0.048$) increased intensity of tanyocyte nuclei staining by week 2 (Fig. 3B, C), while during week 4 after STZ administration, PGC1a staining intensity dropped to control values.

Immunohistochemical identification of GFAP and glutamine synthetase (GS) was used to assess the astroglial changes. In intact animals, GFAP was detected in the substantial proportion of ependymal cells, however, GS expression levels in tanyocytes appeared to be negligible compared to astroglia. Changes in the morphology of the GFAP-positive astrocytes in the arcuate nucleus had been already indicative of the STZ-induced reactive gliosis by week 2: thickening, deformation of processes and increased staining for glial cell markers were observed (Fig. 4A, B). The GS staining intensity increased by week 4 ($p = 0.03$), which was probably due to the increased area of astrocytes on the slice (Fig. 4B, D). However, the number (density) of astrocytes did not increase early after STZ administration and significantly decreased compared to controls by month 3 ($p = 0.019$; Fig. 4C). In general, changes in astroglia were indicative of the increasing neuroinflammatory response in hypothalamic structures adjacent to the third ventricle. Although STZ caused damage to astrocytes, these cells appeared to be more resistant to the toxin compared to tanyocytes.

To summarize the findings, it can be noted that STZ administration resulted in β -amyloid accumulation in hypothalamic structures, including neurons of arcuate nucleus, and in ventricular enlargement, which was probably due to the damage to glial ependymal elements. Tanyocytes of various types were susceptible to STZ, however, both $\alpha 1/\alpha 2$ tanyocytes and $\beta 1$ tanyocytes were damaged early after STZ administration, as manifested in reduced proliferative activity and altered expression of proteins, associated with mitochondria. These alterations occurred before the detection of the prominent tanyocyte morphology impairment. The $\beta 1$ tanyocyte density in

the third ventricle decreased by week 4 after STZ administration. Moreover, STZ caused reactive changes in astrocytes and damage to astroglia, however, there were no changes in the density of both astrocytes and neurons of arcuate nucleus within four weeks after administration of the toxin, which was indicative of higher tanyocyte vulnerability to STZ compared to other hypothalamic cell populations.

DISCUSSION

The majority of papers on studying morphological and neurochemical changes in streptozotocin-induced models are focused on hippocampal research due to the role of hippocampus in cognitive impairment, associated with AD. These data are in line with alterations, revealed during our study. Thus, experiments, involving intraventricular or intracisternal STZ administration, demonstrate β -amyloid accumulation in hippocampus three months after administration of the toxin, altered expression of synaptic proteins, as well as neuronal cell death and reduced hippocampal volume [3, 19]. The effects of STZ on the hippocampal astrocytes have been identified: the reduced number and altered structure of the astrocyte processes have been demonstrated [20]. Reduced hippocampal expression of insulin receptors upon administration of STZ has been found [21]. Since astrocytes are believed to be the target cells for insulin, and the knockout of astrocytic insulin receptors leads to cognitive impairment in animals [22], it can be assumed that dysfunction in glial components plays a vital part in STZ-induced localized metabolic disorders.

No data on tanyocyte alterations in humans with AD have been presented in the literature. Only the age-related changes in the tanyocyte processes' organization have been described [23]. However, degenerative changes, β -amyloid accumulation

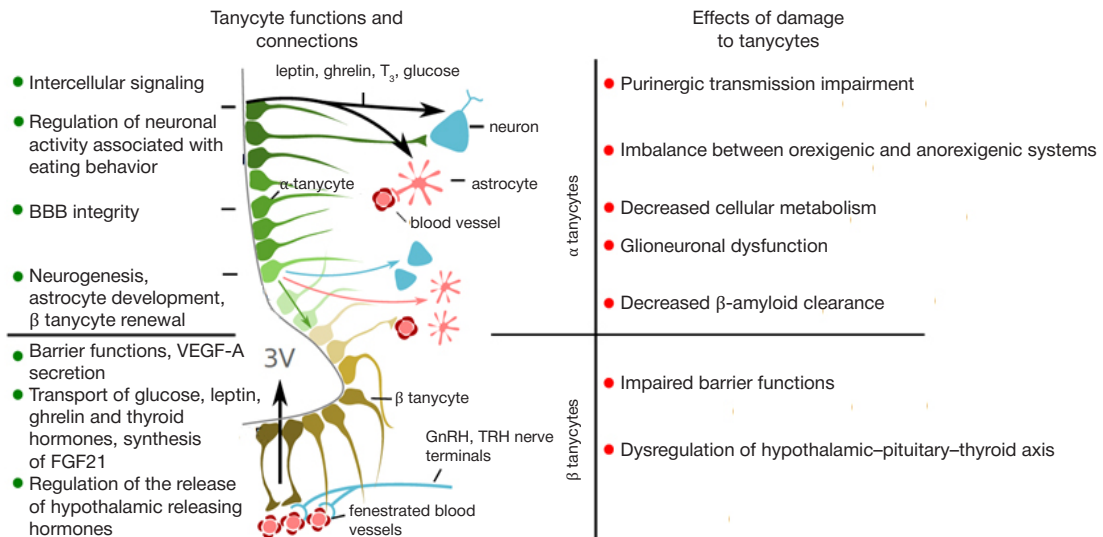


Fig. 5. Interaction between tanyocytes and hypothalamic structures, and potential effects of damage to tanyocytes. BBB — blood-brain barrier; VEGF-A — vascular endothelial growth factor A; FGF21 — fibroblast

and mitochondrial dysfunction in hypothalamic nuclei are found during pathological studies [24].

The mechanisms, underlying hypothalamic dysfunction in humans with AD, are poorly understood. Apart from neurodegeneration, many researchers assign an important role to alterations in synthesis, secretion and transport of hypothalamic hormones and factors [18, 24], involved in homeostatic regulation of hypothalamic-pituitary axis, which could be mediated by dysfunction of tanyocytes. For example, tanyocytes are involved in regulation of the thyroliberin release and serve as a main source of triiodothyronine in the brain. Furthermore, neuroprotective effects of both thyroliberin and triiodothyronine have been demonstrated in AD models [25, 26].

Tanyocytes express the GLUT2 transporter [13, 27] and are therefore one of the target cells for STZ; the damage to tanyocytes, revealed during our study, is the intended effect of the toxin administration. The cause of the more prominent damage to α tanyocytes, observed during our study, may be associated with uneven pattern of glucose transporter expression and the frequency of various tanyocyte populations renewal, as well as with tanyocyte metabolic features, which should be further clarified. The differences seen in dynamic changes in nestin and vimentin levels can be explained by the fact that the content of vimentin in α and β tanyocytes is different, although all types of tanyocytes express these proteins [18]. Moreover, there have been reports of multidirectional changes in regulation of cytoskeletal proteins in tanyocytes [28].

It is important that the STZ-induced changes in tanyocytes preceded other hypothalamic changes, associated with neurodegeneration and neuroinflammation. In general, considering the fact that tanyocytes modulate neurons of ventromedial, dorsomedial and arcuate hypothalamic nuclei, and are involved in regulation of both local and systemic energy metabolism, as well as in regulation of eating behavior [15, 18, 29], the damage to tanyocytes is likely to result in the carbohydrate metabolism disorders, observed in this AD model [30, 31]. However, hypothalamic dysfunction upon STZ administration and the previously reported hypothalamic neurodegeneration during the final stages [31] may be triggered by neuroinflammatory response, involving tanyocytes and other cell populations.

The decreased intensity of tanyocyte staining for MT-CO1 (cytochrome C oxidase subunit I) we have identified is consistent with the decreased cytochrome C oxidase activity

in streptozotocin-induced diabetes model [32]. Studying brain cortex and hippocampus in animals, which received STZ, revealed reduced activity of pyruvate dehydrogenase, α -ketoglutarate dehydrogenase, and cytochrome C oxidase in mitochondria of both neocortex and hippocampus [33]. Moreover, the reduced activity of mitochondrial complexes I–III upon intracerebroventricular injection of STZ was revealed [34]. These data emphasize mitochondrial sensitivity to STZ, previously studied *in vitro* [35]. The increased expression of PGC1 α (regulator of mitochondrial biogenesis), observed early after STZ administration, could be considered a compensatory response to the developing disorders. The return to baseline PGC1 α levels could be indicative of partial function recovery in the intact tanyocytes. In turn, PGC1 α dysregulation is associated with neuroinflammatory processes and could be considered one of the factors, contributing to neuronal damage in AD [36, 37]. The STZ-induced dynamic changes in mitochondrial dysfunction, observed in various structures, have yet to be assessed.

It would be interesting to juxtapose the observed STZ-induced decrease in tanyocyte proliferation with the previously reported effects of this toxin on the hippocampal neural stem cells [38], as well as with its high toxicity in immature neurons [39]. Since tanyocytes are likely to have neurogenic potential [40], the STZ-induced impairment of proliferation and apoptosis in hypothalamic neural stem cells can exert the long-term effects, associated with impaired plasticity of hypothalamic neural networks, involved in homeostatic control.

Fig. 5 (according to [14, 15, 17, 18]) summarizes some functions of α and β tanyocytes, which are suspected of being involved in pathological changes in the streptozotocin-induced AD models. The potential tanyocyte involvement in the pathogenesis of AD suggests the possibility of developing the pharmacological methods for the tanyocyte function correction. Some authors believe that the tanyocyte proliferation regulation via exposure to growth factors could be provided [18].

CONCLUSIONS

The findings demonstrate increased sensitivity of hypothalamic tanyocytes to STZ, reduced tanyocyte proliferative activity and the associated mitochondrial alterations. Astrocyte activation and neuronal damage are preceded by alterations in tanyocytes. The changes, observed in the mediobasal hypothalamus, suggest that the damage to tanyocytes plays a vital part in local

and systemic metabolic disorders occurring in the Alzheimer disease models. The possible functional consequences of damage to tanycytes are as follows: impaired barrier function

and downregulated cellular metabolism in hypothalamic structures, unbalanced orexigenic and anorexigenic effects, dysregulation of the hypothalamic-pituitary-thyroid axis.

References

- Elsner M, Guldbakke B, Tiedge M, Munday R, Lenzen S. Relative importance of transport and alkylation for pancreatic beta-cell toxicity of streptozotocin. *Diabetologia*. 2000; 43 (12): 1528–33.
- Guzyk MM, Dyakun KO, Yanytska LV, Pryvotska IB, Krynytska IY, Pishel IM, et al. Inhibitors of Poly(ADP-Ribose)Polymerase-1 as Agents Providing Correction of Brain Dysfunctions Induced by Experimental Diabetes. *Neurophysiology*. 2017; 49 (3): 183–93.
- Knezovic A, Osmanovic-Barilar J, Curlin M, Hof PR, Simic G, Riederer P, et al. Staging of cognitive deficits and neuropathological and ultrastructural changes in streptozotocin-induced rat model of Alzheimer's disease. *Journal of Neural Transmission*. 2015; 122 (4): 577–92.
- Osmanovic-Barilar J, Knezovic A, Grünblatt E, Riederer P, Salkovic-Petrisic M. Nine-month follow-up of the insulin receptor signalling cascade in the brain of streptozotocin rat model of sporadic Alzheimer's disease. *Journal of Neural Transmission*. 2015; 122 (4): 565–76.
- Grieb P. Intracerebroventricular Streptozotocin Injections as a Model of Alzheimer's Disease: in Search of a Relevant Mechanism. *Molecular Neurobiology*. 2016; 53 (3): 1741–52.
- Grünblatt E, Salkovic-Petrisic M, Osmanovic J, Riederer P, Hoyer S. Brain insulin system dysfunction in streptozotocin intracerebroventricularly treated rats generates hyperphosphorylated tau protein. *Journal of Neurochemistry*. 2007; 101 (3): 757–70.
- Rajasekar N, Dwivedi S, Nath C, Hanif K, Shukla R. Protection of streptozotocin induced insulin receptor dysfunction, neuroinflammation and amyloidogenesis in astrocytes by insulin. *Neuropharmacology*. 2014; 86: 337–52.
- Ravelli KG, Rosário B dos A, Camarini R, Hernandez MS, Britto LR. Intracerebroventricular Streptozotocin as a Model of Alzheimer's Disease: Neurochemical and Behavioral Characterization in Mice. *Neurotoxicity Research*. 2017; 31 (3): 327–33.
- Kandimalla R, Thirumala V, Reddy PH. Is Alzheimer's disease a Type 3 Diabetes? A critical appraisal. *Biochimica et Biophysica Acta (BBA) - Molecular Basis of Disease*. 2017; 1863 (5): 1078–89.
- Gupta S, Yadav K, Mantri SS, Singhal NK, Ganesh S, Sandhir R. Evidence for Compromised Insulin Signaling and Neuronal Vulnerability in Experimental Model of Sporadic Alzheimer's Disease. *Molecular Neurobiology*. 2018; 55 (12): 8916–35.
- Gorina YaV, Komleva YuK, Lopatina OL, Chernyh AI, Salmina AB. Jekspressija molekul — komponentov insulin-oposredovanoj signal'noj transdukcii v kletkah golovnogo mozga pri jeksperimental'noj bolezni Al'cgejmera. *Annaly klinicheskoi i jeksperimental'noj neurologii*. 2019; 13 (4): 28–37. DOI: 10.25692/ACEN.2019.4.5. Russian.
- Vercruyse P, Vieau D, Blum D, Petersen A, Dupuis L. Hypothalamic Alterations in Neurodegenerative Diseases and Their Relation to Abnormal Energy Metabolism. *Front Mol Neurosci*. 2018; 11: 2. DOI: 10.3389/fnmol.2018.00002.
- Rizzoti K, Lovell-Badge R. Pivotal role of median eminence tanycytes for hypothalamic function and neurogenesis. *Molecular and Cellular Endocrinology*. 2017; 445: 7–13.
- Geller S, Arribat Y, Netzahualcoyotzi C, Lagarrigue S, Carneiro L, Zhang L, et al. Tanycytes Regulate Lipid Homeostasis by Sensing Free Fatty Acids and Signaling to Key Hypothalamic Neuronal Populations via FGF21 Secretion. *Cell Metabolism*. 2019; 30 (4): 833–44.
- Bolborea M, Langlet F. What is the physiological role of hypothalamic tanycytes in metabolism? *American Journal of Physiology-Regulatory, Integrative and Comparative Physiology*. 2021; 320 (6): R994–R1003.
- Yoo S, Cha D, Kim S, Jiang L, Cooke P, Adebisin M, et al. Tanycyte ablation in the arcuate nucleus and median eminence increases obesity susceptibility by increasing body fat content in male mice. *Glia*. 2020; 68 (10): 1987–2000.
- Bolborea M, Pollatzek E, Benford H, Sotelo-Hitschfeld T, Dale N. Hypothalamic tanycytes generate acute hyperphagia through activation of the arcuate neuronal network. *Proceedings of the National Academy of Sciences*. 2020; 117 (25): 14473–81.
- Raikwar SP, Bhagavan SM, Ramaswamy SB, Thangavel R, Dubova I, Selvakumar GP, et al. Are Tanycytes the Missing Link Between Type 2 Diabetes and Alzheimer's Disease? *Molecular Neurobiology*. 2019; 56 (2): 833–43.
- Ahn Y, Seo J, Park J, Won J, Yeo HG, Kim K, et al. Synaptic loss and amyloid beta alterations in the rodent hippocampus induced by streptozotocin injection into the cisterna magna. *Lab Anim Res*. 2020; 36: 17.
- Zappa Villar MF, López Hanotte J, Falomir Lockhart E, Trípodí LS, Morel GR, Reggiani PC. Intracerebroventricular streptozotocin induces impaired Barnes maze spatial memory and reduces astrocyte branching in the CA1 and CA3 hippocampal regions. *J Neural Transm (Vienna)*. 2018; 125 (12): 1787–803. DOI: 10.1007/s00702-018-1928-7.
- Agrawal R, Tyagi E, Shukla R, Nath C. Insulin receptor signaling in rat hippocampus: a study in STZ (ICV) induced memory deficit model. *Eur Neuropsychopharmacol*. 2011; 21 (3): 261–73. DOI: 10.1016/j.euroneuro.2010.11.009.
- González-García I, Gruber T, García-Cáceres, C. Insulin action on astrocytes: From energy homeostasis to behaviour. *J Neuroendocrinol*. 2021; 33 (4): e12953. DOI: 10.1111/jne.12953.
- Koopman ACM, Taziaux M, Bakker J. Age-related changes in the morphology of tanycytes in the human female infundibular nucleus/median eminence. *J Neuroendocrinol*. 2017; 29 (5). DOI: 10.1111/jne.12467.
- Ishii M, Iadecola C. Metabolic and Non-Cognitive Manifestations of Alzheimer's Disease: The Hypothalamus as Both Culprit and Target of Pathology. *Cell Metab*. 2015; 22 (5): 761–76. DOI: 10.1016/j.cmet.2015.08.016
- Daimon CM, Chirdon P, Maudsley S, Martin B. The role of Thyrotropin Releasing Hormone in aging and neurodegenerative diseases. *Am J Alzheimer's Dis (Columbia)*. 2013; 1 (1). DOI: 10.7726/ajad.2013.1003
- Rodríguez-Rodríguez A, Lázcano I, Sánchez-Jaramillo E, Uribe RM, Jaimes-Hoy L, Joseph-Bravo P, et al. Tanycytes and the Control of Thyrotropin-Releasing Hormone Flux Into Portal Capillaries. *Front Endocrinol (Lausanne)*. 2019; 10: 401. DOI: 10.3389/fendo.2019.00401.
- García M de los A, Millán C, Balmaceda-Aguilera C, Castro T, Pastor P, Montecinos H, et al. Hypothalamic ependymal-glia cells express the glucose transporter GLUT2, a protein involved in glucose sensing. *Journal of Neurochemistry*. 2003; 86 (3): 709–24.
- Lewis JE, Ebling FJ. Tanycytes As Regulators of Seasonal Cycles in Neuroendocrine Function. *Front Neurol*. 2017; 8: 79. DOI: 10.3389/fneur.2017.00079. PMID: 28344570; PMCID: PMC5344904.
- Uranga RM, Millán C, Barahona MJ, Recabal A, Salgado M, Martínez F, et al. Adenovirus-mediated suppression of hypothalamic glucokinase affects feeding behavior. *Scientific Reports*. 2017; 7 (1): 3697.
- Bloch K, Gil-Ad I, Vanichkin A, Hornfeld SH, Koroukhov N, Taler M, et al. Intracerebroventricular Streptozotocin Induces Obesity and Dementia in Lewis Rats. *Journal of Alzheimer's Disease*. 2017; 60 (1): 121–36.
- Stavrovskaya AV, Voronkov DN, Shestakova EA, Gushchina AS, Olshansky AS, Yamshikova NG. Streptozotocin-inducirovannaja bolezni' Al'cgejmera kak samostojatel'nyj faktor riska razvitiya giperglikemii u krys linii Vistar. *Problemy jendokrinologii*. 2019; 65

- (5): 351–61. Russian.
32. Raza H, Prabu SK, John A, Avadhani NG. Impaired Mitochondrial Respiratory Functions and Oxidative Stress in Streptozotocin-Induced Diabetic Rats. *International Journal of Molecular Sciences*. 2011; 12 (5): 3133–47.
 33. Correia SC, Santos RX, Santos MS, Casadesus G, LaManna JC, Perry G, et al. Mitochondrial Abnormalities in a Streptozotocin-Induced Rat Model of Sporadic Alzheimer's Disease. *Current Alzheimer Research*. 2013; 10 (4). Available from: <https://DOI.org/10.2174/1567205011310040006>
 34. Poddar J, Singh S, Kumar P, Bali S, Gupta S, Chakrabarti S. Inhibition of complex I-III activity of brain mitochondria after intracerebroventricular administration of streptozotocin in rats is possibly related to loss of body weight. *Heliyon*. 2020; 6 (7): e04490.24.
 35. Genrikhs EE, Stelmashook EV, Golyshev SA, Aleksandrova OP, Isaev NK. Streptozotocin causes neurotoxic effect in cultured cerebellar granule neurons. *Brain Research Bulletin*. 2017; 130: 90–94. ht
 36. Sweeney G, Song J. The association between PGC-1 α and Alzheimer's disease. *Anatomy and Cell Biology*. 2016; 49 (1): 1.
 37. Rius-Pérez S, Torres-Cuevas I, Millán I, Ortega ÁL, Pérez S. PGC-1 α , Inflammation, and Oxidative Stress: An Integrative View in Metabolism. *Oxidative Medicine and Cellular Longevity*. 2020; 1–20.
 38. Sun P, Ortega G, Tan Y, Hua Q, Riederer PF, Deckert J, et al. Streptozotocin Impairs Proliferation and Differentiation of Adult Hippocampal Neural Stem Cells in Vitro—Correlation With Alterations in the Expression of Proteins Associated With the Insulin System. *Frontiers in Aging Neuroscience*. 2018; 10. Available from: <https://DOI.org/10.3389/fnagi.2018.00145>.
 39. Isaev NK, Genrikhs EE, Voronkov DN, Kapkaeva MR, Stelmashook EV. Streptozotocin toxicity in vitro depends on maturity of neurons. *Toxicology and Applied Pharmacology*. 2018; 348: 99–104.
 40. Yoo S, Kim J, Lyu P, Hoang TV, Ma A, Trinh V, et al. Control of neurogenic competence in mammalian hypothalamic tanycytes. *Science Advances*. 2021; 7 (22): eabg3777. Available from: <https://DOI.org/10.1126/sciadv.abg3777>.

Литература

1. Elsner M, Guldbakke B, Tiedge M, Munday R, Lenzen S. Relative importance of transport and alkylation for pancreatic beta-cell toxicity of streptozotocin. *Diabetologia*. 2000; 43 (12): 1528–33.
2. Guzyk MM, Dyakun KO, Yanytska LV, Pryvrotska IB, Krynytska IY, Pishel IM, et al. Inhibitors of Poly(ADP-Ribose) Polymerase-1 as Agents Providing Correction of Brain Dysfunctions Induced by Experimental Diabetes. *Neurophysiology*. 2017; 49 (3): 183–93.
3. Knezovic A, Osmanovic-Barilar J, Curlin M, Hof PR, Simic G, Riederer P, et al. Staging of cognitive deficits and neuropathological and ultrastructural changes in streptozotocin-induced rat model of Alzheimer's disease. *Journal of Neural Transmission*. 2015; 122 (4): 577–92.
4. Osmanovic-Barilar J, Knezovic A, Grünblatt E, Riederer P, Salkovic-Petrisic M. Nine-month follow-up of the insulin receptor signalling cascade in the brain of streptozotocin rat model of sporadic Alzheimer's disease. *Journal of Neural Transmission*. 2015; 122 (4): 565–76.
5. Grieb P. Intracerebroventricular Streptozotocin Injections as a Model of Alzheimer's Disease: in Search of a Relevant Mechanism. *Molecular Neurobiology*. 2016; 53 (3): 1741–52.
6. Grünblatt E, Salkovic-Petrisic M, Osmanovic J, Riederer P, Hoyer S. Brain insulin system dysfunction in streptozotocin intracerebroventricularly treated rats generates hyperphosphorylated tau protein. *Journal of Neurochemistry*. 2007; 101 (3): 757–70.
7. Rajasekar N, Dwivedi S, Nath C, Hanif K, Shukla R. Protection of streptozotocin induced insulin receptor dysfunction, neuroinflammation and amyloidogenesis in astrocytes by insulin. *Neuropharmacology*. 2014; 86: 337–52.
8. Ravelli KG, Rosário B dos A, Camarini R, Hernandez MS, Britto LR. Intracerebroventricular Streptozotocin as a Model of Alzheimer's Disease: Neurochemical and Behavioral Characterization in Mice. *Neurotoxicity Research*. 2017; 31 (3): 327–33.
9. Kandimalla R, Thirumala V, Reddy PH. Is Alzheimer's disease a Type 3 Diabetes? A critical appraisal. *Biochimica et Biophysica Acta (BBA) - Molecular Basis of Disease*. 2017; 1863 (5): 1078–89.
10. Gupta S, Yadav K, Mantri SS, Singhal NK, Ganesh S, Sandhir R. Evidence for Compromised Insulin Signaling and Neuronal Vulnerability in Experimental Model of Sporadic Alzheimer's Disease. *Molecular Neurobiology*. 2018; 55 (12): 8916–35.
11. Горина Я. В., Комлева Ю. К., Лопатина О. Л., Черных А. И., Салмина А. Б. Экспрессия молекул — компонентов инсулин-опосредованной сигнальной трансдукции в клетках головного мозга при экспериментальной болезни Альцгеймера. *Анналы клинической и экспериментальной неврологии*. 2019; 13 (4): 28–37. DOI: 10.25692/ACEN.2019.4.5.
12. Vercauysse P, Vieau D, Blum D, Petersen A, Dupuis L. Hypothalamic Alterations in Neurodegenerative Diseases and Their Relation to Abnormal Energy Metabolism. *Front Mol Neurosci*. 2018; 11: 2. DOI: 10.3389/fnmol.2018.00002.
13. Rizzoti K, Lovell-Badge R. Pivotal role of median eminence tanycytes for hypothalamic function and neurogenesis. *Molecular and Cellular Endocrinology*. 2017; 445: 7–13.
14. Geller S, Arribat Y, Netzahualcoyotzi C, Lagarrigue S, Carneiro L, Zhang L, et al. Tanycytes Regulate Lipid Homeostasis by Sensing Free Fatty Acids and Signaling to Key Hypothalamic Neuronal Populations via FGF21 Secretion. *Cell Metabolism*. 2019; 30 (4): 833–44.
15. Bolborea M, Langlet F. What is the physiological role of hypothalamic tanycytes in metabolism? *American Journal of Physiology-Regulatory, Integrative and Comparative Physiology*. 2021; 320 (6): R994–R1003.
16. Yoo S, Cha D, Kim S, Jiang L, Cooke P, Adebesein M, et al. Tanycyte ablation in the arcuate nucleus and median eminence increases obesity susceptibility by increasing body fat content in male mice. *Glia*. 2020; 68 (10): 1987–2000.
17. Bolborea M, Pollatzek E, Benford H, Sotelo-Hitschfeld T, Dale N. Hypothalamic tanycytes generate acute hyperphagia through activation of the arcuate neuronal network. *Proceedings of the National Academy of Sciences*. 2020; 117 (25): 14473–81.
18. Raikwar SP, Bhagavan SM, Ramaswamy SB, Thangavel R, Dubova I, Selvakumar GP, et al. Are Tanycytes the Missing Link Between Type 2 Diabetes and Alzheimer's Disease? *Molecular Neurobiology*. 2019; 56 (2): 833–43.
19. Ahn Y, Seo J, Park J, Won J, Yeo HG, Kim K, et al. Synaptic loss and amyloid beta alterations in the rodent hippocampus induced by streptozotocin injection into the cisterna magna. *Lab Anim Res*. 2020; 36: 17.
20. Zappa Villar MF, López Hanotte J, Falomir Lockhart E, Trípodí LS, Morel GR, Reggiani PC. Intracerebroventricular streptozotocin induces impaired Barnes maze spatial memory and reduces astrocyte branching in the CA1 and CA3 hippocampal regions. *J Neural Transm (Vienna)*. 2018; 125 (12): 1787–803. DOI: 10.1007/s00702-018-1928-7.
21. Agrawal R, Tyagi E, Shukla R, Nath C. Insulin receptor signaling in rat hippocampus: a study in STZ (ICV) induced memory deficit model. *Eur Neuropsychopharmacol*. 2011; 21 (3): 261–73. DOI: 10.1016/j.euroneuro.2010.11.009.
22. González-García I, Gruber T, García-Cáceres C. Insulin action on astrocytes: From energy homeostasis to behaviour. *J Neuroendocrinol*. 2021; 33 (4): e12953. DOI: 10.1111/jne.12953.
23. Koopman ACM, Taziaux M, Bakker J. Age-related changes in the morphology of tanycytes in the human female infundibular nucleus/median eminence. *J Neuroendocrinol*. 2017; 29 (5). DOI: 10.1111/jne.12467.
24. Ishii M, Iadecola C. Metabolic and Non-Cognitive Manifestations of Alzheimer's Disease: The Hypothalamus as Both Culprit and Target of Pathology. *Cell Metab*. 2015; 22 (5): 761–76. DOI: 10.1016/j.cmet.2015.08.016
25. Daimon CM, Chirdon P, Maudsley S, Martin B. The role of

- Thyrotropin Releasing Hormone in aging and neurodegenerative diseases. *Am J Alzheimers Dis (Columbia)*. 2013; 1 (1): 10. DOI: 10.7726/ajad.2013.1003
26. Rodríguez-Rodríguez A, Lazcano I, Sánchez-Jaramillo E, Uribe RM, Jaimes-Hoy L, Joseph-Bravo P, et al. Tanycytes and the Control of Thyrotropin-Releasing Hormone Flux Into Portal Capillaries. *Front Endocrinol (Lausanne)*. 2019; 10: 401. DOI: 10.3389/fendo.2019.00401.
 27. García M de los A, Millán C, Balmaceda-Aguilera C, Castro T, Pastor P, Montecinos H, et al. Hypothalamic ependymal-glia cells express the glucose transporter GLUT2, a protein involved in glucose sensing. *Journal of Neurochemistry*. 2003; 86 (3): 709–24.
 28. Lewis JE, Ebling FJ. Tanycytes As Regulators of Seasonal Cycles in Neuroendocrine Function. *Front Neurol*. 2017; 8: 79. DOI: 10.3389/fneur.2017.00079. PMID: 28344570; PMCID: PMC5344904.
 29. Uranga RM, Millán C, Barahona MJ, Recabal A, Salgado M, Martínez F, et al. Adenovirus-mediated suppression of hypothalamic glucokinase affects feeding behavior. *Scientific Reports*. 2017; 7 (1): 3697.
 30. Bloch K, Gil-Ad I, Vanichkin A, Hornfeld SH, Koroukhov N, Taler M, et al. Intracerebroventricular Streptozotocin Induces Obesity and Dementia in Lewis Rats. *Journal of Alzheimer's Disease*. 2017; 60 (1): 121–36.
 31. Ставровская А. В., Воронков Д. Н., Шестакова Е. А., Гущина А. С., Ольшанский А. С., Ямщикова Н. Г. Стрептозоцин-индуцированная болезнь Альцгеймера как самостоятельный фактор риска развития гипергликемии у крыс линии Вистар. *Проблемы эндокринологии*. 2019; 65 (5): 351–61.
 32. Raza H, Prabu SK, John A, Avadhani NG. Impaired Mitochondrial Respiratory Functions and Oxidative Stress in Streptozotocin-Induced Diabetic Rats. *International Journal of Molecular Sciences*. 2011; 12 (5): 3133–47.
 33. Correia SC, Santos RX, Santos MS, Casadesus G, LaManna JC, Perry G, et al. Mitochondrial Abnormalities in a Streptozotocin-Induced Rat Model of Sporadic Alzheimer's Disease. *Current Alzheimer Research*. 2013; 10 (4). Available from: <https://DOI.org/10.2174/1567205011310040006>
 34. Poddar J, Singh S, Kumar P, Bali S, Gupta S, Chakrabarti S. Inhibition of complex I-III activity of brain mitochondria after intracerebroventricular administration of streptozotocin in rats is possibly related to loss of body weight. *Heliyon*. 2020; 6 (7): e04490.24.
 35. Genrikhs EE, Stelmashook EV, Golyshev SA, Aleksandrova OP, Isaev NK. Streptozotocin causes neurotoxic effect in cultured cerebellar granule neurons. *Brain Research Bulletin*. 2017; 130: 90–94. ht
 36. Sweeney G, Song J. The association between PGC-1 α and Alzheimer's disease. *Anatomy and Cell Biology*. 2016; 49 (1): 1.
 37. Rius-Pérez S, Torres-Cuevas I, Millán I, Ortega ÁL, Pérez S. PGC-1 α , Inflammation, and Oxidative Stress: An Integrative View in Metabolism. *Oxidative Medicine and Cellular Longevity*. 2020; 1–20.
 38. Sun P, Ortega G, Tan Y, Hua Q, Riederer PF, Deckert J, et al. Streptozotocin Impairs Proliferation and Differentiation of Adult Hippocampal Neural Stem Cells in Vitro-Correlation With Alterations in the Expression of Proteins Associated With the Insulin System. *Frontiers in Aging Neuroscience*. 2018; 10. Available from: <https://DOI.org/10.3389/fnagi.2018.00145>.
 39. Isaev NK, Genrikhs EE, Voronkov DN, Kapkaeva MR, Stelmashook EV. Streptozotocin toxicity in vitro depends on maturity of neurons. *Toxicology and Applied Pharmacology*. 2018; 348: 99–104.
 40. Yoo S, Kim J, Lyu P, Hoang TV, Ma A, Trinh V, et al. Control of neurogenic competence in mammalian hypothalamic tanycytes. *Science Advances*. 2021; 7 (22): eabg3777. Available from: <https://DOI.org/10.1126/sciadv.abg3777>.

MOYAMOYA DISEASE AS A POSSIBLE CAUSE OF ISCHEMIC STROKE IN ADULT PATIENTS

Vishnyakova AY¹, Rostovtseva TM¹, Kovrazhkina EA¹, Golovin DA¹, Gubsky IL¹, Lelyuk SE², Lelyuk VG¹¹ Federal Center of Brain Research and Neurotechnologies, Moscow, Russia² Russian Medical Academy of Postgraduate Education, Moscow, Russia

Moyamoya disease (MMD) is a rare progressive idiopathic arteriopathy that usually leads to ischemic stroke (IS) in young children, especially of East Asian origin. MMD can cause IS in the Caucasian race, too, but often remains unverified. The diagnosis of MMD relies on diagnostic radiology findings. Magnetic resonance imaging (MRI) is widely used in Japan to identify asymptomatic individuals with hereditary predisposition to MMD. There are no official statistics on MMD in Russia. A patient experiencing an acute cerebrovascular accident (CVA) is hospitalized to a stroke unit, where they undergo a multislice computed tomography (MSCT) scan of the brain. Below, we report the results of a complex radiological examination, which included MRI (T2, FLAIR, SWI, 3D-TOF), cerebral MSCT perfusion imaging, CT angiography of intracranial arteries, duplex ultrasonography of brachiocephalic arteries and was conducted in 4 adult Caucasian patients (3 men and 1 woman aged 38, 39, 51, and 57 years, respectively) with a past IS caused by MMD. We hope that the findings of different imaging techniques may be helpful in establishing the timely diagnosis of MMD and optimizing the treatment strategies.

Keywords: moyamoya disease, ischemic stroke, brain MRI, MR-angiography, CT-angiography, duplex ultrasonography, transcranial duplex ultrasonography

Funding: the study was part of the State Assignment 056-00171-19-01. Topic ID: AAAA-A19-119042590018-0 (March 29, 2019).

Author contribution: Vishnyakova AY — literature analysis, imaging, data analysis and interpretation, manuscript preparation; Rostovtseva TM — imaging, data analysis and interpretation, figures; Kovrazhkina EA — clinical examination; Golovin DA — imaging; Gubsky IL — data analysis and interpretation; Lelyuk SE — manuscript editing; Lelyuk VG — study concept, manuscript editing.

Compliance with ethical standards: the study was approved by the Ethics Committee of FSBI Federal Center of Brain Research and Neurotechnologies of the Federal Medical Biological Agency (Protocol dated October 4, 2021). All patients gave informed consent to participate in the study.

✉ **Correspondence should be addressed:** Anastasia Yu. Vishnyakova
Ostrovityanova 1, str. 10, Moscow, 117997, Russia; vishau@yandex.ru

Received: 29.09.2021 **Accepted:** 13.10.2021 **Published online:** 31.10.2021

DOI: 10.24075/brsmu.2021.052

БОЛЕЗНЬ МОЯМОЯ КАК ВОЗМОЖНАЯ ПРИЧИНА ИШЕМИЧЕСКОГО ИНСУЛЬТА У ВЗРОСЛЫХ

А. Ю. Вишнякова¹, Т. М. Ростовцева¹, Е. А. Ковражкина¹, Д. А. Головин¹, И. Л. Губский¹, С. Э. Лелюк², В. Г. Лелюк¹¹ Федеральный центр мозга и нейротехнологий, Москва, Россия² Российская медицинская академия непрерывного профессионального образования, Москва, Россия

Болезнь моямоя (БММ) — редкая прогрессирующая идиопатическая артериопатия, являющаяся, как правило, причиной ишемического инсульта (ИИ) у детей младшего возраста, особенно в странах Восточной Азии. В редких случаях БММ может вызвать ИИ у взрослых лиц европеоидной расы, однако зачастую остается неverified. Для диагностики данной патологии применяют разные лучевые методы. В Японии отдается предпочтение магнитно-резонансной томографии (МРТ), где ввиду широкой распространенности БММ МРТ применяют для скрининга асимптомных лиц с наследственной предрасположенностью. Официальная статистика по БММ в России отсутствует. В случае развития острого нарушения мозгового кровообращения (ОНМК) пациенты поступают в стационар инсультной сети, где им проводят рентгеновскую мультиспиральную компьютерную томографию (МСКТ) головного мозга. Представлены клинические случаи применения комплексного лучевого исследования, а именно магнитно-резонансной томографии (МРТ) (T2, FLAIR, SWI, 3D-TOF), перфузионной компьютерной томографии (КТ) головного мозга, КТ-ангиографии интракраниальных артерий, ультразвукового дуплексного сканирования брахиоцефальных артерий (ДС БЦА) четырех взрослых пациентов (трех мужчин и женщины в возрасте 38, 39, 51 и 57 лет) европеоидной расы с БММ, ставшей причиной развития ИИ. Описание результатов применения разных лучевых методов может помочь в своевременной верификации данной патологии и оптимизации дальнейшей тактики лечения.

Ключевые слова: болезнь моямоя, ишемический инсульт, МРТ головного мозга, МР-ангиография, КТ-ангиография, ультразвуковое дуплексное сканирование, транскраниальное дуплексное сканирование.

Финансирование: работа выполнена в рамках Государственного задания № 056-00171-19-01. Регистрационный номер темы AAAA-A19-119042590018-0 от 29 марта 2019.

Вклад авторов: А. Ю. Вишнякова — анализ литературы, лучевое исследование пациентов, анализ и интерпретация данных, подготовка рукописи; Т. М. Ростовцева — лучевое исследование пациентов, анализ и интерпретация данных, подготовка рисунков; Е. А. Ковражкина — клиническое обследование пациентов; Д. А. Головин — лучевое исследование пациентов; И. Л. Губский — анализ и интерпретация полученных данных; С. Э. Лелюк — редактирование статьи; В. Г. Лелюк — концепция, редактирование статьи.

Соблюдение этических стандартов: исследование одобрено локальным этическим комитетом ФЦМН (протокол от 4 октября 2021 г.), Все пациенты подписали информированное согласие на участие в исследовании.

✉ **Для корреспонденции:** Анастасия Юрьевна Вишнякова
ул. Островитянова, д. 1, стр. 10, г. Москва, 117997, Россия; vishau@yandex.ru

Статья получена: 29.09.2021 **Статья принята к печати:** 13.10.2021 **Опубликована онлайн:** 31.10.2021

DOI: 10.24075/vrgmu.2021.052

Moyamoya disease is a rare cerebrovascular disorder, a kind of idiopathic arteriopathy that manifests as progressive stenosis of terminal internal carotid arteries (ICAs) and/or proximal parts of arteries forming the circle of Willis, including the middle (MCA) and anterior (ACA) cerebral arteries, and is accompanied by the development of an abnormal vascular network at the base

of the brain [1]. In Russia, no official statistics are available on MMD but the disease is recognized as a possible cause of stroke in young children [2, 3]. MMD was first described in 1957 by two Japanese doctors Takeuchi and Shimizu; the name “moyamoya” proposed in 1967 means “a puff of smoke” in Japanese and refers to the angiographic appearance of the

abnormal blood vessels at the base of the brain [4, 5]. The highest prevalence of MMD is observed in East Asia (Japan and Korea), reaching ~3.16 cases per 100,000 population, which is 7–10 times higher than in other world regions [6, 7].

The underlying pathogenetic mechanisms of MMD are not fully clear. Common histopathologic findings in the affected vascular wall include fibrocellular intimal thickening, folded and contracted internal elastic lamina, proliferation of smooth muscle cells, and thinning of the media; no signs of inflammation or atherosclerosis are reported [8, 9]. The collateral vessels at the base of the brain traditionally referred to as moyamoya vessels are formed by dilated lenticulostriate, thalamic or choroidal anastomoses [9, 10]. Based on the severity of damage to the main cerebral arteries and the degree of involvement of the collateral vessels, 6 MMD stages are distinguished [11].

Genome-wide linkage analysis and whole-exome sequencing have identified the *RNF213* gene on chromosome 17q25 as the main susceptibility gene for MMD in East Asians [12]; later studies have demonstrated the remarkable variation of this gene across different ethnic groups [13]. According to Korean researchers, the 4950G>A polymorphism of the *RNF213* gene is implicated in MMD in adults and therefore may be a potential biomarker for this disease [14].

MMD is characterized by bimodal age distribution with incidence peaks at 5–10 years and in the fourth decade of life [1, 7, 9]. Women are affected twice as often as men. The disease has ischemic and hemorrhagic presentations [7, 9, 15]. According to studies conducted in small cohorts of adult European patients with idiopathic MMD, cerebral ischemia is a typical manifestation in this subpopulation [16].

Patients with MMD are at high risk for recurrent vascular accidents: the Kaplan-Meier estimate for the risk of recurrent IS within 5 years after the first episode is 80.95% [17].

Therefore, the importance of timely MMD diagnosis cannot be overestimated. The primary treatment option for this condition is surgery (cerebral revascularization) which aims to reduce the risk of recurrent strokes [2, 6, 18].

This article highlights the role of MMD as a potential cause of IS in adults, requiring timely diagnosis.

Clinical cases

In 2020, 426 patients with a past history of CVA underwent a clinical examination at the Federal Center of Brain Research and Neurotechnologies (Moscow, Russia). Three patients with a history of IS were found to have MMD. One patient with MMD was examined at the outpatient facility. Only 1 patient had been diagnosed with MMD prior to this study; 3 patients had never been diagnosed with MMD before.

Patients

Patient B, 38 years old, suffered a lacunar stroke in 2016 manifesting as sudden dizziness that spontaneously resolved shortly afterwards. The patient was referred to Sklifosovsky Research Institute of Emergency Medicine, where he was diagnosed with stage 3 MMD. The patient had two extracranial-intracranial (EC-IC) bypass surgeries for his condition in 2017 and 2018.

Patient G, 39 years old, had IS in the right MCA territory in February 2020. Following treatment and rehabilitation, the patient was able to walk around his house using a cane and perform some self-care activities. On admission to the Center, the patient was in his late rehabilitation period; his stroke subtype was cryptogenic.

Patient Yu, 51 years old, developed clinical symptoms in September 2017, including sudden facial nerve paresis, difficulty

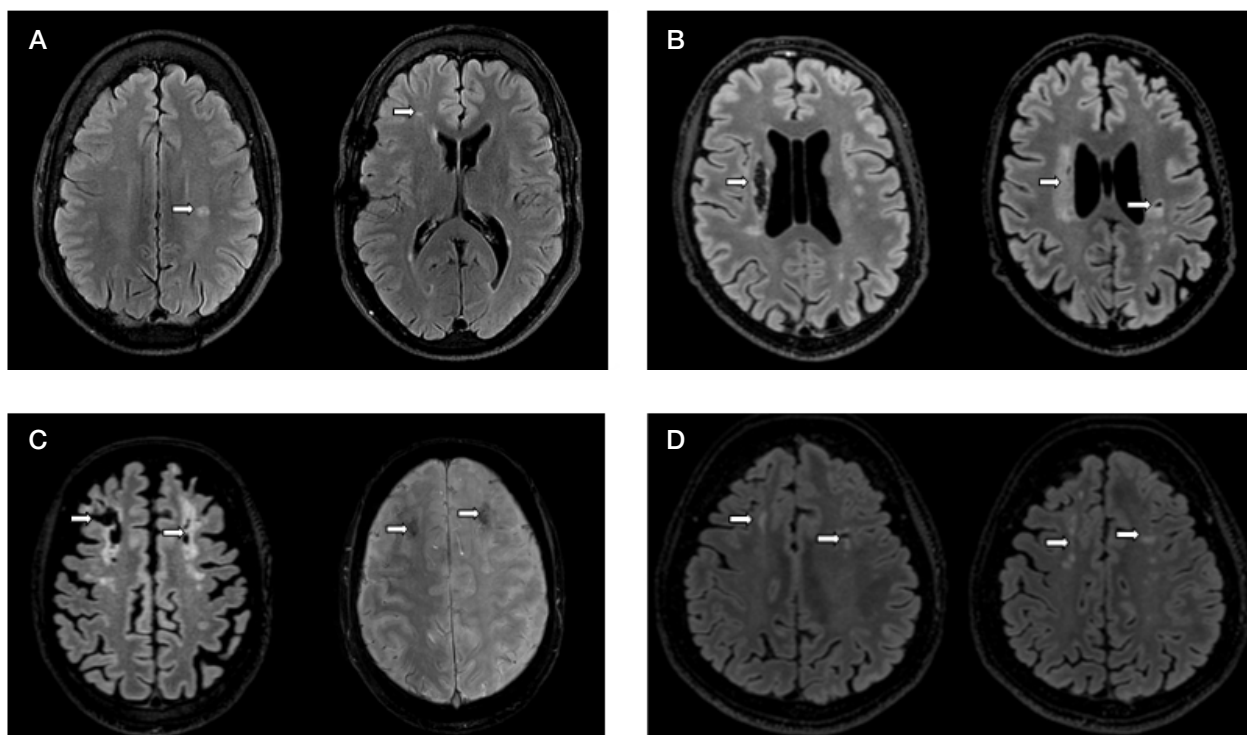


Fig. 1. MR images showing changes in the brain of adult patients with moyamoya disease after a cerebral infarction. **A.** Patient B (axial FLAIR): a small area of reactive changes in the left posterior frontal lobe white matter; small scanty areas of white matter gliosis in the right frontal lobe (the border zone between MCA and ACA) are indicated by arrows. **B.** Patient G (axial FLAIR): gliotic and cystic lesions in the putamen and the semioval center (the lateral lenticulostriate artery territory) in the right hemisphere; similar lesions in the left semioval center (the internal watershed area); the lesions are marked by arrows. **C.** Patient Yu (left image: axial FLAIR; right image: axial SWI): hemorrhagic transformation (petechiae) after a past cerebral infarction (hemorrhage infarction type 1 according to ECASS II) in the frontal lobe white matter (the border zone between MCA and ACA) is indicated by arrows. **D.** Patient V (axial FLAIR): multiple areas of gliosis and a small lesion after a past lacunar stroke in the frontal lobe white matter (the border zone between MCA and ACA) are indicated by arrows.

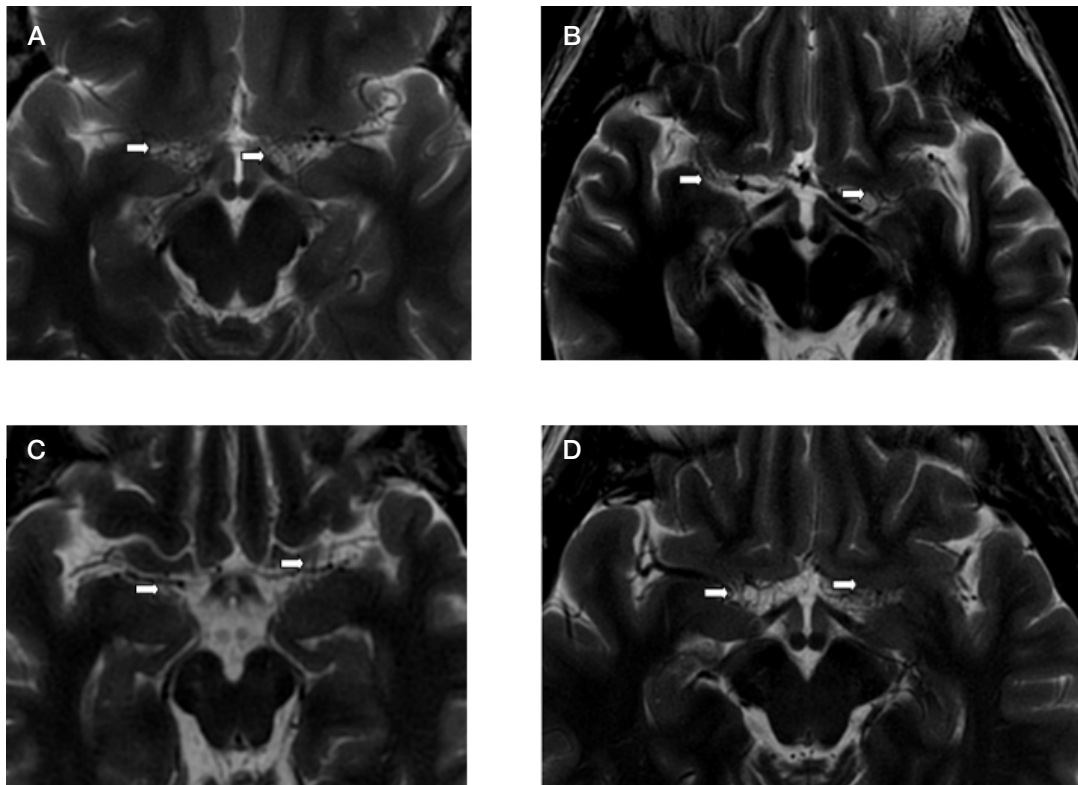


Fig. 2. MR images of the abnormal vascular network at the base of the brain of adult patients with moyamoya disease (axial T2 WI). Proximal parts of MCA segments are not visualized clearly; a network of small blood vessels indicated by *arrows* is visible in their projection. **A.** Patient B. **B.** Patient G. **C.** Patient Yu. **D.** Patient V

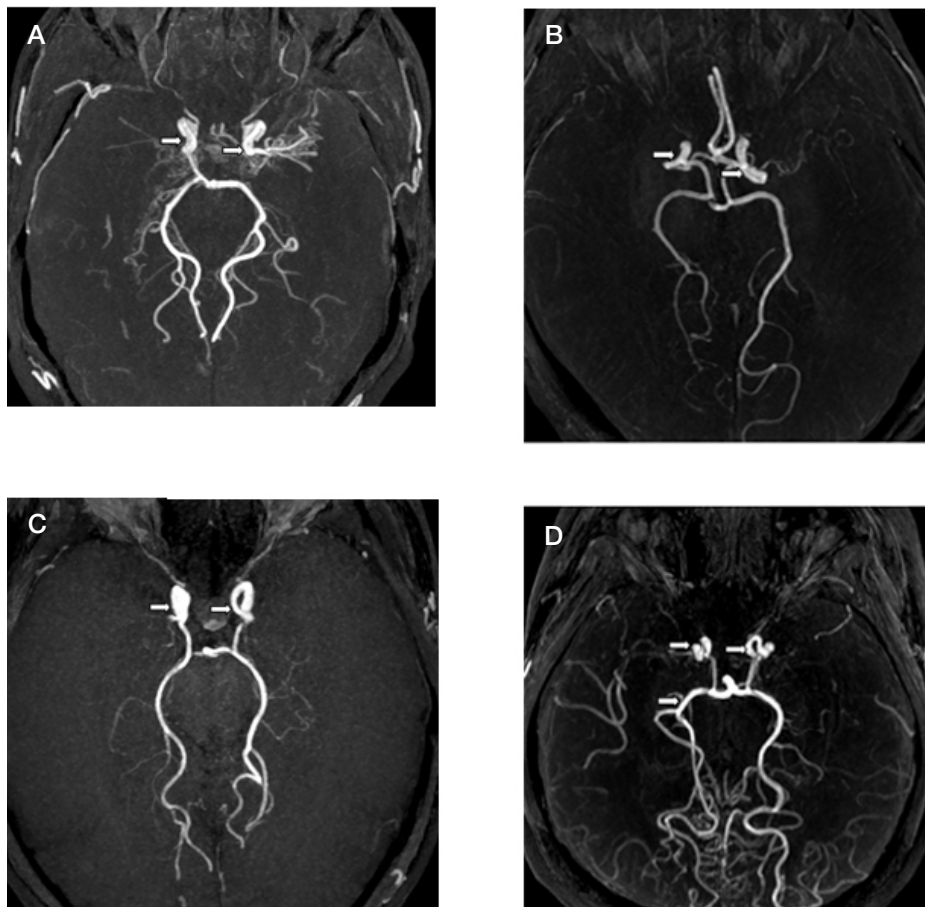


Fig. 3. 3D-TOF MR angiograms showing vascular changes in adult patients with moyamoya disease. **A.** Patient B: the absence of flow signal from distal ICA and MCA (*arrows*). Proximal parts of ACA are visible and stenotic. PCAs are intact. **B.** Patient G: significant luminal narrowing of distal ICA, the absence of flow signal from MCA (*arrows*). ACAs are intact. PCComs and PCAs are slightly dilated. **C.** Patient Yu: the absence of flow signal from distal ICA and MCA and ACA (*arrows*). PCComs and PCAs are intact. **D.** Patient V: the absence of flow signal from distal ICA and MCA and ACA. PCComs and PCAs are dilated (*arrows*)

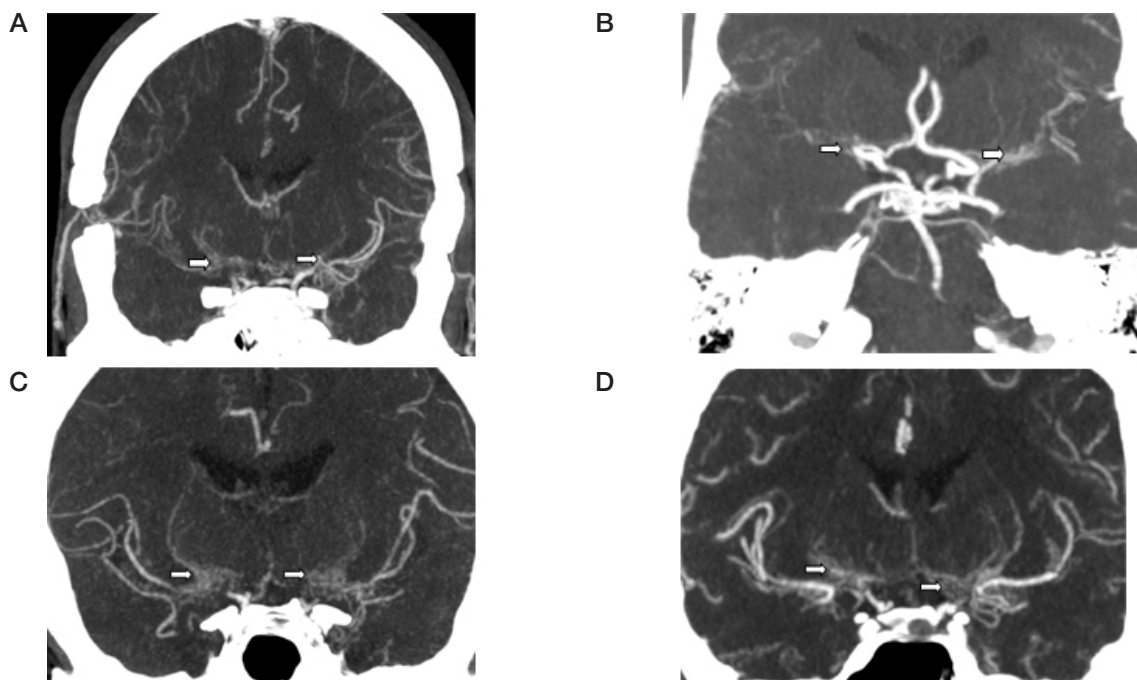


Fig. 4. Oblique coronal CT angiographic images of intracranial arteries showing vascular changes in the brain of adult patients with moyamoya disease. **A.** Patient B: distal segments of both ICAs and proximal parts of both MCAs are not visualized due to occlusion; a network of small anastomotic vessels is visible in their projection. The images show enhancement of lenticulostriate arteries in the basal ganglia area. Craniotomy marks are observed on temporal bones on both sides; circulation is visualized in extra- and intracranial anastomoses. **B.** Patient G: distal segments of both ICAs are stenotic, both MCA are occluded; a network of small anastomotic vessels is visualized in their projection. ACAs are visible along their course and have a normal diameter. **C.** Patient Yu: distal segments of both ICAs and proximal parts of both MCAs are occluded; a network of small anastomotic blood vessels is visualized in their projection. **D.** Patient V: distal segments of both ICAs and proximal parts of both MCAs are occluded, a network of small anastomotic blood vessels is visualized in their projection. Lenticulostriate arteries in the basal ganglia area are contrast-enhanced

swallowing and slurred speech. The patient was hospitalized to a local medical facility. MRI of the brain revealed multiple lesions in the white matter of both cerebral hemispheres. The lesions were interpreted as demyelinating, which determined the choice of further treatment until September 2019, when the patient underwent a few additional tests. The tests did

not confirm multiple sclerosis. On admission to the Center, the official diagnosis was mixed encephalopathy, sequelae of cryptogenic stroke registered in September 2017 and March 2018.

Female patient V, 57 years old, had a lacunar IS in the left MCA when she was 36; at that time the patient developed mild

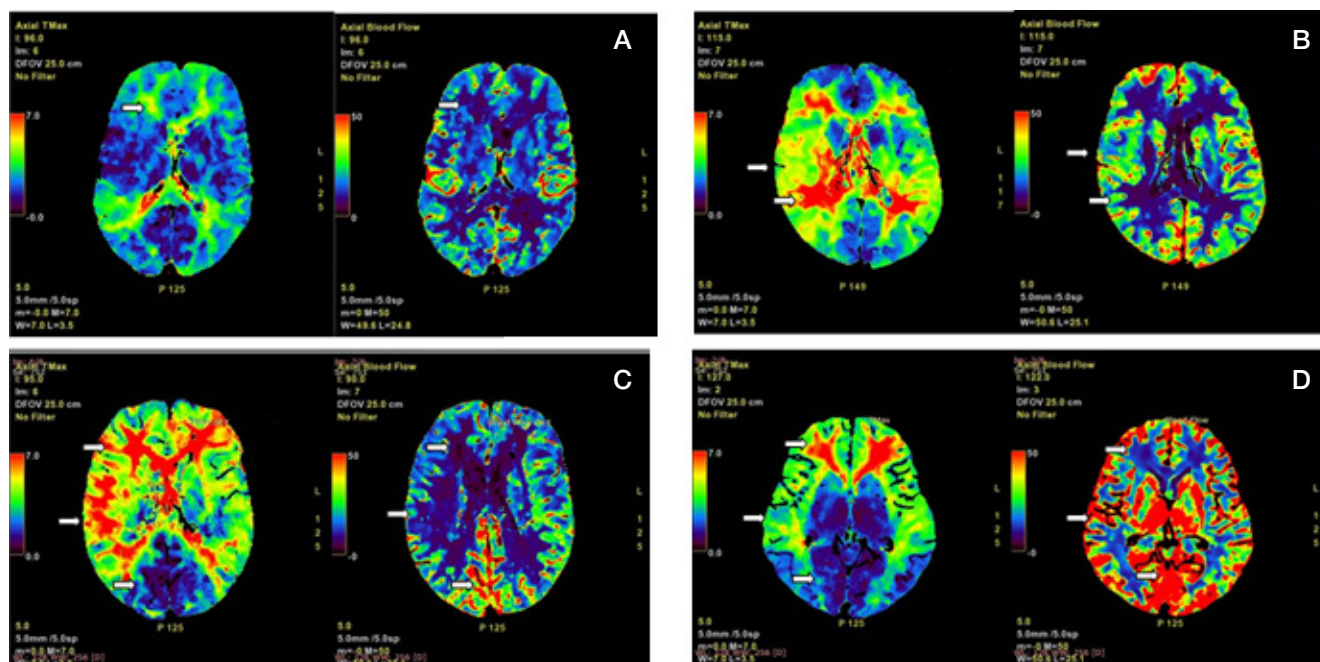


Fig. 5. CT perfusion imaging of the brain (axial planes). Perfusion maps for Tmax and CBF. **A.** Patient B: prolonged enhancement is observed in the border zones between MCA and ACA and between MCA and PCA (prolonged T_{max} : 4–5 s), perfusion is moderately reduced (arrows). **B.** Patient G: critical hypoperfusion in the border zones between MCA and ACA and between MCA and PCA ($T_{max} > 6$ s), moderate hypoperfusion in the MCA territory ($T_{max} \sim 5$ s) (arrows). **C.** Patient Yu: critical hypoperfusion in the border zones between MCA and ACA and between MCA and PCA ($T_{max} > 6$ s), hypoperfusion in the MCA and ACA territories (more pronounced on the right), hyperperfusion in the PCA territory (arrows). **D.** Patient V: critical hypoperfusion ($T_{max} > 6$ s) in the border zones between MCA and ACA, moderate hypoperfusion in the territories of cortical MCA and ACA branches, hyperperfusion in the PCA territory (arrows)

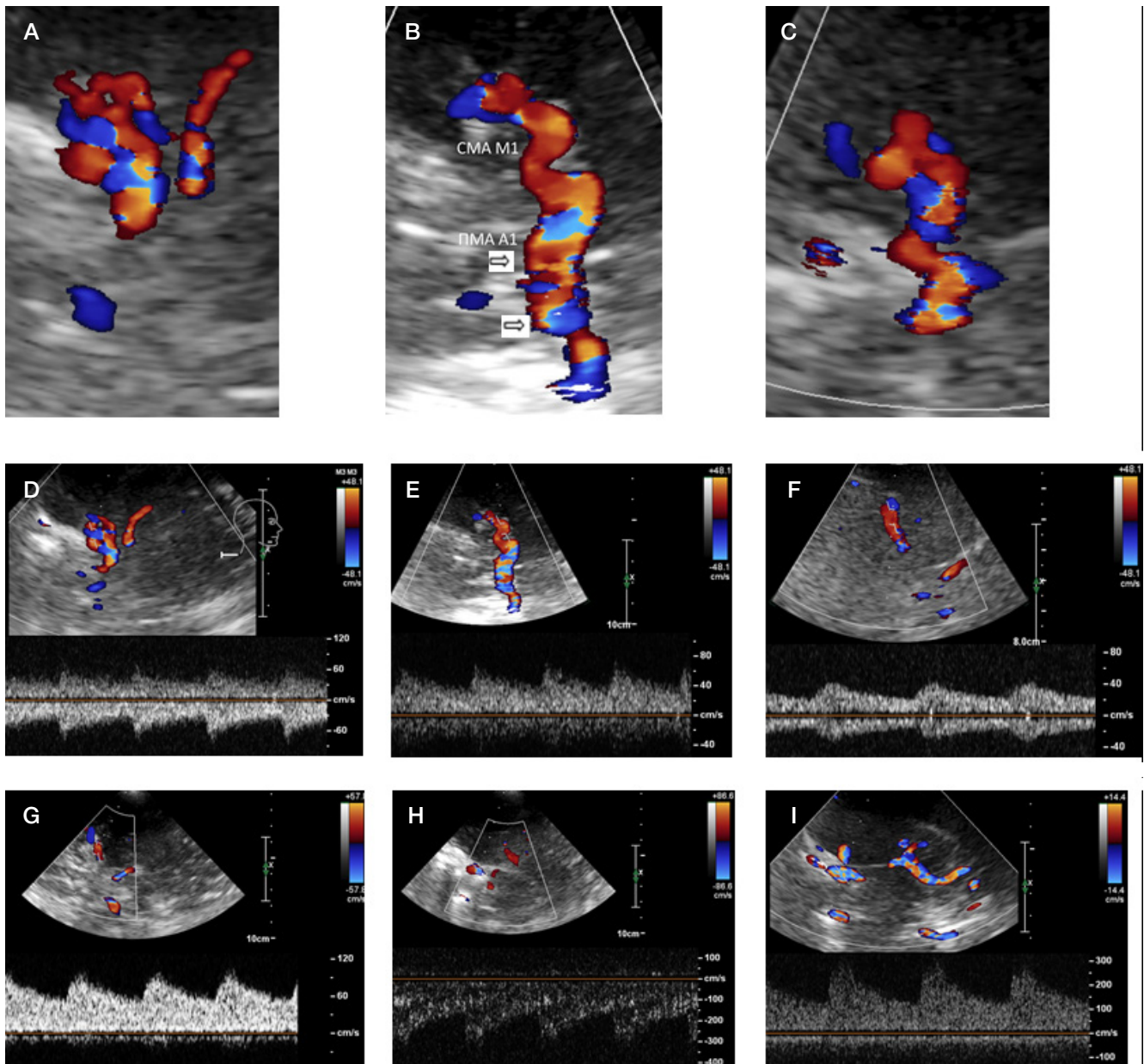


Fig. 6. Transcranial duplex ultrasonography of the anterior circulation, color Doppler (A–C), color Doppler combined with spectral Doppler (D–G). **A, D.** Patient B: differently directed color flows in the projection of the M1 segment of MCA. ACAs cannot be located. **B, E.** Patient G: single flows are located to the projection of the proximal M1 segment of MCA (up to the stenotic segment). Normally directed flows are seen in the A1-segments of ACAs (arrows). **C, F.** Patient V: differently directed intertwining flows can be located to the projection of the M1 segment of MCA; the image shows the Doppler spectrum for the M2 segment of MCA upstream of the stenotic region (collateral type). ACAs cannot be located. **G.** Patient Yu: M1 segments of MCA and A1 segments of ACA cannot be located. The image shows the Doppler spectrum for the M2 segment of MCA upstream of the stenotic region (collateral type) **H.** Patient Yu: the Doppler spectrum for the left terminal ICA, the linear velocity of the blood flow is increased at the sample site, suggesting arterial stenosis. The same flow pattern is observed in the right terminal ICA. **I.** Patient V: the Doppler spectrum for the left terminal ICA, increased linear velocity at the sample site, suggesting arterial stenosis. The same flow pattern is observed in the right terminal ICA

paresis in her right hand, which was interpreted as peripheral neuropathy; the hand restored its function within a week. The patient presented at the Center with complaints of transient loss of consciousness, frequent headaches and dizziness. The sharpened Romberg test revealed mild coordination impairment. The most recent neurological examination had been conducted 10 years prior. MRI findings of that time had been interpreted as variant anatomy of cerebral arteries.

At the Center, the examination protocol was the same for all patients and included MRI and MSCT of the brain and intracranial arteries, cerebral MSCT perfusion imaging, and color duplex ultrasonography of extra- and intracranial brachiocephalic arteries (BCA). MRI scans were performed on a 3T Discovery 370 MR scanner (GE; USA). The following

sequences were obtained: T1-WI, T2-WI, isotropic 3D FLAIR pulse sequence (slice thickness: 1 mm), diffusion-weighted images (DWI), susceptibility weighted angiography sequence (SWAN), and time-of-flight angiography (3D-TOF) of intracranial arteries. Brain MSCT and MSCT perfusion imaging were performed using a 128-slice Optima scanner (GE; USA). Contrast enhancement was achieved with iopromide (370 mg iodine/ml). High-resolution duplex ultrasonography of BCA was performed using a Philips Epiq 7G scanner (Philips; USA).

Brain MRI findings

All patients had signs of a past cerebral infarction and gliotic foci in the hemispheric white matter, in the border zone between

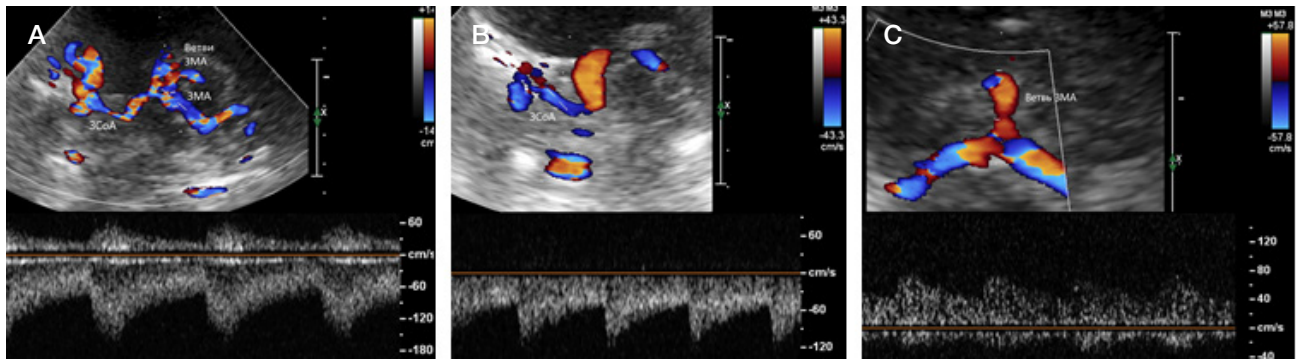


Fig. 7. Transcranial duplex ultrasonography of PCcom and PCA (color Doppler and spectral Doppler). **A.** Patient V: color Doppler for PCcom, PCA (segments P2-P3) and its branches. The pattern may suggest increased blood flow in these arteries. **B.** Patient G: high-velocity blood flow in PCcom. **C.** Patient Yu: high-velocity blood flow in the temporal branch of PCA

MCA and ACA. One patient (patient G) had signs of a past infarction in the deep perforating branches of the right MCA (Fig. 1). Patient Yu had areas of hemorrhagic transformation (petechiae). No intracranial hemorrhages were detected in either patient. The obtained T2-weighted images showed a network of small blood vessels in the proximal MCA territory on both sides both MCA trunks were not detectable at this level (Fig. 2).

Unenhanced MR angiography demonstrated significant narrowing/occlusion of terminal ICA and proximal MCA segments. ACAs were intact in patients B and G, but their diameter was small in one of these patients. Proximal ACAs were affected in patients Yu and V (Fig. 3). Posterior cerebral arteries (PCAs) and posterior communicating arteries (PCcoms) were dilated in all 4 patients.

Findings of multislice computed tomography of the brain

The CT-angiography of intracranial arteries revealed an abnormal vascular network (Fig. 4; *arrows*) in place of M1 MCA trunks and the enhancement of lenticulostriate arteries in the basal ganglia area, corresponding to different stages of MMD. The abnormal vascular network was well defined on the images of patients B and V, which was interpreted as stage 3 of the disease, and not so well developed in patients Yu and G, who had more pronounced neurological deficit and larger (both in number and size) post-infarction lesions, which was interpreted as later MMD stages characterized by the regression of moyamoya vessels at the base of the brain. Distal MCA and ACA were visible, their diameter being normal in some patients.

Signs of cerebral hypoperfusion in the MCA and ACA territories and increased posterior cerebral perfusion were observed in 3 of 4 patients (Fig. 5). The fourth patient (Patient B) had previously received an EC-IC bypass on both sides, so a reduction in cerebral perfusion in the border zones between MCA and ACA and between MCA and PCA was not so pronounced in this patient.

Findings of duplex ultrasonography of brachiocephalic arteries

Duplex ultrasonography did not detect any significant changes in extracranial BCAs; their diameters and velocity characteristics fell within the reference range (in most patients, these parameters approximated the lower limit). Diameters of vertebral arteries (VAs) varied significantly, blood flow in VAs was either normal or slightly increased.

Transcranial scans revealed stenosis of both terminal ICAs in patients Yu and V, inferred from the local hemodynamic changes (Fig. 6H, I). Single and multiple differently directed

intertwining flows were detected in the M1 segments of MCA in the color Doppler mode. Spectral Doppler demonstrated that their velocities were low and peripheral resistance was either moderate or significantly reduced, which is typical for collateral blood flow (Fig. 6A–G). Besides, all patients had high-velocity blood flow in PCcoms directed toward the vertebrobasilar system (VBS) and increased blood flow in PCAs and their branches. Three to four PCA segments were visualized (Fig. 7). Blood flow was compensatorily increased in the distal VA (V4) and the basilar artery (BA) in patients B and V; such compensation was not observed in patients G and Yu.

Discussion

Vascular changes typical for MMD can be detected by different imaging techniques. The T2-weighted images of all 4 patients showed abnormal vascular networks at the base of the brain in place of large M1-segments of MCA. MR-angiography conducted without a contrast agent revealed occlusion of distal (supraclinoid) ICA and proximal parts of MCA; in 2 patients, ACA was also affected. However, the abnormal vascular network had a puff of smoke appearance on MR angiograms in only one case. MSCT angiography allowed us to visualize lenticulostriate arteries in the basal ganglia and abnormal blood vessels at the brain base in greater detail, confirming MMD in all 4 patients.

Duplex ultrasonography of extracranial BCA detected no pronounced specific changes in ICA or VA. A reduced ICA diameter, which is a diagnostic criterion [1], was not detected in any of 4 patients. This might have been due to the degree of occlusion, which is not typical for other types of ICA damage. In MMD, the supraclinoid segments of ICA are occluded upstream of the PCcom divergence site; they are represented by communicating segments of ICA and their bifurcations. This is key in the redistribution of the cerebral blood flow from ICA via PCcom in VBS and then via PCA and its branches through cortical and leptomeningeal anastomoses back to MCA and ACA. Thus, signs of distal ICA occlusion in patients with MMD [1] can be seen on ultrasound scans in the absence of PCcom.

On intracranial scans, the abnormal vascular network at the base of the brain was visible if it was well developed. Otherwise, no signal was captured from the proximal MCA. Yet the M2-segment of MCA could be located, showing a relatively normal blood flow and thus raising a possibility of wrong interpretation. Velocity characteristics of blood flow in MCA branches and the distal segments of their trunks varied significantly but peripheral vascular resistance was reduced in all 4 patients, indicating collateralization.

Bilateral ICA occlusions co-occurred with small areas of past infarctions and gliotic lesions in the border zone between MCA and ACA. The inconsistency between the large arteries occlusions and the size of infarctions suggested an old history of a pathological process leading to the formation of these occlusions and sufficient collateral compensation. Cerebral infarctions occurring in the setting of MMD can be categorized as hemodynamic, associated with a reduction in blood flow due to low arterial blood pressure. Another possible cause of cerebral infarctions in MMD is regression of collateral vessels, leading to circulatory decompensation. In our patients, perfusion deficit (CBF) with prolonged Tmax was inferred from CT perfusion imaging data in the border zones between

MCA and ACA (deep and subcortical white matter of frontal lobes). Hyperperfusion was observed in 3 patients except for the patient with an EC-IC bypass. In patient V, the collateral vascular network was very well developed.

Conclusion

Our findings suggest that MMD can be diagnosed based on the known diagnostic criteria and using different imaging techniques: MRI, MSCT and duplex ultrasonography of brachiocephalic arteries. Diagnostic errors may be due to the unavailability of angiography for neuroimaging or the lack of awareness about MMD as a possible cause of IS in adults.

References

- Osborn AG, Zalcmán KL, Zaveri MD. *Lučevaja diagnostika. Golovnoj mozg. M.: Izdatel'stvo Panfilova, 2018; 1216 s. Russian.*
- Korshunov AE, Pronin IN, Golovtsev AL. *Bolezn' moyamoya — izlechimaja prichina povtornyh ishemicheskikh insultov u detej. Russkij zhurnal detskoj nevrologii. 2010; V (1): 27–34. Russian.*
- Shulgina AA, Lukshin VA, Korshunov AE, Usachev DYU, Pronin IN. *Sochetanie kombinirovannoj dvustvol'noj prjamoj i neprjamoj revaskuljarizacii golovnoj mozgja s dvuh storon v lečenii boleznj moyamoya. Voprosy neirohirurgii imeni N. N. Burdenko, 2020; 84 (2): 93–102. Russian.*
- Takeuchi K, Shimizu K. *Hypoplasia of the bilateral internal carotid arteries. Brain Nerve. 1957; 9: 37–43.*
- Nishimoto A, Takeuchi S. *Abnormal cerebrovascular network related to the internal carotid arteries. J Neurosurg. 1967; 29: 255–60.*
- Guidelines for Diagnosis and Treatment of Moyamoya Disease (Spontaneous Occlusion of the Circle of Willis). *Research Committee on the Pathology and Treatment of Spontaneous Occlusion of Spontaneous Occlusion of the Circle of Willis; Health Labour Sciences Research Grant for Research on Measures for Intractable Diseases. Neurol Med Chir (Tokyo). 2012; 52: 245–66.*
- Wanebo JE, Khan N, Zabramski JM, Spetzler RF, ed. *Moyamoya disease: diagnosis and treatment. New York Stuttgart: Thieme, 2013; 224 p.*
- Yamashita M, Oka K, Tanaka K. *Histopathology of the brain vascular network in moyamoya disease. Stroke. 1983; 14: 50–58.*
- Newell DW, Abdu E. *Moyamoya Disease: Current Concepts. Cureus. 2012; 4 (6): e47. DOI: 10.7759/cureus.47.*
- Ge P, Zhang Q, Ye X, Liu X, Deng X, Wang J, et al. *Different subtypes of collateral vessels in hemorrhagic moyamoya disease with p.R4810K variant. BMC Neurology. 2020; 20: 308. DOI: 10.1186/s12883-020-01884-0.*
- Suzuki J, Takaku A. *Cerebrovascular “moyamoya” disease. Disease showing abnormal net-like vessels in base of brain. Arch Neurol. 1969; 20: 288–99.*
- Kamada F, Aoki Y, Narisawa A, Abe Y, Komatsuzaki S, Kikuchi A, et al. *A genome-wide association study identifies RNF213 as the first Moyamoya disease gene. J Hum Genet. 2011; 56 (1): 34–40. DOI: 10.1038/jhg.2010.132.*
- Koizumi A, Kobayashi H, Hitomi T, Harada KH, Habu T, Youssefian S. *A new horizon of moyamoya disease and associated health risks explored through RNF213. Environ Health Prev Med. 2016; 21: 55–70. DOI: 10.1007/s12199-015-0498-7.*
- Park YS, An HJ, Kim JO, Kim WS, Han IB, Kim OJ, et al. *The Role of RNF213 4810G>A and 4950G>A Variants in Patients with Moyamoya Disease in Korea. Int J Mol Sci. 2017; 18 (11): 2477. DOI: 10.3390/ijms18112477.*
- Fujimura M, Tominaga T. *Diagnosis of moyamoya disease: international standard and regional differences. Neurol Med Chir (Tokyo). 2015; 55 (3): 189–93. DOI: 10.2176/nmc.ra.2014-0307.*
- Kraemer M, Heienbrok W, Berlit P. *Moyamoya disease in Europeans. Stroke. 2008; 39 (12): 3193–200. DOI: 10.1161/STROKEAHA.107.513408.*
- Savolainen M, Mustanoja S, Pekkola J, Tyni T, Uusitalo AM, Ruotsalainen S, et al. *Moyamoya angiopathy: long-term follow-up study in a Finnish population. J Neurol. 2019; 266 (3): 574–81. DOI: 10.1007/s00415-018-9154-7.*
- Acker G, Fekonja L, Vajkoczy P. *Surgical Management of Moyamoya Disease. Stroke. 2018; 49 (2): 476–82. DOI: 10.1161/STROKEAHA.117.018563.*

Литература

- Осборн А. Г., Зальцман К. Л., Завери М. Д. *Лучевая диагностика. Головной мозг. М.: Издательство Панфилова, 2018; 1216 с.*
- Коршунов А. Е., Пронин И. Н., Головтеев А. Л. *Болезнь моямоя — излечимая причина повторных ишемических инсультов у детей. Русский журнал детской неврологии. 2010; V (1): 27–34.*
- Шульгина А. А., Лукшин В. А., Коршунов А. Е., Усачев Д. Ю., Пронин И. Н. *Сочетание комбинированной двуствольной прямой и непрямой реваскуляризации головного мозга с двух сторон в лечении болезни моямоя. Вопросы нейрохирургии имени Н. Н. Бурденко, 2020; 84 (2): 93–102.*
- Takeuchi K, Shimizu K. *Hypoplasia of the bilateral internal carotid arteries. Brain Nerve. 1957; 9: 37–43.*
- Nishimoto A, Takeuchi S. *Abnormal cerebrovascular network related to the internal carotid arteries. J Neurosurg. 1967; 29: 255–60.*
- Guidelines for Diagnosis and Treatment of Moyamoya Disease (Spontaneous Occlusion of the Circle of Willis). *Research Committee on the Pathology and Treatment of Spontaneous Occlusion of Spontaneous Occlusion of the Circle of Willis; Health Labour Sciences Research Grant for Research on Measures for Intractable Diseases. Neurol Med Chir (Tokyo). 2012; 52: 245–66.*
- Wanebo JE, Khan N, Zabramski JM, Spetzler RF, ed. *Moyamoya disease: diagnosis and treatment. New York Stuttgart: Thieme, 2013; 224 p.*
- Yamashita M, Oka K, Tanaka K. *Histopathology of the brain vascular network in moyamoya disease. Stroke. 1983; 14: 50–58.*
- Newell DW, Abdu E. *Moyamoya Disease: Current Concepts. Cureus. 2012; 4 (6): e47. DOI: 10.7759/cureus.47.*
- Ge P, Zhang Q, Ye X, Liu X, Deng X, Wang J, et al. *Different subtypes of collateral vessels in hemorrhagic moyamoya disease with p.R4810K variant. BMC Neurology. 2020; 20: 308. DOI: 10.1186/s12883-020-01884-0.*
- Suzuki J, Takaku A. *Cerebrovascular “moyamoya” disease. Disease showing abnormal net-like vessels in base of brain. Arch*

- Neurol. 1969; 20: 288–99.
12. Kamada F, Aoki Y, Narisawa A, Abe Y, Komatsuzaki S, Kikuchi A, et al. A genome-wide association study identifies RNF213 as the first Moyamoya disease gene. *J Hum Genet.* 2011; 56 (1): 34–40. DOI: 10.1038/jhg.2010.132.
 13. Koizumi A, Kobayashi H, Hitomi T, Harada KH, Habu T, Youssefian S. A new horizon of moyamoya disease and associated health risks explored through RNF213. *Environ Health Prev Med.* 2016; 21: 55–70. DOI: 10.1007/s12199-015-0498-7.
 14. Park YS, An HJ, Kim JO, Kim WS, Han IB, Kim OJ, et al. The Role of RNF213 4810G>A and 4950G>A Variants in Patients with Moyamoya Disease in Korea. *Int J Mol Sci.* 2017; 18 (11): 2477. DOI: 10.3390/ijms18112477.
 15. Fujimura M, Tominaga T. Diagnosis of moyamoya disease: international standard and regional differences. *Neurol Med Chir (Tokyo).* 2015; 55 (3): 189–93. DOI: 10.2176/nmc.ra.2014-0307.
 16. Kraemer M, Heienbrok W, Berlit P. Moyamoya disease in Europeans. *Stroke.* 2008; 39 (12): 3193–200. DOI: 10.1161/STROKEAHA.107.513408.
 17. Savolainen M, Mustanoja S, Pekkola J, Tyni T, Uusitalo AM, Ruotsalainen S, et al. Moyamoya angiopathy: long-term follow-up study in a Finnish population. *J Neurol.* 2019; 266 (3): 574–81. DOI: 10.1007/s00415-018-9154-7.
 18. Acker G, Fekonja L, Vajkoczy P. Surgical Management of Moyamoya Disease. *Stroke.* 2018; 49 (2): 476–82. DOI: 10.1161/STROKEAHA.117.018563.

ACTIVATION OF SENSORIMOTOR INTEGRATION PROCESSES WITH A BRAIN-COMPUTER INTERFACE

Rubakova AA , Ivanova GE, Bulatova MA

Federal Center for Brain Research and Neurotechnologies of FMBA, Moscow, Russia

A BCI-controlled hand exoskeleton activates neuroplasticity mechanisms, promoting motor learning. The contribution of perception to this phenomenon is understudied. The aim of this study was to assess the impact of sensorimotor integration on the effectiveness of neurorehabilitation based on the learning of a hand opening movement by stroke patients using BCI and to investigate the effect of ideomotor training on spasticity in the paretic hand. The study was conducted in 58 patients (median age: 63 (22; 83) years) with traumatic brain injury, ischemic (76%) or hemorrhagic (24%) stroke in the preceding 2 (1.0; 12.0) months. The patients received 15 (12; 21) ideomotor training sessions with a BMI-controlled hand exoskeleton. Hand function was assessed before and after rehabilitation on the Fugl-Meyer, ARAT, Frenchay, FIM, Rivermead, and Ashworth scales. An increase in muscle strength was observed in 40% of patients during flexion and extension of the radiocarpal joint and in 29% of patients during the abduction and adduction of the joint. Muscle strength simultaneously increased during the abduction and adduction of the radiocarpal joint ($p < 0.004$). Ideomotor training is ineffective for reducing spasticity because no statistically significant reduction in muscle tone was detected. Improved motor performance of the paretic hand was positively correlated with improvements in daily activities. Motor training of the paretic hand with a robotic orthosis activates kinesthetic receptors, restores sensation and improves fine motor skills through better sensorimotor integration.

Keywords: stroke, ideomotor training, exoskeleton, brain-computer interface, neurorehabilitation, sensorimotor integration

Author contribution: Rubakova AA — data acquisition, analysis, interpretation; literature analysis; Ivanova GE — study design; manuscript editing; Bulatova MA — data acquisition and analysis.

Compliance with ethical standards: the study was approved by the Ethics Committee of the Federal Center for Brain Research and Neurotechnologies (Protocol № 33 dated June 21, 2021.). Informed consent was obtained from all study participants.

 **Correspondence should be addressed:** Alexandra Rubakova
Ostrovityanova, 1, str. 10, Moscow, 117997, Russia; sandrabiolog@inbox.ru

Received: 26.07.2021 **Accepted:** 15.08.2021 **Published online:** 01.09.2021

DOI: 10.24075/brsmu.2021.039

АКТИВАЦИЯ ПРОЦЕССОВ СЕНСОМОТОРНОЙ ИНТЕГРАЦИИ С ПОМОЩЬЮ ИНТЕРФЕЙСА «МОЗГ–КОМПЬЮТЕР»

А. А. Рубакова , Г. Е. Иванова, М. А. Булатова

Федеральный центр мозга и нейротехнологий Федерального медико-биологического агентства, Москва, Россия

Интерфейс «мозг–компьютер» (ИМК) с экзоскелетом кисти руки активирует механизмы нейропластичности, в результате чего происходит моторное научение, однако вклад перцепции в этот процесс на данный момент изучен недостаточно. Целью исследования было изучить влияние сенсомоторной интеграции на эффективность реабилитационного процесса по обучению парадигме движения раскрытия кисти у пациентов, перенесших острое нарушение мозгового кровообращения, с помощью ИМК и оценить влияние идеомоторного тренинга на снижение спастичности в паретичной руке. Был проведен анализ данных 58 пациентов (медиана возраста 63 года (22; 83)), с перенесенной черепно-мозговой травмой или инсультом давностью 2 месяца (1,0; 12,0), ишемического (76%) и геморрагического характера (24%), получивших 15 (12; 21) идеомоторных тренировок с использованием ИМК и экзоскелета. Функциональную активность руки оценивали до и после прохождения курса процедур по шкалам Fugl-Meyer, ARAT, Frenchay, FIM, Rivermead, Ashworth. Отмечено увеличение мышечной силы в лучезапястном суставе у 40% пациентов при сгибании-разгибании, у 29% — при отведении-приведении. Увеличение мышечной силы при отведении и приведении лучезапястного сустава происходит одновременно ($p < 0,004$). Назначение идеомоторных тренировок для снижения мышечного тонуса неэффективно, так как достоверно значимого снижения спастичности в кисти выявлено не было. Улучшение в воспроизведении движений кистью паретичной руки положительно коррелировало с улучшением повседневных навыков жизненных активностей. Развитие моторной функции паретичной кисти с помощью экзоскелета ведет к активации кинестетических рецепторов, улучшая чувствительность и мелкую моторику за счет сенсомоторной интеграции.

Ключевые слова: инсульт, идеомоторный тренинг, экзоскелет, интерфейс «мозг–компьютер», нейрореабилитация, сенсомоторная интеграция

Вклад авторов: А. А. Рубакова — сбор, анализ, интерпретация данных, анализ литературы; Г. Е. Иванова — планирование исследования, редактирование рукописи; М. А. Булатова — сбор и анализ данных.

Соблюдение этических стандартов: исследование одобрено этическим комитетом ФЦМН ФМБА России (протокол № 33 от 21 июня 2021 г.). Все участники подписали информированное согласие на участие в исследовании.

 **Для корреспонденции:** Александра Алексеевна Рубакова
ул. Островитянова, д. 1, стр. 10, г. Москва, 117997, Россия; sandrabiolog@inbox.ru

Статья получена: 26.07.2021 **Статья принята к печати:** 15.08.2021 **Опубликована онлайн:** 01.09.2021

DOI: 10.24075/vrgmu.2021.039

Integration of sensory and motor information is central to successful goal-directed behavior and movements necessary to interact with the environment. Compromised sensorimotor integration is common to many neurological conditions, including stroke, which may be caused, among other things, by traumatic brain injury (TBI) [1]. In motor control, sensory feedback during movement is predicted from an internal copy of the motor command. If a prediction generated by the motor cortex matches the actual sensory feedback, a stable motor

pattern is formed and the entire sensory experience is retained [2]. The human ability to link a performed action to its immediate consequences presented in the form of perceptual information is called sensorimotor integration.

Stroke is a common disorder that causes disruption of sensorimotor integration through sensory impairments, hemiparesis, limb spasticity, hemianopsia, ataxia, and apraxia [2]. Most stroke patients develop persistent hand paresis, which reduces the functional range of hand motion and

adversely affects the patients' quality of life. Modern post-stroke rehabilitation has harnessed the principles of neuroplasticity to promote motor learning and regain the lost motor function. However, the contribution of perception to motor control and learning is often overlooked and, to this day, remains understudied [1]. In developmental psychology, sensorimotor integration in the cortex is considered an important factor promoting learning [3]. It is thought that learning movement patterns is essential for post-stroke recovery [4].

It is hypothesized that neuroplasticity mechanisms are underpinned by long-term potentiation and long-term depression of brain neurons [5]. In motor learning, the key role is attributed to the primary motor cortex; during active motor learning and at rest, IEGs expression is stimulated in the neurons of the primary motor cortex and neurotrophic factors are synthesized, modulating neural networks and promoting consolidation of the acquired information [5].

Generation of the sensorimotor μ -rhythm registered during motor imagery and motor execution is linked to efferent processes and motor performance but can also take place during afferent nerve activity, such as passive extension of the affected limb with a robotic orthosis. Some studies argue the effectiveness of post-stroke rehabilitation involving premovement sensorimotor rhythm training. It is reported that motor function of the affected limb can be successfully recovered by means of sensorimotor rhythm training in which the amplitude of the rhythm is measured to ensure effective control of a robotic orthosis relying on the principles of biofeedback (based on the actual movement or its mental rehearsal). There is evidence that combined activity of the sensory, motor and temporal cortices is associated with proprioceptive and tactile afferent signals from the moving limb, which allows the effects of motor function training to be measured [6].

Neuroplasticity-based motor learning occurs due to physiological stimulation of peripheral proprioceptors during physical exercise and sensorimotor integration of afferent and efferent signals in the cerebral cortex. Over the past decade, there has been an extensive development of robotic hands and rehabilitation devices for patients with sensorimotor deficits after CNS injury [7]. Innovative robotic rehabilitation devices rely on the principle of biofeedback, which improves the effectiveness of motor learning; however, little attention has been paid to motor learning capacity of stroke patients and factors that may affect it [4].

Robot-assisted motor rehabilitation of upper limb function is being increasingly introduced into clinical practice. One example is robotic orthoses for active and passive hand muscle training after an acute cerebrovascular accident (CVA) in the sensorimotor cortex and/or pyramidal tract injury [8]. Today, robot-assisted rehabilitation is the only method that can activate neuroplastic mechanisms: motor function recovery, which is the ultimate goal of neurorehabilitation in such patients, requires at least 400 repetitions for a movement pattern to be ingrained in the patient's memory. Long-term motor adaptation with biofeedback for simultaneous error correction is possible only with a brain-computer interface (BCI) [9–12].

However, in order to achieve a clinically noticeable improvement, movement repetition is not enough. For a positive outcome, multisensory stimulation, e.g. simultaneous stimulation of visual, vestibular and proprioceptive analyzers, and cognitive function training are needed [13]. It is known that apart from motor function, BCI-controlled feedback training stimulates intrapsychic activity [14]. So, it can be hypothesized that robot-assisted neurorehabilitation of patients

with hemiparesis after CVA effectively promotes sensorimotor integration, which plays the leading role in the formation of movement forming.

Our goal was to examine a hypothesis proposed by Bertani et al., which suggests that although post-stroke neurorehabilitation with a robotic hand potentiates activation of neuroplasticity mechanisms in the affected hemisphere, it does not exert any significant effect on muscular tone reduction in the paretic limb [13]. We decided to test this hypothesis because clinicians often prescribe biofeedback-based ideomotor training to stroke patients to reduce spasticity. So, there is a need to check whether such interventions are reasonable and can improve the outcome of neurorehabilitation.

The aim of this study was to assess the impact of sensorimotor integration on the effectiveness of neurorehabilitation based on the learning of a hand opening movement in stroke patients using BCI and to study the effect of ideomotor training on spasticity in the paretic hand.

METHODS

The study was conducted at the Federal Center for Brain Research and Neurotechnologies; it began on December 19, 2019 and ended on October 8, 2020. Fifty-eight patients were included in the study. The sample was dominated by male patients (42 men vs. 16 women). The mean age of the participants was 62.5 ± 5 years. The youngest participant was 22 years old, the oldest one was 83 years old. The mean time elapsed after stroke was 2 months. Thus, 80% of our patients were in the early rehabilitation period (1 to 6 months after CVA), and 20% were in the late rehabilitation period. All study participants were right-handed, according to the Edinburgh Handedness Inventory.

Of all the patients included in the study, 76% (44 persons) were undergoing rehabilitation after ischemic stroke, 15.5% (9 persons) after hemorrhagic stroke, 5% (3 persons) after ischemic stroke with hemorrhagic transformation, and 3.5% (2 persons) after TBI.

The sample was dominated by patients with subcortical lesions. The right middle cerebral artery was involved in most patients (20 persons; 35.7%); the left middle cerebral artery was involved in 17 (30.3%) patients.

On neurological examination, deep sensation was preserved in 93% of the patients, whereas superficial sensation, in 48% of the patients; 52% of the patients had superficial hemihypesthesia contralateral to the affected hemisphere; 98% of the patients had hemihypesthesia to pain, temperature and touch, i.e. the total loss of sensation. Deep sensation impairments were detected in 11 (19%) patients.

The following inclusion criteria were applied: retained cognitive function (at least 12 points on the Montreal Cognitive Assessment scale); the absence of severe aphasia which could have prevented the patient from understanding instructions for ideomotor training; the absence of severe visual impairment; spasticity in the paretic hand ≤ 4 points on the modified Ashworth scale; mild to moderate disability on the Rankin scale (≤ 3 points); the absence of muscle contractures in the affected limb; the absence of pronounced pain that might have interfered with ideomotor training; informed consent given by the patient or their legal representative.

Exclusion criteria: inability to perform training tasks; refusal to participate in the study; severe aphasia; severe visual impairment preventing the patient from following instructions on the computer screen; spasticity of 5 points on the modified Ashworth scale; severe disability (>3 points on the Rankin

Table 1. Muscle strength assessment before and after ideomotor training with Exihand-2 using a paired *t*-test

	<i>t</i> -value	Significance of differences	Average score before rehabilitation	Average score after rehabilitation
Flexion of radiocarpal joint	4,752	Significant	2,556 ± 1,513	2,963 ± 1,601
Extension of radiocarpal joint	5,442	Significant	2,286 ± 1,581	2,786 ± 1,615
Abduction of radiocarpal joint	4,828	Significant	2,143 ± 1,689	2,5 ± 1,809
Adduction of radiocarpal joint	4,828	Significant	2,143 ± 1,689	2,5 ± 1,809
Flexion of metacarpophalangeal joints	4,529	Significant	2,714 ± 1,398	3,018 ± 1,433
Extension of metacarpophalangeal joints	4,56	Significant	2,054 ± 1,71	2,518 ± 1,748
Thumb opposition	4,511	Significant	1,893 ± 1,734	2,286 ± 1,806
Little finger opposition	4,328	Significant	1,768 ± 1,789	2,143 ± 1,873

Note: the figures in the table are presented as means (M) and standard error of the mean ($\pm m$)

scale); muscle contractures in the affected limb; pronounced pain.

On average, the patients scored 25.4 points on the Montreal Cognitive Assessment scale (MoCA) during the initial neurological assessment, with 75% of patients scoring in the range between 23 and 26 points.

The training sessions were carried out in accordance with a standard (2020) protocol using BMI-controlled Exokist-2 orthoses for both hands (Android Technics; Russa). The interactions between the patient and the Exokist-2 rehabilitation complex were guided by the principles of biofeedback.

Rehabilitation was aided by a biofeedback-based Exokist-2 robotic device. The method relies on 2 approaches to robot-assisted post-stroke rehabilitation of upper limbs: 1) a neurophysiological approach based on the ideas of neuroplasticity and compensatory potential of the brain; 2) motor learning through performing goal-directed tasks by the paretic hand and motor imagery with multisensory feedback. Exokist-2 utilizes multimodal (primarily visual and proprioceptive) biofeedback to a registered intention to execute a movement.

During the session, the patient was sitting in a medical chair, with both hands inside the robotic gloves secured to the armrests. The screen was positioned 1 m in front of the patient. A pictorial instruction for gaze fixation appeared on the screen and was then followed by oral instructions: to perform kinesthetic imagery of left/right hand opening (depending on the direction of the arrow on the screen) or to rest [13].

EEG data were recorded during the session using an NVX52 amplifier (Medical computer systems; Russia), which is a component of the Exohand-2 system. It helps to identify the task a patient performs at a given moment in time. EEG data were collected from 32 electrodes positioned at F3, Fz, F4, Fc5, Fc3, Fc1, Fcz, Fc2, Fc4, Fc6, C5, C3, C1, Cz, C2, C4, C6, Cp5, Cp3, Cp1, Cpz, Cp2, Cp4, Cp6, P3, Pz, P4, Po3, Poz, Po4, O1, and O2. Task recognition was carried out using a Bayesian classifier for the analysis of EEG covariance matrices. The result was presented to the patient as visual and proprioceptive feedback: if the classifier recognized the task given to the patient, the color of the cursor on the screen changed to green and the Exohand opened [15].

The motor imagery training course lasted for 7–9 days, with 2–3 sessions a day. Each session was 9 min long, as recommended in the protocol for adult patients [16]. On average, the patient received 15 (12; 21) sessions with Exokist-2 exercises.

The effectiveness of ideomotor training with Exokist-2 was estimated using scales for the assessment of functional movements necessary for everyday activities. We also

compared the results of neurological examinations conducted before and after the rehabilitation course. The following scales were used: the modified Ashworth scale, the Fugl-Meyer Assessment scale, the ARAT scale, the Frenchay Activities Index, the Rankin scale, the Rivermead Mobility Index, and FIM.

RESULTS

The analysis of clinical data revealed a direct correlation between age and proprioception impairment, previously demonstrated in [17]. The factor analysis exposed a statistically significant moderate correlation (the Chaddock scale) between deep sensory impairments and the improvement of hand function on the Fugl-Meyer Assessment ($p = 0.32$; $p < 0.02$) and ARAT ($p = 0.454$; $p = 0.0006$) scales.

We found that ideomotor training enhances hand muscle strength during movement in the radiocarpal and metacarpophalangeal joints. Muscle strength was assessed on a 5-point scale before and after 15 neurorehabilitation sessions with Exokist-2. The results were compared, to reveal an improvement in the flexion and extension of the radiocarpal joint in 23 (40%) patients and in the adduction and abduction of this joint in 17 (29%) patients. Besides, we found that muscle strength equally increased with the abduction and adduction of the radiocarpal joint, which may be explained by sensorimotor integration recovery due to neuroplasticity and activation of receptors in wrist muscles. Muscle strength improvements are analyzed in Table 1.

Hand function improvement on the Fugl-Meyer scale was observed in 63% of the patients after the neurorehabilitation course with Exokist-2; however, it was clinically significant (by 5 points or more) in only 26% of the patients.

Improvements in the Frenchay Activities Index were observed in 26% of the patients (15 persons).

Statistically significant improvements on the ARAT scale were detected in 38% of the patients. However, their distribution was non-uniform: 13 patients increased their scores by 2–7 points, and 9 patients – by 17–55 points. It should be noted that improvement was demonstrated primarily by those patients who had scored 0 on the ARAT scale on the initial neurological examination.

Improved hand function performance was also reflected in higher FIM and Rivermead Mobility Index. Perhaps, it may be explained by the fact that robot-assisted motor function training for the paretic limb activates kinesthetic receptors, improving fine motor skills and restoring sensation in the upper limb through better sensorimotor integration. Improvements in sensorimotor hand activity and functional independence are analyzed in Table 2.

Table 2. Improvements in the sensorimotor hand activity and functional independence after ideomotor training with Exohand-2

	Number of patients with improvements, %	t-value	p-value
Fugl-Meyer Assessment scale	62%	5,719	$p = 0,0$
ARAT	38%	3,236	$p = 0,002$
Modified Frenchay Activities Index (for hand)	26%	3,454	$p = 0,001$
Modified Rankin scale	21%	3,667	$p = 0,001$
Rivermead Mobility Index	58,60%	4,691	$p = 0,0$
FIM	60,30%	5,028	$p = 0,0$
Modified Ashworth scale	14%	-2,634	$p = 0,011$

Our test of Bertani's hypothesis [13] showed that the degree of spasticity reduction in the paretic hand assessed on the modified Ashworth scale was statistically insignificant ($p = 0.001$); muscle tone reduction was observed in only 8 (14%) patients. Thus, neuroplasticity mechanisms do not exert a significant effect on spasticity in the paretic hand.

DISCUSSION

Patients with hemiparesis and neurological deficits after CVA demonstrated a statistically significant improvement in the motor activity and sensibility of the hand, as well as in their functional everyday activities, after robot-assisted neurorehabilitation with Exohand-2. After 15 sessions, improved upper limb function was reported by most patients.

Perhaps, integration between the primary cortex and Brodmann area 6 of the frontal cortex are disrupted in advanced-age stroke patients not only because of stroke itself, but also due to age-related involution of the grey matter. This explains why neurorehabilitation with Exokist-2 was lowly effective in patients with premotor apraxia, as demonstrated by all applied scales, because the primary task of ideomotor training is motor imagery, which occurs in Brodmann cytoarchitectonic area 6 [17, 18].

The literature data suggests that patients who benefit from ideomotor training recover impaired integration between the posterior parietal cortex, which is responsible for producing a motor intention, the supplementary motor cortex and the primary motor cortex responsible for movement execution recovers through the activation of neuroplasticity mechanisms [19]. As motor function is being regained, sensorimotor integration is improving between the visual cortex, which perceives visual stimuli containing instructions for the patient, the frontal cortex, which plays the key role in the perception of body scheme and kinesthetic inputs, and the parietal, dorsal premotor and motor cortices. Therefore, the term "sensorimotor cortex" can be applied not only to the precentral and postcentral gyri, but to all brain areas mentioned above, although they are spatially

isolated. It is the sensorimotor cortex that generates the 8-12 Hz μ -rhythm registered by EEG during a trainings session with Exokist-2 and further analyzed to classify the result of the performed task. Spontaneous μ -rhythm desynchronization (suppression) occurs before and during the actual movement, whereas spontaneous desynchronization (enhancement) occurs after the movement has been executed. The mechanism underlying μ -rhythm generation is understudied, but there is evidence that it occurs as a result of the coordinated activity of the premotor and motor cortices and subcortical and spinal centers [7, 20].

Our findings suggest that BCI-based neurorehabilitation reduces the degree of disability on the Rankin scale.

Sensorimotor integration, which was expected to be activated by ideomotor training, improved significantly after the rehabilitation course. This was reflected in the clinical data: the functional independence and daily activities of our patients directly depended on their motor activity, accuracy and speed of afferent signal transmission from peripheral receptors. Training with Exokist-2 improves hand motor skills and activates visual, kinesthetic and auditory perception. Regular multimodal biofeedback-based training activates neuroplasticity mechanisms and results in the consolidation of sensory information acquired during task performance. Auditory, visual and kinesthetic analyzers, systems involved in body schema perception, motor functions and intrapsychic processes, such as motivation and memory, interact with each other, which directly indicates stimulation of sensorimotor integration processes.

CONCLUSIONS

Reduction of neurological deficit revealed by the analysis of clinical data and observations indicating activation of sensorimotor integration processes after a course of ideomotor training sessions suggests the effectiveness of post-stroke rehabilitation with Exokist-2. Therefore, a robotic orthosis controlled by non-invasive BCI can be recommended for clinical use as part of complex neurorehabilitation after CVA.

References

1. Edwards LL, King EM, Buetefisch CM, Borich MR. Putting the "Sensory" Into Sensorimotor Control: The Role of Sensorimotor Integration in Goal-Directed Hand Movements After Stroke. *Frontiers in Integrative Neuroscience*. 2019; 13: 16. DOI: 10.3389/fnint.2019.00016.
2. Espenhahn S, Rossiter HE, van Wijk BCM, Redman N, Rondina JM, Diedrichsen J, et al. Sensorimotor cortex beta oscillations reflect motor skill learning ability after stroke. *Brain Communications*. 2020; 2 (2): fcaa161. DOI: 10.1093/braincomms/fcaa161.
3. Mahoney JR, Verghese J. Does Cognitive Impairment Influence Visual-Somatosensory Integration and Mobility in Older Adults? *The journals of gerontology. Series A, Biological sciences and medical sciences*. 2020; 75 (3): 581–8. DOI: 10.1093/gerona/glz117.
4. Jacquey L, Baldassarre G, Santucci VG, O'Regan JK. Sensorimotor Contingencies as a Key Drive of Development: From Babies to Robots. *Frontiers in neurorobotics*. 2019; 13: 98. DOI: 10.3389/fnbot.2019.00098.
5. Luft AR, Buitrago MM, Ringer T, Dichgans J, Schulz JB. Motor

- skill learning depends on protein synthesis in motor cortex after training. *The Journal of neuroscience: the official journal of the Society for Neuroscience*. 2004; 24 (29): 6515–20. DOI: 10.1523/JNEUROSCI.1034-04.2004.
6. Hosp JA, Mann S, Wegenast-Braun BM, Calhoun ME, Luft AR. Region and task-specific activation of arc in primary motor cortex of rats following motor skill learning. *Neuroscience*. 2013; 250: 557–64. DOI: 10.1016/j.neuroscience.2013.06.060.
 7. Norman SL, McFarland DJ, Miner A, Cramer SC, Wolbrecht ET, Wolpaw JR, Reinkensmeyer DJ. Controlling pre-movement sensorimotor rhythm can improve finger extension after stroke. *Journal of neural engineering*. 2018; 15 (5): 056026. DOI: 10.1088/1741-2552/aad724.
 8. Friedrich J, Verrel J, Kleimaker M, Münchau A, Beste C, Bäumer T. Neurophysiological correlates of perception-action binding in the somatosensory system. *Scientific reports*. 2020; 10 (1): 14794. DOI: 10.1038/s41598-020-71779-0.
 9. Kotov SV, Turbina LG, Bobrov PD, Frolov AA, Pavlova OG, Kurganskaya ME, i dr. *Primenenie kompleksa «interfejs «mozg-komp'yuter» i jekzoskelet» i tehniki voobrazhenija dvizhenija dlja reabilitacii posle insulta. Al'manah klinicheskoy mediciny*. 2015; (39): 15–21. DOI: 10.18786/2072-0505-2015-39-15-21. Russian.
 10. Koroleva ES, Alifirova VM, Latypova AV, Cheban SV, Ott VA, Brazovskiy KS, i dr. *Principy i opyt primeneniya robotizirovannyh reabilitacionnyh tehnologij u pacientov posle insulta. Bjulleten' sibirskoy mediciny*. 2019; 18 (2): 223–33. DOI: 10.20538/1682-0363-2019-2-223-233. Russian.
 11. Di Pino G, Pellegrino G, Assenza G, Capone F, Ferreri F, Formica D, et al. Modulation of brain plasticity in stroke: a novel model for neurorehabilitation. *Nat Rev Neurol*. 2014; 10 (10): 597–608. DOI: 10.1038/nrneurol.2014.162.
 12. Nahmani M, Turrigiano GG. Adult cortical plasticity following injury: recapitulation of critical period mechanisms? *Neuroscience*. 2014; 283: 4–16. DOI: 10.1016/j.neuroscience.2014.04.029.
 13. Bertani R, Melegari C, De Cola MC, Bramanti A, Bramanti P, Calabrò RS. Effects of robot-assisted upper limb rehabilitation in stroke patients: a systematic review with meta-analysis. *Neurol Sci*. 2017; 38 (9): 1561–9. DOI: 0.1007/s10072-017-2995-5.
 14. Chivukula S, Jafari M, Aflalo T, Yong NA, Pouratian N. Cognition in Sensorimotor Control: Interfacing With the Posterior Parietal Cortex. *Front Neurosci*. 2019; 13: 140. DOI: 10.3389/fnins.2019.00140.
 15. Frolov A, Husek D, Bobrov PD, Korshakov A, Chernikova L, Konovalov R, Mokienko O. Sources of EEG activity most relevant to performance of brain-computer interface based on motor imagery. *Neural Network World*. 2012; 22 (1): 21–37. DOI: 10.14311/Nnw.2012.22.002.
 16. Frolov AA, Mokienko O, Lyukmanov R, Biryukova E, Kotov S, Turbina L, et al. Post-stroke Rehabilitation Training with a Motor-Imagery-Based Brain-Computer Interface (BCI)-Controlled Hand Exoskeleton: A Randomized Controlled Multicenter Trial. *Front Neurosci*. 2017; 11: 400. DOI: 10.3389/fnins.2017.00400.
 17. Yoshimura N, Tsuda H, Aquino D, Takagi A, Ogata Y, Koike Y, et al. Age-Related Decline of Sensorimotor Integration Influences Resting-State Functional Brain Connectivity. *Brain sciences*. 2020; 10 (12): 966.
 18. Tanji J, Shima K. Role for supplementary motor area cells in planning several movements ahead. *Nature*. 1994; 371 (6496): 413–6. DOI: 0.1038/371413a0.
 19. Mazurek KA, Richardson D, Abraham N, Foxe JJ, Freedman EG. Utilizing High-Density Electroencephalography and Motion Capture Technology to Characterize Sensorimotor Integration While Performing Complex Actions. *IEEE transactions on neural systems and rehabilitation engineering: a publication of the IEEE Engineering in Medicine and Biology Society*. 2020; 28 (1): 287–96. DOI: 10.1109/TNSRE.2019.2941574.
 20. Gassert R, Dietz V. Rehabilitation robots for the treatment of sensorimotor deficits: a neurophysiological perspective. *Neuroeng Rehabil*. 2018; 15 (1): 46. DOI: 10.1186/s12984-018-0383-x.

Литература

1. Edwards LL, King EM, Buetefisch CM, Borich MR. Putting the "Sensory" Into Sensorimotor Control: The Role of Sensorimotor Integration in Goal-Directed Hand Movements After Stroke. *Frontiers in Integrative Neuroscience*. 2019; 13: 16. DOI: 10.3389/fnint.2019.00016.
2. Espenhahn S, Rossiter HE, van Wijk BCM, Redman N, Rondina JM, Diedrichsen J, et al. Sensorimotor cortex beta oscillations reflect motor skill learning ability after stroke. *Brain Communications*. 2020; 2 (2): fcaa161. DOI: 10.1093/braincomms/fcaa161.
3. Mahoney JR, Verghese J. Does Cognitive Impairment Influence Visual-Somatosensory Integration and Mobility in Older Adults? *The journals of gerontology. Series A, Biological sciences and medical sciences*. 2020; 75 (3): 581–8. DOI: 10.1093/gerona/gz117.
4. Jacquy L, Baldassarre G, Santucci VG, O'Regan JK. Sensorimotor Contingencies as a Key Drive of Development: From Babies to Robots. *Frontiers in neurobotics*. 2019; 13: 98. DOI: 10.3389/fnbot.2019.00098.
5. Luft AR, Buitrago MM, Ringer T, Dichgans J, Schulz JB. Motor skill learning depends on protein synthesis in motor cortex after training. *The Journal of neuroscience: the official journal of the Society for Neuroscience*. 2004; 24 (29): 6515–20. DOI: 10.1523/JNEUROSCI.1034-04.2004.
6. Hosp JA, Mann S, Wegenast-Braun BM, Calhoun ME, Luft AR. Region and task-specific activation of arc in primary motor cortex of rats following motor skill learning. *Neuroscience*. 2013; 250: 557–64. DOI: 10.1016/j.neuroscience.2013.06.060.
7. Norman SL, McFarland DJ, Miner A, Cramer SC, Wolbrecht ET, Wolpaw JR, Reinkensmeyer DJ. Controlling pre-movement sensorimotor rhythm can improve finger extension after stroke. *Journal of neural engineering*. 2018; 15 (5): 056026. DOI: 10.1088/1741-2552/aad724.
8. Friedrich J, Verrel J, Kleimaker M, Münchau A, Beste C, Bäumer T. Neurophysiological correlates of perception-action binding in the somatosensory system. *Scientific reports*. 2020; 10 (1): 14794. DOI: 10.1038/s41598-020-71779-0.
9. Котов С. В., Турбина Л. Г., Бобров П. Д., Фролов А. А., Павлова О. Г., Курганская М. Е., Бирюкова Е. В. Применение комплекса «интерфейс «мозг-компьютер» и экзоскелет» и техники вообращения движения для реабилитации после инсульта. *Альманах клинической медицины*. 2015; (39): 15–21. DOI: 10.18786/2072-0505-2015-39-15-21.
10. Королева Е. С., Алифинова В. М., Латыпова А. В., Чебан С. В., Отт В. А., Бразовский К. С., и др. Принципы и опыт применения роботизированных реабилитационных технологий у пациентов после инсульта. *Бюллетень сибирской медицины*. 2019; 18 (2): 223–33. DOI: 10.20538/1682-0363-2019-2-223-233.
11. Di Pino G, Pellegrino G, Assenza G, Capone F, Ferreri F, Formica D, et al. Modulation of brain plasticity in stroke: a novel model for neurorehabilitation. *Nat Rev Neurol*. 2014; 10 (10): 597–608. DOI: 10.1038/nrneurol.2014.162.
12. Nahmani M, Turrigiano GG. Adult cortical plasticity following injury: recapitulation of critical period mechanisms? *Neuroscience*. 2014; 283: 4–16. DOI: 10.1016/j.neuroscience.2014.04.029.
13. Bertani R, Melegari C, De Cola MC, Bramanti A, Bramanti P, Calabrò RS. Effects of robot-assisted upper limb rehabilitation in stroke patients: a systematic review with meta-analysis. *Neurol Sci*. 2017; 38 (9): 1561–9. DOI: 0.1007/s10072-017-2995-5.
14. Chivukula S, Jafari M, Aflalo T, Yong NA, Pouratian N. Cognition in Sensorimotor Control: Interfacing With the Posterior Parietal Cortex. *Front Neurosci*. 2019; 13: 140. DOI: 10.3389/fnins.2019.00140.
15. Frolov A, Husek D, Bobrov PD, Korshakov A, Chernikova L, Konovalov R, Mokienko O. Sources of EEG activity most relevant to performance of brain-computer interface based on motor imagery. *Neural Network World*. 2012; 22 (1): 21–37. DOI: 10.14311/Nnw.2012.22.002.

16. Frolov AA, Mokienko O, Lyukmanov R, Biryukova E, Kotov S, Turbina L, et al. Post-stroke Rehabilitation Training with a Motor-Imagery-Based Brain-Computer Interface (BCI)-Controlled Hand Exoskeleton: A Randomized Controlled Multicenter Trial. *Front Neurosci.* 2017; 11: 400. DOI: 10.3389/fnins.2017.00400.
17. Yoshimura N, Tsuda H, Aquino D, Takagi A, Ogata Y, Koike Y, et al. Age-Related Decline of Sensorimotor Integration Influences Resting-State Functional Brain Connectivity. *Brain sciences.* 2020; 10 (12): 966.
18. Tanji J, Shima K. Role for supplementary motor area cells in planning several movements ahead. *Nature.* 1994; 371 (6496): 413–6. DOI: 0.1038/371413a0.
19. Mazurek KA, Richardson D, Abraham N, Foxe JJ, Freedman EG. Utilizing High-Density Electroencephalography and Motion Capture Technology to Characterize Sensorimotor Integration While Performing Complex Actions. *IEEE transactions on neural systems and rehabilitation engineering: a publication of the IEEE Engineering in Medicine and Biology Society.* 2020; 28 (1): 287–96. DOI: 10.1109/TNSRE.2019.2941574.
20. Gassert R, Dietz V. Rehabilitation robots for the treatment of sensorimotor deficits: a neurophysiological perspective. *Neuroeng Rehabil.* 2018; 15 (1): 46. DOI: 10.1186/s12984-018-0383-x.

ANTITUMOR EFFECT OF RADIATION THERAPY ON ORTHOTOPIC PDX MODELS OF HUMAN ESOPHAGEAL ADENOCARCINOMA

Kiblitckaya AA , Goncharova AS, Anisimov AE, Snezhko AV, Dimitriadi SN, Maslov AA, Gevorkyan YA, Kolesnikov EN

National Medical Research Center for Oncology, Rostov-on-Don, Russia

As a rule, esophageal adenocarcinoma develops in the lower esophagus. Life expectancy and survival rates depend on the cancer stage and the general health of the patient. Chemoradiotherapy is the most successful treatment approach to this type of cancer. The choice of optimal radiation doses for achieving the best possible therapeutic effect is still a challenge. The aim of this paper was to study effective radiation doses and assess response of human esophageal adenocarcinoma to radiation using a PDX model. The study was conducted in female Balb/c nude mice ($n = 25$). Fragments of the donor tumor were implanted into the cervical esophagus of immunodeficient mice. Effects of radiation on the obtained orthotopic xenografts were studied after each of 3 irradiation sessions (4, 6, 8, and 10 Gy in each of the experimental groups, respectively). First-passage xenografts reproduced the morphology of the donor tumor. The mean tumor volume differed significantly between the control group and the experimental groups exposed to 6, 8 or 10 Gy ($p \leq 0.01$) after each irradiation session. Tumor growth delay was significant after exposure to the total dose of 18 Gy. The further radiation dose increase was ineffective. The reduction of tumor volume in the xenografts was correlated to the increase in the one-time radiation dose. The total dose over 18 Gy produced a detrimental effect on the hematopoietic system and blood biochemistry of the experimental mice.

Keywords: esophageal adenocarcinoma, orthotopic xenograft, radiotherapy, PDX-model, immunodeficient mouse

Author contribution: Kiblitckaya AA — data processing, manuscript preparation, technical editing, reference list, figures; Goncharova AS, Maslov AA — study concept and design, manuscript preparation; Anisimov AE — study concept and design, manuscript preparation, data acquisition, analysis and interpretation; Snezhko AV — content editing, manuscript preparation; Dimitriadi SN — data analysis and interpretation, technical editing; Gevorkyan YA — content editing; Kolesnikov EN — content and technical editing.

Ethical standards: the study fully complied with the principles of the Declaration of Helsinki; all requirements for animal housing were met; surgical interventions were conducted following the guidelines on the Care and Use of Laboratory Animals. The donors provided informed consent for their biological samples to be used in the study.

 **Correspondence should be addressed:** Alexandra A. Kiblitckaya
14 Liniya, 63, Rostov-on-Don, 344037, Russia; kibaleand@gmail.com

Received: 16.09.2021 **Accepted:** 04.10.2021 **Published online:** 20.10.2021

DOI: 10.24075/brsmu.2021.047

ПРОТИВООПУХОЛЕВОЕ ВЛИЯНИЕ ЛУЧЕВОЙ ТЕРАПИИ НА ОРТОТОПИЧЕСКУЮ PDX-МОДЕЛЬ АДЕНОКАРЦИНОМЫ ПИЩЕВОДА ЧЕЛОВЕКА

А. А. Киблицкая , А. С. Гончарова, А. Е. Анисимов, А. В. Снежко, С. Н. Димитриади, А. А. Маслов, Ю. А. Геворкян, Е. Н. Колесников

Национальный медицинский исследовательский центр онкологии, Ростов-на-Дону, Россия

Аденокарцинома пищевода развивается, как правило, в нижней части органа. Продолжительность жизни и выживаемость при данном заболевании зависят от стадии патологического процесса и состояния здоровья пациента. Наиболее успешный метод для лечения аденокарциномы пищевода — химиолучевая терапия. Проблема подбора оптимальных доз облучения для получения максимального эффекта по сей день актуальна. Целью исследования было изучить эффективные дозы и оценить противоопухолевую активность лучевой терапии на ортотопической PDX аденокарциномы пищевода человека. Исследование провели на самках мышей линии Balb/c nude ($n = 25$). Ортотопическую трансплантацию осуществляли путем имплантации образцов опухоли пациента в шейный отдел пищевода иммунодефицитной мыши. Лучевое воздействие на ортотопические ксенографты исследовали в 3 этапа с кратностью облучения 1 раз в дозах 4, 6, 8 и 10 Гр. По результатам гистологического анализа ксенографты 1-й генерации воспроизводили основные морфологические характеристики опухоли пациента. Оценка динамики роста объемов опухолевых узлов экспериментальных животных позволяет сделать вывод, что у животных, облученных в однократной дозе 6, 8 или 10 Гр, средние значения объемов опухолевых узлов статистически значимо отличались ($p \leq 0,01$) от значений в контрольной группе после каждой из трех процедур лучевого воздействия. По расчетам показателя торможения роста опухоли при суммарной дозе 18 Гр наблюдали значительное подавление роста опухоли. Дальнейшее повышение дозы лучевого воздействия было неэффективно. Установили, что снижение объемов опухолевых узлов в ксенографтах коррелирует с увеличением разовой дозы, при этом суммарная доза более 18 Гр пагубно влияет на систему кроветворения и биохимические показатели крови мышей.

Ключевые слова: аденокарцинома пищевода, ортотопический ксенографт, лучевая терапия, PDX-модель, иммунодефицитная мышь

Вклад авторов: А. А. Киблицкая — обработка материала, написание текста, техническое редактирование, оформление библиографии, подготовка иллюстраций; А. С. Гончарова, А. А. Маслов — концепция и дизайн исследования, подготовка статьи; А. Е. Анисимов — концепция и дизайн исследования, подготовка статьи, сбор, анализ и интерпретация данных, написание текста; А. В. Снежко — научное редактирование, подготовка статьи; С. Н. Димитриади — анализ и интерпретация данных, техническое редактирование; Ю. А. Геворкян — научное редактирование; Е. Н. Колесников — научное редактирование, техническое редактирование

Соблюдение этических стандартов: исследование проведено с соблюдением требований Хельсинкской декларации; условия содержания животных соответствовали стандартам работы с животными; все хирургические манипуляции в эксперименте были выполнены с соблюдением «Правил проведения работ с использованием лабораторных животных». От пациентов было получено письменное информированное согласие на передачу биологического материала.

 **Для корреспонденции:** Александра Андреевна Киблицкая
ул. 14-я линия, д. 63, г. Ростов-на-Дону, 344037, Россия; kibaleand@gmail.com

Статья получена: 16.09.2021 **Статья принята к печати:** 04.10.2021 **Опубликована онлайн:** 20.10.2021

DOI: 10.24075/vrgmu.2021.047

Esophageal cancer (EC) is an extremely aggressive malignancy and one of the leading causes of cancer mortality and morbidity worldwide [1]. Due to nodal involvement, the five-year survival rate is only ~10–15% [2]. Risk factors for EC include consumption of hot foods and beverages, smoking, alcohol abuse, inhalation of toxic gases, exposure to drinking water contaminated with heavy metals, and ingestion of caustic substances [3].

There are 2 main histologic subtypes of EC: esophageal squamous cell carcinoma and esophageal adenocarcinoma (EAC) [4]. In Russia, squamous cell carcinoma is more common than EAC. However, the incidence of EAC localized to the distal esophagus or gastroesophageal junction has been on the rise in the past few years [5, 6]. Unlike squamous cell carcinoma, EAC is characterized by early metastasis to regional lymph nodes and subserosal invasion with omental bursa involvement. This cancer rarely metastasizes to the liver [7]. It can spread to the submucosal lining of the thoracic esophagus, invading the diaphragm, pleura and pericardium. EAC is often characterized by exophytic growth, making surgical treatment difficult or lowly effective [8].

At present, chemoradiotherapy remains the optimal treatment approach to cervical esophageal cancer. Esophagectomy with pharyngogastric anastomosis often leads to postoperative complications and patient deterioration. The 5-year survival rate after chemoradiotherapy is 27% [9]. Two forms of radiation therapy are used: teletherapy and brachytherapy. Radiotherapy can be delivered perioperatively or in combination with chemotherapy. The instruments and methodology for radiotherapy have been refined over the years, but radioresistance observed in different histological types of EC still remains a serious challenge.

In theory, high doses of radiation will increase the probability of a more pronounced cytotoxic effect. In practice, tumor breakdown products are toxic to the patient and disrupt their homeostasis. This raises the question as to what radiation methods and optimal doses should be used to achieve the maximum antitumor effect with minimal harm to the patient.

One of the hurdles to the improvement of treatment efficacy for human EAC is the absence of reliable preclinical models for translational studies [10]. Traditional experimental models, like cell-line derived xenografts injected subcutaneously or directly into the esophageal wall of immunodeficient mice, do not recapitulate the intratumoral heterogeneity of the donor tumor [11]. By contrast, patient-derived xenograft (PDX) models hold promise for developing novel strategies for cancer treatment [12].

In a PDX model, fragments of the donor tumor are implanted into immunodeficient mice [13]. Translational cancer studies utilize athymic Balb/c nude mice carrying the Foxn1 mutation [14, 15]. Immune deficiency due to T-cell deficit facilitates successful engraftment and metastasis of the donor tumor [16]. PDX models retain morphological characteristics and heterogeneity of the donor tumor and therefore predict the patient's response to treatment better than cell line-derived xenografts [17]. Although the human stroma is replaced with the murine stroma in a PDX model, the model retains intratumor heterogeneity through multiple passages [18].

Because of their technical simplicity, heterotypic (subcutaneous) PDX models are extensively used in translational cancer research. However, subcutaneous xenografts do not reproduce the initial microenvironment of the donor tumor, are subject to encapsulation, advance locally, and do not metastasize [19].

An orthotopic PDX model of human EAC is generated by direct implantation of the tumor fragment into the distal



Fig. 1. The orthotopic PDX model of human esophageal adenocarcinoma (passage 6)

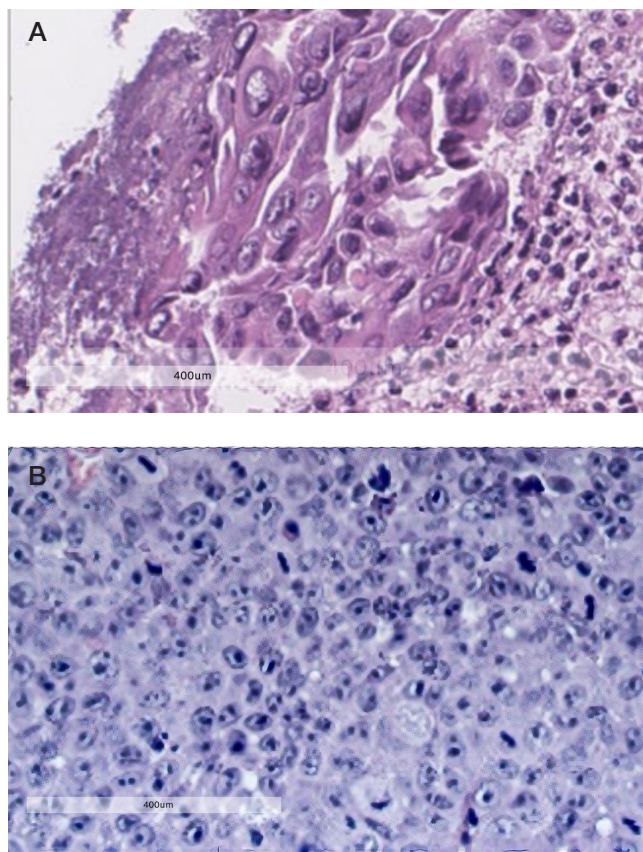


Fig. 2. Histology slices of moderately differentiated human EAC. A. The donor tumor. B. The orthotopic xenograft, passage 1. Hematoxylin-eosin staining; $\times 400$

esophageal wall of the mouse. The growing nodule and the effect of radiotherapy are easily measurable; yet, the anatomy and size of the murine esophagus make this cancer model technically sophisticated [20]. The esophageal wall provides a specific microenvironment to EAC, so the model can recapitulate the pathomorphologic and molecular features of the donor tumor [21]. Consequently, orthotopic PDX models are employed in the studies of tumor behavior and therapeutic approaches to cancer. In our experiment, the anticancer effect of radiotherapy was measured based on tumor growth delay (TGD) [22].

The aim of this paper was to study effective radiation doses for EAC treatment and assess response of human EAC to radiation using a PDX model generated by transplanting fragments of the donor tumor into the cervical esophagus of immunodeficient mice.

METHODS

The study was conducted at Rostov Cancer Research Institute. Orthotopic xenografts were prepared from fresh tumor material collected from a donor patient with EAC. The first 5 preparatory passages were conducted in 12 female Balb/c nude mice. The final 6th passage was conducted in 25 female Balb/c nude mice (age: 6–8 weeks, weight: 21–25 g). The animals were housed in an SPF animal facility in individually ventilated cages at 22–24 °C and 60% humidity under 12/12 light/dark conditions. At the end of the experiment, the animals were sacrificed in a CO₂ chamber; the tumors were immediately harvested for further manipulations.

EAC response to radiation was studied using orthotopic PDX tissue from passage 6 (Fig. 1). Xenografts were exposed to radiation once they reached 100 mm³ in size on day 30 after transplantation. The mice were divided into 5 groups: the control group and intervention groups 1, 2, 3, and 4 subjected to different radiation regimens. Each group consisted of 5 animals. Group 1 received a total dose of 12 Gy delivered in 3 fractions (4 Gy each); group 2, 18 Gy delivered in 3 fractions (6 Gy); group 3, 24 Gy delivered in 3 fractions (8 Gy); group 4, 30 Gy delivered in 3 fractions (10 Gy). The experiment lasted for 7 days. Irradiation was performed on the Xstrahl 150 X-ray

system (Xstrahl; UK) with an 0.2 mm Al filter and 1.5 cm and 2 cm applicators.

Tumor dimensions were measured with a caliper. Tumor volume was calculated using the following ellipsoid formula:

$$V = a \times b \times c \times \pi/6,$$

where V is tumor volume (mm³); a, b, c are the maximum diameters of the ellipsoid in 3 planes (mm).

Tumor growth delay was calculated by the formula:

$$\text{TGD} = (V_{\text{control}} - V_{\text{exper}}) / V_{\text{control}} \times 100.$$

Hematology tests were performed using an Exigo veterinary hematology analyzer (BoleMedical; USA). Biochemistry tests were performed using a VETSCANVS2 analyzer (Zoetis; USA).

Statistical analysis was conducted in STATISTICA 10. Quantitative variables are presented below as means and standard deviations $M \pm SD$. Differences between the means of each 2 independent variables were assessed using the Mann-Whitney U and the Wilcoxon rank-sum tests.

Orthotopic transplantation of donor tumor to the esophagus of immunodeficient mice

For the transplantation procedure, the animals were premedicated with intramuscularly administered xylazine hydrochloride (20 mg/g) and anesthetized 15 min later with an intramuscular injection of tiletamine hydrochloride and zolazepam hydrochloride (22.57 mg/g).

Prior to surgery, samples of the donor tumor were divided into ~27 mm³ fragments; patches of necrotized tissue were removed in advance. The fragments were transplanted 30 min after resection. The skin at the surgical site was treated with a povidone-iodine solution 10%.

To access the esophagus, a neck skin incision was made from the right ear base to the left ear base. The trachea and the underlying esophagus were isolated using blunt dissection. The adventitia and the muscular layer were dissected with a scalpel. The tumor fragment was sutured to the esophageal wall above the incision using 5-0 Prolene sutures. The wound was closed with Glover's suture [23].

After the transplanted tumor reached 150–250 mm³ in size, it was harvested and passaged. A total of 6 passages were performed.

Table 1. Mean EAC xenograft volumes and mouse body weight in the control and experimental groups

Group	Parameter	Day 0		Day 1		Day 5		Day 7	
		V, mm ³	Weight, g						
Control	Mean	86	21	626	22.7	1250.7	22.3	2136.6	22.3
	Standard deviation	2.8	0.5	4.9	0.3	148.5	0.8	74.5	0.8
1 (4 Gy)	Mean	91.1*	21.7	554.8*	23	1052.0*	21.1	1145.9*	21.1
	Standard deviation	2.4	0.6	9	0.4	72.9	1.2	120.7	1
2 (6 Gy)	Mean	88	20.5	235.1*	22.2	249.3*	22.7	248.1*	22.5
	Standard deviation	1.6	0.5	2.7	0.8	2	0.8	1.3	1.2
3 (8 Gy)	Mean	80.9*	22.2	210.8*	23.5	228.9*	23.5	227.8*	23.5
	Standard deviation	2	0.4	5.8	0.4	14	0.5	8.2	0.5
4 (10 Gy)	Mean	89.5	21.5	195.2*	22.7	200.1*	19.7	198.9*	19.8
	Standard deviation	2.8	0.8	6	1.3	3.3	3	4.4	0.9

Note: * — differences are significant between groups 1 (4 Gy), 2 (6 Gy), 3 (8 Gy), 4 (10 Gy) and the control group; Mann-Whitney U test ($p < 0.05$); • — differences are significant between groups 1 (4 Gy), 2 (6 Gy), 3 (8 Gy), 4 (10 Gy) and the control group; Mann-Whitney U test ($p \leq 0.01$).

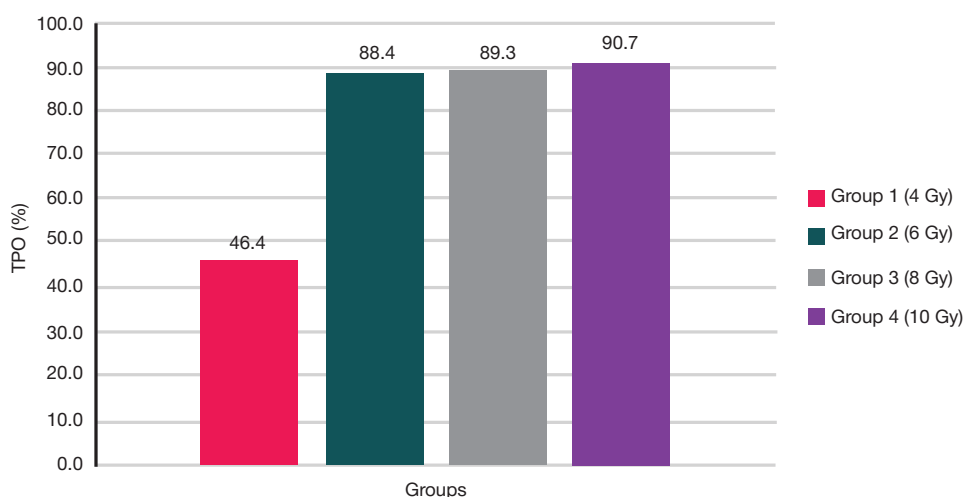


Fig. 3. TGW of the PDX model of human EAC in the experimental groups of mice irradiated with 4 Gy (group 1), 6 Gy (group 2), 8 Gy (group 3), and 10 Gy (group 4)

RESULTS

Engraftment was improving with each passage. At passages 1, 2 and 3, the rate of engraftment was 55%, 70% and 80%, respectively. From passage 4 to passage 6, orthotopic xenograft survival was 100%.

Histologic verification of human EAC PDX models

Histologically, the donor tumor was a moderately differentiated adenocarcinoma. Along with typical adenocarcinoma cells, the sample contained atypical spindle-shaped cells with karyopyknotic or karyorrhectic nuclei. First-passage xenografts reproduced the main characteristics of the donor tumor quite well and were histologically a moderately differentiated adenocarcinoma, with mostly typically shaped cells with degenerative nuclei or pathological mitoses (Fig. 2).

Effects of radiation on orthotopic xenografts of human EAC

The mean xenograft volumes and the mean weight of mice in the control and experimental groups are provided in Table 1. After the 1st and 3rd irradiation sessions, significant differences in the mean xenograft volume were observed between group 1 (4 Gy) and the untreated control group ($p \leq 0.01$). Significant differences ($p \leq 0.01$) in the mean tumor volume were also registered after each irradiation session between the control group and the experimental groups subjected to different irradiation regimens (one-time doses of 6, 8 and 10 Gy). On day 7, the tumors stopped growing at 248.1, 227.8 and 198.9 mm³ in groups receiving 6, 8 and 10 Gy fractions, respectively; these sizes differed significantly from tumor sizes in the control group.

Table 2. Complete blood counts on day 25 of the experiment

Group	Hemoglobin	Platelets	White blood cells, 10 ⁹ /L	Lymphocytes, 10 ⁹ /L	Monocytes, 10 ⁹ /L	Red blood cells, 10 ⁹ /L
Control	118 ± 4.9	481 ± 79	3.7 ± 0.6	1.6 ± 0.4	0.9 ± 0.2	6.8 ± 0.5
1 (4 Gy)	115 ± 4.3*	477 ± 60*	3.3 ± 0.5*	1.4 ± 0.4	0.85 ± 0.2	6.6 ± 0.4
2 (6 Gy)	111 ± 4.4*	474 ± 55*	3.0 ± 0.4*	1.2 ± 0.3*	0.7 ± 0.3	6.0 ± 0.4*
3 (8 Gy)	99 ± 5.8*	470 ± 58*	2.7 ± 0.4*	1.0 ± 0.4*	0.5 ± 0.2*	5.7 ± 0.4*
4 (10 Gy)	93 ± 3.9*	464 ± 52*	2.5 ± 0.3*	0.7 ± 0.1*	0.4 ± 0.1*	5.2 ± 0.3*

Note: * — differs from the control group, $p < 0.01$; the Wilcoxon rank sum test.

No reliable differences in body weight dynamics were observed between the groups throughout the experiment. The mean body weight ranged from 19.7 ± 3.0 g to 23.5 ± 0.5 g. This suggests that the studied radiation doses did not produce a considerable impact on the animal weight.

At the end of the experiment, TGD was 46.4, 88.4, 89.3, and 90.7% in groups 1, 2, 3, and 4, respectively (Fig. 3). The analysis revealed that the total dose of 18 Gy caused a significant tumor growth delay; so, it may be ineffective to further increase the delivered dose due to the adverse effects of radiation.

Clinical examination of group 4 that had received the total radiation dose of 30 Gy revealed the presence of tumor necrosis. The tumors produced milky-colored discharge and were ulcerating on the surface. In the control group, the tumors were larger, dark purple-blue, well-vascularized, without signs of necrosis or ulceration.

According to the pathomorphological examination of tumor fragments subjected to the total radiation dose of 30 Gy, glandular cells were undergoing transformation without keratinization; there was pronounced tissue necrosis (~ 50% of the total sample area) and sites of pathological mitosis. Besides, there were cells undergoing karyolysis and cytolysis (Fig. 4).

Hematological and biochemical blood profile of orthotopic PDXs of human EAC after irradiation

After the full course of irradiation was completed, hematological profiles of the irradiated mice were prepared (Table 2).

The average hemoglobin concentration was inversely proportional to the applied radiation dose and differed between the control group and groups 1, 2, 3 and 4 ($p < 0.01$). Total red blood cell, white blood cell, lymphocyte, monocyte and platelet counts were lower in the experimental groups. Specifically,

lymphocyte, monocyte and platelet counts were significantly lower in groups 2, 3 and 4 ($p < 0.01$), whereas red and white blood cell counts differed significantly between the control group and groups 1, 2, 3, and 4 ($p < 0.01$).

Results of the blood biochemistry test are provided in Table 3. Differences in total protein were significant between the control group and groups 2, 3 and 4 ($p < 0.01$). The increase in the delivered radiation dose led to a gradual rise in urea, creatinine and alanine aminotransferase concentrations; differences in these blood parameters between the control group and the groups exposed to 8 and 10 Gy were statistically significant ($p < 0.01$). The shifts in the biochemical profile of the irradiated animals can be explained by active necrosis developing in the irradiated tumors. Blood sugar did not differ significantly between the groups. Alkaline phosphatase in groups 1, 2, 3, and 4 was significantly lower ($p < 0.01$) than in the control group. Reduced alkaline phosphatase activity can be explained by a decline in hemoglobin concentrations observed in all experimental groups. After the radiation dose totaled to 24 Gy, the animals became less active and acquired a hunch posture.

DISCUSSION

There is an interesting publication investigating the antitumor effect of a combination therapy with fractionated radiation (3×2 Gy) and intraperitoneally administered TH-302 (50 mg/kg) on the subcutaneous xenografts of esophageal squamous cell carcinoma (OE21) and EAC (OE19) [24]. The study has demonstrated a significant tumor growth delay for OE19 ($p = 0.02$) and OE21 ($p = 0.03$) cancers following a combination therapy with TH-302 and fractionated radiation, as compared with radiation therapy alone. The models generated through the subcutaneous implantation of cancer cells lacked intratumor heterogeneity typical for human carcinomas. This means that preclinical data may differ significantly from the results of clinical studies [12].

According to another study, a combination of PI3K α -selective inhibitor CYH33 and radiotherapy produces a synergic inhibiting effect on the growth of subcutaneous xenografts of human esophageal squamous cell carcinoma [25]. Although subcutaneous xenografts created from the fragments of human donor tumors retained the heterogeneity of the donor material, the site of heterotopic implantation precluded mimicking the microenvironment of the donor tumor, blocked metastasis and did not reproduce the major signaling pathways involved in oncogenesis.

Table 3. Results of blood biochemistry tests on day 25 of the experiment

Group	Protein, mg/dL	Urea nitrogen, mg/dL	Creatinine, mg/dL	Glucose, mg/dL	ALT, un/L	ALP, un/L
Control	5.4 \pm 0.3	0.4 \pm 0.1	0.6 \pm 0.05	190 \pm 14	51 \pm 6.7	65 \pm 8.2
1 (4 Gy)	5.5 \pm 0.3	0.5 \pm 0.1	0.75 \pm 0.1	185 \pm 15	53 \pm 7	62 \pm 4.8*
2 (6 Gy)	5.7 \pm 0.5*	0.6 \pm 0.2	0.9 \pm 0.1*	189 \pm 10	58 \pm 6.5*	63 \pm 4*
3 (8 Gy)	6.1 \pm 0.4*	0.8 \pm 0.1*	1.2 \pm 0.2*	192 \pm 16	59 \pm 8.6*	61 \pm 5.5*
4 (10 Gy)	6.3 \pm 0.4*	1.1 \pm 0.3*	1.3 \pm 0.1*	191 \pm 12	62 \pm 6.7*	55 \pm 7.5*

Note: * — differs from the control group, $p < 0.01$; the Mann–Whitney U test. ALT — alanine aminotransferase; ALP — alkaline phosphatase.

In this study, we used the orthotopic model of human EAC since it is the closest to the actual patient's clinical response to therapy [26]. The choice of the model allowed us to study how exposure to radiation affected the growth of the obtained xenografts and to establish its dose-depending effect. In earlier works, PDX models of human tumors were studied as potential models for metastasis and were not used to evaluate the effects of radiation [27].

CONCLUSIONS

After each irradiation session, the average tumor volume differed significantly between the experimental groups exposed to 6, 8 and 10 Gy and the control group ($p \leq 0.01$). At the end of the experiment, TGD was 46.4, 88.4, 89.3 and 90.7% in groups 1, 2, 3, and 4, respectively. Although the body weight did not change throughout the experiment in any of the groups, exposure to radiation had a detrimental dose-dependent effect on the health of the experimental animals manifesting in their low complete blood counts and blood biochemistry tests. Exposure to the total radiation dose over 18 Gy resulted in reduced hemoglobin, low red and white blood cell counts, increased degradation of protein molecules in the setting of tumor necrosis. Therefore, further in vivo research of radiation therapy alone or in combination with antitumor agents using murine models of human EAC should not use the total radiation dose of over 18 Gy, considering the harm it does to the animal's health.

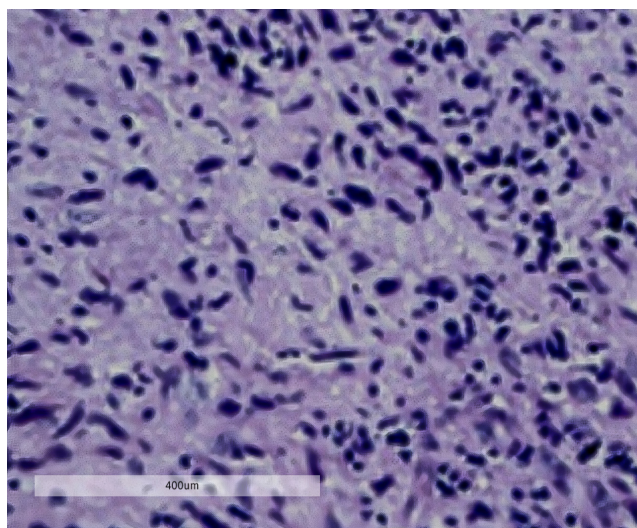


Fig. 4. Histology slices of the PDX model of human EAC generated in Balb/cNude mice after irradiation with a total dose of 30 Gy. Hematoxylin-eosin staining; $\times 400$

References

1. Gladilina IA, Tryakin AA, Zahidova FO, Malihova OA, Ivanov SM, Kravec OA, i dr. Rak pishhevoda: jepidemiologija, faktory riska i metody diagnostiki. *Onkologicheskij zhurnal: luchejavaja diagnostika, luchejavaja terapija*. 2020; 3 (1): 69–76. Russian.
2. Ho ALK, Smyth EC. A global perspective on esophageal cancer: two diseases in one. *The Lancet Gastroenterology & Hepatology*. 2020; 5 (6): 521–2. DOI: 10.1016/S2468-1253(20)30047-9.
3. Enzinger PC, Mayer RJ. Esophageal cancer. *New England Journal of Medicine*. 2003; 349 (23): 2241–52.
4. Lin EW, Karakasheva TA, Hicks PD, Bass AJ, Rustgi AK. The tumor microenvironment in esophageal cancer. *Oncogene*. 2016; 35 (41): 5337–49.
5. Aksel EM. Statistika zlokachestvennyh novoobrazovaniy zheludochno-kishechnogo trakta. *Sibirskij onkologicheskij zhurnal*. 2017; 16 (3): 5–11. DOI: 10.21294/1814-4861-2017-3-5-11. Russian.
6. Kit OI. Nejroendokrinnye, klinicheskie i morfologicheskie aspekty raka zheludka. *Novocherkassk: Lik*, 2014; 221 s. Russian.
7. Ishihara R, Oyama T, Abe S, Takahashi H, Ono H, Fujisaki J et al. Risk of metastasis in adenocarcinoma of the esophagus: a multicenter retrospective study in a Japanese population. *Journal of gastroenterology*. 2017; 52 (7): 800–8. DOI: 10.1007/s00535-016-1275-0.
8. Mahoney JL, Condon R. E. Adenocarcinoma of the esophagus. *Annals of surgery*. 1987; 205 (5): 557.
9. Urmonov UB, Dobrodeev AYU, Afanasev SG, Avgustinovich AV, Cheremisina OV. Sovremennye aspekty lechenija raka pishhevoda. *Sibirskij onkologicheskij zhurnal*. 2019; 18 (4): 78–84. DOI: 10.21294/1814-4861-2019-18-4-78-84. Russian.
10. Hidalgo M, Amant F, Biankin AV, Budinská E, Byrne AT, Caldas C, et al. Patient-derived xenograft models: an emerging platform for translational cancer research. *Cancer Discov*. 2014; 4: 998–1013. DOI: 10.1158/2159-8290.
11. Wilding JL, Bodmer WF. Cancer Cell Lines for Drug Discovery and Development. *Cancer Res*. 2014; 74 (9): 2377–84. DOI: 10.1158/0008-5472.CAN-13-2971.
12. Sung-Yup Cho. Patient-derived xenografts as compatible models for precision oncology. *Laboratory Animal Research*. 2020; 36: 14. DOI: 10.1186/s42826-020-00045-1.
13. Zhuo J, Su R, Tan W, Lian Z, Lu D, Xu X. The ongoing trends of patient-derived xenograft models in oncology. *Cancer Commun (Lond)*. 2020; 40 (11): 559–63. DOI: 10.1002/cac2.12096.
14. Fernandes DP, Pimentel MML, Santos FAD, Praxedes ÉA, Brito PD, Lima MA, Lelis ICNG, Macedo MF, Bezerra MB. Hematological and biochemical profile of BALB/c nude and C57BL/6 SCID female mice after ovarian xenograft. *An Acad Bras Cienc*. 2018; 90 (4): 3941–48. DOI: 10.1590/0001-3765201820180586.
15. Zhukova GV, Shihlyarova AI, Sagakyanc AB, Protasova TP. O rasshirenii variantov ispol'zovaniya myshej BALB/c nude dlja jeksperimental'nogo izuchenija zlokachestvennyh opuholej cheloveka in vivo. *Juzhno-Rossijskij onkologicheskij zhurnal*. 2020; 1 (2): 28–35. Russian.
16. Szadvari I, Krizanova O, Babula P. Athymic nude mice as an experimental model for cancer treatment. *Physiol Res*. 2016; 65 (Suppl 4): S441–53. DOI: 10.33549/physiolres.933526.
17. Pompili L, Porru M, Caruso C, Biroccio A, Leonetti C. Patient-derived xenografts: a relevant preclinical model for drug development. *J Exp Clin Cancer Res*. 2016; 35 (1): 189. DOI: 10.1186/s13046-016-0462-4.
18. Choi YY, Lee JE, Kim H, Sim MH, Kim K.-K., Lee G, et al. Establishment and characterisation of patient-derived xenografts as paraclinical models for gastric cancer. *Sci Rep*. 2016; 6: 22172. DOI: 10.1038/srep22172.
19. Hoffman RM. Patient-derived orthotopic xenografts: better mimic of metastasis than subcutaneous xenografts. *Nat Rev Cancer*. 2015; 15: 451–2. DOI: 10.1038/nrc3972.
20. Tétreault MP. Esophageal cancer: insights from mouse models. *Cancer growth and metastasis*. 2015; 8: 37–46. DOI: 10.4137/CGM.S21218.
21. Bhargava S, Hotz B, Buhr HJ, Hotz HG. An orthotopic nude mouse model for preclinical research of gastric cardia cancer. *Int J Colorectal Dis*. 2009; 24: 31–9. DOI: 10.1007/s00384-008-0584-z.
22. Rostovcev NM, Kotljarov NA. Sravnitel'nyj analiz jeffektivnosti luchevoje i fotodinamicheskogo lechenija jeksperimental'noj opuholi. *Pediatricheskij vestnik Juzhnogo Urala*. 2015; 1: 29–32. Russian.
23. Kolesnikov EN, Kit SO, Lukbanova EA, Goncharova AS, Maksimov AYU, avtory. Federal'noe gosudarstvennoe bjudzhetnoe uchrezhdenie "Rostovskij nauchno-issledovatel'skij onkologicheskij institut" Ministerstva zdravoochranenija Rossijskoj Federacii, patentoobladatel'. Sposob ortotopicheskoj transplantacii kul'tury opuholevyh kletok pishhevoda cheloveka v shejnyj otdel pishhevoda immunodeficitnyh myshej. Patent RF 2713798. G09B 23/28. Zajavka # 2019113616 ot 30.04.19. Russian.
24. Spiegelberg L, van Hoof SJ, Biemans R, Lieuwes NG, Marcus D, Niemanns R, et al. Evofosfamide sensitizes esophageal carcinomas to radiation without increasing normal tissue toxicity. *Radiother Oncol*. 2019; 141: 247–55. DOI: 10.1016/j.radonc.2019.06.034.
25. Shi J-J, Xing H, Wang Y-X, Zhang X, Zhan Q-M, Geng M-Y, et al. PI3K α inhibitors sensitize esophageal squamous cell carcinoma to radiation by abrogating survival signals in tumor cells and tumor microenvironment. *Cancer Letters*. 2019; 459: 145–55. DOI: 10.1016/j.canlet.2019.05.040.
26. Teicher BA, Andrews PA, editors. *Anticancer Drug Development Guide. Preclinical screening, clinical trials, and approval*. 2nd ed. Totowa, New Jersey: Humana Press; 2004. DOI: 10.1007/978-1-59259-739-0.
27. Treshhalina EM. Immunodeficitnye myshej Balb/c nude i modelirovanie razlichnyh variantov opuholevogo rosta dlja doklinicheskikh issledovanij. *RBZh*. 2017; 16 (3): 6–13. DOI: 10.17650/1726-9784-2017-16-3-6-13. Russian.

Литература

1. Гладиллина И. А., Трякин А. А., Захидова Ф. О., Малихова О. А., Иванов С. М., Кравец О. А. и др. Рак пищевода: эпидемиология, факторы риска и методы диагностики. *Онкологический журнал: лучевая диагностика, лучевая терапия*. 2020; 3 (1): 69–76.
2. Ho ALK, Smyth EC. A global perspective on esophageal cancer: two diseases in one. *The Lancet Gastroenterology & Hepatology*. 2020; 5 (6): 521–2. DOI: 10.1016/S2468-1253(20)30047-9.
3. Enzinger PC, Mayer RJ. Esophageal cancer. *New England Journal of Medicine*. 2003; 349 (23): 2241–52.
4. Lin EW, Karakasheva TA, Hicks PD, Bass AJ, Rustgi AK. The tumor microenvironment in esophageal cancer. *Oncogene*. 2016; 35 (41): 5337–49.
5. Аксель Е. М. Статистика злокачественных новообразований желудочно-кишечного тракта. *Сибирский онкологический журнал*. 2017; 16 (3): 5–11. DOI: 10.21294/1814-4861-2017-3-5-11.
6. Кит О. И. Нейроэндокринные, клинические и морфологические аспекты рака желудка. *Новочеркасск: Лик*, 2014; 221 с.
7. Ishihara R, Oyama T, Abe S, Takahashi H, Ono H, Fujisaki J et al. Risk of metastasis in adenocarcinoma of the esophagus: a multicenter retrospective study in a Japanese population. *Journal of gastroenterology*. 2017; 52 (7): 800–8. DOI: 10.1007/s00535-016-1275-0.
8. Mahoney JL, Condon R. E. Adenocarcinoma of the esophagus. *Annals of surgery*. 1987; 205 (5): 557.
9. Урмонов У. Б., Добродеев А. Ю., Афанасьев С. Г., Августинович А. В., Черемисина О. В. Современные аспекты лечения рака пищевода. *Сибирский онкологический журнал*. 2019; 18 (4): 78–84. DOI: 10.21294/1814-4861-2019-18-4-78-84.

10. Hidalgo M, Amant F, Biankin AV, Budinská E, Byrne AT, Caldas C, et al. Patient-derived xenograft models: an emerging platform for translational cancer research. *Cancer Discov.* 2014; 4: 998–1013. DOI: 10.1158/2159-8290.
11. Wilding JL, Bodmer WF. Cancer Cell Lines for Drug Discovery and Development. *Cancer Res.* 2014; 74 (9): 2377–84. DOI: 10.1158/0008-5472.CAN-13-2971.
12. Sung-Yup Cho. Patient-derived xenografts as compatible models for precision oncology. *Laboratory Animal Research.* 2020; 36: 14. DOI: 10.1186/s42826-020-00045-1.
13. Zhuo J, Su R, Tan W, Lian Z, Lu D, Xu X. The ongoing trends of patient-derived xenograft models in oncology. *Cancer Commun (Lond).* 2020; 40 (11): 559–63. DOI: 10.1002/cac2.12096.
14. Fernandes DP, Pimentel MML, Santos FAD, Praxedes ÉA, Brito PD, Lima MA, Lelis ICNG, Macedo MF, Bezerra MB. Hematological and biochemical profile of BALB/c nude and C57BL/6 SCID female mice after ovarian xenograft. *An Acad Bras Cienc.* 2018; 90 (4): 3941–48. DOI: 10.1590/0001-3765201820180586.
15. Жукова Г. В., Шихлярова А. И., Саракянц А. Б., Протасова Т. П. О расширении вариантов использования мышей BALB/c nude для экспериментального изучения злокачественных опухолей человека *in vivo*. *Южно-Российский онкологический журнал.* 2020; 1 (2): 28–35.
16. Szadvari I, Krizanova O, Babula P. Athymic nude mice as an experimental model for cancer treatment. *Physiol Res.* 2016; 65 (Suppl 4): S441–53. DOI: 10.33549/physiolres.933526.
17. Pompili L, Porru M, Caruso C, Biroccio A, Leonetti C. Patient-derived xenografts: a relevant preclinical model for drug development. *J Exp Clin Cancer Res.* 2016; 35 (1): 189. DOI: 10.1186/s13046-016-0462-4.
18. Choi YY, Lee JE, Kim H, Sim MH, Kim K.-K., Lee G, et al. Establishment and characterisation of patient-derived xenografts as paraclinical models for gastric cancer. *Sci Rep.* 2016; 6: 22172. DOI: 10.1038/srep22172.
19. Hoffman RM. Patient-derived orthotopic xenografts: better mimic of metastasis than subcutaneous xenografts. *Nat Rev Cancer.* 2015; 15: 451–2. DOI: 10.1038/nrc3972.
20. Tétreault MP. Esophageal cancer: insights from mouse models. *Cancer growth and metastasis.* 2015; 8: 37–46. DOI: 10.4137/CGM.S21218.
21. Bhargava S, Hotz B, Buhr HJ, Hotz HG. An orthotopic nude mouse model for preclinical research of gastric cardia cancer. *Int J Colorectal Dis.* 2009; 24: 31–9. DOI: 10.1007/s00384-008-0584-z.
22. Ростовцев Н. М., Котляров Н. А. Сравнительный анализ эффективности лучевого и фотодинамического лечения экспериментальной опухоли. *Педиатрический вестник Южного Урала.* 2015; 1: 29–32.
23. Колесников Е. Н., Кит С. О., Лукбанова Е. А., Гончарова А. С., Максимов А. Ю., авторы. Федеральное государственное бюджетное учреждение "Ростовский научно-исследовательский онкологический институт" Министерства здравоохранения Российской Федерации, патентообладатель. Способ ортотопической трансплантации культуры опухолевых клеток пищевода человека в шейный отдел пищевода иммунодефицитных мышей. Патент РФ 2713798. G09B 23/28. Заявка № 2019113616 от 30.04.19.
24. Spiegelberg L, van Hoof SJ, Biemans R, Lieuwes NG, Marcus D, Niemans R, et al. Evofosfamide sensitizes esophageal carcinomas to radiation without increasing normal tissue toxicity. *Radiother Oncol.* 2019; 141: 247–55. DOI: 10.1016/j.radonc.2019.06.034.
25. Shi J-J, Xing H, Wang Y-X, Zhang X, Zhan Q-M, Geng M-Y, et al. PI3K α inhibitors sensitize esophageal squamous cell carcinoma to radiation by abrogating survival signals in tumor cells and tumor microenvironment. *Cancer Letters.* 2019; 459: 145–55. DOI: 10.1016/j.canlet.2019.05.040.
26. Teicher BA, Andrews PA, editors. *Anticancer Drug Development Guide. Preclinical screening, clinical trials, and approval.* 2nd ed. Totowa, New Jersey: Humana Press; 2004. DOI: 10.1007/978-1-59259-739-0.
27. Трещалина Е. М. Иммунодефицитные мыши Balb/c nude и моделирование различных вариантов опухолевого роста для доклинических исследований. *РБЖ.* 2017; 16 (3): 6–13. DOI: 10.17650/1726-9784-2017-16-3-6-13.

SIMILARITIES AND DIFFERENCES BETWEEN THE *CHAETOPTERUS VARIOPEDATUS* POLYCHAETE LUCIFERASES DEPENDING ON THE TYPE OF HABITAT

Purtov KV¹, Petushkov VN¹, Rodionova NS¹, Chepurnykh TV², Kozhemyako VB³, Zagitova RI², Shcheglov AS^{2,4}✉, Ziganshin RH², Tsarkova AS^{2,4}

¹ Institute of Biophysics, Krasnoyarsk Science Center of the Siberian Branch of the Russian Academy of Sciences, Russia

² Shemyakin–Ovchinnikov Institute of Bioorganic Chemistry, Moscow, Russia

³ Pacific State Medical University, Vladivostok, Russia

⁴ Pirogov Russian National Research Medical University, Moscow, Russia

The marine polychaete *Chaetopterus varioopedatus* (Renier) (family *Chaetopteridae*) is a cosmopolitan species complex, consisting of distinct populations/subspecies. The worms release glowing (460 nm) clouds of mucus when disturbed, and their parapodia often glow brightly. Currently, it is still unclear how exactly the bioluminescence system of these polychaetes functions. It has been previously assumed that the *C. varioopedatus* luciferase may be used for detection of ferroptosis, the recently explored pathway of programmed cell death, resulting from accumulation of the ferrous ions. This study was aimed to extract and characterize the *C. varioopedatus* luciferases, as well as to compare luciferases obtained from *C. varioopedatus* of different populations. When extracting the enzyme responsible for bioluminescence from the frozen samples of Brazilian *C. varioopedatus* using the improved method, two active luciferases, L1 and L2, were obtained. We assumed that one of the listed above luciferases was responsible for luminescence of the mucus and the other luciferase was responsible for luminescence in parapodia, and used the method for the distinct samples of mucus and parapodia of the living Far Eastern *C. varioopedatus*. However, mucus of the latter turned out to be non-glowing. It is shown that luciferase L2 is responsible for luminescence in the parapodia of the *C. varioopedatus* polychaete, since this luciferase has been found in the total biomass of Brazilian polychaetes and parapodia of Far Eastern polychaetes. Luminescence of the Brazilian *C. varioopedatus* mucus is attributed to the functioning of luciferase L1, which is lacking in the mucus of the Far Eastern subspecies. The range of luciferase isoforms in polychaetes *C. varioopedatus* depends on the place of origin.

Keywords: bioluminescence, luciferase, polychaetes, *Chaetopterus varioopedatus*, marine worms

Acknowledgements: we would like to thank Anderson Oliveira, Professor, and Jeremy Mirza, junior researcher at the Oceanographic Institute of the University of São Paulo for assistance in collecting the biomass of Brazilian polychaetes, and Kirill Vinnikov, Director at the Institute of Marine Biology, Far Eastern Federal University, for advice on the *Chaetopterus* taxonomy.

Author contribution: Purtov KV, Petushkov VN, Rodionova NS — luciferase extraction; Chepurnykh TV — DNA extraction, PCR; Kozhemyako VB — biomass collection and preparation for luciferase extraction; Zagitova RI, Shcheglov AS — studying the properties of luciferases; Ziganshin RH — mass spectrometry; Tsarkova AS — overall project management.

✉ **Correspondence should be addressed:** Aleksandr S. Shcheglov
Miklukho-Maklaya, 16/10, Moscow, 117997, Russia; jukart@mail.ru

Received: 28.09.2021 **Accepted:** 12.10.2021 **Published online:** 26.10.2021

DOI: 10.24075/brsmu.2021.049

СХОДСТВО И РАЗЛИЧИЯ ЛЮЦИФЕРАЗ ПОЛИХЕТ *CHAETOPTERUS VARIOPEDATUS* В ЗАВИСИМОСТИ ОТ МЕСТА ИХ ОБИТАНИЯ

К. В. Пуртов¹, В. Н. Петушков¹, Н. С. Родионова¹, Т. В. Чепурных², В. Б. Кожемяко³, Р. И. Загитова², А. С. Щеглов^{2,4}✉, Р. Х. Зиганшин², А. С. Царькова^{2,4}

¹ Институт биофизики, Красноярский научный центр Сибирского отделения Российской Академии наук, Россия

² Институт биорганической химии имени академиков М. М. Шемякина и Ю. А. Овчинникова, Москва, Россия

³ Тихоокеанский государственный медицинский университет, Владивосток, Россия

⁴ Российский национальный исследовательский медицинский университет имени Н. И. Пирогова, Москва, Россия

Морские полихеты *Chaetopterus varioopedatus* (Renier) (семейство *Chaetopteridae*) — космополиты, представляющие собой видовой комплекс из отдельных популяций-подвидов. При раздражении черви выпускают светящиеся (460 нм) облака слизи, при этом часто ярко светятся и их параподии. На сегодняшний день по-прежнему не ясно, как именно работает биологическая система этих полихет. Ранее было выдвинуто предположение, что люцифераза *C. varioopedatus* может быть использована для детекции ферроптоза — недавно открытого пути программируемой клеточной гибели, вызванной накоплением ионов двухвалентного железа. Целью исследования было выделить и охарактеризовать люциферазы *C. varioopedatus*, а также сравнить люциферазы *C. varioopedatus* из разных популяций. При выделении ответственного за биологическую люминесценцию фермента из замороженных образцов бразильских *C. varioopedatus* по усовершенствованной методике были получены две активные люциферазы — L1 и L2. Предположив, что одна из указанных люцифераз определяет свечение слизи, а другая — свечение параподий червей, эту же методику применили к отдельным образцам слизи и параподий живых дальневосточных *C. varioopedatus*. Однако их слизь оказалась несветящейся. Показано, что функцию свечения параподий полихет *C. varioopedatus* обеспечивает люцифераза L2, так как она обнаружена в общей биомассе бразильских полихет и в параподиях дальневосточных полихет. Свечение слизи бразильских *C. varioopedatus* обусловлено функционированием люциферазы L1, которая отсутствует в слизи дальневосточного подвида. Набор изоформ люцифераз полихет *C. varioopedatus* зависит от места их обитания.

Ключевые слова: биологическая люминесценция, люцифераза, полихеты, *Chaetopterus varioopedatus*, морские черви

Благодарности: профессору Андерсону Оливейра и младшему научному сотруднику Джереми Мирза (Океанографический институт Университета Сан-Паулу) за помощь в сборе биомассы бразильских полихет, а также директору Института Мирового океана Дальневосточного федерального университета Кириллу Винникову за консультации по вопросам систематики *Chaetopterus*.

Вклад авторов: К. В. Пуртов, В. Н. Петушков, Н. С. Родионова — выделение люциферазы; Т. В. Чепурных — выделение ДНК, проведение ПЦР; В. Б. Кожемяко — сбор и подготовка биомассы для выделения люциферазы; Р. И. Загитова, А. С. Щеглов — исследование свойств люцифераз; Р. Х. Зиганшин — масс-спектрометрический анализ; А. С. Царькова — общее руководство проектом.

✉ **Для корреспонденции:** Александр Сергеевич Щеглов
ул. Миклухо-Маклая, д. 16/10, г. Москва, 117997, Россия; jukart@mail.ru

Статья получена: 28.09.2021 **Статья принята к печати:** 12.10.2021 **Опубликована онлайн:** 26.10.2021

DOI: 10.24075/vrgmu.2021.049

Chaetopterus variopedatus (Renier) belongs to the family *Chaetopteridae*, one of the most differentiated family of marine polychaetes inhabiting the benthic sediments during the adult stage, except for the uncommon pelagic species *C. pugaporcinus* (Osborn) [1]. Various researchers describe *C. variopedatus* as a species complex consisting of distinct populations/subspecies [2–4]. *C. variopedatus* is a cosmopolitan species living in temperate and tropical regions across the world. Various *C. variopedatus* subspecies are found in the coastal zones in Russia, Japan, Australia, Brazil, Europe and the USA [5]. A few years ago, phylogenetic relationships within *Chaetopteridae* were revised [1, 6], however, there remains considerable uncertainty about *C. variopedatus* sensu lato (Hartman).

C. variopedatus lives, hiding in the self-constructed U-shaped parchment-like tube, which is buried in the substrate. It has a segmented body with paired appendages, termed parapodia. *C. variopedatus* releases the blue-glowing (λ_{max} 460 nm) clouds of mucus in response to aggressive external stimuli [7]. Concurrently, parapodia of all body segments also glow brightly. This phenomenon historically attracted the attention of curious observers, which is confirmed by numerous reports. Many researchers have tried to understand the biochemical aspects of the *C. variopedatus* luminescence over the past 70 years [8–10]. However, the results are still controversial. To date, it is yet unclear how exactly the bioluminescence system of these polychaetes functions.

As previously reported, preparation of luciferase, which was used to reproduce the characteristic bioluminescence reaction *in vitro*, was obtained from the *C. variopedatus* biomass, collected in the São Sebastião Strait off the coast of Brazil. In order to achieve *in vitro* bioluminescence, the alcoholic extract of *C. variopedatus*, containing the main substrate (luciferin) and the ferrous ions, was added to the preparation of luciferase [11].

We have suggested that the *C. variopedatus* luciferase may be used to detect ferroptosis [12], the recently discovered pathway of programmed cell death, resulting from accumulation of the ferrous ions [13]. Ferroptosis investigations are important for both fundamental and applied biomedical science. It has been shown that the processes similar to ferroptosis occur in some neurodegenerative diseases [14]. Moreover, ferroptosis inducers have a high potential as anticancer drugs [15].

Thus, detailed characterization and decoding of the *C. variopedatus* bioluminescence system is considered an urgent scientific challenge. This study was aimed at the extraction and characterization of *C. variopedatus* luciferases, and at comparative examination of luciferases, obtained from *C. variopedatus* of different populations.

METHODS

Collection of *C. variopedatus* biomass

C. variopedatus was collected at two locations: São Sebastião Strait of the coast of Brazil and Trinity bay in the Possiet Gulf of Japan Sea. The worms were pulled out of their tubes and immediately frozen in liquid nitrogen. The frozen polychaetes were shipped on dry ice and stored at -70°C .

In order to obtain the glowing mucus, the worms were pulled out of the tubes, placed in the seawater and subjected to mechanical stimulation in the dark. The glowing mucus was collected with a pipette and frozen in liquid nitrogen.

Luciferase extraction

A total of 100 g of the frozen *C. variopedatus* biomass were homogenized in 900 mL of 50 mM Tris buffer, pH 7.5. The

homogenate was sonicated using Ultrasonic Disintegrator UD-20 (Techpan; Poland) 5 times for 2 min on ice and subsequently centrifuged (25 000 g x 20 min) at 4°C . Supernatant was supplemented with ammonium sulfate to the final concentration of 500 mM and passed through a cellulose DEAE column (Cellulose DEAE-32, Serva; Germany), equilibrated with 500 mM ammonium sulfate. The resulting filtrate was loaded onto the 25 x 100 mm Phenyl Sepharose CL-4B column (Cytiva; USA), equilibrated with 500 mM ammonium sulfate. Luciferase was eluted with 5 mM Tris-HCl buffer, pH 7.5.

Fractions, possessing luciferase activity, were combined and loaded onto the 16 x 200 mm Sepharose DEAE FF column (Cytiva; USA), equilibrated with 20 mM Tris-HCl, pH 7.5; the column was washed with the same buffer, and the linear gradient elution was performed. Buffer A: 20 mM Tris-HCl, pH 7.5; buffer B: 500 mM NaCl, 20 mM Tris-HCl, pH 7.5. The flow rate was 4 mL/min, and the time of gradient was 25 min.

The resulting preparation was concentrated on the 10 kDa cell (Amicon; Ireland) and loaded onto the 26 x 400 mm Sephacryl S200 column (Cytiva; USA), equilibrated with 200 mM NaCl and 20 mM Tris-HCl, pH 7.5. Elution was performed with the same buffer at a rate of 1.5 mL/min. The pooled fractions possessing luciferase activity were supplemented with ammonium sulfate to the final concentration of 500 mM, the resulting solution was loaded onto the 5 x 90 mm C8 column (Cytiva; USA). The linear gradient elution was carried out. Buffer A: 500 mM ammonium sulfate, 5 mM Tris-HCl, pH 7.5; buffer B: 5 mM Tris-HCl, pH 7.5. The flow rate was 0.5 mL/min, and the time of gradient was 80 min.

The resulting luciferase preparation was diluted twice with distilled water and loaded onto the 3 x 50 mm monoQ column (Cytiva; USA), equilibrated with 20 mM Tris-HCl, pH 7.5; the column was washed with the same buffer, and the linear gradient elution was performed. Buffer A: 20 mM Tris-HCl, pH 7.5; buffer B: 500 mM NaCl, 20 mM Tris-HCl, pH 7.5. The flow rate was 0.5 mL/min, and the time of gradient was 80 min.

The preparation was concentrated to a volume of 200 μL on the 10 kDa centrifuge filter (Amicon; Ireland) with subsequent gel filtration through the 10 x 300 mm Superdex 200 column (Cytiva; USA), equilibrated with 100 mM NaCl, 50 mM Tris-HCl, pH 7.5. Elution was performed with the same buffer at a rate of 0.8 mL/min.

Luciferase was extracted from the glowing mucus (10 mL) by the same method. Luciferase activity was measured in accordance with the previously developed protocol [11].

The species specificity of the available *Chaetopterus* specimens was defined using the following primers: HC02198 (5'-TAAACTTCAGGGTGACCAAAAATCA-3') and LCO1490 (5'-TCAACAAATCATAAAGATATTGG-3'). DNA was extracted from each *C. variopedatus* frozen tissue sample with the use of the ExtractDNA Blood & Cells kit (Evrogen; Russia). After that the COI gene fragment sequences with a length of 650 bps were amplified using the listed above primers, and DNA extracted from each frozen tissue specimen was used as a template. PCR products were used for Sanger sequencing.

Mass spectrometry analysis of purified luciferase preparations, obtained from Brazilian and Far Eastern *C. variopedatus*, was carried out using the Q Exactive Plus mass spectrometer (Thermo Fisher Scientific; USA) coupled with the Ultimate 3000 Nano LC System (Thermo Fisher Scientific; USA) by means of the nanoelectrospray ionization source (Thermo Fisher Scientific; USA). Full scan MS acquisition was carried out with the following parameters: 140k resolution, normal mass range (500–2000 amu), AGC target 3×10^6 , max. injection time

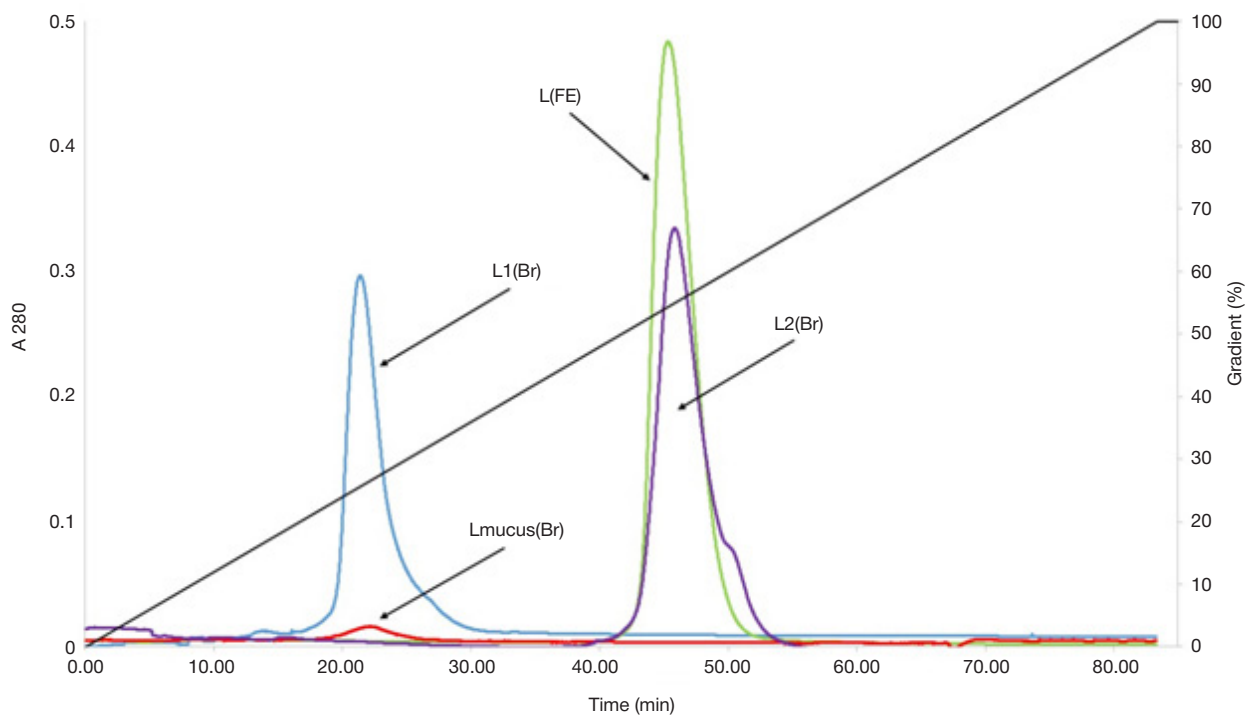


Fig. 1. Retention time values obtained for different *C. variopedatus* luciferases by chromatography involving the use of the monoQ anion exchange column, linear gradient; Br — Brazilian polychaetes, FE — Far Eastern polychaetes

30 ms. The raw data obtained were visualized with the XCalibur software (Thermo Fisher Scientific; USA).

RESULTS

The use of high-resolution anion exchange chromatography resulted in the target preparation separated into two almost homogeneous luciferases: L1, retention time 21.5 min, and L2, retention time 46 min (Fig. 1). The native molecular weight of those, calculated based on the results of gel filtration, was 70 kDa and 60 kDa, respectively (Fig. 2).

Under denaturing conditions of SDS electrophoresis, luciferase L1 consisted of two mono subunits, each about 18 kDa, and L2 consisted of at least two different subunits with a mass of about 18 and 15 kDa (Fig. 3).

The existence of two different luciferases in one animal may be indicative either of their differing origins or of their specific

functions [16, 17]. Although the *C. variopedatus* luminescence is monochrome (blue), each of the worm's luciferases probably functions locally: for example, one could be responsible for parapodia luminescence, and the other could be responsible for luminescence of mucus, released by the worm into the external environment.

To test this hypothesis, we used the sample of mucus, collected and frozen separately when catching Brazilian *C. variopedatus*. Chromatographic analysis of the preparation, purified in accordance with the described above method, revealed the presence of one luciferase only, and the retention time on the monoQ column (45.5 min) for this luciferase showed reasonable agreement with the retention time measured for L1, previously extracted from the total worm biomass (see Fig. 1). No specific samples of the Brazilian polychaetes were available, and the amount of the obtained L1 and L2 turned out to be insufficient for sequencing. That is why the authors

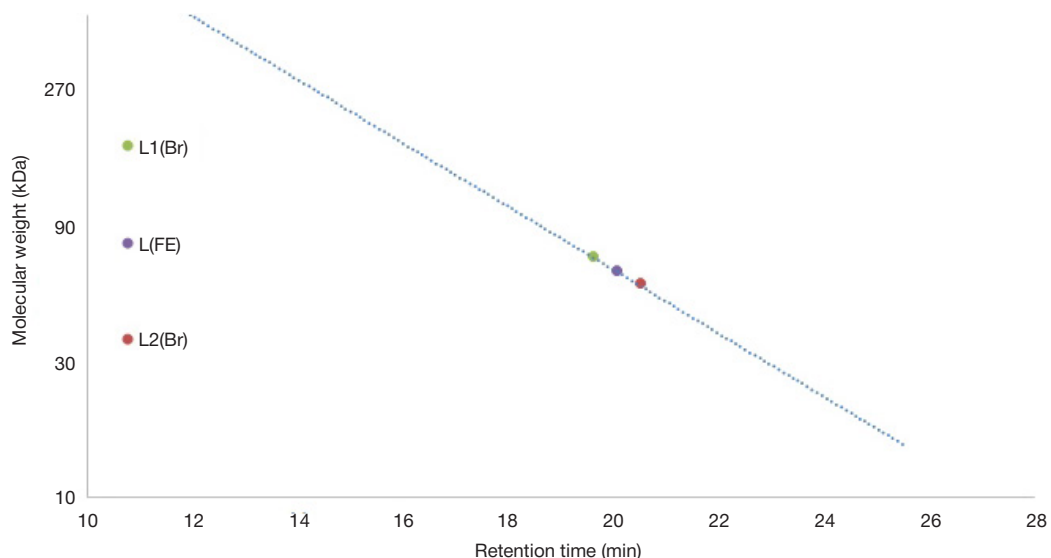


Fig. 2. Molecular weight of different *C. variopedatus* luciferases defined by gel filtration; Br — Brazilian polychaetes, FE — Far Eastern polychaetes

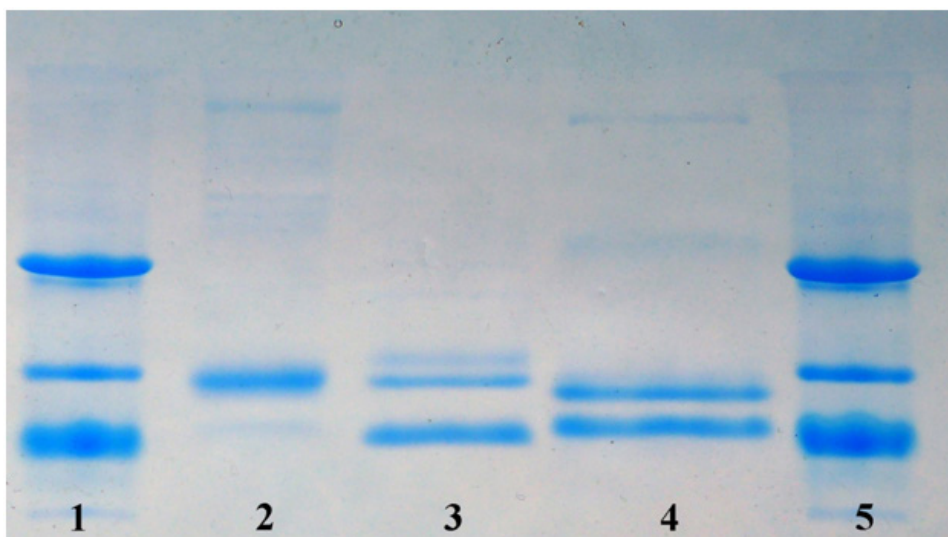


Fig. 3. Denaturing electrophoresis (15% SDS-PAGE) of the preparations L1 (2) and L2 (3) obtained from Brazilian *C. variopedatus* and luciferase obtained from Far Eastern *C. variopedatus* (4). Tracks 1 and 5 — protein calibration mixture for SDS-PAGE electrophoresis: 29,000, 21,000, 12,500, 6,500 kDa

turned to the closer source of these worms, the Far East coast of Russia.

Polychaetes, collected in the Trinity bay in the Gulf of Possiet of Japan Sea, were initially identified as *C. variopedatus* based on morphological features and delivered to the laboratory alive. In order to better define the species specificity of the available *Chaetopterus*, the authors performed sequencing of the 650 bp fragment of the cytochrome C oxidase subunit I gene (COI). Sequence analysis using the GenBank database showed that the COI fragments of Brazilian and Far Eastern samples were highly homologous (over 99%) to those of two different subspecies: *C. variopedatus* (AM503096.1) and *C. cautus* Marenzeller (LC533809.1), respectively. To date, these subspecies have been merged into one species complex, *C. variopedatus* [6].

When collecting the Far Eastern polychaetes, their mucus was frozen separately. We failed to detect luminescence after defrosting the mucus at the laboratory. The portions of fresh mucus, obtained by mechanical and chemical stimulation of living worms, did not glow as well. Adding luciferin and ferrous iron to the mucus samples also did not lead to light emission. The efforts to extract luciferase from the mucus samples in accordance with the described above method were unsuccessful.

No problems with the detection of the Far Eastern polychaete parapodia luminescence were encountered. From those we managed to extract a highly purified luciferase L(FE)

with a native molecular weight of 65 kDa (see Fig. 2). The retention time on the monoQ column for this luciferase was 45.5 min, which was almost equal with the retention time of the luciferase L2 (see Fig. 1). Denaturing SDS electrophoresis demonstrates that both L(FE) and L2 of Brazilian polychaetes consist of two different subunits' molecular masses are also almost similar (see Fig. 3).

We performed mass spectrometry analysis of the preparations of purified luciferases, obtained from Brazilian and Far Eastern *Chaetopterus*. The results, mass-to-charge ratio (m/z), charge (z) and calculated molecular weight (m), are presented in the Table.

Preparations of luciferases L2(Br) and L(FE) are significantly more heterogeneous compared to the L1(Br) preparation, which is probably due to posttranslational modifications and terminal amino acid cleavage. Mass sets, obtained for L2(Br) and L(FE), are almost the same, which attests to the enzymes similarity, and differ significantly from those obtained for L1(Br).

DISCUSSION

Bioluminescence systems are widely implemented in various biomedical technologies [18, 19]. Luminescence bioimaging, the intravital imaging of cells and intracellular processes, is one of the important areas [20]. In case of successful decoding, the *C. variopedatus* luciferase may conceivably be used for development of ferroptosis sensor [12]. We have optimized the

Table. Mass spectrometry analysis of the preparations of purified luciferases, obtained from Brazilian (Br) and Far Eastern (FE) *Chaetopterus*

L1(Br)			L2(Br)			L(FE)		
m/z	z	m	m/z	z	m	m/z	z	m
1355.5	12	16253	1352.49	11	14866.39	1352.67	11	14868.37
1364	12	16356	1364.5	11	14998.5	1355.5	12	16254
1374.94	11	15113.34	1365.94	11	15014.34	1364.09	12	16357
1383.58	11	15208.38	1373.31	11	15095.41	1366.13	11	15016.43
			1374.77	11	15111.47	1373.41	11	15096.51
			1383.76	11	15210.36	1374.95	11	15113.45
			1396.93	12	16751.16	1383.85	11	15211.35
			1405.35	12	16852.2	1396.94	12	16751.28
						1404.44	12	16853.28

Note: m/z — mass-to-charge ratio; z — charge; m — molecular weight.

previously developed method for the *C. variopedatus* luciferase extraction [11], thereby obtaining an almost pure preparation, suitable for mass spectrometry analysis.

Originally, *C. variopedatus* caught in Brazil were used for analysis, however, logistical challenges forced us to use *C. variopedatus* caught in Primorsky Krai in Russia. It is interesting that unlike Brazilian polychaetes, Far Eastern *C. variopedatus* did not produce any glowing mucus. Two different isoforms of luciferase (L1 and L2) were found in Brazilian *C. variopedatus*, while only one (L) was found in Far Eastern polychaetes. Mass spectrometry and chromatography showed that L2 and L were extremely likely and differed from L1. Presumably, the function of parapodia luminescence in *C. variopedatus* polychaetes is ensured by luciferase L2 (L), since this luciferase has been found in the total biomass of Brazilian polychaetes and parapodia of Far Eastern polychaetes.

Luminescence of mucus in Brazilian *C. variopedatus* is due to the functioning of luciferase L1, which is lacking in the mucus of the Far Eastern subspecies.

CONCLUSIONS

The findings lead to the following conclusions: 1. the *C. variopedatus* polychaete parapodia luminescence is attributed to the function of luciferase L2, since this luciferase has been identified in the total biomass of Brazilian polychaetes as L2(Br) and in parapodia of Far Eastern polychaetes as L(FE) identical to L2(Br); 2. the Brazilian *C. variopedatus* mucus luminescence is ensured by luciferase L1, which is lacking in the mucus of the Far Eastern subspecies; 3. the range of luciferase isoforms in *C. variopedatus* polychaetes might correlate with their place of origin.

References

- Osborn KJ, Rouse GW, Goffredi SK, Robison BH. Description and relationships of *Chaetopterus pugaporcinus*, an unusual pelagic polychaete (*Annelida*, *Chaetopteridae*). *Biol Bull.* 2007; 212 (1): 40–54. DOI: 10.2307/25066579.
- Petersen ME. *Chaetopterus variopedatus* (Renier) (*Annelida*: *Polychaeta*: *Chaetopteridae*): a species complex. What species are being used at MBL? *Biol Bull.* 1984; 167: 513.
- Petersen ME. Contribution to a revision of *Chaetopterus* Cuvier (*Polychaeta*: *Chaetopteridae*): redescription of *C. appendiculatus* Grube and *C. cautus* Marenzeller, with comments on some other species. *Bull Mar Sci.* 1997; 60: 619.
- Bhaud M. The spreading potential of polychaete larvae does not predict adult distributions; consequences for conditions of recruitment. *Hydrobiologia.* 1998; 375: 35. DOI: 10.1023/A:1017073409259.
- Mirza JD, Migotto AE, Yampolsky IV, de Moraes GV, Tsarkova AS, Oliveira AG. *Chaetopterus variopedatus* bioluminescence: a review of light emission within a species complex. *Photochem Photobiol.* 2020; 96: 768–78. DOI: 10.1111/php.13221.
- Moore JM, Nishi E, Rouse GW. Phylogenetic analyses of *Chaetopteridae* (*Annelida*). *Zoologica Scripta.* 2017; 46 (5): 596–610. Available from: <https://doi.org/10.1111/zsc.12238>.
- Ancil M. The epithelial luminescent system of *Chaetopterus variopedatus*. *Can J Zool.* 1979; 57 (6): 1290–310. DOI: 10.1139/Z79-166.
- Shimomura O, Johnson FH, Haneda Y. Partial purification and properties of the *Chaetopterus* luminescence system. *Bioluminescence in Progress.* Princeton University Press; 1966: 495521. Available from: <https://doi.org/10.1515/9781400875689-031>.
- Branchini BR, Behney CE, Southworth TL, Rawat R, Deheyn DD. Chemical analysis of the luminous slime secreted by the marine worm *Chaetopterus* (*Annelida*, *Polychaeta*). *Photochem Photobiol.* 2014; 90 (1): 247–51. DOI: 10.1111/php.12169.
- Shimomura O, Johnson FH. *Chaetopterus* photoprotein: crystallization and cofactor requirements for bioluminescence. *Science.* 1968; 159 (3820): 1239–40. DOI: 10.1126/science.159.3820.1239.
- Purtov KV, Petushkov VN, Rodionova NS, et al. Luciferin-luciferase system of marine polychaete *Chaetopterus variopedatus*. *Dokl Biochem Biophys.* 2019; 486 (1): 209–12. DOI: 10.1134/S1607672919030104.
- Shcheglov AS, Tsarkova AS. The potential of using the bioluminescent system of *Chaetopterus variopedatus* to study ferroptosis in living organisms. *Bulletin of RSMU.* 2021; (3): 79–81. DOI: 10.24075/vrgmu.2021.024.
- Dixon SJ, Lemberg KM, Lamprecht MR, Skouta R, Zaitsev EM, Gleason CE, et al. Ferroptosis: an iron-dependent form of nonapoptotic cell death. *Cell.* 2012; 149: 1060–72. DOI: 10.1016/j.cell.2012.03.042.
- Li J, Cao F, Yin H-L, Huang Z-J, Lin Z-T, Mao N, et al. Ferroptosis: past, present and future. *Cell Death Dis.* 2020; 11 (2): 88. DOI: 10.1038/s41419-020-2298-2.
- Yan H-F, Zou T, Tuo Q-Z, Xu S, Li H, Belaidi AA, et al. Ferroptosis: mechanisms and links with diseases. *Signal Transduct Target Ther.* 2021; 6 (1): 49. DOI: 10.1038/s41392-020-00428-9.
- Viviani VR, et al. Active-site properties of *Phrixotrix* railroad worm green and red bioluminescence-eliciting luciferases. *J Biochem.* 2006; 140 (4): 467–74. DOI: 10.1093/jb/mvj190.
- Arnoldi FG, da Silva Neto AJ, Viviani VR. Molecular insights on the evolution of the lateral and head lantern luciferases and bioluminescence colors in mastinocerini railroad-worms (*Coleoptera*: *Phengodidae*). *Photochem Photobiol Sci.* 2010; 9 (1): 87–92. DOI: 10.1039/B9PP00078J.
- Nakajim, Y, Ohmiya Y. Bioluminescence assays: multicolor luciferase assay, secreted luciferase assay and imaging luciferase assay. *Expert Opin Drug Discov.* 2010; 5 (9): 835–49. DOI: 10.1517/17460441.2010.506213.
- Syed AJ, Anderson JC. Applications of bioluminescence in biotechnology and beyond. *Chem Soc Rev.* 2021; 50: 5668–705. DOI: 10.1039/D0CS01492C.
- Slavine NV, McColl RW. Semi-automated Image processing for preclinical bioluminescent imaging. *J Appl Bioinform Comput Biol.* 2015; 4 (1): pii: 114. DOI: 10.4172/2329-9533.1000114.

Литература

- Osborn KJ, Rouse GW, Goffredi SK, Robison BH. Description and relationships of *Chaetopterus pugaporcinus*, an unusual pelagic polychaete (*Annelida*, *Chaetopteridae*). *Biol Bull.* 2007; 212 (1): 40–54. DOI: 10.2307/25066579.
- Petersen ME. *Chaetopterus variopedatus* (Renier) (*Annelida*: *Polychaeta*: *Chaetopteridae*): a species complex. What species are being used at MBL? *Biol Bull.* 1984; 167: 513.
- Petersen ME. Contribution to a revision of *Chaetopterus* Cuvier (*Polychaeta*: *Chaetopteridae*): redescription of *C. appendiculatus* Grube and *C. cautus* Marenzeller, with comments on some other species. *Bull Mar Sci.* 1997; 60: 619.
- Bhaud M. The spreading potential of polychaete larvae does not predict adult distributions; consequences for conditions of recruitment. *Hydrobiologia.* 1998; 375: 35. DOI: 10.1023/A:1017073409259.

- 10.1023/A:1017073409259.
5. Mirza JD, Migotto AE, Yampolsky IV, de Moraes GV, Tsarkova AS, Oliveira AG. *Chaetopterus variopedatus* bioluminescence: a review of light emission within a species complex. *Photochem Photobiol.* 2020; 96: 768–78. DOI: 10.1111/php.13221.
 6. Moore JM, Nishi E, Rouse GW. Phylogenetic analyses of *Chaetopteridae* (Annelida). *Zoologica Scripta.* 2017; 46 (5); 596–610. Available from: <https://doi.org/10.1111/zsc.12238>.
 7. Anctil M. The epithelial luminescent system of *Chaetopterus variopedatus*. *Can J Zool.* 1979; 57 (6): 1290–310. DOI: 10.1139/Z79-166.
 8. Shimomura O, Johnson FH, Haneda Y. Partial purification and properties of the *Chaetopterus* luminescence system. *Bioluminescence in Progress.* Princeton University Press; 1966: 495521. Available from: <https://doi.org/10.1515/9781400875689-031>.
 9. Branchini BR, Behney CE, Southworth TL, Rawat R, Deheyn DD. Chemical analysis of the luminous slime secreted by the marine worm *Chaetopterus* (Annelida, Polychaeta). *Photochem Photobiol.* 2014; 90 (1): 247–51. DOI: 10.1111/php.12169.
 10. Shimomura O, Johnson FH. *Chaetopterus* photoprotein: crystallization and cofactor requirements for bioluminescence. *Science.* 1968; 159 (3820): 1239–40. DOI: 10.1126/science.159.3820.1239.
 11. Purtov KV, Petushkov VN, Rodionova NS, et al. Luciferin-luciferase system of marine polychaete *Chaetopterus variopedatus*. *Dokl Biochem Biophys.* 2019; 486 (1): 209–12. DOI: 10.1134/S1607672919030104.
 12. Щеглов А. С., Царькова А. С. Перспективы использования биолюминесцентной системы *Chaetopterus variopedatus* для мониторинга ферроптоза в живых организмах. *Вестник РГМУ.* 2021; (3): 79–81. DOI: 10.24075/vrgmu.2021.024.
 13. Dixon SJ, Lemberg KM, Lamprecht MR, Skouta R, Zaitsev EM, Gleason CE, et al. Ferroptosis: an iron-dependent form of nonapoptotic cell death. *Cell.* 2012; 149: 1060–72. DOI: 10.1016/j.cell.2012.03.042.
 14. Li J, Cao F, Yin H-L, Huang Z-J, Lin Z-T, Mao N, et al. Ferroptosis: past, present and future. *Cell Death Dis.* 2020; 11 (2): 88. DOI: 10.1038/s41419-020-2298-2.
 15. Yan H-F, Zou T, Tuo Q-Z, Xu S, Li H, Belaidi AA, et al. Ferroptosis: mechanisms and links with diseases. *Signal Transduct Target Ther.* 2021; 6 (1): 49. DOI: 10.1038/s41392-020-00428-9.
 16. Viviani VR, et al. Active-site properties of *Phrixotrix* railroad worm green and red bioluminescence-eliciting luciferases. *J Biochem.* 2006; 140 (4): 467–74. DOI: 10.1093/jb/mvj190.
 17. Arnoldi FG, da Silva Neto AJ, Viviani VR. Molecular insights on the evolution of the lateral and head lantern luciferases and bioluminescence colors in mastinocerini railroad-worms (*Coleoptera: Phengodidae*). *Photochem Photobiol Sci.* 2010; 9 (1): 87–92. DOI: 10.1039/B9PP00078J.
 18. Nakajim, Y, Ohmiya Y. Bioluminescence assays: multicolor luciferase assay, secreted luciferase assay and imaging luciferase assay. *Expert Opin Drug Discov.* 2010; 5 (9): 835–49. DOI: 10.1517/17460441.2010.506213.
 19. Syed AJ, Anderson JC. Applications of bioluminescence in biotechnology and beyond. *Chem Soc Rev.* 2021; 50: 5668–705. DOI: 10.1039/D0CS01492C.
 20. Slavine NV, McColl RW. Semi-automated Image processing for preclinical bioluminescent imaging. *J Appl Bioinform Comput Biol.* 2015; 4 (1): pii: 114. DOI: 10.4172/2329-9533.1000114.

PREDICTIVE POTENTIAL OF MACROPHAGE POPULATION PHENOTYPING IN MALIGNIZATION OF *H. PYLORI*-ASSOCIATED CHRONIC GASTRITIS

Golubinskaya EP¹, Sataieva TP^{1,2}, Fomochkina II¹, Kubyshkin AV¹, Makalish TP¹, Shkolyar NA², Galyshevskaya AA¹, Varghese DV¹

¹ V.I. Vernadsky Crimea Federal University, Simferopol, Russia

² Sechenov University, Moscow, Russia

Tumor-associated macrophages are able to regulate the tumor cell proliferation and to affect the tumor cell dissemination. The study was aimed to assess the predictive potential of the macrophage population immunohistochemical phenotyping in early malignization of *H. pylori*-associated chronic gastritis. Gastric biopsy samples of male and female patients aged 48 ± 7.2 infected with *Helicobacter pylori* were used as the research material. The patients were divided into three groups: non-atrophic chronic gastritis (NACG, *n* = 10), atrophic chronic gastritis (ACG, *n* = 10), G1/G2 gastric adenocarcinoma (GAC, *n* = 10). The macrophage population was visualized using the CD68 pan-macrophage marker and the type 2 monocyte/macrophage marker CD163. Intensity of neoangiogenesis was defined using the CD31 endothelial marker by assessing the total cross sectional area of blood vessels. It was found that chronic gastritis was accompanied by the dynamic increase in the size of the general macrophage population with the progression of atrophic and metaplastic processes. According to immunohistochemical study of biopsies obtained from patients with NCG, the CD163 : CD68 ratio was 0.67 ± 0.02, and the total cross sectional area of blood vessels was 3590.92 ± 356.27 μm². Atrophic gastritis and adenocarcinoma were characterized by vector redistribution of monocytes/macrophages into the 2nd functional phenotype. The CD163 : CD68 expression index in the group with ACG was 0.81 ± 0.04, and in the group with GAC it was 0.88 ± 0.03. Microvascular area was significantly increased in the groups with ACG and GAC, which reflected tumor neoangiogenesis intensification under the influence of M2 monocytes/macrophages. The increased expression of CD163 can serve as a predictor of chronic gastritis malignization together with evaluation of the glandular epithelium atrophy and metaplasia degree.

Keywords: gastric cancer, gastritis, adenocarcinoma, tumor-associated macrophages, *Helicobacter pylori*

Funding: the study was carried out within the framework of the Government Assignment № FZEG-2020-0060 of the Ministry of Science and Higher Education of the Russian Federation in the field of scientific research "Algorithms for molecular genetic diagnosis of malignant neoplasms and approaches to their targeted therapy using cellular and genetic technologies".

Author contribution: Golubinskaya EP — clinical data analysis, immunohistochemistry, manuscript editing; Sataieva TP, Fomochkina II — systematic analysis, manuscript writing; Kubyshkin AV — statistical analysis, manuscript editing; Makalish TP — sample preparation for morphological assessment, immunohistochemistry; Shkolyar NA — biopsy sample collection and preparation; Galyshevskaya AA, Varghese DV — morphometric data processing.

Compliance with ethical standards: the study was approved by the Ethics Committee of the Medical Academy named after S. I. Georgievsky (protocol № 15 dated December 5, 2020); the study was conducted in accordance with the Declaration of Helsinki 1964 (revised in 1975 and 1983), Good Clinical Practice (GCP) standards and the Federal Law № 323-FZ "On the Basics of Protecting the Health of Citizens in the Russian Federation" dated November 21, 2011. The informed consent was submitted by all patients.

✉ **Correspondence should be addressed:** Tatiana P. Sataieva
Bulvar Lenina, 5/7, Simferopol, 295006; tanzcool@mail.ru

Received: 19.08.2021 **Accepted:** 03.09.2021 **Published online:** 13.09.2021

DOI: 10.24075/brsmu.2021.044

ПРЕДИКТИВНЫЙ ПОТЕНЦИАЛ ФЕНОТИПИРОВАНИЯ МАКРОФАГАЛЬНОЙ ПОПУЛЯЦИИ В МАЛИГНИЗАЦИИ *H. PYLORI*-АССОЦИИРОВАННОГО ХРОНИЧЕСКОГО ГАСТРИТА

Е. П. Голубинская¹, Т. П. Сатаева^{1,2}, И. И. Фомочкина¹, А. В. Кубышкин¹, Т. П. Макалиш¹, Н. А. Школяр², А. А. Галышевская¹, Д. В. Варгхесе¹

¹ Крымский федеральный университет имени В. И. Вернадского, Симферополь, Россия

² Первый Московский государственный медицинский университет имени И. М. Сеченова (Сеченовский Университет), Москва, Россия

Опухоль-ассоциированные макрофаги способны регулировать пролиферацию опухолевых клеток и влиять на процессы их диссеминации. Целью исследования было оценить предиктивный потенциал иммуногистохимического фенотипирования макрофагальной популяции при ранней малигнизации *H. pylori*-ассоциированного хронического гастрита. Материалом для исследования послужили гастробиоптаты инфицированных *Helicobacter pylori* пациентов обоего пола в возрасте 48 ± 7,2 лет, разделенных на три группы: хронический неатрофический гастрит (ХНГ, *n* = 10), хронический атрофический гастрит (ХАГ, *n* = 10), аденокарцинома желудка G1-G2 (АКЦ, *n* = 10). Макрофагальную популяцию визуализировали с помощью панмакрофагального маркера CD68 и маркера моноцитов/макрофагов 2-го типа CD163. Интенсивность неоангиогенеза определяли с использованием маркера эндотелия сосудов CD31 путем оценки суммарной площади поперечного сечения сосудов. Установлено, что хронический гастрит сопровождается динамическим увеличением общей популяции макрофагов по мере нарастания атрофических и неопластических процессов. По данным иммуногистохимического исследования биоптатов, у группы пациентов с ХНГ соотношение CD163 : CD68 составило 0,67 ± 0,02, а суммарная площадь поперечного сечения сосудов была равна 3590,92 ± 356,27 мкм². Атрофический гастрит и аденокарцинома характеризуются векторным перераспределением моноцитов/макрофагов во второй функциональный фенотип. Индекс экспрессии CD163 : CD68 в группе с ХАГ составляет 0,81 ± 0,04, а в группе с АКЦ — 0,88 ± 0,03. Площадь микроциркуляторного русла в группах с ХАГ и АКЦ значительно возрастает, что отражает интенсификацию процессов неоангиогенеза в опухоли под влиянием моноцитов/макрофагов M2. Усиленная экспрессия CD163 может служить предиктором малигнизации хронического гастрита в комплексе с оценкой степени атрофии и метаплазии эпителия железистого компонента.

Ключевые слова: рак желудка, гастрит, аденокарцинома, опухоль-ассоциированные макрофаги, *Helicobacter pylori*

Финансирование: исследование выполнено в рамках государственного задания № ФЗЭГ-2020-0060 Министерства науки и высшего образования Российской Федерации в области научных исследований по теме «Алгоритмы молекулярно-генетической диагностики злокачественных новообразований и подходы к их таргетной терапии с использованием клеточных и генетических технологий».

Вклад авторов: Е. П. Голубинская — анализ клинических данных, проведение иммуногистохимического исследования, редактирование рукописи; Т. П. Сатаева, И. И. Фомочкина — систематический анализ, написание рукописи; А. В. Кубышкин — статистический анализ полученных данных, редактирование рукописи; Т. П. Макалиш — подготовка материала для морфологического исследования, проведение иммуногистохимического исследования; Н. А. Школяр — сбор и подготовка биоптатов; А. А. Галышевская, Д. В. Варгхесе — обработка морфометрических данных.

Соблюдение этических стандартов: исследование одобрено этическим комитетом Медицинской академии имени С. И. Георгиевского (протокол №15 от 5 декабря 2020 г.), проведено в соответствии с Хельсинкской Декларацией 1964 г. (исправленной в 1975 и 1983 гг.), Стандартами надлежащей клинической практики (GCP) и ФЗ № 323-ФЗ от 21 ноября 2011 г. «Об основах охраны здоровья граждан в Российской Федерации». Все пациенты подписали добровольное информированное согласие на участие в исследовании.

✉ **Для корреспонденции:** Татьяна Павловна Сатаева
Бульвар Ленина д. 5/7, г. Симферополь, 295006; tanzcool@mail.ru

Статья получена: 19.08.2021 **Статья принята к печати:** 03.09.2021 **Опубликована онлайн:** 13.09.2021

DOI: 10.24075/vrgmu.2021.044

Currently, gastric cancer is ranked fifth for incidence and third for morbidity not just in the Russian Federation, but throughout the world. A significant increase in the number of young patients with this disorder has given rise to numerous studies aimed at identifying early predictors for carcinogenesis and critical risk factors for malignization [1, 2].

Among the gastric cancer pathogenesis factors, the *Helicobacter pylori* (HP) infection is the leading cause of the disorder. It's been proven that 80% of patients with gastric cancer have had a history of HP infection [3, 4]. There is no doubt that HP is one of the crucial factors for a cascade of carcinogenesis, which initiates the development of acute gastritis, and progression from acute to chronic gastritis with subsequent atrophy, metaplasia, and dysplasia, ultimately leading to the development of adenocarcinoma [5].

In recent years, a growing body of research has been focused on the changes in the tumor microenvironment. Studying the tumor-associated macrophages (TAMs) can be very promising in the aspect of cancer research [6]. TAMs are associated with the occurrence of tumors playing a vital part in metastasis and immune regulation of neoplasms. Today, the macrophage functional heterogeneity has been established. There are type 1 macrophages, which initiate the pro-inflammatory response, and type 2 macrophages involved in remodeling, which can promote tumor cell migration and invasion due to activation of neoangiogenesis [7–9].

It is known that HP can actively recruit macrophages, monocytes and dendritic cells to the gastric mucosa. HP forces these cells to secrete pro-inflammatory cytokines and chemokines, causing inflammation and gastric mucosal injury [10, 11]. Several studies report the influence of HP infection on the macrophage polarization due to promotion of free radicals induced oxidative processes. According to the results of a number of research studies, bacterial factors contribute to the increased production of reactive oxygen species and hypoxia-inducible factor 1 α [8, 9]. Furthermore, HP is able to synthesize large amounts of inducible nitric oxide synthase (iNOS), contributing to macrophage polarization into M2 phenotype, which, in contrast to M1, exhibit a rather low phagocytic activity, thus facilitating the further pathogen persistence [12].

Currently, endoscopy with targeted biopsies is the main method for diagnosing atrophic gastritis and its complications. However, focal lesions are quite common for HP-associated atrophic gastritis, that is why it is essential to ensure obtaining adequate biopsy samples, which is often difficult to accomplish in the outpatient setting [13]. Nevertheless, early detection of atrophy and subsequent precancerous changes (intestinal metaplasia and dysplasia) is essential for gastric cancer prevention. Immunohistochemical verification of morphological changes in gastric mucosal immune cells could be part of the solution to this problem.

In view of the above, the study was aimed to assess the predictive potential of the macrophage population immunohistochemical phenotyping in the early malignization of the HP-associated chronic gastritis.

METHODS

Morphological studies were performed in the Center for the Shared Use of Scientific Equipment "Molecular Biology" of the S.I. Georgievsky Medical Academy, V.I. Vernadsky Crimean Federal University, with support from the Crimean Federal University development program. Gastric biopsy samples of male and female patients aged 48 ± 7.2 infected with HP were used as the research material. The patients were

divided into three groups: non-atrophic chronic gastritis ($n = 10$), atrophic chronic gastritis ($n = 10$), G1/G2 Lauren intestinal type gastric tubular adenocarcinoma ($n = 10$). Inclusion criteria: positive HP test. Exclusion criteria: negative HP test or no information about this test in medical history. According to their medical history, all patients were HP-positive. HP was verified based on the serum anti-HP immunoglobulin G (IgG) quantification by the enzyme-linked immunosorbent assay and the rapid urease test.

The control group included fragments of visually intact gastric mucosa obtained from patients, who died from causes other than gastrointestinal disorders, with no histological signs of gastritis and not infected with HP.

To perform morphological assessment of the biopsy and necropsy samples, the fragments of gastric mucosa were fixed in the 10% neutral buffered formalin. Tissue processing and histological slide preparation were performed by standard methods with subsequent hematoxylin and eosin staining [14].

Immunohistochemical staining (IHC) was performed on the slices 3–4 μm thick by peroxidase-antiperoxidase (PAP) complex technique in accordance with the Thermo Scientific protocols (USA) with the use of Leica Biosystems visualization system (Novocastra; USA) and DAB Chromogen (Abcam; UK). Subsequently, cell nuclei were stained with hematoxylin. Macrophage population was visualized using the CD68 pan-macrophage/monocyte marker (clone PG-M1, dilution 1 : 50, DAKO; Denmark) and the CD163 marker of typical 2 α reparative phenotype macrophages CD163 (clone EPR-19518, dilution 1 : 500, Abcam; UK). According to meta-analysis, studying the CD68 and CD163 markers is more informative than studying the other M2 marker, CD206 [15]. Meanwhile, CD163 can be expressed as an additional surface marker of blood monocytes, which are also capable of phenotypic polarization. However, monocytes demonstrate lower expression of this marker compared to macrophages.

Intensity of neoangiogenesis was defined using the CD31 endothelial marker (clone 1A10, Leica Bond; USA) by assessing the total cross-sectional area of blood vessels.

The samples obtained were analyzed with the CX41 light microscope (Olympus; Japan). Morphometric assessment was performed using the Image J software (NIH; USA) on the standardized area of the histology section image. Cells with positive cytoplasmic staining were counted in 10 fields of view using the 20x/0.50 UPlanFL N objective (Olympus; Japan) with subsequent counting the average number of cells in the biopsy sample.

Statistical analysis was carried out using the STATISTICA 10.0 software for Windows (StatSoft Inc.; USA). Testing for normal distribution was performed by the Kolmogorov–Smirnov test. The following statistical parameters were defined: mean (M), error of the mean (m). The inter-group comparisons of morphological parameters were carried out by one-way analysis of variance (One-Way ANOVA) with the use of the Dunnett test (Q) for comparison of the small samples with the control group. The intra-group differences were considered significant when $p \leq 0.05$.

RESULTS

According to serological study, the antibody titer of 1 : 5 was observed in 33% of patients with NACG; in 67% of patients the antibody titer exceeded 1 : 10. In the group with ACG, the antibody titer exceeding 1 : 5 was observed only in 10% of patients; 49% of the examined patients had the antibody titer exceeding 1 : 10, and another 41% of patients demonstrated

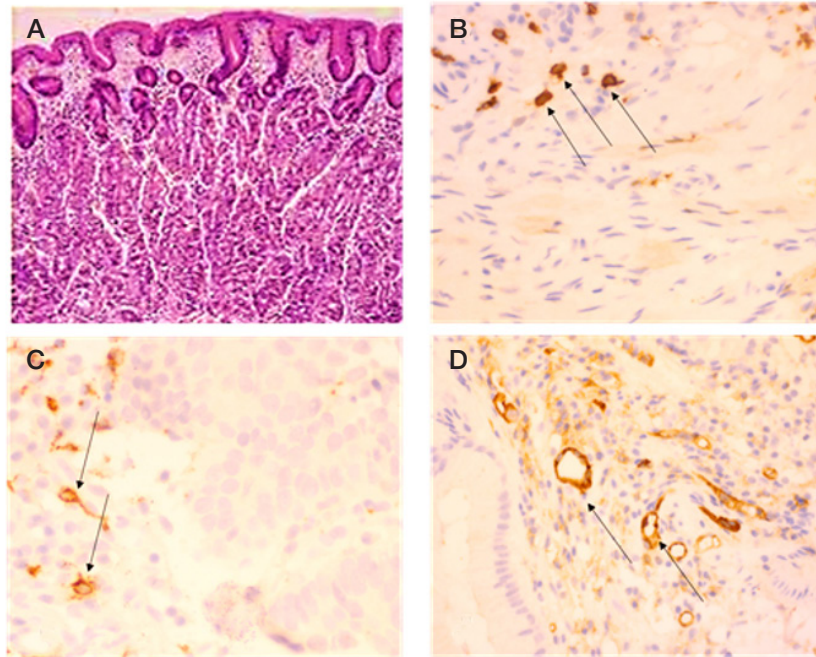


Fig. 1. Gastric mucosal pattern in controls. **A.** Regularly shaped columnar epithelium forming the gastric pits, hematoxylin and eosin stain ($\times 10$). **B.** CD163-positive cytoplasmic stain in solitary type 2 monocytes/macrophages, IHC ($\times 40$). **C.** CD68-positive cytoplasmic stain in general macrophage population, IHC ($\times 40$). **D.** CD31-positive cytoplasmic stain in small vessel endothelium, IHC ($\times 40$)

the high antibody titer (in the range of 1 : 20–1 : 80). In 77% of patients with verified tubular adenocarcinoma (GAC), the antibody titer was 1 : 20 or higher, and 23% of patients had the antibody titer of 1 : 5–1 : 10.

According to morphological assessment, gastric mucosa of the controls had a typical pattern, represented by the lining of regularly shaped columnar epithelium, forming the gastric pits with no signs of gastritis (Fig. 1A). In the submucosal layer, there were solitary resident macrophages of both 1st and 2nd phenotype (Fig. 1B, C). The moderately prominent vascular pattern was clearly visible. Blood

vessels were represented mainly by capillaries and venules (Fig. 1D).

When performing the overview staining, it was found that gastric biopsy specimens of patients with NCG were characterized by lymphoplasmacytic infiltration of various degree (mild to moderate), as well as by formation of solitary hyperplastic lymphoid aggregates within the stroma, increased mucoidization of the columnar epithelium of the integument and pits, and foveolar hyperplasia. In some zones of biopsy specimens there were foci of fundic gland hyperplasia (Fig. 2A).

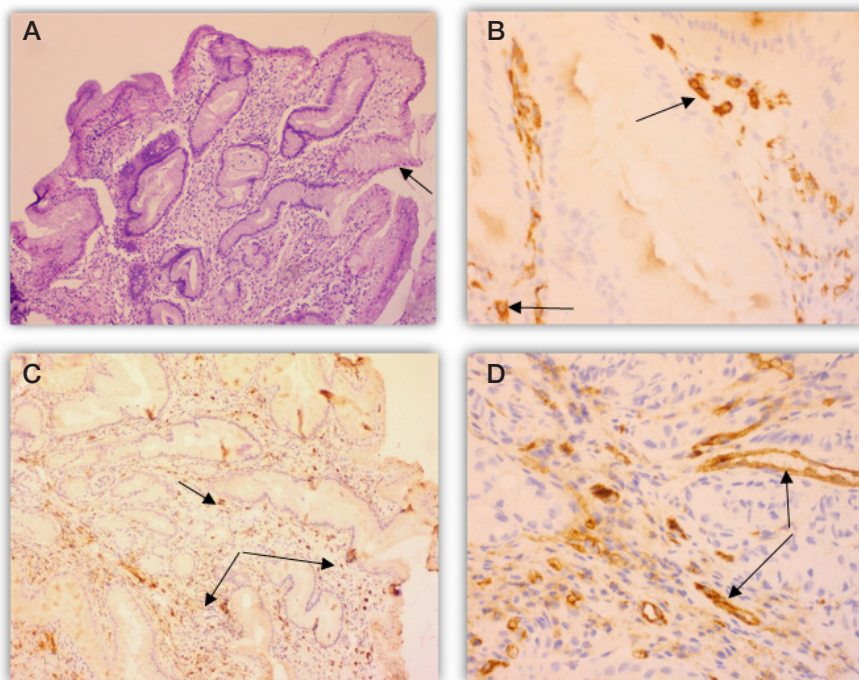


Fig. 2. Non-atrophic chronic gastritis. **A.** Moderate lymphoplasmacytic infiltration with admixed solitary leukocytes in the lamina propria of the antral mucosa, increased mucoidization of the columnar epithelium of the integument and pits, hematoxylin and eosin stain ($\times 10$). **B.** CD163-positive cytoplasmic stain in type 2 monocytes/macrophages, IHC ($\times 40$). **C.** CD68-positive cytoplasmic stain in general macrophage population, IHC ($\times 10$). **D.** CD31-positive cytoplasmic stain in blood vessel endothelium, IHC ($\times 40$)

Table. Immunohistochemical study of macrophages and microvascular bed in patients with chronic gastritis and adenocarcinoma

IHC marker	NACG (n = 10)	ACG (n = 10)	GAC (n = 10)	Control group (n = 10)
CD 68 Abs., (M ± m)	39.9 ± 3.12* Q = 5.90 (p = 0.00243)	62.7 ± 3.39* Q = 21.59 (p = 0.00000)	132.4 ± 6.71* Q = 68.99 (p = 0.00000)	31.1 ± 4.71
CD 163 Abs., (M ± m)	27.5 ± 2.83* Q = 8.69 (p = 0.00003)	50.5 ± 3.54* Q = 24.17 (p = 0.00000)	116.7 ± 10.14* Q = 68.47 (p = 0.00000)	14.7 ± 3.15
CD 31 µm ² , (M ± m)	3590.92 ± 356.27 Q = 2.07 (p = 0.48170)	8647.02 ± 359.29* Q = 27.95 (p = 0.00000)	19065.12 ± 1042.94* Q = 82.37 (p = 0.00000)	3203.68 ± 347.21
CD163 : CD68	0.67 ± 0.02* Q = 13.97 (p = 0.00000)	0.81 ± 0.04* Q = 23.75 (p = 0.00000)	0.88 ± 0.03* Q = 28.64 (p = 0.00000)	0.47 ± 0.07

Note: * — significant differences with the control group, $p \leq 0.05$.

According to IHC study of biopsies obtained from patients with NACG, CD68⁺ cells were distributed homogeneously in the lamina propria of the gastric mucosa; type 2 monocytes/macrophages made up about a half of these cells. The CD163 : CD68 ratio of 0.67 ± 0.02 (Fig. 2B, C) was significantly larger compared to values obtained for the control group ($p < 0.05$). In our view, the monocyte/macrophage population ratio index shift compared to the control group is indicative of the proinflammatory response cascade initiation.

The total cross-sectional area of blood vessels in patients with NACG was $3590.92 \pm 356.27 \mu\text{m}^2$, which was indicative of insignificant intensification of angiogenesis compared with the control group specimens ($p > 0.05$). The cross-sectional area of blood vessels in patients with this type of gastritis was minimal in comparison with the groups of patients with ACG and GAC (Fig. 2D; Table).

Biopsies of patients with ACG also demonstrated polymorphic histological changes. Glandular atrophy resulted from two fundamentally different processes: fibrous stroma transformation or intestinal metaplasia (small/large intestine or the combination of these metaplasia types). Atrophic gastritis

with the lamina propria fibrosis was characterized by the marked lymphoplasmacytic infiltration, often with lymphoid follicles consisting of expanded germinal centers (Fig. 3A).

The monocyte/macrophage population was also distributed homogeneously throughout the whole biopsy specimens, both in foveolar zones and in the vicinity of the lymphoid accumulation. The majority of cells had the type 2 monocyte/macrophage immunophenotype. The CD163 : CD68 ratio was 0.81 ± 0.04 (Fig. 3B, C). Furthermore, microvascular area in biopsies of this subgroup was significantly increased compared to values obtained both for NACG group and control group (Fig. 3D).

Morphological and immunohistochemical changes in biopsies of patients with verified tubular adenocarcinoma were particularly illustrative in terms of the macrophage population functional re-profiling and the intensity of neoangiogenesis. Among tubular structures with signs of cellular and nuclear atypia, and areas of solid structure, the desmoplastic stroma with moderate and marked dense inflammatory cell infiltrate of lymphoid cells, histiocytes, neutrophils were observed (Fig. 4A).

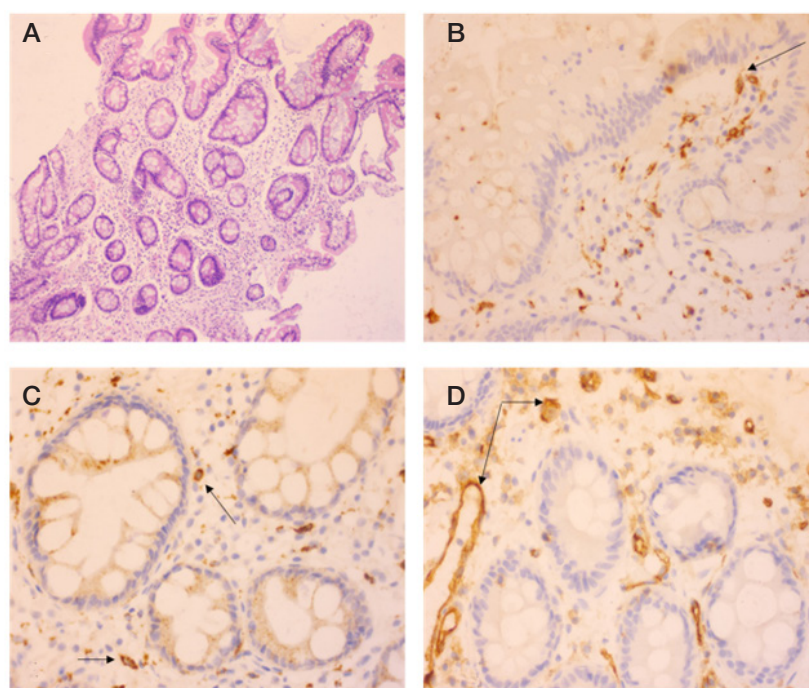


Fig. 3. Moderate subacute metaplastic atrophic chronic gastritis. **A.** Large intestinal metaplasia, hematoxylin and eosin stain ($\times 10$). **B.** CD163-positive cytoplasmic stain in type 2 monocytes/macrophages within lamina propria mucosae, IHC ($\times 40$). **C.** CD68-positive cytoplasmic stain in macrophages within lamina propria mucosae, IHC ($\times 40$). **D.** CD31-positive cytoplasmic stain in blood vessel endothelium, IHC ($\times 40$)

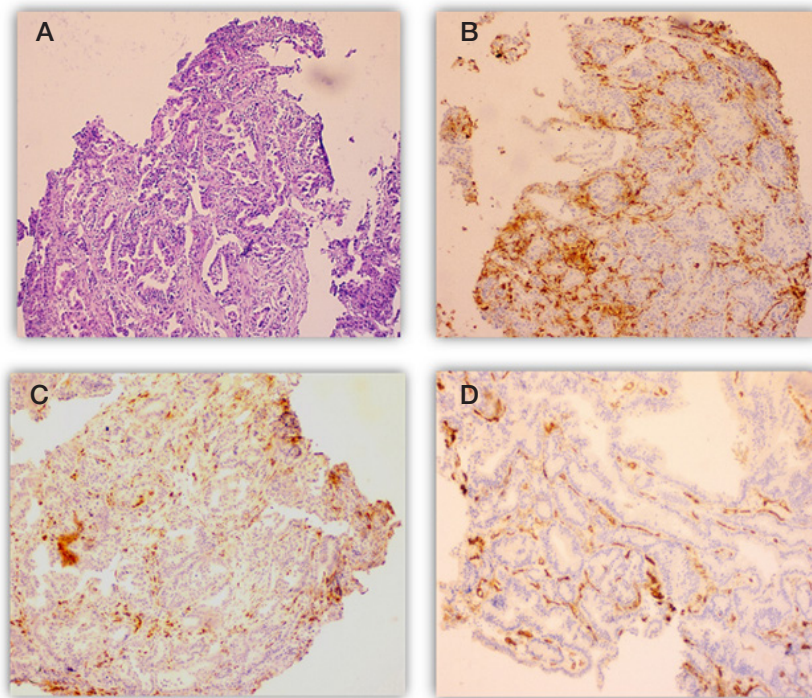


Fig. 4. Adenocarcinomas. **A.** Tubular adenocarcinoma with ulceration, hematoxylin and eosin stain ($\times 10$). **B.** CD163-positive cytoplasmic stain, IHC ($\times 100$). **C.** CD68-positive cytoplasmic stain, IHC ($\times 100$). **D.** CD31-positive cytoplasmic stain, IHC ($\times 200$)

The number of cells in monocyte/macrophage population increased twice compared to values obtained for ACG and four times compared to value obtained for NACG. The CD163 : CD68 expression ratio was 0.88 ± 0.03 (Fig. 4B, C). The maximum microvascular area, significantly exceeding the control values, was also observed (Fig. 4D), which could be indicative of the intensified neoangiogenesis aimed at forming the comfortable microenvironment, and contributed to metastatic tumor cell dissemination [16].

DISCUSSION

The known molecular biomarkers of monocytes/macrophages demonstrate the considerable diagnostic capacity and could serve as malignancy risk predictors due to specific identification of particular immune cell subpopulations, allowing one to predict the course of a number of disorders. There is evidence that macrophages can play a dual role in inflammation depending on the signals from their microenvironment due to different phenotypes [17].

Chronic HP-associated gastritis is accompanied by the dynamic increase in the size of the general monocyte/macrophage population, since it is known that HP actively triggers the cytokine cascade playing a vital part in realization of chronic inflammatory and destructive processes in the gastric mucosa [4]. During the acute inflammatory response, macrophages are usually polarized into M1 phenotype by interferon- γ and microbial products, such as lipopolysaccharide, and exhibit strong antimicrobial activity due to production of bactericidal components (nitric oxide and oxygen radicals) [9]. However, this bacterium can inhibit the effects of active substances produced by macrophages due to neutralization of these substances with catalase and superoxide dismutase, which provides survival of the bacteria. However, the reactive oxygen species, abundantly secreted by macrophages, cause the death of the gastric mucosal cells, which contributes to the risk of atrophy [18].

According to our study, atrophic gastritis is characterized by vector redistribution of monocytes/macrophages into the

2nd functional type. M2 macrophages are induced by type 2 T-helper cells or anti-inflammatory cytokines and growth factors, including IL4, IL10 [6]. Apparently, monocyte/macrophage polarization shift towards M2 with the progression of inflammation should ensure tissue regeneration and enhance humoral response. However, the long-term increased production of the HP pathogenicity factors may lower the ability of macrophages to eliminate bacterial antigens, which results in the long-term persistence of the pathogen and chronic inflammation [19, 20]. At the same time, chronic inflammation with persistent M2 monocyte/macrophage polarization is associated with increased risk of developing gastric cancer [1, 13, 21].

Thus, the dynamic increase in the pan-macrophage population size and progressive re-profiling of macrophages into the 2nd functional phenotype with the transition from non-atrophic gastritis to atrophic gastritis, and peak values in biopsies with gastric adenocarcinoma, were observed during our study. In our opinion, these changes are related to remodeling functional activity of the alternatively activated M2 monocytes/macrophages due to increased expression of pro-angiogenic growth factors, which on the one hand contributes to fibrotic changes in the gastric stroma in the conditions of chronic progressive inflammation and tissue hypoxia, and on the other hand creates a comfortable microenvironment for the dysplastic and neoplastic changes in the glandular epithelium [11, 22]. Furthermore, it is well-known that certain M2 macrophage populations exhibit the vivid tumor-stimulating activity, since these populations are involved in the local immunosuppression of immunocompetent cells, which results in the tumor cell escape from the immune surveillance [23].

The diversity of monocyte/macrophage phenotypes requires further study and standardization of their predictive potential. For this purpose, the studies of the larger number of patient samples should be carried out, as well as the assessment of the other macrophage markers, typical for monocytes and macrophages. In particular, monocytes are able to express the CD163 and CD204 surface markers in

addition to the CD1 and CD16 surface markers, which could be defined by double staining immunohistochemistry [24]. Furthermore, regardless of the generally accepted division of macrophages into classical and alternative macrophages, the other macrophage subtypes have been described, including the pro-fibrotic M2-like macrophages, which produce growth factors, and ischemia-induced fibrolytic M2-like macrophages, which secrete proteases [12].

In general, identification of the TAM functional programming mechanisms would make it possible to identify therapeutic targets, and to develop new approaches to treatment of cancer patients based on the combination of chemotherapy and immunomodulatory agents in order to induce the immune response to the tumor [13]. Synergistic effects of these

modalities may significantly increase the efficiency of antitumor therapy.

CONCLUSIONS

Chronic *H. pylori*-associated gastritis is accompanied by the dynamic increase in the size of the general macrophage population with the progression of atrophic and metaplastic processes. Atrophic gastritis and adenocarcinoma are characterized by vector redistribution of macrophages into the 2nd functional type. Increased expression of CD163 marker of monocytes/macrophages can serve as a predictor of chronic gastritis malignancy together with histological study of the glandular epithelium atrophy and metaplasia degree.

References

- Jemal A, Bray F, Center MM, Ferlay J, Ward E, Forman D. Global cancer statistics. *CA Cancer J Clin.* 2011; 61 (2): 69–90.
- Massarrat S, Stolte M. Development of gastric cancer and its prevention. *Arch Iran Med.* 2014; 17 (7): 514–20.
- Cover TL. *Helicobacter pylori* diversity and gastric cancer risk. *MBio.* 2016; 7: e01869–915.
- Mentis AA, Dardiotis E. *Helicobacter pylori* eradication for metachronous gastric cancer: an unsuitable methodology impeding broader clinical usage. *Front Oncol.* 2019 Feb 20; 9: 90. DOI: 10.3389/fonc.2019.00090.
- Mentis AA, Boziki M, Grigoriadis N, Papavassiliou AG. *Helicobacter pylori* infection and gastric cancer biology: tempering a double-edged sword. *Cell Mol Life Sci.* 2019; 76: 2477–86.
- Biswas SK, Mantovani A. Macrophage plasticity and interaction with lymphocyte subsets: cancer as a paradigm. *Nat Immunol.* 2010; 11: 889.
- Kim J, Bae J-S. Tumor-associated macrophages and neutrophils in tumor microenvironment. *Mediators Inflamm.* 2016; 6058147.
- Niu Z, Shi Q, Zhang W, et al. Caspase-1 cleaves PPAR (for potentiating the pro-tumor action of TAMs). *Nat Commun.* 2017; 8: 766.
- Lu Y, Rong J, Lai Y, Tao L, Yuan X, Shu X. The degree of *Helicobacter pylori* infection affects the state of macrophage polarization through crosstalk between ROS and HIF-1 α . *Oxid Med Cell Longev.* 2020; 2020: 5281795.
- Quiding-Järbrink M, Raghavan S, Sundquist M. Enhanced M1 macrophage polarization in human *Helicobacter pylori*-associated atrophic gastritis and in vaccinated mice. *PLoS One.* 2010; 5 (11): p.e15018. DOI: 10.1371/journal.pone.0015018.
- Li W, Zhang X, Wu F, et al. Gastric cancer-derived mesenchymal stromal cells trigger M2 macrophage polarization that promotes metastasis and Emt in gastric cancer. *Cell Death & Disease.* 2019; 10 (12): 918. DOI: 10.1038/s41419-019-2131-y.
- Atri C, Guerfali FZ, Laouini D. Role of human macrophage polarization in inflammation during infectious diseases. *Int J Mol Sci.* 2018; 19 (6): 1801. DOI: 10.3390/ijms19061801.
- Song JH, Kim SG, Jin EH, Lim JH, Yang SY. Risk factors for gastric tumorigenesis in underlying gastric mucosal atrophy. *Gut Liver.* 2017; 11: 612–19.
- Janin VL, Bondarenko OM, Sazonova NA. Metody issledovaniya v citologii i gistologii. Hanty-Mansijsk: BU "Hanty-Mansijskaja gosudarstvennaja medicinskaja akademija", 2015; 65 s. Russian.
- Ni C, Yang L, Xu Q, Yuan H, et al. CD68- and CD163-positive tumor infiltrating macrophages in non-metastatic breast cancer: a retrospective study and meta-analysis. *J Cancer.* 2019 Jul 23; 10 (19): 4463–72. DOI: 10.7150/jca.33914.
- Kloepper J, et al. Ang-2/VEGF bispecific antibody reprograms macrophages and resident microglia to anti-tumor phenotype and prolongs glioblastoma survival. *Proc Natl Acad Sci USA.* 2016; 113: 4476–81.
- Murray PJ. Macrophage Polarization. *Annu Rev Physiol.* 2017; 79 (1): 541–66. DOI: 10.1146/annurev-physiol-022516-034339.
- Wang YH, Lv ZF, Zhong Y, Liu DS, Chen SP, Xie Y. The internalization of *Helicobacter pylori* plays a role in the failure of *H. pylori* eradication. *Helicobacter.* 2017; 22 (1). DOI: 10.1111/hel.12324.
- Ihrig M, Whary MT, Dangler CA, Fox JG. Gastric helicobacter infection induces a Th2 phenotype but does not elevate serum cholesterol in mice lacking inducible nitric oxide synthase. *Infect Immun.* 2005; 73: 1664–70.
- Kaparakis M, Walduck AK, Price JD, Pedersen JS, van Rooijen N, et al. Macrophages are mediators of gastritis in acute *Helicobacter pylori* infection in C57BL/6 mice. *Infect Immun.* 2008; 76: 2235–9.
- Liu LP, Sheng XP, Shuai TK, Zhao YX, Li B, Li YM. *Helicobacter pylori* promotes invasion and metastasis of gastric cancer by enhancing heparanase expression. *World J Gastroenterol.* 2018; 24 (40): 4565–77. DOI: 10.3748/wjg.v24.i40.4565.
- Binnemars-Postma K, Bansal R, Storm G, et al. Targeting the Stat6 pathway in tumor-associated macrophages reduces tumor growth and metastatic niche formation in breast cancer. *FASEB J.* 2017; 32: 969–78.
- Cortese N, Donadon M, Rigamonti A, Marchesi F. Macrophages at the crossroads of anticancer strategies. *Front Biosci (Landmark Ed).* 2019 Jun 1; 24: 1271–83.
- Kzhyshkowska J, Gudima A, Moganti K, Gratchev A, Orekhov A. Perspectives for monocyte/macrophage-based diagnostics of chronic inflammation. *Transfus Med Hemother.* 2016; 43 (2): 66–77. DOI: 10.1159/000444943.
- DOI: 10.3389/fonc.2019.00090.
- Mentis AA, Boziki M, Grigoriadis N, Papavassiliou AG. *Helicobacter pylori* infection and gastric cancer biology: tempering a double-edged sword. *Cell Mol Life Sci.* 2019; 76: 2477–86.
- Biswas SK, Mantovani A. Macrophage plasticity and interaction with lymphocyte subsets: cancer as a paradigm. *Nat Immunol.* 2010; 11: 889.
- Kim J, Bae J-S. Tumor-associated macrophages and neutrophils in tumor microenvironment. *Mediators Inflamm.* 2016; 6058147.

Литература

- Jemal A, Bray F, Center MM, Ferlay J, Ward E, Forman D. Global cancer statistics. *CA Cancer J Clin.* 2011; 61 (2): 69–90.
- Massarrat S, Stolte M. Development of gastric cancer and its prevention. *Arch Iran Med.* 2014; 17 (7): 514–20.
- Cover TL. *Helicobacter pylori* diversity and gastric cancer risk. *MBio.* 2016; 7: e01869–915.
- Mentis AA, Dardiotis E. *Helicobacter pylori* eradication for metachronous gastric cancer: an unsuitable methodology impeding broader clinical usage. *Front Oncol.* 2019 Feb 20; 9: 90. DOI: 10.3389/fonc.2019.00090.
- Mentis AA, Boziki M, Grigoriadis N, Papavassiliou AG. *Helicobacter pylori* infection and gastric cancer biology: tempering a double-edged sword. *Cell Mol Life Sci.* 2019; 76: 2477–86.
- Biswas SK, Mantovani A. Macrophage plasticity and interaction with lymphocyte subsets: cancer as a paradigm. *Nat Immunol.* 2010; 11: 889.
- Kim J, Bae J-S. Tumor-associated macrophages and neutrophils in tumor microenvironment. *Mediators Inflamm.* 2016; 6058147.

8. Niu Z, Shi Q, Zhang W, et al. Caspase-1 cleaves PPAR (for potentiating the pro-tumor action of TAMs. *Nat Commun.* 2017; 8: 766.
9. Lu Y, Rong J, Lai Y, Tao L, Yuan X, Shu X. The degree of *Helicobacter pylori* infection affects the state of macrophage polarization through crosstalk between ROS and HIF-1 α . *Oxid Med Cell Longev.* 2020; 2020: 5281795.
10. Quiding-Järbrink M, Raghavan S, Sundquist M. Enhanced M1 macrophage polarization in human *Helicobacter pylori*-associated atrophic gastritis and in vaccinated mice. *PLoS One.* 2010; 5 (11): p.e15018. DOI: 10.1371/journal.pone.0015018.
11. Li W, Zhang X, Wu F, et al. Gastric cancer-derived mesenchymal stromal cells trigger M2 macrophage polarization that promotes metastasis and EMT in gastric cancer. *Cell Death & Disease.* 2019; 10 (12): 918. DOI: 10.1038/s41419-019-2131-y.
12. Atri C, Guerfali FZ, Laouini D. Role of human macrophage polarization in inflammation during infectious diseases. *Int J Mol Sci.* 2018; 19 (6): 1801. DOI: 10.3390/ijms19061801.
13. Song JH, Kim SG, Jin EH, Lim JH, Yang SY. Risk factors for gastric tumorigenesis in underlying gastric mucosal atrophy. *Gut Liver.* 2017; 11: 612–19.
14. Янин В. Л., Бондаренко О. М., Сазонова Н. А. Методы исследования в цитологии и гистологии. Ханты-Мансийск: БУ «Ханты-Мансийская государственная медицинская академия», 2015; 65 с.
15. Ni C, Yang L, Xu Q, Yuan H, et al. CD68- and CD163-positive tumor infiltrating macrophages in non-metastatic breast cancer: a retrospective study and meta-analysis. *J Cancer.* 2019 Jul 23; 10 (19): 4463–72. DOI: 10.7150/jca.33914.
16. Kloepper J, et al. Ang-2/VEGF bispecific antibody reprograms macrophages and resident microglia to anti-tumor phenotype and prolongs glioblastoma survival. *Proc Natl Acad Sci USA.* 2016; 113: 4476–81.
17. Murray PJ. Macrophage Polarization. *Annu Rev Physiol.* 2017; 79 (1): 541–66. DOI: 10.1146/annurev-physiol-022516-034339.
18. Wang YH, Lv ZF, Zhong Y, Liu DS, Chen SP, Xie Y. The internalization of *Helicobacter pylori* plays a role in the failure of *H. pylori* eradication. *Helicobacter.* 2017; 22 (1). DOI: 10.1111/hel.12324.
19. Ihrig M, Whary MT, Dangler CA, Fox JG. Gastric helicobacter infection induces a Th2 phenotype but does not elevate serum cholesterol in mice lacking inducible nitric oxide synthase. *Infect Immun.* 2005; 73: 1664–70.
20. Kaparakis M, Walduck AK, Price JD, Pedersen JS, van Rooijen N, et al. Macrophages are mediators of gastritis in acute *Helicobacter pylori* infection in C57BL/6 mice. *Infect Immun.* 2008; 76: 2235–9.
21. Liu LP, Sheng XP, Shuai TK, Zhao YX, Li B, Li YM. *Helicobacter pylori* promotes invasion and metastasis of gastric cancer by enhancing heparanase expression. *World J Gastroenterol.* 2018; 24 (40): 4565–77. DOI: 10.3748/wjg.v24.i40.4565.
22. Binnemars-Postma K, Bansal R, Storm G, et al. Targeting the Stat6 pathway in tumor-associated macrophages reduces tumor growth and metastatic niche formation in breast cancer. *FASEB J.* 2017; 32: 969–78.
23. Cortese N, Donadon M, Rigamonti A, Marchesi F. Macrophages at the crossroads of anticancer strategies. *Front Biosci (Landmark Ed).* 2019 Jun 1; 24: 1271–83.
24. Kzhyshkowska J, Gudima A, Moganti K, Gratchev A, Orekhov A. Perspectives for monocyte/macrophage-based diagnostics of chronic inflammation. *Transfus Med Hemother.* 2016; 43 (2): 66–77. DOI: 10.1159/000444943.

MICROBIOTA OF SEMEN SAMPLES WITH NORMOZOOSPERMIA: ANALYSIS OF REAL-TIME PCR DATA

Voroshilina ES^{1,2}✉, Zornikov DL¹, Ivanov AV^{3,4}, Pochernikov DG⁵, Panacheva EA^{1,2}¹ Ural State Medical University, Yekaterinburg, Russia² Medical Center "Garmonia", Yekaterinburg, Russia³ Yeltsin Ural Federal University, Yekaterinburg, Russia⁴ Institute of Mathematics and Mechanics, Yekaterinburg, Russia⁵ Ivanovo State Medical Academy, Ivanovo, Russia

The analysis of semen microbiota is difficult due to the lack of established criteria for interpretation of microbiological tests. The aim of the study was to determine the stable clusters of semen microbiota analyzed by real-time PCR in samples with normozoospermia. Semen samples of 227 men with normal spermograms were included in the study. The quantity of total bacterial DNA and at least one group of microorganisms was more than 10^3 GE/ml in 107 (41.7%) samples. Four stable microbiota clusters with the prevalence of a specific microorganism group were distinguished in these samples: obligate anaerobes (OA) cluster (proportion in the centroid — 81.1%); *Lactobacillus spp.* cluster (proportion in the centroid — 64.3%); gram-positive facultative anaerobes (GPFA) cluster (proportion in the centroid — 92.5%); *Enterobacteriaceae/Enterococcus* (EE) cluster (proportion in the centroid — 80.8%). The clusters were ranked by frequency of occurrence: OA cluster was the most prevalent (43 (40.2%) of 107), second-most frequent were GPFA-cluster (27 (25.2%)) and *Lactobacillus*-cluster (22 (20.6%)). EE-dominated cluster was found in 15 (14.0%) cases.

Keywords: semen microbiota, real-time PCR, cluster analysis, semen analysis, normozoospermia

Acknowledgments: the authors would like to thank VN Khayutin, director of "Garmonia" Medical Center, for allowing them to conduct the study in the clinic's laboratory department.

Author contribution: Voroshilina ES — organization of the study, data analysis, writing the article; Zornikov DL — data analysis, writing the article; Ivanov AV — statistical processing, data analysis, writing the article; Pochernikov DG — patient selection, writing the article; Panacheva EA — literature review, data analysis, patient selection, conducting semen analyses and PCR tests, writing the article.

Compliance with ethical standards: the study was approved by the Ethics Committee of Ural State Medical University, Federal State Budget Educational Institution of Higher Education under the Ministry of Health of the Russian Federation (Protocol № 7 dated September 20, 2019). All patients signed the informed written consent to participation in the study.

✉ **Correspondence should be addressed:** Ekaterina S. Voroshilina
Repina, 3, Yekaterinburg, 620014, Russia; voroshilina@gmail.com

Received: 16.09.2021 **Accepted:** 06.10.2021 **Published online:** 28.10.2021

DOI: 10.24075/brsmu.2021.048

МИКРОБИОТА ЭЯКУЛЯТА У ПАЦИЕНТОВ С НОРМОЗООСПЕРМИЕЙ ПО РЕЗУЛЬТАТАМ ИССЛЕДОВАНИЯ МЕТОДОМ ПЦР В РЕАЛЬНОМ ВРЕМЕНИ

Е. С. Ворошилина^{1,2}✉, Д. Л. Зорников¹, А. В. Иванов^{3,4}, Д. Г. Почерников⁵, Е. А. Паначева^{1,2}¹ Уральский государственный медицинский университет, Екатеринбург, Россия² Медицинский центр «Гармония», Екатеринбург, Россия³ Уральский федеральный университет имени первого Президента России Б. Н. Ельцина, Екатеринбург, Россия⁴ Институт математики и механики имени Н. Н. Красовского, Екатеринбург, Россия⁵ Ивановская государственная медицинская академия, Иваново, Россия

Оценка микробиоты эякулята осложнена из-за отсутствия четких критериев для интерпретации микробиологических тестов. Целью работы было определить устойчивые варианты микробиоты, исследованной методом ПЦР-РВ, в образцах эякулята с нормозооспермией. В исследование включили 227 проб эякулята, отвечающих критериям нормозооспермии. В 107 (41,7%) образцах фиксировали наличие суммарной бактериальной ДНК и хотя бы одной из исследованных групп микроорганизмов в значениях не менее 10^3 ГЭ/мл. В данных образцах выделили четыре устойчивых кластера микробиоты, характеризующихся преобладанием определенной группы микроорганизмов: облигатных анаэробов (кластер 1; доля преобладающих микроорганизмов в центроиде — 81,1%), *Lactobacillus spp.* (кластер 2; доля преобладающих микроорганизмов в центроиде — 64,3%) грамположительных факультативных анаэробов (кластер 3; доля преобладающих микроорганизмов в центроиде — 92,5%), *Enterobacteriaceae/Enterococcus* (кластер 4; доля преобладающих микроорганизмов в центроиде — 80,8%). Кластеры ранжированы по частоте встречаемости: кластер 1 (43 (40,2%)), кластер 3 (27 (25,2%)), кластер 2 (22 (20,6%)), кластер 4 (15 (14,0%)).

Ключевые слова: микробиота эякулята, ПЦР-РВ, кластерный анализ, спермограмма, нормозооспермия

Благодарности: авторы благодарят директора медицинского центра «Гармония» (г. Екатеринбург) В. Н. Хаютина за возможность выполнения исследования на базе центра.

Вклад авторов: Е. С. Ворошилина — планирование эксперимента, проведение ПЦР-РВ, анализ данных, написание статьи; Д. Л. Зорников — анализ литературы, анализ данных, написание статьи; А. В. Иванов — статистическая обработка, кластерный анализ, написание статьи; Д. Г. Почерников — отбор пациентов, написание статьи; Е. А. Паначева — отбор пациентов, выполнение спермограмм и ПЦР-РВ, анализ литературы, анализ данных, написание статьи.

Соблюдение этических стандартов: исследование одобрено этическим комитетом Уральского государственного медицинского университета (протокол № 7 от 20 сентября 2019 г.). Все участники исследования подписали добровольное информированное согласие.

✉ **Для корреспонденции:** Екатерина Сергеевна Ворошилина
ул. Репина, д. 3, г. Екатеринбург, 620028, Россия; voroshilina@gmail.com

Статья получена: 16.09.2021 **Статья принята к печати:** 06.10.2021 **Опубликована онлайн:** 28.10.2021

DOI: 10.24075/vrgmu.2021.048

Semen microbiota remains an under investigated part of human microbiome despite the strong interest in it, as well as the capabilities of modern molecular technologies. This biomaterial is especially significant in the context of infertility treatment [1]. The male factor is responsible for infertility in half of all the couples [2], however, the cause of infertility in men often remains unidentified [3]. Infection is behind only 6–10% of all male infertility cases [4]. It was shown that some bacteria can cause direct damage to spermatozoa decreasing their motility and viability [5].

The use of molecular-based technique, primarily next-generation sequencing (NGS), made it possible to detect complex bacterial communities both in the ejaculate of patients with infectious and inflammatory processes and in healthy men with normozoospermia [1, 6–10]. Some of the detected microorganisms were fastidious or non-culturable (including obligate anaerobes) [8, 10, 11], which could explain a larger number of positive samples compared to the results of culture method. However, the detection of microorganisms in the semen of patients with normozoospermia forced researchers to abandon the concept of bacteriospermia as a marker of an exclusively pathological condition [6, 7, 9]. Instead, cautious assumptions have been made about the association between the semen microbiota composition and abnormalities in the semen analysis [6, 9].

The few semen microbiota studies from patients with normozoospermia were conducted on a limited number of samples, which prevented researchers from forming a clear idea about the norm for this biomaterial [1]. Moreover, the NGS used in these studies has a number of disadvantages preventing its wide implementation in routine medical practice: high cost and labor input, the complexity of standardizing the procedure and interpreting the results.

In practice, real-time PCR, another molecular-based technique, is more promising for routine analyses of semen microbiota. The release of a registered test kit for assessing male urogenital microbiota has opened up new possibilities for detecting a wide range of pathogenic and opportunistic bacteria in semen. These microorganisms include fastidious and non-culturable bacteria, as well as *Lactobacillus spp.* [12, 13], which are commonly considered the inhabitants of the female reproductive tract. The availability of real-time PCR raises the question of correctly interpreting its results. The presence of many bacterial groups in various combinations and quantities required the use of mathematical modeling methods to identify patterns in semen microbiota composition. Cluster analysis allowed us to reduce the entire variety of identified microorganisms to four stable types of microbial communities, characterized by the predominance of different bacterial groups [12]. Further studies of samples with normal and abnormal spermogram parameters are required to evaluate the clinical significance of the microbiota types.

The aim of the study was to identify stable variants of microbiota analyzed by means of real-time PCR in semen samples with normozoospermia.

METHODS

Patient groups

The study included 227 semen samples with normozoospermia from men (aged 20–59, mean age 33 ± 4.7) who came to the “Garmonia” Medical Center (Yekaterinburg, $n = 142$) and to the urological clinic of the Ivanovo State Medical Academy (Ivanovo, $n = 85$) seeking preconception care from January 2019 to March 2020.

Inclusion criteria: all examined patients during the last four weeks did not receive medications that could affect the semen microbiota, such as hormonal or antibacterial drugs; normozoospermia according to semen analysis results.

Exclusion criteria: hypogonadotropic and hypergonadotropic hypogonadism, type 1 and 2 diabetes, hypo- and hyperthyroidism; sexually transmitted infections (*Chlamydia trachomatis*, *Neisseria gonorrhoeae*, *Mycoplasma genitalium*, *Trichomonas vaginalis*); clinical manifestations of prostatitis such as pain and dysuria; karyotype abnormalities, mutations in the *CFTR* gene, microdeletions in the AZF locus of the Y chromosome.

Semen samples were collected from each patient in accordance with the following guidelines; semen analysis parameters and semen microbiota composition were evaluated.

Semen sampling

Patient preparation and sampling were conducted in compliance with WHO's guidelines for the examination and processing of human semen (p. 2.2.4 of the Manual). Ejaculatory abstinence for the period of 2–5 days was mandatory. Prior to semen collection, patients urinated and washed their external genitalia. Semen was collected through masturbation into a sterile container [14].

Semen analysis parameters

The semen analysis was carried out after a 30–60-minute liquefaction of the material; the quantity (concentration) and motility of spermatozoa was calculated using a Biola SCA sperm analyzer (NPF Biola; Russia). Sperm morphology was assessed in stained preparations at a microscope magnification $\times 1000$ using a Spermac Stain diagnostic kit (Ferti Pro; Belgium).

Obtained data were interpreted in accordance with the WHO criteria [14].

DNA extraction

PREP-NA-PLUS kit (DNA-Technology; Russia) was used for DNA-extraction. Semen samples were prepared using the following technique: 1.0 ml of semen was put into an Eppendorf tube with 1.0 ml of transport medium (“Transport media with mucolytic agent”; InterLabService Ltd., Russia) which was then shaken in the vortex until the substances mixed completely. The tube was centrifuged at 13,000 rpm for 10 minutes (Mini-Spin centrifuge; Eppendorf, Germany). After removing the supernatant, 50 μ l of the precipitate was used for extraction of the DNA.

Semen microbiota analysis

The study was conducted using Androflor reagent kit (DNA-Technology; Russia) and DTprime detection thermal cycler (DNA-Technology; Russia) following the manufacturer's instructions. Once the amplification is over, the special software (DNA-Technology; Russia) automatically calculates the quantities (expressed in genome equivalents per 1 ml (GE/ml)) of the total bacterial load (TBL), lactobacilli and each of the detected opportunistic microorganisms (OM) in a given sample. The kit allows detecting the following microbial groups: gram-positive facultative anaerobes (*Streptococcus spp.*, *Staphylococcus spp.*, *Corynebacterium spp.*); gram-negative facultative anaerobes (*Haemophilus spp.*, *Pseudomonas aeruginosa* / *Ralstonia spp.* / *Burkholderia spp.*); *Enterobacteriaceae* /

Table 1. Detection rate of specific bacterial groups in quantities exceeding the threshold value ($n = 227$)*

Microorganism groups	n	%
<i>Corynebacterium spp.</i>	39	17.2
<i>Streptococcus spp.</i>	30	13.2
<i>Bacteroides spp. / Porphyromonas spp. / Prevotella spp.</i>	28	12.3
<i>Peptostreptococcus spp. / Parvimonas spp.</i>	28	12.3
<i>Lactobacillus spp.</i>	26	11.5
<i>Enterobacteriaceae spp. / Enterococcus spp.</i>	24	10.6
<i>Eubacterium spp.</i>	22	9.7
<i>Megasphaera spp. / Veillonella spp. / Dialister spp.</i>	22	9.7
<i>Ureaplasma parvum</i>	20	8.8
<i>Atopobium cluster</i>	18	7.9
<i>Gardnerella vaginalis</i>	17	7.5
<i>Staphylococcus spp.</i>	17	7.5
<i>Sneathia spp. / Leptotrichia spp. / Fusobacterium spp.</i>	13	5.7
<i>Haemophilus spp.</i>	12	5.3
<i>Anaerococcus spp.</i>	10	4.4
<i>Mycoplasma hominis</i>	10	4.4
<i>Pseudomonas aeruginosa / Ralstonia spp. / Burkholderia spp.</i>	8	3.5
<i>Ureaplasma urealyticum</i>	8	3.5

Note: * — for *Ureaplasma urealyticum*, *Ureaplasma parvum*, *Mycoplasma hominis* threshold values are > 0 , for other bacterial groups they are $\geq 10^3$ GE/ml.

Enterococcus spp. group; obligate anaerobes (*Gardnerella vaginalis*, *Eubacterium spp.*, *Sneathia spp. / Leptotrichia spp. / Fusobacterium spp.*, *Megasphaera spp. / Veillonella spp. / Dialister spp.*, *Bacteroides spp. / Porphyromonas spp. / Prevotella spp.*, *Anaerococcus spp.*, *Peptostreptococcus spp.*, *Atopobium cluster*), mycoplasmas (*Mycoplasma hominis*, *Ureaplasma urealyticum*, *Ureaplasma parvum*), transient microbiota (*Lactobacillus spp.*), yeast-like fungi (*Candida spp.*).

Sterile deionized water was used as the negative control sample (NCS). Positive signals were detected in the negative control sample for some bacterial groups no earlier than in the 35th amplification cycle. In these cases, the bacterial load was less than 10^3 GE/ml. Thus, the quantity of microorganisms needed to be at least 10^3 GE/ml for it to be considered above threshold, which meant that a positive signal was received in real-time PCR before the 35th cycle. The exceptions were *U. urealyticum*, *U. parvum*, *M. hominis* since there was no positive signal for these microorganisms in the negative control sample. If the signal was detected at any amplification cycle for these microorganisms groups, real-time PCR result for them was regarded as positive. Yeast-like fungi of the *Candida spp.* were not included in this study.

Statistical methods

Analysis of the structural characteristics of semen microbiota was carried out using the MSSC clustering model, which minimizes the sum over all clusters of intra-cluster sums of squared distances from cluster elements to their centroids [15]. The clustering problem was solved using the k -means++ algorithm [16], implemented in the scikit-learn machine learning library. The optimal clustering was selected on the basis of internal assessments of the clustering quality: the Silhouette coefficient [17] and the Davies–Bouldin index (DBI) [18].

To run the k -means ++ clustering algorithm, each of the analyzed samples was represented as a vector $(p, s) \in R^{50}$, consisting of a vector of primary signs $p \in R^{19}$, taken from the data of semen microbiota analysis by real-time PCR, and of a vectors of secondary signs $s \in R^{31}$, calculated using the primary signs.

The primary signs were the absolute values of the values determined by the Androflor kit (TBL and 18 bacterial groups).

Based on the primary characteristics, the following secondary characteristics were calculated: corrected TBL (CTBL), equal to the total mass of the 18 determined bacterial

Table 2. Clustering quality values given different number of clusters

Cluster N	Silhouette Coefficient	Davies–Bouldin Index
2	0,19	1.68
3	0,25	1.73
4	0,32	1.30
5	0,30	1.42
6	0,32	1.34
7	0,32	1.27
8	0,32	1.28
9	0,34	1.17
10	0,34	1.24

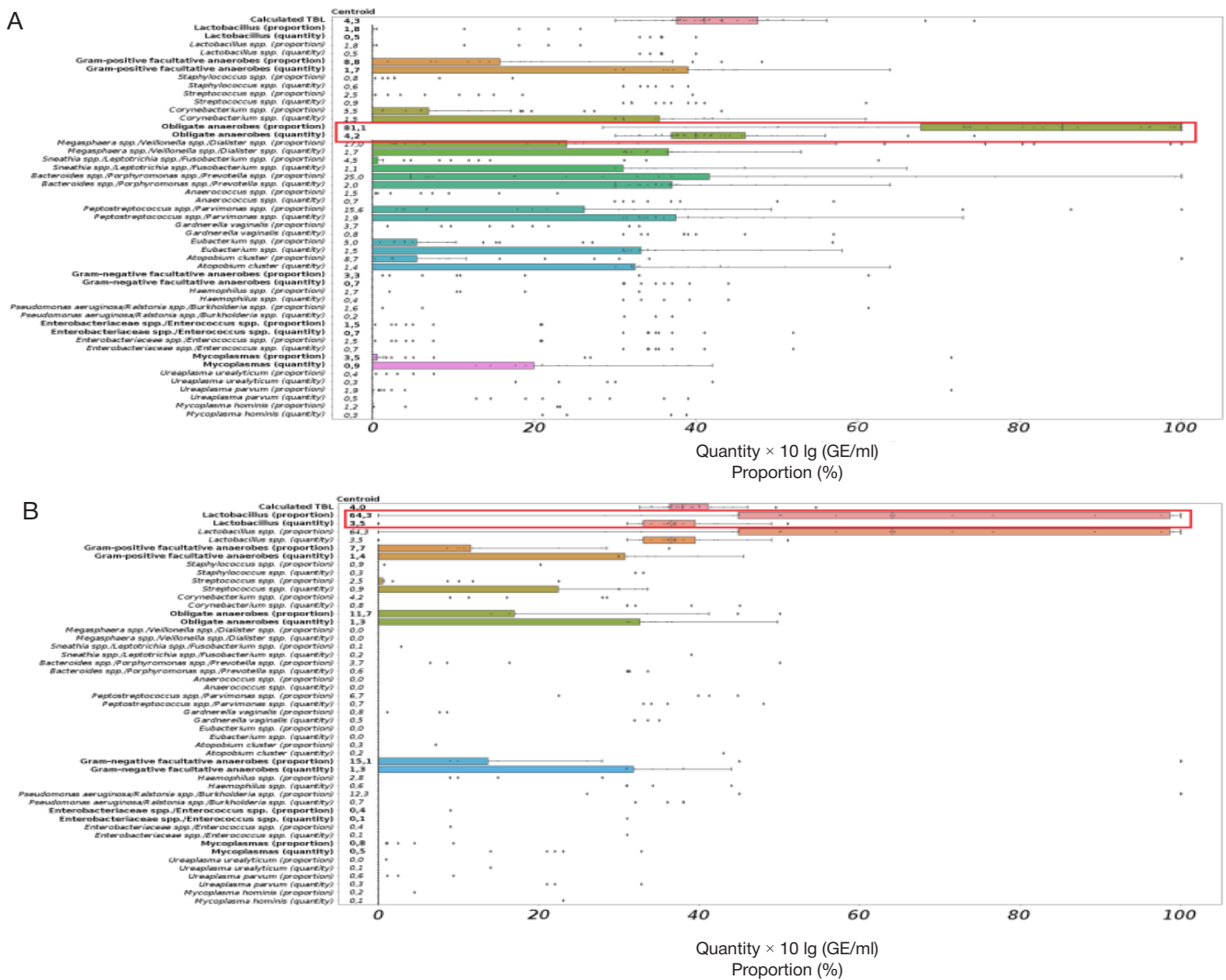


Fig. 1. Results of cluster analysis of semen microbiota analyzed by means of real-time PCR ($n = 107$). The ordinate shows the values of the features in the centroid. Diagrams of the predominant groups of microorganisms are highlighted using red rectangles. Cluster 1 ($n = 43$) is characterized by the predominance of obligate anaerobes (A); cluster 2 ($n = 22$) is characterized by the predominance of *Lactobacillus spp.* (B); cluster 3 ($n = 27$) is characterized by the predominance of gram-positive facultative anaerobes (C); cluster 4 ($n = 15$) is characterized by the predominance of *Enterobacteriaceae spp.* / *Enterococcus spp.* (D)

groups; mass fractions of microorganisms in relation to CTBL; masses of bacterial groups consolidated in accordance with the Androflor kit: *Lactobacillus spp.*, gram-positive facultative anaerobes (GPFA), obligate anaerobes (OA), gram-negative facultative anaerobes (GNFA), *Enterobacteriaceae spp.* / *Enterococcus spp.* (EE) and mycoplasmas, mass fractions of consolidated bacterial groups in relation to CTBL.

For optimal clustering, the stability of clusters to changes in the sample size was tested. For this purpose, random subsamples of 1 to 100% of the original sample were clustered and the cluster stability index was calculated using the following formula:

$$Stability\ Index(k) = \frac{\sum_{i=1}^n \sum_{j=1}^n \mathbf{1}_{\{true\}}([A(x_i)A(x_j) \in k] \wedge [\exists l A^l(x_i)A^l(x_j) \in l])}{\sum_{i=1}^n \sum_{j=1}^n \mathbf{1}_{\{true\}}([A(x_i)A(x_j) \in k]) \vee \mathbf{1}_{\{false\}}([\exists l A^l(x_i)A^l(x_j) \in l])}$$

where $\mathbf{1}_{\{true\}}: \{true, false\} \rightarrow \{0, 1\}$ — logical argument indicator function; $A(x)$, $A^l(x)$ — the label of the observed cluster x , resulting from clustering based on the original dataset and subsample respectively; $k = \{1, 2, 3, 4\}$, $l = \{1, 2, 3, 4\}$ — cluster labels.

RESULTS

Bacterial DNA (TBL) was not detected or was detected in the quantities lower than 10^3 GE/ml in 81 (35.7%) semen samples.

TBL was detected in quantities higher than 10^3 GE/ml in 39 (17.1%) samples, however the quantities of specific bacterial groups were below the threshold value.

In 107 (47.1%) samples out of 227, TBL was at least 10^3 GE/ml (median — $10^{3.8}$, interquartile range — $10^{3.5}-10^{4.4}$ GE/ml) with 1 to 14 bacterial groups detected in quantities, exceeding the threshold value, simultaneously. Detection rate of specific bacterial groups is given in Table 1.

Different bacterial groups were found in a variety of associations with each other. Thus, we have decided to perform cluster analysis in order to identify the microbial communities typical of semen microbiota.

Semen microbiota cluster analysis

For cluster analysis, 107 samples were selected in accordance with the following criteria: TBL in the quantity of at least 10^3 GE/ml, at least one group of bacteria in the quantity of at least 10^3 GE / ml.

The optimal number of clusters in the examined dataset was determined on the basis of the values of the silhouette coefficient and Davies–Bouldin index (Table 2). The best clustering quality corresponds to the highest silhouette coefficient and the lowest Davies–Bouldin Index. In accordance

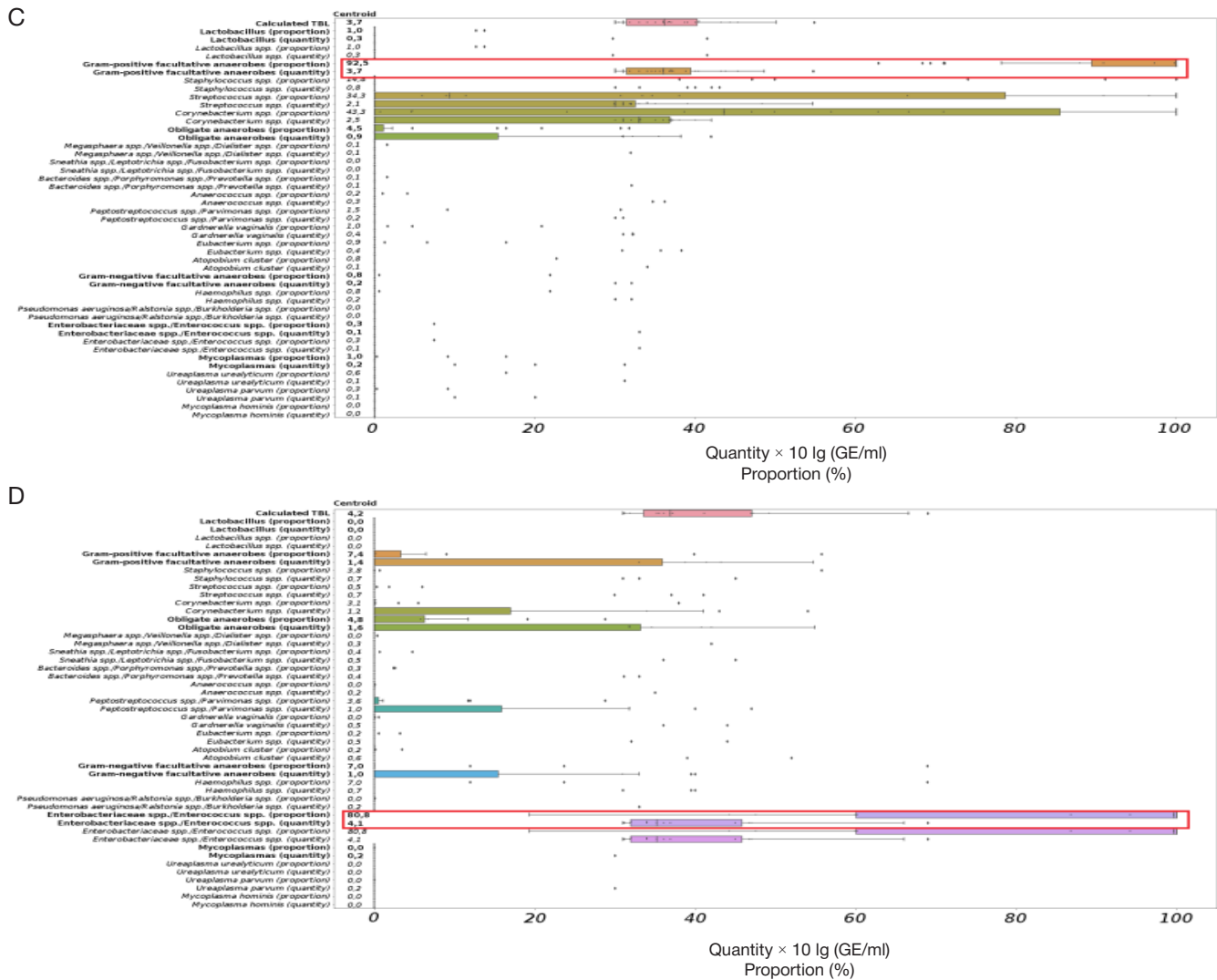


Fig. 1. (continue)

with the obtained values of the indices, it was optimal to select 4, 9 or 10 clusters. However, after testing cluster stability, the ones obtained as a result of 9- and 10-clustering, were found to be less stable than the ones obtained as a result of 4-clustering. Thus, 4 main clusters of semen microbiota were identified.

Each of the resulting clusters was characterized by the predominance of a particular consolidated bacterial group. The diagrams in Fig. 1 show the range of characteristics of the objects in their respective clusters.

Cluster 1 — the OA-dominated variant. CTBL amounted to $10^{4.3}$ GE / ml in the centroid. The absolute quantity of all the OA was comparable to the CTBL and amounted to $10^{4.2}$ GE/ml in the centroid (Fig. 1A). The proportion of OA in the centroid reached 81.1% in relation to the CTBL. We were unable to determine the predominant OA group with the test; several OA groups were present simultaneously. This microbiota variant was identified in 43 (40.2%) out of 107 samples.

Cluster 2 — the lactobacilli-dominated variant. It was identified in 22 (20.6%) out of 107 samples. CTBL amounted to $10^{4.0}$ GE/ml in the centroid. The absolute quantity of all lactobacilli was lower than the CTBL in the centroid and amounted to $10^{3.5}$ GE/ml (Fig. 1B). The proportion of lactobacilli in the centroid reached 64.3% in relation to the CTBL. OA, GPFA, and GNFA were present simultaneously with *Lactobacillus spp.*

Cluster 3 — characterized by the predominance of GPFA, was identified in 27 (25.2%) out of 107 samples. CTBL was $10^{3.7}$ GE/ml in the centroid. The absolute quantity of all GPFA was comparable to the CTBL and amounted to $10^{3.7}$ GE/ml in the centroid (Fig. 1C). The proportion of GPFA in the centroid reached 89.4% in relation to the CTBL. Most often this cluster was formed around *Corynebacterium spp.* and *Streptococcus spp.* in patients with normozoospermia.

Cluster 4 — the EE-dominated variant. CTBL was $10^{4.2}$ GE/ml in the centroid. The absolute quantity of all EE was less than the CTBL and amounted to $10^{4.1}$ GE/ml in the centroid (Fig. 1D). The proportion of EE in the centroid reached 80.8% in relation to the CTBL. This microbiota variant was identified in 15 (14.0%) out of 107 samples.

Analysis of the microbial clusters' stability

To analyze the stability of the identified clusters, subsamples of 1–100% volume of the original sample were generated (1000 random subsamples without return for each value of the volume).

Figure 2 shows the graphs depicting stability of the clusters obtained on the basis of 4-clustering semen microbiota samples with normozoospermia. The most stable are the clusters with the predominance of GPFA (cluster 3; Fig. 2C) and with the predominance of EE (cluster 4; Fig. 2D).

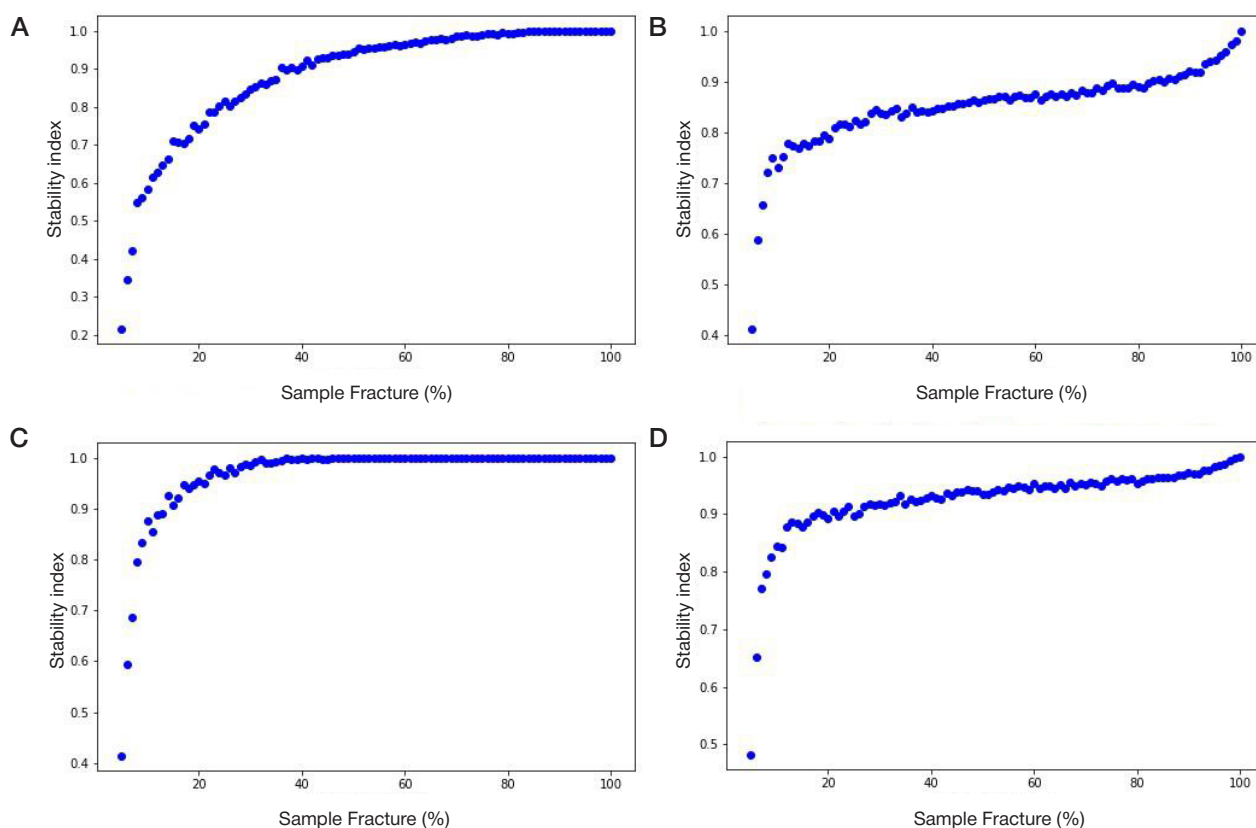


Fig. 2. Results of the cluster stability analysis 1 (A), 2 (B), 3 (C), 4 (D). The blue marker shows the cluster stability index on a set of the f volume. EE — *Enterobacteriaceae* spp. / *Enterococcus* spp.; GPFA — gram-positive facultative anaerobes; OA — obligate anaerobes

DISCUSSION

In this study, microbial DNA in above-threshold values (at least 10^3 GE/ml) was found in 146 (64.3%) of 227 semen samples meeting the criteria for normozoospermia. In 81 (35.7%) samples bacterial DNA was absent or was detected in an amount of less than 10^3 GE/ml and could be kitome DNA (microbial DNA present in reagent kits) [19]. The results are consistent with the data of other researchers who noted the presence of microorganisms in the semen of men with normal semen parameters [1, 6–8, 20]. In 107 (47.1%) samples with the TBL of at least 10^3 GE/ml, up to 14 bacterial groups were found in above-threshold values. This is also consistent with the previously obtained data on the presence of polymicrobial associations in the seminal fluid of healthy men [1, 8, 20].

Bacteria of the *Corynebacterium* genus were identified in 17.2% of the studied samples, which was more often than other bacterial groups. *Streptococcus* spp., *Peptostreptococcus* spp. / *Parvimonas* spp., *Bacteroides* spp. / *Porphyromonas* spp. / *Prevotella* spp., *Lactobacillus* spp., *Enterobacteriaceae* spp. / *Enterococcus* spp. were present in 10.6–13.2% of samples. The rest of the analyzed bacterial groups were found in 3.5–9.7% of the samples. The simultaneous detection of several bacterial groups in various combinations makes it impossible to interpret the obtained results without additional mathematical analysis.

The positive samples, depending on the predominant group of microorganisms, were grouped into four clusters, similar to those obtained in the study of all semen types [21]: variants with the predominance of OA, *Lactobacillus* spp., GPFA, EE. The last two clusters are more stable than the first two. Although the clusters were identified exclusively mathematically, they are formed by microorganisms with similar physiological characteristics. In particular, three of the four identified clusters (with the predominance

of OA, GPFA, EE) are formed by phylogenetically heterogeneous microorganisms with the same oxygen requirements, which was also noted in other studies [1]. Apparently, this is due to the presence of various ecological niches for the microorganisms colonizing semen, which is not surprising, since semen is a mixture of biomaterials from different parts of the urogenital tract [6].

Most of the positive samples (40.2%) were attributed to the cluster with the OA predominance; their amount in the centroid reached 81.1% of all detected microorganisms. Microbiota in these samples was characterized by significant heterogeneity within the OA group without dominance of any particular species. A similar cluster, consisting of obligate anaerobic bacteria, was identified in the work which studied semen microbiota by NGS sequencing [1]. However, the use of a routine culture-based analysis allowed us to identify OA as the predominant group of microorganisms only in 15% of semen samples which had been OA-prevalent when tested by means of real-time PCR [12].

A quarter of all samples (25.2%) were assigned to a cluster with the predominance of GPFA. This is the microbiota variant that was previously described as typical for the urogenital tract of healthy men [4]. Among other microorganisms, bacteria of the *Staphylococcus*, *Streptococcus*, and *Corynebacterium* genera (assigned to the GPFA group) were detected in the semen of men without signs of sexually transmitted infections by the culture-based method [22]. However, identifying GPFA in semen does not always mean that this bacterial group is predominant in this biomaterial [12]. The use of modern molecular-based techniques also makes it possible to identify fastidious and non-culturable microorganisms, which clarifies their contribution to semen microbiota composition.

A smaller number of semen samples (20.6%) were attributed to the cluster with the predominance of *Lactobacillus* spp. The role of these bacteria, the main representatives of the vaginal normal

microbiota, in the semen microbiota composition is not so obvious. Some researchers noted the presence of lactobacilli in semen samples with normozoospermia and associate this with male fertility [8, 9]. Others believe that increased numbers of *Lactobacillus* spp. in semen are a marker of hormonal disorders and the basis for further comprehensive examination of the patient [23].

The EE-dominated cluster was the smallest in the sample pool; the presence of this bacterial group was noted only in 14.0% of cases. Some representatives of EE, primarily *Escherichia coli* and *Enterococcus faecalis*, are considered to be a common cause of inflammatory pathology of male urogenital tract [24]. Perhaps this is due to the high incidence of their detection by culture-based technique. For example, during the parallel study of semen samples using the culture-based technique and real-time PCR, it was shown that in almost half of the cases when enterobacteria and enterococci were determined by the cultures as predominant, other predominant microorganisms were detected by real-time PCR. Most often, these were OA, which, most likely, is due to the reduced ability to identify anaerobes during *in vitro* culturing [12]. The role of *E. coli* and *E. faecalis*, as well as other representatives of the EE group, in fertility disorders and sperm quality has not been definitively identified and requires further study.

This study once again demonstrates the frequent presence of microorganisms in semen samples meeting the criteria for normozoospermia. In most of the analyzed samples, microbiota was predominantly represented by obligate anaerobic bacteria,

rather than gram-positive facultative anaerobes, which were detected using the culture-based method [22].

CONCLUSIONS

In half of the cases, semen samples that met the criteria for normozoospermia contained microbiota in the above-threshold values. The identified microorganisms were grouped using cluster analysis into four stable types according to the predominance criterion of a certain group of microorganisms: obligate anaerobes, *Lactobacillus* spp., Gram-positive facultative anaerobes, *Enterobacteriaceae* spp. / *Enterococcus* spp. The clusters were ranked by frequency of occurrence: the variant with the predominance of obligate anaerobes; gram-positive facultative anaerobes-dominated variant; *Lactobacillus* spp. — dominated variant; *Enterobacteriaceae* spp. / *Enterococcus* spp. — dominated variant (identified in 40.2, 25.2, 20.6 and 14.0% of positive samples respectively). The use of molecular methods may lead us to the rethinking of ideas about the composition of the microbiota identified in semen samples with normozoospermia. Association of certain variants of semen microbiota with inflammatory pathologies of the reproductive tract and fertility disorders remains an unresolved question. It is possible that there are informative microbiological markers associated with these conditions. The study of the microbial composition of pathological semen samples is the next necessary step in the search for such diagnostic markers.

References

- Baud D, Pattaroni C, Vulliemoz N, Castella V, Marsland BJ, Stojanov M. Sperm Microbiota and Its Impact on Semen Parameters. *Front Microbiol.* 2019;10:234. Published 2019 Feb 12. DOI: 10.3389/fmicb.2019.00234.
- EAU Guidelines. Edn. presented at the EAU Annual Congress Milan Italy 2021. Available from: <https://uroweb.org/guideline/urological-infections/>.
- Ochsendorf FR. Sexually transmitted infections: impact on male fertility. *Andrologia.* 2008; 40 (2): 72–5. DOI: 10.1111/j.1439-0272.2007.00825.x.
- Schuppe HC, Pilatz A, Hossain H, Diemer T, Wagenlehner F, Weidner W. Urogenital Infection as a Risk Factor for Male Infertility. *Dtsch Arztebl Int.* 2017; 114 (19): 339–46. DOI: 10.3238/arztebl.2017.0339.
- Baud D, Vulliemoz N, Ammerdorffer A, Gyger J, Greub G, Castella V, et al. Waddlia chondrophila, a Chlamydia-related bacterium, has a negative impact on human spermatozoa. *Hum Reprod.* 2018; 33 (1): 3–10. DOI: 10.1093/humrep/dex342.
- Hou D, Zhou X, Zhong X, Settles ML, Herring J, Wang L, et al. Microbiota of the seminal fluid from healthy and infertile men. *Fertil Steril.* 2013; 100 (5): 1261–9. DOI: 10.1016/j.fertnstert.2013.07.1991.
- Liu CM, Osborne BJ, Hungate BA, Liu CM, Osborne BJ, Hungate BA, et al. The semen microbiome and its relationship with local immunology and viral load in HIV infection. *PLoS Pathog.* 2014; 10 (7): e1004262. DOI: 10.1371/journal.ppat.1004262.
- Mändar R, Punab M, Korrovits P, Türk S, Ausmees K, Lapp E, et al. Seminal microbiome in men with and without prostatitis. *Int J Urol.* 2017; 24 (3): 211–6. DOI: 10.1111/iju.13286.
- Weng SL, Chiu CM, Lin FM, Huang WC, Liang C, Yang T, et al. Bacterial communities in semen from men of infertile couples: metagenomic sequencing reveals relationships of seminal microbiota to semen quality. *PLoS One.* 2014; 9 (10): e110152. DOI: 10.1371/journal.pone.0110152.
- Štšepetova J, Baranova J, Simm J, Parm Ü, Rööp T, Sokmann S, et al. The complex microbiome from native semen to embryo culture environment in human in vitro fertilization procedure. *Reprod Biol Endocrinol.* 2020; 18 (1): 3. DOI: 10.1186/s12958-019-0562-z.
- Kiessling AA, Desmarais BM, Yin HZ, Loverde J, Eyre RC. Detection and identification of bacterial DNA in semen. *Fertil Steril.* 2008; 90 (5): 1744–56. DOI: 10.1016/j.fertnstert.2007.08.083.
- Voroshilina ES, Zornikov DL, Panacheva EA. Evaluation of the ejaculate microbiota by real-time PCR and culture-based technique. *Bulletin of RSMU.* 2019; 1: 41–6. DOI: 10.24075/brsmu.2019.009.
- Pochernikov DG, Vitvickaya YuG, Boldyreva MN, Galkina IS. Informativnost' biomateriala dlja issledovanija mikrobioty urogenital'nogo trakta muzhchin metodom PCR-RV (pilotnoe issledovanie). *Jeksperimental'naja i klinicheskaja urologija.* 2019; 2: 128–133. DOI: 10.29188/2222-8543-2019-11-2-128-132. Russian.
- WHO. Laboratory manual for the examination and processing of human semen. 5th ed. Geneva: WHO; 2010.
- Jain AK, Murty MN, Flynn PJ. Data clustering: a review. *ACM computing surveys (CSUR).* 1999; 31 (3): 264–323.
- Arthur D, Vassilvitskii S. K-means++: the advantages of careful seeding. In: Hal Gabow, editor. *Proceedings of the Eighteenth Annual ACM-SIAM Symposium on Discrete Algorithms (Proceedings in Applied Mathematics) 18th ed.* Society for Industrial and Applied Mathematics (3 January 2007); p. 1027–35. DOI: 10.1145/1283383.1283494.
- Rousseeuw PJ. Silhouettes: A graphical aid to the interpretation and validation of cluster analysis. *J Comput Appl Math.* 1987; 20: 53–65.
- Davies DL, Bouldin DW. A Cluster Separation Measure. *IEEE Transactions on Pattern Analysis and Machine Intelligence.* PAMI-1. 1979; 2: 224–7.
- de Goffau MC, Lager S, Salter SJ, Wagner J, Kronbichler A, Charnock-Jones DS, et al. Recognizing the reagent microbiome. *Nat Microbiol.* 2018; 3 (8): 851–3.
- Yang H, Zhang J, Xue Z, Zhao C, Lei L, Wen Y, et al. Potential Pathogenic Bacteria in Seminal Microbiota of Patients with Different Types of Dysspermatism. *Sci Rep.* 2020;10 (1): 6876. DOI: 10.1038/s41598-020-63787-x.
- Voroshilina ES, Zornikov DL, Ivanov AV, Pochernikov DG, Panacheva EA. Semen microbiota: cluster analysis of real-time

- PCR data. Bulletin of RSMU. 2020; 5: 62–70. DOI: 10.24075/brsmu.2020.064.
22. Ivanov IB, Kuzmin MD, Gritsenko VA. Microflora of the seminal fluid of healthy men and men suffering from chronic prostatitis syndrome. Int J Androl. 2009; 32 (5): 462–7. DOI: 10.1111/j.1365-2605.2008.00878.x.
23. Pochernikov DG, Postovoytenko NT, Getman VV, Galkina IS. Diagnostic significance of *Lactobacillus* spp. identification in ejaculate. Bulletin of RSMU. 2020; 3: 38–45. DOI: 10.24075/brsmu.2020.039.
24. Lipsky BA, Byren I, Hoey CT. Treatment of bacterial prostatitis. Clin Infect Dis. 2010; 50 (12): 1641–52. DOI: 10.1086/652861.

Литература

- Baud D, Pattaroni C, Vulliemoz N, Castella V, Marsland BJ, Stojanov M. Sperm Microbiota and Its Impact on Semen Parameters. Front Microbiol. 2019; 10: 234. Published 2019 Feb 12. DOI: 10.3389/fmicb.2019.00234.
- EAU Guidelines. Edn. presented at the EAU Annual Congress Milan Italy 2021. Available from: <https://uroweb.org/guideline/urological-infections/>.
- Ochsendorf FR. Sexually transmitted infections: impact on male fertility. Andrologia. 2008; 40 (2): 72–5. DOI: 10.1111/j.1439-0272.2007.00825.x.
- Schuppe HC, Pilatz A, Hossain H, Diemer T, Wagenlehner F, Weidner W. Urogenital Infection as a Risk Factor for Male Infertility. Dtsch Arztebl Int. 2017; 114 (19): 339–46. DOI: 10.3238/arztebl.2017.0339.
- Baud D, Vulliemoz N, Ammerdorffer A, Gyger J, Greub G, Castella V, et al. *Waddlia chondrophila*, a *Chlamydia*-related bacterium, has a negative impact on human spermatozoa. Hum Reprod. 2018; 33 (1): 3–10. DOI: 10.1093/humrep/dex342.
- Hou D, Zhou X, Zhong X, Settles ML, Herring J, Wang L, et al. Microbiota of the seminal fluid from healthy and infertile men. Fertil Steril. 2013; 100 (5): 1261–9. DOI: 10.1016/j.fertnstert.2013.07.1991.
- Liu CM, Osborne BJ, Hungate BA, Liu CM, Osborne BJ, Hungate BA, et al. The semen microbiome and its relationship with local immunology and viral load in HIV infection. PLoS Pathog. 2014; 10 (7): e1004262. DOI: 10.1371/journal.ppat.1004262.
- Mándar R, Punab M, Korrovits P, Türk S, Ausmees K, Lapp E, et al. Seminal microbiome in men with and without prostatitis. Int J Urol. 2017; 24 (3): 211–6. DOI: 10.1111/iju.13286.
- Weng SL, Chiu CM, Lin FM, Huang WC, Liang C, Yang T, et al. Bacterial communities in semen from men of infertile couples: metagenomic sequencing reveals relationships of seminal microbiota to semen quality. PLoS One. 2014; 9 (10): e110152. DOI: 10.1371/journal.pone.0110152.
- Štšepetova J, Baranova J, Simm J, Pam Ü, Röpö T, Sokmann S, et al. The complex microbiome from native semen to embryo culture environment in human in vitro fertilization procedure. Reprod Biol Endocrinol. 2020; 18 (1): 3. DOI: 10.1186/s12958-019-0562-z.
- Kiessling AA, Desmarais BM, Yin HZ, Loverde J, Eyre RC. Detection and identification of bacterial DNA in semen. Fertil Steril. 2008; 90 (5): 1744–56. DOI: 10.1016/j.fertnstert.2007.08.083.
- Ворошилина Е. С., Зорников Д. Л., Паначева Е. А. Сравнительное исследование микробиоты эякулята методом количественной ПЦР и культуральным методом. Вестник Российского государственного медицинского университета. 2019; 1: 44–9. DOI: 10.24075/vrgmu.2019.009.
- Почерников Д. Г., Витвицкая Ю. Г., Болдырева М. Н., Галкина И. С. Информативность биоматериала для исследования микробиоты урогенитального тракта мужчин методом ПЦР-ПВ (пилотное исследование). Экспериментальная и клиническая урология. 2019; 2: 128–133. DOI: 10.29188/2222-8543-2019-11-2-128-132.
- WHO. Laboratory manual for the examination and processing of human semen. 5th ed. Geneva: WHO; 2010.
- Jain AK, Murty MN, Flynn PJ. Data clustering: a review. ACM computing surveys (CSUR). 1999; 31 (3): 264–323.
- Arthur D, Vassilvitskii S. K-means++: the advantages of careful seeding. In: Hal Gabow, editor. Proceedings of the Eighteenth Annual ACM-SIAM Symposium on Discrete Algorithms (Proceedings in Applied Mathematics) 18th ed. Society for Industrial and Applied Mathematics (3 January 2007); p. 1027–35. DOI: 10.1145/1283383.1283494.
- Rousseeuw PJ. Silhouettes: A graphical aid to the interpretation and validation of cluster analysis. J Comput Appl Math. 1987; 20: 53–65.
- Davies DL, Bouldin DW. A Cluster Separation Measure. IEEE Transactions on Pattern Analysis and Machine Intelligence. PAMI-1. 1979; 2: 224–7.
- de Goffau MC, Lager S, Salter SJ, Wagner J, Kronbichler A, Charnock-Jones DS, et al. Recognizing the reagent microbiome. Nat Microbiol. 2018; 3 (8): 851–3.
- Yang H, Zhang J, Xue Z, Zhao C, Lei L, Wen Y, et al. Potential Pathogenic Bacteria in Seminal Microbiota of Patients with Different Types of Dysspermatism. Sci Rep. 2020; 10 (1): 6876. DOI: 10.1038/s41598-020-63787-x.
- Ворошилина Е. С., Зорников Д. Л., Иванов А. В., Почерников Д. Г., Паначева Е. А. Микробиота эякулята: кластерный анализ результатов, полученных при исследовании методом ПЦР-ПВ. Вестник Российского государственного медицинского университета. 2020; 5: 66–73. DOI: 10.24075/vrgmu.2020.064.
- Ivanov IB, Kuzmin MD, Gritsenko VA. Microflora of the seminal fluid of healthy men and men suffering from chronic prostatitis syndrome. Int J Androl. 2009; 32 (5): 462–7. DOI: 10.1111/j.1365-2605.2008.00878.x.
- Почерников Д. Г., Постовойтенко Н. Т., Гетьман В. В., Галкина И. С. Диагностическая значимость выявления *Lactobacillus* spp. в эякуляте. Вестник Российского государственного медицинского университета. 2020; 3: 42–48. DOI: 10.24075/vrgmu.2020.039.
- Lipsky BA, Byren I, Hoey CT. Treatment of bacterial prostatitis. Clin Infect Dis. 2010; 50 (12): 1641–52. DOI: 10.1086/652861.

ASSESSMENT OF COVID-19 CLINICAL COURSE IN PATIENTS VACCINATED WITH SPITNIK V, SARS-COV-2 S PROTEIN RBD DOMAIN VARIATION AND SERUM VIRUS NEUTRALIZING ACTIVITY

Kolobukhina LV^{1,3}✉, Burgasova OA^{1,2,3}, Kruzhkova IS^{1,3}, Bakalin VV², Generalova LV², Shagaev AV³, Ogarkova DA¹, Nikiforova MA¹, Vasina DV¹, Gushchin VA^{1,4}, Smetanina SV³

¹ Gamaleya National Center of Epidemiology and Microbiology, Moscow, Russia

² Peoples' Friendship University of Russia, Moscow, Russia

³ Infectious Clinical Hospital № 1, Moscow, Russia

⁴ Lomonosov Moscow State University, Moscow, Russia

The COVID-19-associated mortality remains high. Studying the features of the COVID-19 course in vaccinated patients, who have got ill on different dates after vaccination, compared to unvaccinated individuals is relevant. The study was aimed to assess clinical and immunological features of the COVID-19 course, as well as to assess humoral immunity (virus neutralizing activity, VNA) and SARS-CoV-2 S protein RBD domain variation in the groups of patients, previously vaccinated with Sputnik V, and unvaccinated patients. A total of 251 patients with confirmed diagnosis of COVID-19 were enrolled, of them 116 individuals were previously vaccinated with one or two Sputnik V vaccine components, and 135 patients were not vaccinated (comparison group). Individuals over 50 years of age prevailed (82.8%). The patients, who received two vaccine components, had mild to moderate COVID-19 (92.1%). In the group of unvaccinated patients, 11 individuals received treatment in the ICU, 10 of them died. The viral load was significantly lower in vaccinated patients. Mutations of SARS-CoV-2, such as S477N, S477N+A522S, E484K and E484K+S494P, were identified both in vaccinated and unvaccinated patients. Assessment of the neutralizing activity of sera revealed no significant differences in VNA against different variants of SARS-CoV-2 mutations. The data obtained demonstrate that the lack of vaccination is an aggravating factor and is capable of increasing the risk of severe course and death in patients with COVID-19.

Keywords: vaccine, Sputnik V, vaccination, COVID-19, patients

Acknowledgments: we would like to thank Antipyat NA, Deputy Chief Physician for Medical Affairs, and Bazarova MV, PhD, Deputy Chief Physician for Sanitary and Epidemiological Issues, Infectious Clinical Hospital № 1, for the study management and support.

Author contributions: Kolobukhina LV — study proponent, design, manuscript writing, clinical research management; Burgasova OA — literature analysis, manuscript writing and editing, clinical research data processing; Kruzhkova IS — clinical observation, literature analysis, processing of the results; Bakalin VV — clinical observation, clinical and laboratory data processing; Generalova LV — clinical data processing; Shagaev AV — monitoring of infected individuals after vaccination; Ogarkova DA — statistical analysis; Nikiforova MA — coordination of virological studies, virus isolation and VNA; Vasina DV — ELISA data processing, coordination of immunological studies; Gushchin VA — study concept, molecular biological and virological research management; Smetanina SV — clinical research general management.

Compliance with ethical standards: the study was approved by the Ethics Committee of Moscow Infectious Clinical Hospital (protocol № 11/A dated November 16, 2020). The informed consent was submitted by all patients.

✉ **Correspondence should be addressed:** Ludmila V. Kolobukhina
Gamaleya St. 18, Moscow, 123098, Russia; lkolobuchina@yandex.ru

Received: 29.09.2021 **Accepted:** 13.10.2021 **Published online:** 17.10.2021

DOI: 10.24075/brsmu.2021.046

ОЦЕНКА КЛИНИЧЕСКОГО ТЕЧЕНИЯ COVID-19 У ПАЦИЕНТОВ, ВАКЦИНИРОВАННЫХ «СПУТНИК V», ИЗМЕНЧИВОСТИ RBD-ДОМЕНА S-БЕЛКА SARS-COV-2 И ВИРУСНЕЙТРАЛИЗУЮЩИХ СВОЙСТВ СЫВОРОТКИ

Л. В. Колобухина^{1,3}✉, О. А. Бургасова^{1,2,3}, И. С. Кружкова^{1,3}, В. В. Бакалин², Л. В. Генералова², А. В. Шагаев³, Д. А. Огаркова¹, М. А. Никифорова¹, Д. В. Васина¹, В. А. Гушчин^{1,4}, С. В. Сметанина³

¹ Национальный исследовательский центр эпидемиологии и микробиологии имени Н. Ф. Гамалеи, Москва, Россия

² Российский университет дружбы народов, Москва, Россия

³ Инфекционная клиническая больница № 1, Москва, Россия

⁴ Московский государственный университет имени М. В. Ломоносова, Москва, Россия

Показатель смертности от COVID-19 сохраняется достаточно высоким. Актуально изучение особенностей течения COVID-19 у вакцинированных пациентов, заболевших в разные сроки после прививки, по сравнению с невакцинированными. Целью работы было оценить клинико-иммунологические особенности течения COVID-19, проанализировать данные гуморального иммунитета (вируснейтрализующей активности, ВНА) и изменчивости RBD-домена S-белка SARS-CoV-2 в группах пациентов, ранее вакцинированных «Спутником V», и у невакцинированных. В исследование включили 251 пациента с верифицированным диагнозом COVID-19, из них 116 были ранее вакцинированы одним или двумя компонентами препарата «Спутник V» и 135 невакцинированных (группа сравнения). Преобладали лица старше 50 лет (82,8%). Пациенты, получившие оба компонента вакцины, перенесли COVID-19 в легкой и среднетяжелой форме (92,1%). В группе невакцинированных пациентов 11 человек лечили в условиях ОПИТ, 10 из них умерли. Вирусная нагрузка была достоверно ниже у вакцинированных пациентов. Мутации SARS-CoV-2, включая S477N, S477N+A522S, E484K и E484K+S494P, были выявлены у пациентов как вакцинированных, так и невакцинированных. По результатам анализа нейтрализующей активности сывороток не обнаружена достоверная разница уровня ВНА против различных вариантов мутаций SARS-CoV-2. Полученные данные свидетельствуют, что отсутствие вакцинации является отягчающим фактором и увеличивает риск тяжелого течения и смерти пациентов с COVID-19.

Ключевые слова: вакцина, «Спутник V», вакцинация, COVID-19, пациенты

Благодарности: заместителю главного врача по медицинской части ИКБ № 1 Н. А. Антипята и заместителю главного врача по санитарно-эпидемиологическим вопросам ИКБ № 1 М. В. Базаровой — за организацию и поддержку процесса исследования.

Вклад авторов: Л. В. Колобухина — инициатор исследования, дизайн, подготовка рукописи, руководство клинической частью; О. А. Бургасова — анализ источников, подготовка и правка статьи, обработка результатов клинической части; И. С. Кружкова — клинические наблюдения, анализ источников, обработка результатов; В. В. Бакалин — клинические наблюдения, обработка клинических и лабораторных данных; Л. В. Генералова — обработка клинических данных; А. В. Шагаев — мониторинг заболевших лиц после вакцинации; Д. А. Огаркова — статистический анализ; М. А. Никифорова — координация вирусологических исследований, выделение вируса и ВНА; Д. В. Васина — обработка данных ИФА, координация иммунологической части исследования; В. А. Гушчин — концепция исследования, руководство молекулярно-биологическим и вирусологическим направлениями исследований; С. В. Сметанина — общее руководство клинической частью исследования.

Соблюдение этических стандартов: исследование одобрено этическим комитетом Инфекционной клинической больницы № 1 г. Москвы (протокол № 11/A от 16 ноября 2020 г.). Все пациенты подписали добровольное информированное согласие.

✉ **Для корреспонденции:** Людмила Васильевна Колобухина
ул. Гамалеи, д. 18, г. Москва, 123098, Россия; lkolobuchina@yandex.ru

Статья получена: 29.09.2021 **Статья принята к печати:** 13.10.2021 **Опубликована онлайн:** 17.10.2021

DOI: 10.24075/vrgmu.2021.046

The COVID-19 pandemic, declared by the World Health Organization in 2020, swept across the world. In the majority of cases (80%), COVID-19 is subclinical, and the patients do not require hospitalization. Many factors associated with severe course of the disease are well understood, however, the COVID-19-associated mortality remains rather high, especially in unvaccinated individuals of the older age groups [1].

The history of medicine demonstrates that the pandemic can be stopped by successful vaccination and reaching the herd immunity threshold of at least 70–80%. Furthermore, vaccination reduces the risk of severe disease and death [2].

To date, credible levels of protection against the infection (over 90%) and severe course have been achieved for all the vaccines against COVID-19 [3]. In the countries, being the leaders of the universal immunization programme, a downward trend in morbidity and mortality is observed [4]. Official statistics indicates the decrease in COVID-19-associated morbidity and mortality in the countries, being the leaders in terms of vaccination coverage (50 vaccine doses per 100 individuals), such as Israel, United Arab Emirates, USA and United Kingdom [5].

The results of assessing the vaccine efficacy within the framework of post-registration trials confirm the results of clinical trials on vaccine safety and efficacy [6, 7].

Sputnik V vaccine, providing high neutralizing antibody titers and substantial cellular immune response, has been developed, tested and put into practice in the Russian Federation (RF) [8]. The vaccine mechanism of action is based on the use of two adenovirus serotype Ad26 and Ad5 vectors, which are unable to replicate in the human body, but are capable of delivering the gene, encoding the SARS-CoV-2 S glycoprotein. According to the results of the phase III clinical trials conducted in Russia, Sputnik V vaccine efficacy was 91.6% [3]. However, clinical practice in many countries around the world confirm the risk of COVID-19 infection even after vaccination with two vaccine components [9]. The importance of this issue and the need for monitoring the COVID-19 cases in the population of vaccinated individuals emphasize the existence of the SARS-CoV-2 virus mutations, their potential clinical significance, and the risk of emerging new strains, which could potentially evade the immune response.

The study was aimed to assess the features of the COVID-19 clinical course in the groups of patients, previously vaccinated with Sputnik V, compared to unvaccinated patients.

METHODS

Patients

A total of 251 patients with confirmed novel coronavirus infection were enrolled. Inclusion criteria: RNA of SARS-CoV-2, detected by PCR. Exclusion criteria: no SARS-CoV-2 RNA in biological material.

In order to assess the features of COVID-19 clinical course in patients, previously vaccinated with Sputnik V, the patients who were staying in the Infectious Clinical Hospital No. 1 were December 2020 to April 2021 were randomized into two groups ($n = 251$). Of them 116 patients were admitted to hospital on various dates after vaccination with Sputnik V; the comparison group was represented by 135 unvaccinated patients. The disease severity was assessed using the NEWS scale [10] on the day of admission and on the day of enrollment (bed-days).

The group of vaccinated patients was divided into three subgroups based on the dates of vaccine component administration and the date of the disease onset. A total of 46 individuals, who got ill on days 1–7 after the first vaccine

component administration, were included in the first subgroup; the second subgroup included 32 patients, who got ill on days 8–14 after the first vaccine component administration. The third subgroup included 38 patients, who got ill on days 1–132 after administration of two Sputnik V vaccine components. There were 121 males (48.3%) and 130 females (51.7%) (Table 1). Persons over the age of 50 prevailed (82.8%; $n = 208$), individuals aged 30–50 accounted for 17.1% ($n = 43$) of patients.

The algorithm for etiological confirmation of COVID-19 involved testing the nasal swab for SARS-CoV-2 RNA by PCR, assessing blood serum to detect the antibodies against SARS-CoV-2 by ELISA, and identifying the protective antibodies by neutralization assay.

Viral load determination method

Nasopharyngeal swab samples were assessed using the reagent kit for SARS-CoV-2 coronavirus RNA extraction and qualitative analysis by RT-PCR, SARS-CoV-2 FRT (Gamaleya National Center of Epidemiology and Microbiology; Russia). Laboratory differential diagnosis of COVID-19 and other respiratory infections was performed by RT-PCR.

The relative quantities of SARS-CoV-2 RNA were defined using the calibration line, plotted for each analysis by the calibration standards testing. The latter were represented by recombinant constructs, containing the known concentration of the SARS-CoV-2 genome fragment to be amplified. Since the relative quantities of the fragments were compared, no RNA fragments were used. The step of reverse transcription was controlled by PCR passage through the internal control RNA provided by the system.

RNA/DNA of influenza viruses and viruses, causing ARVI, were identified using the AmpliSens Influenza viruses A/B, AmpliSens Influenza virus A/H1-swine-FL, AmpliSens Influenza virus A-type-FL, AmpliSens ARVI-screen-FL reagent kits (Central Research Institute of Epidemiology; Russia) in accordance with the manufacturer's guidelines using the PCR systems, working in the real-time mode: Rotor Gene 6000 (Corbett Research; Australia) and DT-96 (DNA-Technology; Russia).

Quantification of IgG against SARS-CoV-2 RBD

The recombinant RBD antigen No. 8COV1 (HyTest; Russia) was used for assessment of IgG antibodies against the SARS-CoV-2 spike protein S1 receptor-binding domain (RBD). We added 100 μ L of RBD in phosphate buffered saline PBS (Amresco; USA) with a concentration of 1 μ g/mL to each well of the 96-well ELISA microplate Costar High Binding (Corning; USA) and subsequently incubated the microplates for 24 hours at +4 $^{\circ}$ C. On the next day we removed the antigen solution and blocked the microplates overnight at +4 $^{\circ}$ C by incubation with the blocking buffer S002X (Xema; Russia), containing 0.5% casein.

The studied sera were diluted 1 : 100 with the ELISA buffer S011 (Xema; Russia), 100 μ L were added to each well and incubated for 1 h in the thermo-shaker at a temperature of +37 $^{\circ}$ C in the 600 rpm mixing mode. Then the microplates were washed three times with PBS, containing 0.1% Tween 20, and 100 μ L of the goat anti-human IgG horseradish peroxidase-conjugated antibody (Novex; USA) diluted at a ratio of 1 : 40,000 were added to each well. After an hour of incubation at a temperature of +37 $^{\circ}$ C and mixing in the 600 rpm mode, the microplates were washed six times. We added 100 μ L of

Table 1. General characteristics of patients

Parameters	Total number of patients $n = 251$				
	Unvaccinated $n = 135$	Vaccinated			
		Subgroup 1 $n = 46$	Subgroup 2 $n = 32$	Subgroup 3 $n = 38$	
		Dates of disease onset after vaccination			
	1–7 days after V1	8–14 days after V1	1–132 days after V1+V2		
Males	61 (45.20%)	29 (63.0%)	10 (31.3%)	21 (55.3%)	0.039* (Pearson's χ^2 test)
Females	74 (54.80%)	17 (37.0%)	22 (68.8%)	17 (44.7%)	
Male to female ratio	01 : 01.0	01 : 01.0	01 : 02.0	01 : 01.0	
Average age (years) $M \pm SE$ (min–max)	64.9 \pm 1.2 (30–89)	64.5 \pm 2.1 (31–84)	68.9 \pm 2.1 (46–89)	67.7 \pm 1.9 (37–90)	0.335 (Pearson's F-test)
Age, years 30–50	28 (20.7%)	8 (17.4%)	3 (9.4%)	4 (10.5%)	0.656 (Pearson's χ^2 test)
51–70	54 (40.00%)	20 (43.5%)	16 (50.0%)	19 (50.0%)	
71–90	53 (39.30%)	18 (39.1%)	13 (40.6%)	15 (39.5%)	
Dates of admission to hospital, days $M \pm SE$ (min–max). Me [Q ₁ –Q ₃]	6.22 \pm 0.20 (1–13) 6 [5–8]	7.5 \pm 0.5 (2–19) 7.5 [4–9]	6.5 \pm 0.4 (2–13) 6.5 [5–8]	8.3 \pm 0.8 (1–28) 7 [6–10]	0.014* (Mann–Whitney U Test)
Disease severity evaluation upon admission to hospital					
Mild	52 (38.50%)	17 (36.90%)	13 (40.60%)	19 (50.0%)	0.498 (Pearson's χ^2 test)
Moderate	35 (30.00%)	16 (34.8%)	9 (28.10%)	9 (23.70%)	
		34 (29.3%)			
Severe	48 (35.50%)	13 (28.3%)	10 (31.30%)	10 (26.3%)	
		33 (28.4%)			
Of them transferred to ICU	11	2	2	0	
Deaths in ICU	10	2	0	0	
Length of hospital stay (days) depending on severity: $M \pm SE$ (min–max). Me [Q ₁ –Q ₃]	11.12 \pm 0.6 (4–52) 10 [7–13]	10.35 \pm 0.8 (4–36) 8 [7–12]	9.0 \pm 1.5 (2–53) 8 [6.5–9]	8.03 \pm 0.4 (4–14) 8 [7–9]	< 0.001* (Mann–Whitney U Test)
		9.22 \pm 0.5 (2–53) 8 [7–9.5]			

Note: * — significant differences between groups ($p < 0.05$).

the single-component TMB containing substrate buffer R055 (Xema; Russia) to each well, incubated for 10 minutes at room temperature, and terminated the reaction by adding 100 μ L of 10% HCl per well. Absorbance was measured at a wavelength of 450 nm. When recording the results, the cutoff absorbance value was defined (the sum of the negative control mean absorbance and the experimentally determined coefficient), then the positivity rate was calculated for each sample, being the ratio of sample absorbance to cutoff absorbance value.

The results were interpreted based on the following criteria: the test for IgG antibodies was considered positive with the studied sample positivity rate ≥ 1.1 , and negative with the positivity rate < 0.9 . The results of the test for IgG antibodies were considered inconclusive with $0.9 \leq$ positivity rate < 1.1 . For these values, the laboratory system was validated using the reference sera. The previously characterized sera of

convalescent subjects with confirmed diagnosis were used as a positive control, and the archived sera, collected in the first half of 2019, from the collection of deliberately negative sera were used as a negative control.

Cells and viruses

The VERO E6 cells (ATCC, CRL-1586) were cultured in complete DMEM medium (PanEco; Russia), supplemented with 10% FBS (HyClone; USA), 1 \times GlutaMAX (Gibco; USA) and penicillin/streptomycin (100 IU/mL; 100 μ g/mL) (PanEco; Russia). SARS-CoV-2 strains PMVL-4 (GISAID EPI_ISL_470898), PMVL-38 (GISAID EPI_ISL_1710856), PMVL-47 (GISAID EPI_ISL_1710865) were isolated from nasopharyngeal swabs. PMVL-38 and PMVL-47 carry mutations in the RBD domain (S477N and E484K respectively).

Table 2. Assessment of dynamic changes in COVID-19 course severity in vaccinated and unvaccinated patients

Checkpoints for severity assessment (bed-days)	Patients (n = 57)						p
	Vaccinated n = 22			Unvaccinated n = 35			
	Disease severity evaluation (NEWS)						
	Mild	Moderate	Severe	Mild	Moderate	Severe	
Upon admission to hospital (checkpoint 1)	10 (45.5%)	7 -31.80%	5 -22.70%	13 (37.1%)	10 (28.6%)	12 (34.3%)	0.699 (Fischer's exact test)
Average bed-days 3.5 ± 1.2 (1-7 days) (checkpoint 2)	15 (68.2%)	5 -22.70%	2 -9.10%	15 (42.8%)	14 (40.0%)	6 -17.20%	0.184 (Fischer's exact test)
Average bed-days 9.2 ± 1.4 (8-12 days) (checkpoint 3)	22 (100%)	0	0	22 (62.8%)	5 (14.3%)	8 -22.90%	0.002* (Fischer's exact test)
	All patients were discharged by day 12 of hospital stay						

Assessment of the patients' sera virus neutralization activity

The VERO E6 cells were seeded in the 96-well plate, 0.2×10^5 cells per well, one day before the experiment. The following day 100 TCID₅₀ of the corresponding SARS-CoV-2 variant were incubated with serial dilutions of sera for one hour at + 37 °C, and subsequently added to the 96-well plates with the Vero E6 cells. After 72 h the virus-induced cytopathic effect (CPE)

was assessed by MTT assay [11]. The percentage of inhibition of CPE was normalized and converted into percentage of neutralization. NT₅₀ was calculated with the GraphPad Prism 7 software (GraphPad Software; USA).

Assessment of the virus variation in the RBD region

Total RNA was extracted from the patients' swabs and/or SARS-CoV-2 isolates using the RIBO-prep kit (Central

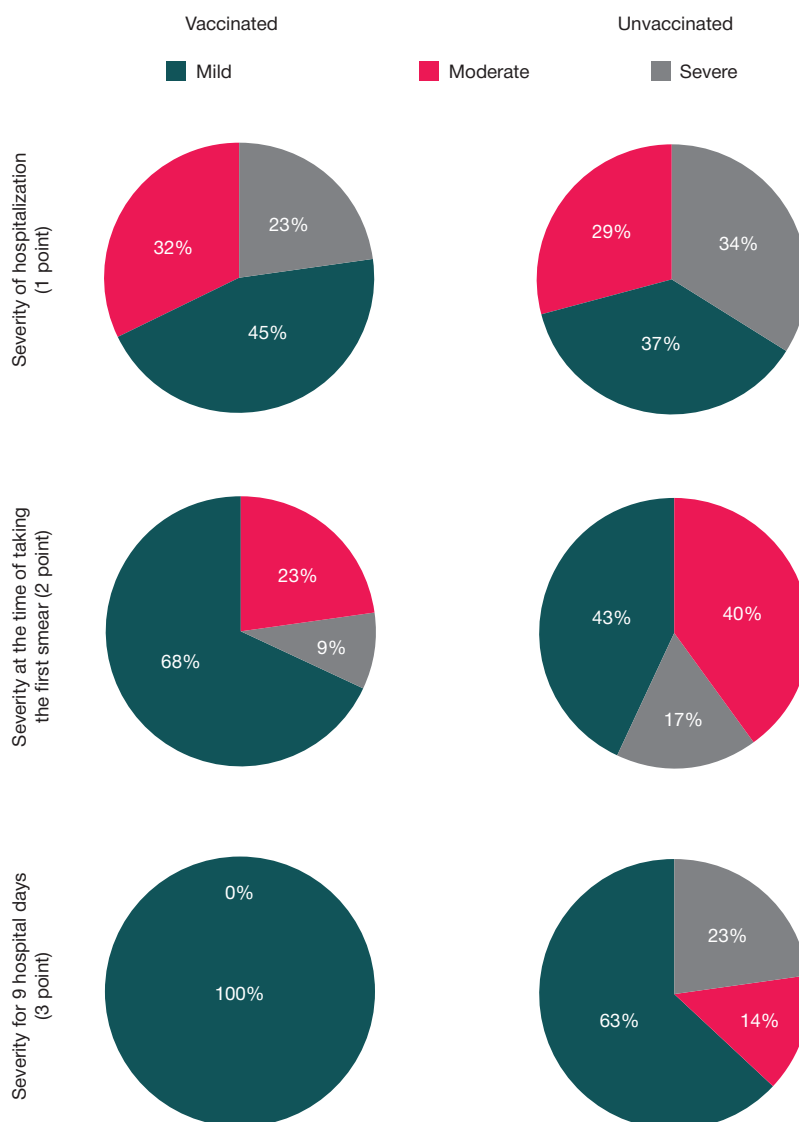


Fig. 1. Patients' distribution based on the disease severity for the assessed checkpoints (bed-days)

Table 3. Viral load in vaccinated and unvaccinated patients

Viral load, Ct			
Groups of patients	N	Me [Q ₁ –Q ₃]	<i>p</i>
Unvaccinated	34	31,45 [27,20–33,72]	0.026* (Mann–Whitney U test)
Fully vaccinated	8	34,78 [31,41–36,48]	

Note: * — significant differences for the sample (vaccinated $n = 22$, unvaccinated $n = 35$) ($p < 0.05$).

Research Institute of Epidemiology; Russia) in accordance with the manufacturer's instructions. Amplification was performed by the one-step RT-PCR method with the use of the reaction mixture, containing (per one reaction) 10 pmol of each primer, 0.025 mM of each dNTP (Evrogen; Russia), 5 μ L of 5X buffer (100 mM Tris-HCl (pH 8.3 at 25 °C), 150 mM KCl, 10 mM MgCl₂, 8 mM DTT), 0.25 μ L of M-MLV reverse transcriptase (200 U), 0.25 μ L of intrinsic Taq polymerase (10 U) and 10 μ L of RNA (about 0.5 μ g). The total volume of one reaction mixture was 25 μ L. The following oligonucleotides were selected for amplification of the SARS-CoV-2 fragment: upstream primer 5'-AACTTTAGAGTCCAACCAACAGAA-3' and downstream primer 5'-TGAAGTTGAAATTGACACATTTG-3'. Oligonucleotides make it possible to obtain the fragment of spike glycoprotein, beginning at amino acid 334 and ending at amino acid 538. Amplification was performed in the T100TM Thermal Cycler (Bio-Rad; USA). The protocol for one-step RT-PCR was as follows: 50 °C for 60 min, 95 °C for 5 min, then 35 cycles at 95 °C for 15 s, 55 °C for 10 s, and 72 °C for 30 s, then 72 °C for 5 min. After amplification some of the product was applied to agarose gel, and the target fragment was detected by electrophoresis. Then the amplified products were purified to remove primers and nucleotides using the ExoSAP-IT™ PCR Product Cleanup Reagent (Thermo Fisher Scientific; USA), and the concentration was measured with the Qubit Fluorometer (Thermo Fisher Scientific; USA) in accordance with the manufacturer's instructions. Sequencing of the fragments obtained was performed with the Applied Biosystems 3500 genetic analyzer (Thermo Fisher Scientific; USA). The obtained sequences structure was analyzed using the Unipro UGENE v37.0 software.

Statistical methods

Statistical processing and plotting the curves were performed with the IBM SPSS Statistics software, version 26. Distributions were tested for normality using the Shapiro–Wilk test (when $n < 50$) or Lilliefors corrected Kolmogorov–Smirnov test (when $n > 50$). The significance level was defined as $p = 0.05$. For distributions other than normal, the intergroup comparisons were performed with the Kruskal–Wallis test with subsequent post hoc analysis using the Mann–Whitney U Test with Bonferroni correction for multiple comparisons or using the Mann–Whitney U Test (for a number of groups $n = 2$). Analysis of contingency tables was carried out using the chi-squared (χ^2) test or Fisher's exact test. When performing the analysis of multi-field tables, a posteriori pairwise comparisons were performed, and the multiplicity problem was solved using the Benjamini–Hochberg procedure. The impact of vaccination and

the existence of mutations on the viral load was assessed by multivariate ANOVA.

RESULTS

Comparative analysis of the vaccinated and unvaccinated groups' age structure revealed no significant differences in age ($p = 0.656$). There were also no differences in the average age between groups ($p = 0.335$ (Pearson's chi-squared test)).

No significant differences in the rates of comorbidity between vaccinated and unvaccinated patients with COVID-19 were revealed: arterial hypertension — 79.0 and 72.4%, cardiovascular diseases — 43.0 and 26.7%, diabetes mellitus — 27.0 and 16.4%, obesity — 47.4 and 39.6% respectively.

All the patients enrolled ($n = 251$) were hospitalized on days 1–28 after the symptom onset. There were significant differences in admission dates after the disease onset between vaccinated and unvaccinated patients: the patients, who had received at least one vaccine dose, were hospitalized significantly later ($p = 0.014$). The median time between disease onset and hospitalization was 7.5 days in vaccinated and 6 days in unvaccinated patients.

To perform clinical characterization of COVID-19, all patients ($n = 251$) were divided based on the disease severity on the day of admission as follows: in the vaccinated group ($n = 116$), 49 (42.2 %) patients had mild, 34 (29.3%) had moderate, and 33 (26.5%) had severe disease; in the unvaccinated group ($n = 135$), 52 (38.5%) patients had mild, 35 (30.0%) had moderate, and 48 (35.5%) had severe disease. It should be emphasized that there were no significant differences in the number of patients with different disease severity within each group both in the unvaccinated group and in individuals, who had received at least one vaccine component ($p = 0.498$).

During treatment, the trend towards worsening was recognized in 2 (4.5%) vaccinated patients: both patients of the 1st subgroup were transferred to ICU, and died on days 17 and 36 of hospital stay. It is important that both patients got ill during the first week (days 1 and 7) after administration of the first vaccine component, and couldn't have any protective antibodies. Two patients (6.3%) of the 2nd subgroup also needed intensive care management. They were provided noninvasive respiratory support. One of these patients had lymphogranulomatosis, he was transferred to the other hospital on day 10 of hospital stay with the large right gluteal hematoma spreading onto the inguinal region and pelvic retroperitoneal space, posthemorrhagic anemia. The other patient had hypertension in combination with obesity, he stayed in ICU for 32 days and was discharged from the hospital on day 56. Both patients had not received the second vaccine component.

Table 4. Comparison of anti-RBD antibody levels in vaccinated and unvaccinated patients

Groups of patients	<i>n</i>	positivity rate RBD	<i>p</i>
		Me [Q ₁ –Q ₃]	
Unvaccinated	17	0,34 [0,22–0,48]	< 0.001* (Mann–Whitney U test)
Fully vaccinated	22	7,75 [2,30–10,80]	

Note: * — significant differences ($p < 0.05$).

Table 5. RBD domain mutation rate in the groups being compared

Groups of patients	No mutations in RBD domain (<i>n</i> = 9)	Mutations in RBD domain (<i>n</i> = 10)
Unvaccinated (<i>n</i> = 11)	8 (72.7%)	3 (27.3%)
Vaccinated (<i>n</i> = 8)	1 (12.5%)	7 (87.5%)

Note: * — *p* = 0.020 (Fisher's exact test).

No deaths were observed in the 2nd and 3rd subgroups of vaccinated patients; in the unvaccinated group, 11 individuals needed intensive care management, 10 of them died.

The median length of hospital stay was 8 days in vaccinated patients (including those, who received single vaccine component), and 10 days in unvaccinated patients (*p* < 0.001).

In addition, to evaluate the dynamic changes throughout the clinical course of the disease, the disease severity was assessed on days 1–7 and 8–12 of hospital stay in patients, who had received both vaccine components (*n* = 22) and got ill after 14 days, compared to the group of unvaccinated patients (*n* = 35), who got ill within the same period (Table 2; Fig. 1).

Thus, it has been shown that based on the Fisher's exact test there were no significant differences in the number of patients with different disease severity in the vaccinated and unvaccinated groups upon admission to hospital (checkpoint 1) (*p* = 0.699). During the first week of hospital stay (checkpoint 1, days 1–7 of hospital stay) no significant differences were revealed as well (*p* = 0.184). However, assessment of checkpoint 3 (days 8–12 of hospital stay) showed that 100% of vaccinated patients had a mild disease; the proportion of patients with a mild disease in the unvaccinated group was significantly lower (63%, *p* = 0.002) (see Fig. 1). Comparative analysis of checkpoints in the studied groups based on the disease severity (with the use of Friedman test for related samples) showed that there was a significant decrease (*p* < 0.001) in the disease severity in the vaccinated group; in the unvaccinated group this trend was of borderline significance (*p* = 0.058).

The further research tactics was defined by the search for the disease severity criteria taking into account the RBD domain mutations, viral load levels and humoral immune response in the patients.

The viral load in the vaccinated and unvaccinated groups was low, however, significant viral load was lower in the group of vaccinated patients (*p* < 0.05) (Table 3).

Assessment of the humoral immune response in the studied groups showed that the IgG antibody levels were significantly

(*p* < 0.001) higher in the vaccinated group compared to unvaccinated group (Table 4). Further research is needed to evaluate the duration of the protective immune response.

The spread of the virus involves introduction into the human population, high host mortality, and the ability of the virus to mutate in order to survive in biological environment.

Identification of the SARS-COV-2 RBD domain mutations in biological samples, obtained from the patients (*n* = 19), showed that the virus mutated in RBD region both in the vaccinated and unvaccinated groups, however, mutations occurred more frequently in the vaccinated group (Table 5; Fig. 2). The presence of mutations demonstrates the need for monitoring the disease clinical features in vaccinated patients and sequencing the virus in order to upgrade the specific preventive measures in a rapid and timely manner.

Viral load testing showed that vaccination reduced viral load in the infected individuals. It has been found that in case of the disease development, the downward trend in viral load in the samples containing the virus, carrying mutations in the RBD domain, was observed both in vaccinated and unvaccinated patients. Multivariate ANOVA revealed a significant correlation between the viral load and the fact of being vaccinated/unvaccinated (*p* < 0.001), the variance contribution was 39.0%. Correlation with the presence of mutations also appeared to be significant (*p* = 0.038), the variance contribution was 8.0%. The relationship between vaccination and the presence of mutations was not significant (*p* = 0.650) (Fig. 3).

Differential assessment of virus neutralization activity (VNA) in sera of the patients, vaccinated with two doses of vaccine, although infected with COVID-19, was performed in order to investigate the possible mechanisms of the new virus variants evading protective antibodies in vaccinated individuals. Since there were RBD domain mutations in the majority of samples (*n* = 6), including S477N, S477N+A522S, E484K and E484K+S494P, VNA was assessed in all the samples provided in relation to the original variant of the virus, containing D614G substitution, and two variants with mutations S477N and E484K, available from our collection of viral isolates.

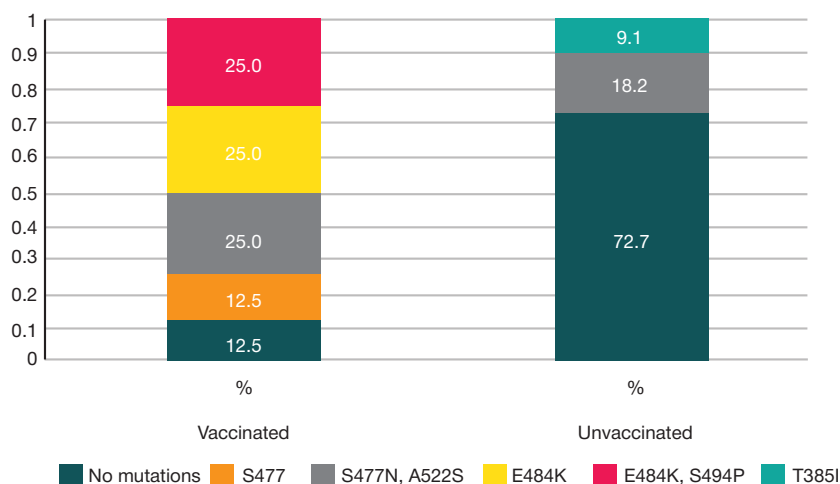


Fig. 2. Distribution of mutations in the RBD domain of SARS-CoV-2 viruses

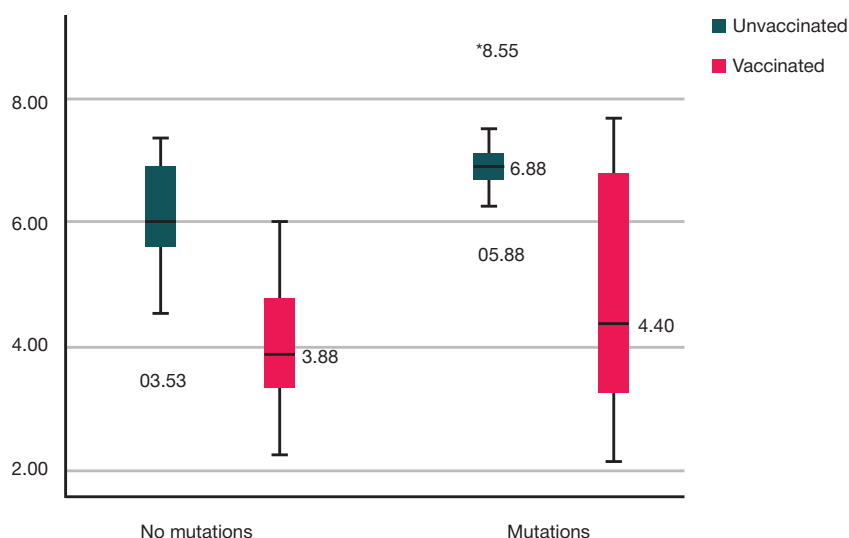


Fig. 3. Comparative assessment of viral load in biological samples of vaccinated and unvaccinated patients, carrying mutations in the RBD domain

Table 6 presents the VNA levels against different variants of SARS-CoV-2 virus mutations in the samples, obtained from the patients ($n = 6$). The neutralizing titers (NT₅₀) were calculated using the GraphPad Prism 7 software.

Then the comparative assessment of the VNA levels against different variants of SARS-CoV-2 virus mutations was performed. Fig. 4 (upper row) demonstrates p-values with 95% confidence interval (Wilcoxon test).

No significant differences in VNA of sera with different SARS-CoV-2 variants were revealed both when assessing all sera and when assessing single sera, obtained from the patients carrying characteristic mutations.

DISCUSSION

The results obtained show that, like any other immunobiological preparation, Sputnik V vaccine, developed and successfully used in healthcare practice as a preventive medicine, is not 100% effective, especially during the ongoing pandemic. However, the use of vaccines in such an extraordinary situation would enable to reduce both the number of patients with severe disease and the number of deaths.

Currently, Sputnik V is successfully used in more than 67 countries around the world [12]. A total of 39,589,464 people (27.11%) have been fully vaccinated in the Russian Federation before September 11, 2021 [13].

Consequently, studying the factors, which result in COVID-19 infection in vaccinated individuals, as well as monitoring the clinical course of the disease would provide practical healthcare and society in general with additional information on vaccination.

In this study we tried to assess the clinical and laboratory parameters in patients, vaccinated with Sputnik V, on various dates after administration of the first and second doses of vaccine compared with the group of unvaccinated patients.

Assessment of dynamic changes in COVID-19 severity in fully vaccinated individuals, who had got ill 14 days after administration of the second component, and unvaccinated patients, who had got ill within the same time period, showed that 100% of vaccinated patients had mild disease on days 8–12 of hospital stay. There were no cases of transfer to ICU or deaths in the group of fully vaccinated individuals, possessing protective immunity against SARS-CoV-2.

In addition to the clinical course severity assessment, testing by RT-PCR and real-time RT-PCR, viral RNA RBD region sequencing, differential monitoring of neutralizing antibody titers, and evaluation of IgG-response towards the S protein RBD domain were performed.

The viral load levels in the studied groups were diverse. As could be expected, the viral load in fully vaccinated patients (who had got ill 14 days after administration of the second vaccine component) was significantly ($p = 0.026$) lower compared to unvaccinated group. Reduced viral load in the group of individuals, vaccinated with Sputnik V, makes this group less contagious with high probability.

The significant level of anti-RBD IgG antibodies in the group of fully vaccinated patients exceeded the values, obtained in the unvaccinated group ($p < 0.001$). The results obtained showed that full-fledged specific immune response was formed within two weeks after administration of the booster Sputnik V vaccine dose.

IgG antibody levels (positivity rate 4.72 [1.47–9.88]) in the subgroups of incompletely vaccinated individuals were rather low, which could partly explain COVID-19 infection

Table 6. Levels of virus neutralizing antibodies (VNA) against the variants of SARS-CoV-2 mutations

№	Sample name	NT ₅₀		
		PMVL-4_D614G	PMVL-38_S477N	PMVL-47_E484K
1	3222_S477N	373.8	452.6	451.9
2	4003_S477N, A522S	186.7	293.5	153.2
3	4310_E484K,S494P	452.3	452.6	451.6
4	573_E484K,S494P	256.2	202.5	452.6
5	4267_E484K	226.5	> 640	> 640
6	4160_E484K	65.52	29.26	320

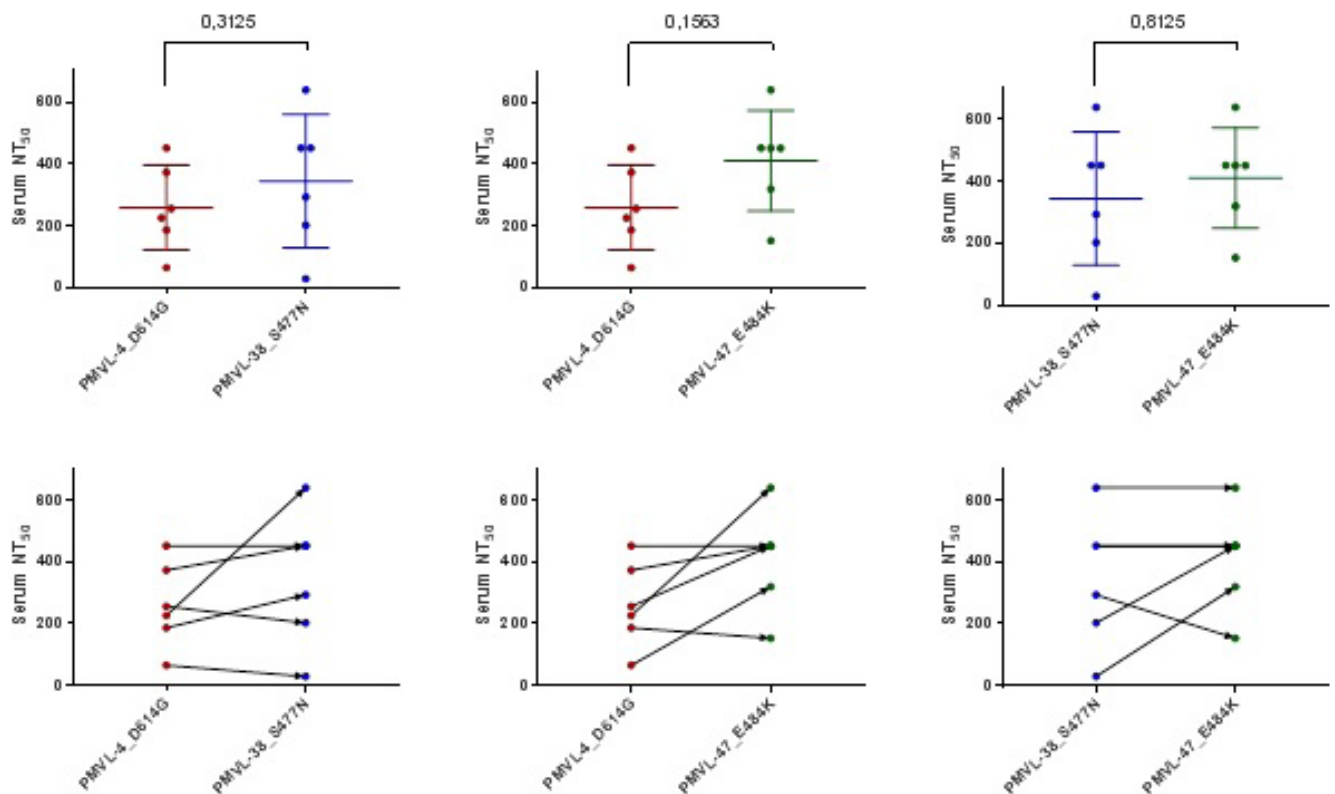


Fig. 4. Comparative assessment of the titers of neutralizing antibodies against different SARS-CoV-2 variants. * — upper row is represented by p -values with 95% confidence interval (Wilcoxon test)

in the enrolled vaccinated patients. Furthermore, a number of researchers point out that a significant proportion of people demonstrates insufficient specific response to infection, which is probably due to insufficient B cell maturation [14].

Assessment of the virus mutations in RBD region, performed in the limited number of biological samples, showed that mutations in RBD domain occurred both in vaccinated and unvaccinated patients. Mutations were more frequent in the vaccinated group. However, it should be recalled that vaccination itself has no effect on mutations or mutation rate, which provides the basis for preventive vaccination.

Experimental design showed no apparent differences in VNA of antibodies in the studied patients. No significant differences in VNA of sera with different SARS-CoV-2 variants were revealed both when assessing all sera and when assessing single sera, obtained from the patients carrying characteristic mutations. It is worth noting that the average VNA against the viruses carrying mutations was a little higher compared to VNA against the wild-type virus. However, a significant decline in the neutralizing activity of antibodies and sera against the chimeric SARS-CoV-2 strains or isogenic variants containing mutations [15].

Research findings point to protective properties of Sputnik V. The fully vaccinated individuals are at lower risk of COVID-19 infection compared to unvaccinated individuals, especially in the context of the ongoing pandemic. The data on the vaccine assessment, obtained by foreign researches, are in line with our data [2].

A major limitation of this study is the small sample of fully vaccinated patients, not allowing to assess fully the impact of rare virus mutations on the clinical course of the disease. It is unclear to what extent the new variants of the virus mutations can differentially lead to infection in vaccinated individuals compared to unvaccinated individuals within the same population. This study involves observation during the specific time period in the Moscow Region, which is characterized by the presence of specific regional mutations in strains.

CONCLUSIONS

The patients vaccinated with two components of Sputnik V vaccine, who had got ill, had a mild disease (100%), they were discharged from the hospital on days 8–12 of hospital stay. There were no deaths in the group of fully vaccinated patients. The viral load in fully vaccinated patients was significantly lowered compared to the unvaccinated group. Mutations within the RBD domain were observed in the groups of both vaccinated and unvaccinated patients. Significant levels of anti-RBD IgG antibodies were observed in the group of vaccinated individuals compared to unvaccinated individuals. Duration of the pandemic, mutations of the virus, altered structure of circulating strains, assessment of clinical features in vaccinated and infected individuals require a more detailed and objective analysis.

References

1. Kolobukhina LV, Burgasova OA, Kraeva LA, Gushchin VA, Burtseva EI, Kruzhkova IS, et al. Clinical and laboratory profile of patients with COVID-19 hospitalized in an infectious hospital in Moscow in the period from May to July 2020. Infectious diseases. 2021; 19 (2): 5–15. Russian.
2. Rzymiski P, Pazgan-Simon M, Krzysztof Simon T, Zarębska-Michaluk D, Szczepańska B, et al. Clinical Characteristics of Hospitalized COVID-19 Patients Who Received at Least One

- Dose of COVID-19 Vaccine. 2021; 9 (7): 78. Available from: <https://www.mdpi.com/2076-393X/9/7/781>.
3. Logunov DY, Dolzhikova IV, Shcheblyakov DV, Tukhvatullin AI, Zubkova OV, Dzharullaeva AS, et al. Safety and efficacy of an RAD26 and RAD5 vector-based heterologous prime-boost COVID-19 vaccine: an interim analysis of a randomised controlled phase 3 trial in Russia. *The Lancet*. 2021; 397 (10275): 671.
 4. Statistics and Research Coronavirus (COVID-19) Vaccinations. Available from: <https://ourworldindata.org/covid-vaccinations>.
 5. Dong E, Du H, Gardner L. An interactive web-based dashboard to track COVID-19 in real time. *Lancet Infect Dis*. 2020; 20 (5): 533–4. DOI: 10.1016/S1473-3099(20)30120-1. Erratum in: *Lancet Infect Dis*. 2020 Sep; 20 (9): e215.
 6. Haas EJ, Angulo FJ, McLaughlin JM, Anis E, Singer SR, Khan F, et al. Impact and effectiveness of mRNA BNT162b2 vaccine against SARS-CoV-2 infections and COVID-19 cases, hospitalisations, and deaths following a nationwide vaccination campaign in Israel: an observational study using national surveillance data. *Lancet*. 2021; 397 (10287): 1819–829. DOI: 10.1016/S0140-6736(21)00947-8.
 7. Hodick G, Tene L, Rotem RS, Patalon T, Gazit S, Ben-Tov A, et al. The effectiveness of the TWO-DOSE BNT162b2 vaccine: analysis of real-world data. *Clin Infect Dis*. 2021; ciab438. DOI: 10.1093/cid/ciab438. Epub ahead of print. PMID: 33999127.
 8. Logunov DY, Dolzhikova IV, Zubkova OV, Tukhvatullin AI, Shcheblyakov DV, Dzharullaeva AS, et al. Safety and immunogenicity of an rAd26 and rAd5 vector-based heterologous prime-boost COVID-19 vaccine in two formulations: two open, non-randomised phase 1/2 studies from Russia. *The Lancet*. 2020; 396 (10255): 887–97.
 9. Keehner J, et al. SARS-CoV-2 Infection after Vaccination in Health Care Workers in California. *N Engl J Med*. 2021; 384: 1774–5. DOI: 10.1056/NEJMc2101927.
 10. NEWS (or NEWS2) score when assessing possible COVID-19 patients in primary care. Available from: <https://www.cebm.net/covid-19/should-we-use-the-news-or-news2-score-when-assessing-patients-with-possible-covid-19-in-primary-care/>.
 11. Amanat F, White KM, Miorin L, Strohmaier S, McMahon M, Meade P, et al. An In Vitro Microneutralization Assay for SARS-CoV-2 Serology and Drug Screening. *Curr Protoc Microbiol*. 2020; 58 (1): e108. DOI: 10.1002/cpmc.108.
 12. V kakih stranah vakcina "Sputnik V" odobrena k primenjeniju. Dostupno po sсылке: <https://sputnik-meedia.ee/infographics/20210607/573214/V-kakikh-stranakh-vaktsina-Sputnik-V-odobrena-k-primenjeniyu.html>. Russian.
 13. Statistika vakcinacii ot koronavirusa (COVID-19) v Rossii. Dostupno po sсылке: <https://index.minfin.com.ua/reference/coronavirus/vaccination/russia/>. Russian.
 14. Schmidt F, Weisblum Y, Muecksch F, et al. Measuring SARS-CoV-2 neutralizing antibody activity using pseudotyped and chimeric viruses. *J Exp Med*. 2020; 217 (11): e20201181–e20201181.
 15. Diamond M, Chen R, Xie X, Case J, Zhang X, VanBlargan L, et al. SARS-CoV-2 variants show resistance to neutralization by many monoclonal and serum-derived polyclonal antibodies. *Res Sq*. 2021; 3: 228079. DOI: 10.21203/rs.3.rs-228079/v1. Preprint.

Литература

1. Колобухина Л. В., Бургасова О. А., Краева Л.А., Гуцин В. А., Бурцева Е. И., Кружкова И. С. и др. Клинико-лабораторный профиль пациентов с COVID-19, госпитализированных в инфекционный стационар г. Москвы в период с мая по июль 2020 года. *Инфекционные болезни*. 2021; 19 (2): 5–15.
2. Rzymiski P, Pazgan-Simon M, Krzysztof Simon T, Zarębska-Michaluk D, Szczepańska B, et al. Clinical Characteristics of Hospitalized COVID-19 Patients Who Received at Least One Dose of COVID-19 Vaccine. 2021; 9 (7): 78. Available from: <https://www.mdpi.com/2076-393X/9/7/781>.
3. Logunov DY, Dolzhikova IV, Shcheblyakov DV, Tukhvatullin AI, Zubkova OV, Dzharullaeva AS, et al. Safety and efficacy of an RAD26 and RAD5 vector-based heterologous prime-boost COVID-19 vaccine: an interim analysis of a randomised controlled phase 3 trial in Russia. *The Lancet*. 2021; 397 (10275): 671.
4. Statistics and Research Coronavirus (COVID-19) Vaccinations. Available from: <https://ourworldindata.org/covid-vaccinations>.
5. Dong E, Du H, Gardner L. An interactive web-based dashboard to track COVID-19 in real time. *Lancet Infect Dis*. 2020; 20 (5): 533–4. DOI: 10.1016/S1473-3099(20)30120-1. Erratum in: *Lancet Infect Dis*. 2020 Sep; 20 (9): e215.
6. Haas EJ, Angulo FJ, McLaughlin JM, Anis E, Singer SR, Khan F, et al. Impact and effectiveness of mRNA BNT162b2 vaccine against SARS-CoV-2 infections and COVID-19 cases, hospitalisations, and deaths following a nationwide vaccination campaign in Israel: an observational study using national surveillance data. *Lancet*. 2021; 397 (10287): 1819–829. DOI: 10.1016/S0140-6736(21)00947-8.
7. Hodick G, Tene L, Rotem RS, Patalon T, Gazit S, Ben-Tov A, et al. The effectiveness of the TWO-DOSE BNT162b2 vaccine: analysis of real-world data. *Clin Infect Dis*. 2021; ciab438. DOI: 10.1093/cid/ciab438. Epub ahead of print. PMID: 33999127.
8. Logunov DY, Dolzhikova IV, Zubkova OV, Tukhvatullin AI, Shcheblyakov DV, Dzharullaeva AS, et al. Safety and immunogenicity of an rAd26 and rAd5 vector-based heterologous prime-boost COVID-19 vaccine in two formulations: two open, non-randomised phase 1/2 studies from Russia. *The Lancet*. 2020; 396 (10255): 887–97.
9. Keehner J, et al. SARS-CoV-2 Infection after Vaccination in Health Care Workers in California. *N Engl J Med*. 2021; 384: 1774–5. DOI: 10.1056/NEJMc2101927.
10. NEWS (or NEWS2) score when assessing possible COVID-19 patients in primary care. Available from: <https://www.cebm.net/covid-19/should-we-use-the-news-or-news2-score-when-assessing-patients-with-possible-covid-19-in-primary-care/>.
11. Amanat F, White KM, Miorin L, Strohmaier S, McMahon M, Meade P, et al. An In Vitro Microneutralization Assay for SARS-CoV-2 Serology and Drug Screening. *Curr Protoc Microbiol*. 2020; 58 (1): e108. DOI: 10.1002/cpmc.108.
12. В каких странах вакцина "Спутник V" одобрена к применению. Доступно по ссылке: <https://sputnik-meedia.ee/infographics/20210607/573214/V-kakikh-stranakh-vaktsina-Sputnik-V-odobrena-k-primenjeniyu.html>.
13. Статистика вакцинации от коронавируса (COVID-19) в России. Доступно по ссылке: <https://index.minfin.com.ua/reference/coronavirus/vaccination/russia/>.
14. Schmidt F, Weisblum Y, Muecksch F, et al. Measuring SARS-CoV-2 neutralizing antibody activity using pseudotyped and chimeric viruses. *J Exp Med*. 2020; 217 (11): e20201181–e20201181.
15. Diamond M, Chen R, Xie X, Case J, Zhang X, VanBlargan L, et al. SARS-CoV-2 variants show resistance to neutralization by many monoclonal and serum-derived polyclonal antibodies. *Res Sq*. 2021; 3: 228079. DOI: 10.21203/rs.3.rs-228079/v1. Preprint.

ANALYSIS OF CAUSES OF EARLY NEONATAL MORTALITY DURING COVID-19 PANDEMIC IN 2020 IN RUSSIA

Tumanova UN¹, Shchegolev AI^{1,2} ✉, Chausov AA¹, Shuvalova MP¹

¹ Kulakov National Medical Research Center for Obstetrics, Gynecology and Perinatology, Moscow, Russia

² Pirogov Russian National Medical Research University, Moscow, Russia

In March 2020, the World Health Organization declared a COVID-19 pandemic. The aim of this study was to compare the causes of and statistics on neonatal mortality in Russia in 2020 and 2019 using the Rosstat A-5 forms that aggregate data from perinatal death certificates. In 2020, there was a 7.6% reduction in the absolute number of live births relative to 2019. In 2020, the overall early neonatal death rate (1.59%) fell by 4.4% in comparison with 2019 (1.67%). However neonatal mortality rates in the Southern and Far Eastern Federal Districts rose by 20.5% and 6.1%, respectively. Respiratory diseases were the most common cause of early neonatal mortality across Russia (37.3% and 40.2% relative to the total number of neonatal deaths in 2019 and 2020, respectively). Congenital sepsis accounted for 43.6% and 46.6% of early neonatal deaths from infectious diseases and for 7.3% and 7.9% of all early neonatal deaths reported in 2019 and 2020, respectively. There was an increase in the proportion of respiratory diseases among neonates, including congenital pneumonia and other respiratory conditions, and infections, including congenital sepsis, which reflects the direct and indirect effects of SARS-CoV-2 infection on pregnant women and neonates.

Keywords: neonate, early neonatal mortality, cause of death, regional features, COVID-19

Author contribution: Tumanova UN — study design, Rosstat data analysis, literature search and analysis, manuscript preparation; Shchegolev AI — Rosstat data analysis and summarization, literature analysis, manuscript editing; Chausov AA — Rosstat data analysis, statistical analysis; Shuvalova MP — Rosstat data analysis, manuscript editing.

✉ **Correspondence should be addressed:** Alexandr I. Shchegolev
Oparina, 4, Moscow, 117997, Russia; ashchegolev@oparina4.ru

Received: 15.09.2021 **Accepted:** 29.09.2021 **Published online:** 05.10.2021

DOI: 10.24075/brsmu.2021.045

АНАЛИЗ ПРИЧИН РАННЕЙ НЕОНАТАЛЬНОЙ СМЕРТНОСТИ В РОССИЙСКОЙ ФЕДЕРАЦИИ В 2020 Г. (ГОД ПАНДЕМИИ COVID-19)

У. Н. Туманова¹, А. И. Щеголев^{1,2} ✉, А. А. Чаусов¹, М. П. Шувалова¹

¹ Национальный медицинский исследовательский центр акушерства, гинекологии и перинатологии имени В. И. Кулакова, Москва, Россия

² Российский национальный медицинский исследовательский университет имени Н. И. Пирогова, Москва, Россия

В марте 2020 г. Всемирная организация здравоохранения объявила о пандемии COVID-19. Целью работы было провести сравнительный анализ причин и показателей ранней неонатальной смертности в Российской Федерации (РФ) в 2020 и 2019 г. с помощью статистических форм А-05 Росстата за 2019 и 2020 г., составленных на основании записей в медицинских свидетельствах о перинатальной смерти и относящихся к случаям ранней неонатальной смерти. В 2020 г. в РФ зарегистрировано уменьшение абсолютного числа живых новорожденных на 7,6% по сравнению с данными 2019 г. Показатель ранней неонатальной смертности в 2020 г. (1,59‰) снизился на 4,4% по сравнению с показателем 2019 г. (1,67‰). Однако в Южном и Дальневосточном федеральных округах показатели ранней неонатальной смертности повысились на 20,5 и 6,1% соответственно. В целом по РФ наиболее частой причиной ранней неонатальной смертности были заболевания, входящие в группу респираторных нарушений, составившие 37,3 и 40,2% от общего числа умерших новорожденных в 2019 и 2020 г. соответственно. Доля врожденного сепсиса как первоначальной причины смерти составила 43,6 и 46,6% в группе инфекционных заболеваний и 7,3 и 7,9% от всех умерших новорожденных в 2019 и 2020 г. соответственно. Установлено увеличение доли заболеваний, входящих в группу респираторных нарушений, включая врожденную пневмонию и так называемые другие респираторные состояния, а также инфекций, в том числе врожденного сепсиса, что отражает негативное прямое и опосредованное влияние SARS-CoV-2-инфицирования у беременных и у новорожденных.

Ключевые слова: новорожденный, ранняя неонатальная смерть, причина смерти, региональные особенности, COVID-19

Вклад авторов: У. Н. Туманова — дизайн работы, анализ данных Росстата, поиск и анализ данных литературы, написание текста; А. И. Щеголев — анализ и обобщение данных Росстата, анализ данных литературы, редактирование текста; А. А. Чаусов — анализ данных Росстата, статистическая обработка; М. П. Шувалова — анализ данных Росстата, редактирование текста.

✉ **Для корреспонденции:** Александр Иванович Щеголев
ул. Опарина, д. 4, г. Москва, 117997, Россия; ashchegolev@oparina4.ru

Статья получена: 15.09.2021 **Статья принята к печати:** 29.09.2021 **Опубликована онлайн:** 05.10.2021

DOI: 10.24075/vrgmu.2021.045

The first cases of the novel coronavirus infection caused by SARS-CoV-2 (severe acute respiratory syndrome, coronavirus-2) and later termed COVID-19 (coronavirus disease 2019) were reported in Wuhan, China, in December 2019 [1]. The virus was highly transmissible and rapidly spread across the globe. By March 11, 2020 there were over 100,000 confirmed COVID-19 cases worldwide, and WHO had to declare a pandemic [2].

Unfortunately, the implemented containment measures, the proposed treatments and the mass vaccination campaign have failed to stop the spread of the infection. Clinical presentations of COVID-19 vary from asymptomatic to severe infection and death. By March 2020, mortality from COVID-19 had reached

5–6% in China and 15% in other world's regions [3]. The elderly are the most affected by COVID-19; the prevalence of the severe disease is also the highest in this age group [4]. COVID-19 is detected in children and neonates less frequently, and pediatric outcomes are much better [5]. However, placental damage due to COVID-19 and SARS-CoV-2 infection in neonates may affect overall neonatal morbidity and mortality. In light of this, it may be important to analyze the rates and causes of neonatal mortality in 2020, the year of COVID-19 pandemic, and compare them to 2019.

The aim of this study was to compare the causes and rates of early neonatal mortality in Russia in 2020 and 2019.

Table 1. The number of neonates who died in the early neonatal period in Russia in 2019 and 2020. The table shows absolute values and the percentage from the total number of early neonatal deaths in Russia

Russia	Total	Female	Male	Urban	Rural
2019	2475	1377 (55,6)*	1098 (44,4)	1855 (74,9)**	620 (25,1)
2020	2288	1332* (58,2)	956 (41,8)	1696 (74,1)**	592 (25,9)

Note: * — $p < 0.01$ for comparison between male and female deaths, ** — $p < 0.01$ for comparison between urban and rural areas.

METHODS

We analyzed A-05 statistical forms collected in 2019 and 2020. These forms are available from Rosstat (Russian Federal State Statistics Service) and aggregate data from perinatal death certificates. We chose those that reported early neonatal mortality. Since January 1, 2012, early neonatal death has been officially defined as the death of a neonate born at gestational week 22 or later with a body weight of 500 g or higher within 168 h after birth.

The primary causes of early neonatal death were arranged in 8 groups: birth trauma (group I); diseases of the respiratory system (group II); infectious diseases (group III); hemorrhagic and hematologic disorders (group IV); endocrine, metabolic and other disorders specific to the perinatal period (group V); congenital malformations (group VI); injuries and poisoning (group VII); other or unspecified causes (group VIII).

The early neonatal mortality rate was calculated as the number of neonates dying within 168 h after birth per 1,000 live births. Quantitative variables were compared using the chi-squared test.

RESULTS

According to the data extracted from the obtained A-05 forms, there were 1,481, 074 live births in Russia in 2019; of them 2,475 neonates died within 168 h after birth (Table 1). In 2020, the absolute number of live births fell by 7.6% relative to the number of live births in 2019, and the early neonatal mortality rate fell by 4.4% (1.59% in 2020 vs 1.67% in 2019).

This reflects the downward trend in early neonatal mortality observed in Russia in the past few years. So, for better accuracy

of analysis, we decided to compare data accumulated in 2020 to the data from 2019. In 2012, when the current criteria of a birth (weight ≥ 500 g, gestational week 22 or later) were introduced, there were 6,969 reports of neonatal deaths within 168 h after birth, with the early neonatal mortality rate of 3.66% [6]. To put that into perspective, there were 4,948 early neonatal deaths with the early neonatal mortality rate of 2.75% in 2010 when early neonatal death was still defined as the death of a neonate born at week 28 of gestation with a body weight of 1,000 g or higher within 168 h after birth [7]. So, the early neonatal mortality rate fell by 42.2% and 56.6% relative to the figures reported in 2010 and 2012, respectively.

From all neonatal deaths within 168 h after birth, male deaths made up 54.7% in 2019 and 58.2% in 2020 and female deaths amounted to 45.3% and 41.8%, respectively. This means that in 2020 the proportion of early neonatal deaths among boys increased by 6.4% but dropped by 7.7% for girls. Most early neonatal deaths were reported in urban as compared to rural areas: 74.9% in 2019 and 74.1% in 2020 (Table 1).

The annual early neonatal death toll differed between Federal Districts (Table 2). In both years, the maximum number of neonatal deaths was reported in the Central FD (19.4% and 19.0% of all early neonatal deaths in 2019 and 2020, respectively) and the Volga FD (19.4% and 18.9%, respectively). The lowest death toll was reported in the Far Eastern FD. Overall, there was a decline in neonatal deaths across Russia in 2020 in comparison with 2019, but the Southern and the Far Eastern FDs reported an increase by 17.2% and 5.4%, respectively ($p = 0.004$). In 2020, the early neonatal mortality rate in these regions rose by 20.5% and 6.1%, respectively.

It is important to analyze the causes of neonatal mortality (Tables 3, 4). Overall, the majority of early neonatal deaths in

Table 2. The number of early neonatal deaths in the Federal Districts of Russia in 2019 and 2020. The table shows absolute values and the percentage from the total number of early neonatal deaths in Russia

District	2019		2020	
	<i>n</i> (%)	ENMR	<i>n</i> (%)	ENMR
Russia, total	2475	1,67	2288	1,59
Central	480 (19,4)	1,31	435 (19,0)	1,22
Northwestern	216 (8,7)	1,62	167 (7,3)	1,31
Southern	244 (9,9)	1,51	286 (12,5)*	1,82
North Caucasian	343 (13,9)	2,53	315 (13,8)	2,31
Volga	482 (19,5)	1,72	433 (18,9)	1,61
Ural	215 (8,7)	1,6	188 (8,2)	1,44
Siberian	347 (14,0)	1,95	308 (13,5)	1,81
Far Eastern	148 (6,0)	1,63	156 (6,8)	1,73

Note: ENMR: early neonatal mortality rate; * — $p < 0.05$ for comparison with 2019.

Table 3. The primary causes of early neonatal mortality in different Federal Districts of Russia in 2019. The table shows absolute values and the percentage from the total number of early neonatal deaths in Russia/District

District	Primary causes of death							
	I	II	III	IV	V	VI	VII	VIII
Russia, total	17 (0,7)	924 (37,3)	413 (16,7)	412 (16,6)	213 (8,6)	434 (17,5)	16 (0,6)	46 (1,9)
Central	2 (0,4)	121 (25,2)	56 (11,7)	84 (17,5)	69 (14,4)	138 (28,8)	0	10 (2,8)
Northwestern	1 (0,5)	98 (45,4)	48 (22,2)	26 (12,0)	12 (5,6)	28 (13,0)	2 (0,9)	1 (0,5)
Southern	3 (1,2)	102 (41,8)	47 (19,3)	44 (18,0)	13 (5,3)	27 (11,1)	1 (0,4)	7 (2,9)
North Caucasian	0	148 (43,1)	50 (14,6)	51 (14,9)	34 (9,9)	59 (17,2)	0	1 (0,3)
Volga	3 (0,6)	171 (35,5)	79 (16,4)	134 (27,8)	18 (3,7)	68 (14,1)	5 (1,0)	4 (0,8)
Ural	1 (0,5)	75 (34,9)	53 (24,7)	24 (11,2)	9 (4,2)	44 (20,5)	5 (2,3)	4 (1,9)
Siberian	5 (1,4)	137 (39,5)	66 (19,0)	25 (7,2)	42 (12,1)	55 (15,8)	3 (0,9)	14 (4,0)
Far Eastern	2 (1,4)	72 (48,6)	14 (9,5)	24 (16,2)	16 (10,8)	15 (10,1)	0	5 (3,4)

Russia throughout the analyzed period were caused by respiratory system disorders (group II). In 2019, such conditions accounted for 37.3% of all early neonatal deaths. In 2020, the contribution of respiratory conditions to the total neonatal death toll was 40.2%, i.e. it increased by 7.8% ($p = 0.042$) in comparison with 2019. Most of such deaths occurred due to hyaline membrane disease (16.6% and 15.3% of all early neonatal deaths in 2019 and 2020, respectively). A high proportion of deaths was attributed to birth asphyxia and congenital pneumonia. In 2019, these 2 conditions killed 212 and 200 newborns, or 8.6% and 8.1%, respectively. In 2020, deaths from birth asphyxia fell by 9.5% but their proportion in the total number of early neonatal deaths lowered by only 2.0%. Congenital pneumonia was more prevalent in 2020 (by 17.0%; $p = 0.011$) and its contribution to the early neonatal death toll increased by 26.6%. There was a surge in the number (by 43.4%; $p = 0.003$) and proportion (54.8%) of respiratory conditions referred to as other respiratory conditions originating in the perinatal period, including lung immaturity, atelectasis, aspiration syndrome, etc.

Congenital malformations (group VI) ranked second among the primary causes of early neonatal mortality in 2019. They caused death of 434 newborns (17.5% of all early neonatal deaths). In 2020, congenital malformations ranked fourth and were diagnosed in 354 (15.5%) cases.

The most common type of congenital malformation was a multiple congenital anomaly. Congenital malformations were the primary cause of death in 196 cases (7.9% of all early neonatal deaths) in 2019 and in 190 (8.3%) cases in 2020. The second most prevalent congenital malformation was congenital malformation of the heart that killed 123 neonates (28.3% of all congenital anomalies in group VI and 5.0% of total neonatal deaths) in 2019. In 2020, congenital malformations of the heart were much less frequent and caused 87 neonatal deaths (24.6% of all congenital malformations and 3.8% of the total number of neonatal deaths).

Infectious diseases (group III) were the third most common cause of death in 2019 and the second most common cause of death in 2020 (16.7%, or 413 cases and 17.0%, or 388

Table 4. The primary causes of early neonatal mortality in different Federal Districts of Russia in 2020. The table shows absolute values and the percentage from the total number of early neonatal deaths in Russia/District

District	Primary causes of death							
	I	II	III	IV	V	VI	VII	VIII
Russia, total	19 (0,8)	920 (40,2)	388 (17,0)	359 (15,7)	198 (8,7)	354 (15,5)	20 (0,9)	30 (1,3)
Central	3 (0,7)	117 (26,9)	74 (17,0)	80 (18,4)	54 (12,4)	92 (21,1)	7 (1,6)	8 (1,8)
Northwestern	1 (0,6)	73 (43,7)	35 (21,0)	20 (12,0)	9 (5,4)	29 (17,4)	0	0
Southern	2 (0,7)	150 (52,4)	30 (10,5)	51 (17,8)	7 (2,4)	39 (13,6)	2 (0,7)	5 (1,7)
North Caucasian	4 (1,3)	120 (38,1)	57 (18,1)	34 (10,8)	4 (14,3)	51 (16,2)	2 (0,6)	2 (0,6)
Volga	1 (0,2)	181 (41,8)	71 (16,4)	95 (21,9)	25 (5,8)	53 (12,2)	3 (0,7)	4 (0,9)
Ural	0	76 (40,4)	49 (26,1)	17 (9,0)	13 (6,9)	26 (13,8)	4 (2,1)	3 (1,6)
Siberian	6 (1,9)	124 (40,3)	60 (19,5)	41 (13,3)	27 (8,8)	44 (14,3)	1 (0,3)	5 (1,6)
Far Eastern	2 (1,3)	79 (50,6)	12 (7,7)	21 (13,5)	18 (11,5)	20 (12,8)	1 (0,6)	3 (1,9)

cases, respectively). Congenital sepsis was the primary cause of death in 180 and 181 cases in 2019 and 2020, respectively. It accounted for 43.6% and 46.6% of infectious diseases in this group and made up 7.3% and 7.9% of all neonatal deaths in 2019 and 2020, respectively. Other infections specific to the perinatal period caused death of 232 and 205 neonates in 2019 and 2020, respectively; these infections made up 56.2% and 52.8% of all infectious diseases in group III, respectively, and caused 9.4% and 9.0% of all neonatal deaths, respectively.

Hemorrhagic and hematologic disorders (group IV) were the primary cause of neonatal mortality in 412 cases (16.6% of all early neonatal deaths) in 2019 and the fourth most common cause of neonatal death overall. In 2020, the absolute (359) and relative (15.7%) numbers of early neonatal deaths associated with this group of conditions were lower but the disorders still ranked third among the most common causes of early neonatal mortality. The total number of endocrine, metabolic and other disorders specific to the perinatal period (group V) decreased from 213 in 2019 to 198 in 2020 but their contribution to the total neonatal death toll increased from 8.6% to 8.7%. It should be noted that there were fewer perinatal deaths due to unspecified causes in 2020 than in 2019 (42, or 1.7% of all neonatal deaths vs 27, or 1.2% of all neonatal deaths).

The incidence of the described primary conditions in neonates differed between the Federal Districts in both 2019 and 2020 (Tables 3 and 4). The incidence of respiratory system disorders (group II) as the primary condition varied from 25.2% to 48.6% in 2019 and from 26.9% to 52.4% in 2020. These conditions were the least frequent primary condition in the Central FD (25.2% and 26.9% of all early neonatal deaths, respectively, in 2019 and 2020) and the most frequent cause of early neonatal death in the Far Eastern FD (45.4%) in 2019 and in the Southern FD (52.4%) in 2020. Notably, there was a rise in the total number of neonates who died of respiratory system diseases in 2020 in comparison with 2019: by 47.1% and 9.7% ($p < 0.01$) in the Southern and Far Eastern FDs, respectively.

The greatest contribution of infectious diseases (group III) to early neonatal mortality in both years was observed in the Ural FD (24.7% and 26.1% in 2019 and 2020, respectively). The Central and North Caucasian FDs reported an increase in neonatal deaths caused by infectious diseases in 2020, as compared to 2019 (by 32.1% and 14%, respectively; $p < 0.04$). At the same time, neonatal deaths plunged by 36.2% and 27.1% ($p < 0.01$) in the Southern and Northwestern FDs, respectively.

The contribution of hemorrhagic and hematologic disorders constituting group IV to the causes of early neonatal mortality varied from 7.2% (Siberian FD) to 27.8% (Volga FD) in 2019 and from 9.0% (Ural FD) to 21.9% (Volga FD) in 2020. A rise in the number of early neonatal deaths caused by group IV diseases in 2020 as compared to 2019 occurred in the Siberian FD (by 64%; $p = 0.022$) and Southern FD (by 15.9%). In the North Caucasian and Volga FDs, early neonatal deaths fell by 33.3% and 31.7% %, respectively ($p = 0.042$).

The contribution of congenital malformations (group VI) varied from 10.1% (in the Far Eastern FD) to 28.8% (Central FD) in 2019 and from 12.2% (Volga FD) to 21.1% (Central FD) in 2020. An increase in the number of neonatal deaths caused by congenital malformations was reported in the Southern FD (by 44.4%) and Far Eastern FD (by 33.3%) in 2020 in comparison with 2019; a decline was observed in the Ural FD (by 40.1%) and the Central FD (by 33.3%; $p = 0.013$).

The analysis of Rosstat data on early neonatal deaths in 2019 and 2020 revealed their decline in absolute and relative numbers. Besides, there were some changes in the structure

of neonatal mortality causes and an increase in the number of neonatal deaths in a few FDs. Naturally, the contribution of SARS-CoV-2 to neonatal mortality has to be analyzed.

DISCUSSION

According to WHO recommendations and guidelines developed in Russia [8], all deaths associated with COVID-19 are broken down in 2 groups:

- COVID-19 as a primary cause of death;
- COVID-19 as another cause of death, significantly aggravating the primary condition or promoting its complications.

WHO has introduced additional codes to ICD to identify diseases and conditions that develop in the setting of COVID-19, for example: U07.1 (COVID-19, virus identified) and U07.2 (COVID-19, virus not identified). These codes are specified in neonatal death certificates and used in statistical analysis by Rosstat. Again, the primary causes of early neonatal death are classified according to Chapters XVI (Certain conditions originating in the perinatal period; P00-P96) and XVII (Congenital malformations, deformations and chromosomal abnormalities; Q00-Q99) of ICD-10. In Rosstat A-05 forms, the primary causes of neonatal death are reported as groups of diseases. Chapter XXII of ICD-10 (Codes for special purposes; U00-U85), which includes U07 (COVID-19), is reported as part of the class "Other causes of perinatal death". Therefore, it is impossible to extract the exact number of neonates who died from COVID-19 from Rosstat forms due to the absence of such data.

According to other reports of Rosstat, there were only 3 cases of other causes of perinatal death in 2020: in the Central, Southern and North Caucasian FDs. In 2019, a total of 4 such cases were reported: 2 in the Southern FD, one in the Volga FD and the other one in the Far Eastern FD. Even if all of these deaths were associated with COVID-19, which is highly unlikely, they accounted for only 0.17% of total early neonatal deaths in 2020. Therefore, as a primary condition COVID-19 did not increase early neonatal mortality.

At the same time, any comorbidity to a greater or lesser extent aggravates the course of a disease. In order to identify the primary cause of death and thanatogenesis components, the primary disease, the underlying condition and the co-occurring disease should be identified. The pathogenesis and thanatogenesis of COVID-19 are still not fully clear, so it would be logical to provide literature data on the neonatal incidence of COVID-19, its clinical manifestations and autopsy findings.

There are reports of SARS-CoV-2 infection in neonates. Transmission of the virus may occur in the uterus, at birth through exposure to maternal blood and/or uterine discharge or postpartum [9, 10]. Intrauterine transplacental transmission has been reported not only in single case studies but also in systematic reviews. WHO has proposed a classification for vertical SARS-CoV-2 transmission. It allows comparing data generated by different studies and assessing clinical outcomes in neonates born to infected mothers [11].

SARS-CoV-2 was detected in 14.2% of pregnant women in Spain [12] and 16–20% of pregnant women in New-York, USA [13]. As of July 1, 2020, there were 4,855 cases of COVID-19 among pregnant, parturient and postparturient females. By January 2021, their number had increased to 30,609.

Some researchers think that neonates are at risk for SARS-CoV-2 during vaginal unmedicated or minimally medicated delivery [14] because SARS-CoV-2 RNA was detected in maternal uterine swabs [15]. This is why Caesarean section was recommended to pregnant women infected with SARS-CoV-2 in the early days of the pandemic. At present,

Caesarean sections are indicated based on the general health of the pregnant woman and the fetus but not on the presence of COVID-19 infection.

The systematic analysis of publications on 176 SARS-CoV-2-infected neonates has established that intrauterine SARS-CoV-2 infection occurred in only 30% of cases; 70% of the neonates contracted the infection after birth from an infected individual [16]. This means that most transmissions occur through direct contact with infected individuals, including the mother, medical staff, family, and through contact with infected surfaces, especially steel and plastic, where the virus persists the longest [17].

The incidence of COVID-19 in neonates is much lower than in adults. However, to stabilize the condition of a neonate born to the infected mother, intensive care may be needed [18], which suggests the negative role of the infection. According to the most informative systematic review which included data on 176 SARS-CoV-2-infected neonates, only 97 (55.1%) were symptomatic [16]. Of them, 52.5% (51) had respiratory disorders, 44.3% (43) had fever, 36.0% (35) had gastrointestinal disorders, 18.6% (18) had neurological conditions, 10.3% (10) had cardiovascular disorders, and 9.2% (9) had hypothermia, conjunctivitis or skin rashes.

Common clinical symptoms of COVID-19 in neonates include fever, nausea, diarrhea, hypotension, tachycardia, hypoglycemia, hypothermia, meconium aspiration, respiratory distress syndrome, hypoxic ischemic encephalopathy, and congenital malformations: atrial septal defects, patent foramen ovale, hemodynamically significant patent ductus arteriosus, and tetralogy of Fallot [19]. At the same time, a multicenter study conducted in Spain reports no difference in the incidence of congenital malformations of the fetus in pregnant women infected with SARS-CoV-2 vs healthy pregnant women [20].

Most researchers indicate a higher frequency of premature labor [21, 22] and fetal distress among women infected with COVID-19 [23, 24], which again suggests the detrimental effect of COVID-19 on neonatal health. For example, the frequency of premature labor among pregnant women infected with SARS-CoV-2 was 11.4% vs 7.2% among healthy females ($p = 0.054$), and fetal distress was observed in 14% vs 9.1% of cases, respectively ($p = 0.036$) [20]. The proportion of prematurely born neonates with severe disorders was higher among pregnant women with COVID-19 than among healthy females: 9.6% vs 1% ($p = 0.006$) [24].

Some authors think that fetal distress is conditioned by poor blood oxygenation and systemic inflammation in the mother [24]. Morphological and functional defects of the placenta also play a role in intrauterine growth restriction. The overwhelming majority of researchers report that women with SARS-CoV-2 have placental damage manifesting as impaired blood flow between the maternal and fetal compartments and inflammation [25, 26]. Our earlier morphometric and immunohistochemical study conducted in pregnant women with COVID-19 has revealed increased numbers of syncytial knots, reduced vascularization and elevated VEGF expression in the villi indicating development of preplacental and placental hypoxia [27, 28]. Importantly, placental damage can lead to both intrauterine and early neonatal death. According to ICD-10,

placental damage cannot be interpreted as the primary cause of death but should be viewed as a condition that promotes death. Rosstat data reveals that placental damage led to early neonatal death in 17.2% of cases in 2010 [7], and in 22.2% of cases in 2016 [6].

Although COVID-19 is clinically manifested in neonates, the outcomes are mostly positive in comparison with the outcomes in adult and elderly patients. According to the Italian National Institute of Health, mortality from COVID-19 among children aged 0–9 years was 0.01% as of March 29, 2021 [29]. A systematic review of 24 publications (9 case series and 15 individual cases) on the effects of COVID-19 on pregnant women, fetuses and neonates reported only 4 intrauterine deaths, including a pair of twins, and 3 neonatal deaths, including a pair of twins, caused by COVID-19 [30]. Another analysis of literature published before June 3, 2020 comprised data on 920 neonates born to SARS-CoV-2-infected women, revealing only 2 (1.3%) neonatal deaths [31] caused by pneumonia; in both cases tests for SARS-CoV-2 were negative. Two more neonates developed neonatal sepsis, of them one had septic shock. Both received treatment and were discharged in a satisfactory condition.

However, there was a case of neonatal death from septic shock 2 h after birth to the SARS-CoV-2-infected mother [32]. There was another report of death of a prematurely born neonate who died from refractory shock, multiple organ failure and disseminated intravascular coagulation 9 days after birth [33].

Recently, the World Association of Perinatal Medicine working group reported the results of an extensive multicenter multinational retrospective cohort study which included women with singlet pregnancy and confirmed SARS-CoV-2 infection and was conducted at 72 centers in 22 countries across Europe, Latin America, Asia Australia and USA from February 1 to April 30 [34]. According to the report, there were 5 / 251 (2.0%) neonatal deaths: 3 babies were born prematurely, 2 died from sepsis. Notably the nasopharyngeal swab of 1 (0.4%) of 251 neonates born alive tested positive for SARS-CoV-2. This partly explains the relatively low rate of neonatal mortality due to COVID-19 in general and in Russia in particular.

CONCLUSIONS

According to Rosstat, the absolute number of neonatal deaths within 168 h after birth and the early neonatal mortality rate fell in 2020 (the year of COVID-19). The A-05 form of Rosstat does not contain information on neonatal mortality from COVID-19 for the year 2020. The analysis of Rosstat data has revealed an increase in rate of respiratory system disorders, including congenital pneumonia and the so called other respiratory conditions, and infections, including congenital sepsis, which, in our opinion, reflects the immediate and indirect impacts of SARS-CoV-2 infection and COVID-19 in pregnant women and SARS-CoV-2 infection in neonates. To better understand the role of COVID-19 in early neonatal mortality, statistics on the primary cause of death and pre-existing conditions should be collected. There is also the need for the clinical and pathomorphological analysis of each neonatal death followed by systematization of the obtained data.

References

- Zhu N, Zhang D, Wang W, Wang W, Li X, Yang B, et al. A novel coronavirus from patients with pneumonia in China. 2019. *N Engl J Med.* 2020; 382 (8): 727–33.
- Coronavirus Disease (COVID-19) Pandemic. <https://www.who.int/emergencies/diseases/novel-coronavirus-2019>.
- Baud D, Qi X, Nielsen-Saines K, Musso D, Pomar L, Favre G, et al. Real estimates of mortality following COVID-19 infection. *Lancet Infect Dis.* 2020; 20 (7): 773.
- Li J, Huang DQ, Zou B, Yang H, Hui WZ, Rui F, et al. Epidemiology of COVID-19: A systematic review and meta-analysis of clinical characteristics, risk factors, and outcomes. *J Med Virol.* 2021; 93 (3): 1449–58.
- Liguoro I, Pilotto C, Bonanni M, Ferrari ME, Pusiolo A, Nocerino A, et al. SARS-CoV-2 infection in children and newborns: A systematic review. *Eur J Pediatr.* 2020; 179 (7): 1029–46.
- Tumanova UN, Shuvalova MP, Shchegolev AI. Horioamnionit i rannijaja neonatal'naja smertnost' (po dannym Rosstata v 2012–2016 godah). *Mezhdunarodnyj zhurnal prikladnyh i fundamental'nyh issledovanij.* 2018; (8): 49–53. Russian.
- Shchegolev AI, Pavlov KA, Dubova EA., Frolova O. G. Rannijaja neonatal'naja smertnost' v Rossijskoj Federacii v 2010 g. *Arhiv patologii.* 2013; (4): 15–19. Russian.
- Metodicheskie rekomendacii po kodirovaniju i vyboru osnovnogo sostojanija v statistike zabolevaemosti i pervonachal'noj prichiny v statistike smertnosti, svjazannyh s COVID-19. 2020, 24 s. Dostupno po ssylke: https://static-1.rosminzdrav.ru/system/attachments/000/050/527/original/27052020_MR_STAT_1.pdf. Russian.
- Schwartz DA. An analysis of 38 pregnant women With COVID-19, their newborn infants, and maternal-fetal transmission of SARS-CoV-2: Maternal coronavirus infections and pregnancy outcomes. *Arch Pathol Lab Med.* 2020; 144 (7): 799–805.
- Neef V, Buxmann H, Rabenau HF, Zacharowski K, Raimann FJ. Characterization of neonates born to mothers with SARS-CoV-2 infection: Review and meta-analysis. *Pediatr Neonatol.* 2021; 62 (1): 11–20.
- WHO COVID-19 LENS (Living Evidence Synthesis) Working Group. Definition and categorization of the timing of mother-to-child transmission of SARS-CoV-2. Available from: www.who.int/publications/i/item/WHO-2019-nCoV-mother-tochild-transmission-2021.1.
- Garcia-Basteiro AL, Moncunill G, Tortajada M, Vidal M, Guinovart C, Jiménez A, et al. Seroprevalence of antibodies against SARS-CoV-2 among health care workers in a large Spanish reference hospital. *Nat Commun.* 2020; 11 (1): 3500.
- Sutton D, Fuchs K, D'Alton M, Goffman D. Universal screening for SARS-CoV-2 in women admitted for delivery. *N Engl J Med.* 2020; 382 (22): 2163–4.
- Ferrazzi E, Frigerio L, Savasi V, Vergani P, Prefumo F, Barresi S, et al. Vaginal delivery in SARS-CoV-2-infected pregnant women in Northern Italy: A retrospective analysis. *BJOG.* 2020; 127 (9): 1116–21.
- Vivanti AJ, Vauloup-Fellous C, Prevot S, Zupan V, Suffee C, Do Cao J, et al. Transplacental transmission of SARS-CoV-2 infection. *Nat Commun.* 2020; 11 (1): 3572.
- Raschetti R, Vivanti AJ, Vauloup-Fellous C, Loi B, Benachi A, De Luca D. Synthesis and systematic review of reported neonatal SARS-CoV-2 infections. *Nat Commun.* 2020; 11 (1): 5164.
- Shchegolev AI, Tumanova UN. Persistence of SARS-CoV-2 in deceased patients and safe handling of infected bodies. *Bulletin of RSMU.* 2021; (3): 5–11.
- Degtyarev DN. Mozhno li rassmatrivat' virus SARS-CoV-2 v kachestve vozбудitelja TORCH-infekcij u novorozhdennyh? *Neonatologija: novosti, mnenija, obuchenie.* 2021; (1): 5–7. Russian.
- Li X, Sun L, Tao L. Updates in neonatal coronavirus disease 2019: What can we learn from detailed case reports? (Review). *Mol Med Rep.* 2021; 23 (5): 351.
- Crovetto F, Crispi F, Llurba E, Pascal R, Larroya M, Trilla C, et al. Impact of SARS-CoV-2 infection on pregnancy outcomes: A population-based study. *Clin Infect Dis.* 2021: ciab104.
- Yan J, Guo J, Fan C, Juan J, Yu X, Li J, et al. Coronavirus disease 2019 in pregnant women: a report based on 116 cases. *Am J Obstet Gynecol.* 2020; 223 (111): e1–14.
- Knight M, Bunch K, Vousden N, Morris E, Simpson N, Gale C, et al. UK obstetric surveillance system SARSCoV-2 infection in Pregnancy Collaborative Group. Characteristics and outcomes of pregnant women admitted to hospital with confirmed SARS-CoV-2 infection in UK: national population based cohort study. *BMJ.* 2020; 369: m2107.
- Lee DH, Lee J, Kim E, Woo L, Park HY, An J. Emergency cesarean section performed in a patient with confirmed severe acute respiratory syndrome coronavirus-2 — a case report. *Korean J Anesthesiol.* 2020; 73 (4): 347–51.
- Gracia-Perez-Bonfils A, Martinez-Perez O, Llurba E, Chandrharan E. Fetal heart rate changes on the cardiotocograph trace secondary to maternal COVID-19 infection. *Eur J Obstet Gynecol Reprod Biol.* 2020; 252: 286–93.
- Oltean I, Tran J, Lawrence S, Ruschkowski BA, Zeng N, Bardwell C, et al. Impact of SARS-CoV-2 on the clinical outcomes and placental pathology of pregnant women and their infants: A systematic review. *Heliyon.* 2021; 7 (3): e06393.
- Shchegolev AI, Tumanova UN, Serov VN. Porazhenija placenty u beremennyh s SARS-CoV-2-infekciej. *Akusherstvo i ginekologija.* 2020; (12): 44–52. Russian.
- Shchegolev AI, Kulikova GV, Tumanova UN, Shmakov RG, Sukhikh GT. Morfometricheskaja harakteristika vorsin placenty rozhenic s COVID-19. *Bjulleten' jeksperimental'noj biologii i mediciny.* 2021; 172 (7): 102–7. Russian.
- Shchegolev AI, Kulikova GV, Lyapin VM, Shmakov RG, Sukhikh GT. The number of syncytial knots and vegf expres-sion in placental villi in parturient woman with COVID-19 depends on the disease severity. *Bull Exp Biol Med.* 2021; 171 (3): 399–403.
- Italian National Institute of Health. COVID-19: National Update 24 March 2021 (Italian Version). Available from: www.epicentro.iss.it/coronavirus/bollettino/Bollettino-sorveglianza-integrata-COVID-19_24-marzo-2021.pdf.
- Juan J, Gil MM, Rong Z, Zhang Y, Yang H, Poon LC. Effect of coronavirus disease 2019 (COVID-19) on maternal, perinatal and neonatal outcome: systematic review. *Ultrasound Obstet Gynecol.* 2020; 56 (1): 15–27.
- Bellos I, Pandita A, Panza R. Maternal and perinatal outcomes in pregnant women infected by SARS-CoV-2: A meta-analysis. *Eur J Obstet Gynecol Reprod Biol.* 2021; 256: 194–204.
- Li J, Wang Y, Zeng Y, Song T, Pan X, Jia M, et al. Critically ill pregnant patient with COVID-19 and neonatal death within two hours of birth. *Int J Gynaecol Obstet.* 2020; 150 (1): 126–128.
- Zhu H, Wang L, Fang C, Peng S, Zhang L, Chang G, et al. Clinical analysis of 10 neonates born to mothers with 2019-nCoV pneumonia. *Transl Pediatr.* 2020; 9: 51–60.
- WAPM (World Association of Perinatal Medicine) Working Group on COVID-19. Maternal and perinatal outcomes of pregnant women with SARS-CoV-2 infection. *Ultrasound Obstet Gynecol.* 2021; 57 (2): 232–41.

Литература

- Zhu N, Zhang D, Wang W, Wang W, Li X, Yang B, et al. A novel coronavirus from patients with pneumonia in China. 2019. *N Engl J Med.* 2020; 382 (8): 727–33.
- Coronavirus Disease (COVID-19) Pandemic. <https://www.who.int/emergencies/diseases/novel-coronavirus-2019>.
- Baud D, Qi X, Nielsen-Saines K, Musso D, Pomar L, Favre G, et al. Real estimates of mortality following COVID-19 infection. *Lancet Infect Dis.* 2020; 20 (7): 773.
- Li J, Huang DQ, Zou B, Yang H, Hui WZ, Rui F, et al. Epidemiology of COVID-19: A systematic review and meta-analysis of clinical

- characteristics, risk factors, and outcomes. *J Med Virol.* 2021; 93 (3): 1449–58.
5. Liguoro I, Pilotto C, Bonanni M, Ferrari ME, Pusioli A, Nocerino A, et al. SARS-CoV-2 infection in children and newborns: A systematic review. *Eur J Pediatr.* 2020; 179 (7): 1029–46.
 6. Туманова У. Н., Шувалова М. П., Щеголев А. И. Хориоамнионит и ранняя неонатальная смертность (по данным Росстата в 2012–2016 годах). *Международный журнал прикладных и фундаментальных исследований.* 2018; (8): 49–53.
 7. Щеголев А. И., Павлов К. А., Дубова Е. А., Фролова О. Г. Ранняя неонатальная смертность в Российской Федерации в 2010 г. *Архив патологии.* 2013; (4): 15–19.
 8. Методические рекомендации по кодированию и выбору основного состояния в статистике заболеваемости и первоначальной причины в статистике смертности, связанных с COVID-19. 2020; 24 с. Доступно по ссылке: https://static-1.rosminzdrav.ru/system/attachments/attaches/000/050/527/original/27052020_MR_STAT_1.pdf.
 9. Schwartz DA. An analysis of 38 pregnant women With COVID-19, their newborn infants, and maternal-fetal transmission of SARS-CoV-2: Maternal coronavirus infections and pregnancy outcomes. *Arch Pathol Lab Med.* 2020; 144 (7): 799–805.
 10. Neef V, Buxmann H, Rabenau HF, Zacharowski K, Raimann FJ. Characterization of neonates born to mothers with SARS-CoV-2 infection: Review and meta-analysis. *Pediatr Neonatol.* 2021; 62 (1): 11–20.
 11. WHO COVID-19 LENS (Living Evidence Synthesis) Working Group. Definition and categorization of the timing of mother-to-child transmission of SARS-CoV-2. Available from: www.who.int/publications/i/item/WHO-2019-nCoV-mother-to-child-transmission-2021.1.
 12. Garcia-Basteiro AL, Moncunill G, Tortajada M, Vidal M, Guinovart C, Jiménez A, et al. Seroprevalence of antibodies against SARS-CoV-2 among health care workers in a large Spanish reference hospital. *Nat Commun.* 2020; 11 (1): 3500.
 13. Sutton D, Fuchs K, D'Alton M, Goffman D. Universal screening for SARS-CoV-2 in women admitted for delivery. *N Engl J Med.* 2020; 382 (22): 2163–4.
 14. Ferrazzi E, Frigerio L, Savasi V, Vergani P., Prefumo F, Barresi S, et al. Vaginal delivery in SARS-CoV-2-infected pregnant women in Northern Italy: A retrospective analysis. *BJOG.* 2020; 127 (9): 1116–21.
 15. Vivanti AJ, Vauloup-Fellous C, Prevot S, Zupan V, Suffee C, Do Cao J, et al. Transplacental transmission of SARS-CoV-2 infection. *Nat Commun.* 2020; 11 (1): 3572.
 16. Raschetti R, Vivanti AJ, Vauloup-Fellous C, Loi B, Benachi A, De Luca D. Synthesis and systematic review of reported neonatal SARS-CoV-2 infections. *Nat Commun.* 2020; 11 (1): 5164.
 17. Shchegolev AI, Tumanova UN. Persistence of SARS-CoV-2 in deceased patients and safe handling of infected bodies. *Bulletin of RSMU.* 2021; (3): 5–11.
 18. Дегтярев Д. Н. Можно ли рассматривать вирус SARS-CoV-2 в качестве возбудителя TORCH-инфекций у новорожденных? *Неонатология: новости, мнения, обучение.* 2021; (1): 5–7.
 19. Li X, Sun L, Tao L. Updates in neonatal coronavirus disease 2019: What can we learn from detailed case reports? (Review). *Mol Med Rep.* 2021; 23 (5): 351.
 20. Crovetto F, Crispi F, Llubra E, Pascal R, Larroya M, Trilla C, et al. Impact of SARS-CoV-2 infection on pregnancy outcomes: A population-based study. *Clin Infect Dis.* 2021: ciab104.
 21. Yan J, Guo J, Fan C, Juan J, Yu X, Li J, et al. Coronavirus disease 2019 in pregnant women: a report based on 116 cases. *Am J Obstet Gynecol.* 2020; 223 (111): e1–14.
 22. Knight M, Bunch K, Vousden N, Morris E, Simpson N, Gale C, et al. UK obstetric surveillance system SARSCoV-2 infection in Pregnancy Collaborative Group. Characteristics and outcomes of pregnant women admitted to hospital with confirmed SARS-CoV-2 infection in UK: national population based cohort study. *BMJ.* 2020; 369: m2107.
 23. Lee DH, Lee J, Kim E, Woo L, Park HY, An J. Emergency cesarean section performed in a patient with confirmed severe acute respiratory syndrome coronavirus-2 — a case report. *Korean J Anesthesiol.* 2020; 73 (4): 347–51.
 24. Gracia-Perez-Bonfils A, Martinez-Perez O, Llubra E, Chandrarahan E. Fetal heart rate changes on the cardiotocograph trace secondary to maternal COVID-19 infection. *Eur J Obstet Gynecol Reprod Biol.* 2020; 252: 286–93.
 25. Oltean I, Tran J, Lawrence S, Ruschkowski BA, Zeng N, Bardwell C, et al. Impact of SARS-CoV-2 on the clinical outcomes and placental pathology of pregnant women and their infants: A systematic review. *Heliyon.* 2021; 7 (3): e06393.
 26. Щеголев А. И., Туманова У. Н., Серов В. Н. Поражения плаценты у беременных с SARS-CoV-2-инфекцией. *Акушерство и гинекология.* 2020; (12): 44–52.
 27. Щеголев А. И., Куликова Г. В., Туманова У. Н., Шмаков Р. Г., Сухих Г. Т. Морфометрическая характеристика ворсин плаценты рожениц с COVID-19. *Бюллетень экспериментальной биологии и медицины.* 2021; 172 (7): 102–7.
 28. Shchegolev AI, Kulikova GV, Lyapin VM, Shmakov RG, Sukhikh GT. The number of syncytial knots and vegf expression in placental villi in parturient woman with COVID-19 depends on the disease severity. *Bull Exp Biol Med.* 2021; 171 (3): 399–403.
 29. Italian National Institute of Health. COVID-19: National Update 24 March 2021 (Italian Version). Available from: www.epicentro.iss.it/coronavirus/bollettino/Bollettino-sorveglianza-integrata-COVID-19_24-marzo-2021.pdf.
 30. Juan J, Gil MM, Rong Z, Zhang Y, Yang H, Poon LC. Effect of coronavirus disease 2019 (COVID-19) on maternal, perinatal and neonatal outcome: systematic review. *Ultrasound Obstet Gynecol.* 2020; 56 (1): 15–27.
 31. Bellos I, Pandita A, Panza R. Maternal and perinatal outcomes in pregnant women infected by SARS-CoV-2: A meta-analysis. *Eur J Obstet Gynecol Reprod Biol.* 2021; 256: 194–204.
 32. Li J, Wang Y, Song T, Pan X, Jia M, et al. Critically ill pregnant patient with COVID-19 and neonatal death within two hours of birth. *Int J Gynaecol Obstet.* 2020; 150 (1): 126–128.
 33. Zhu H, Wang L, Fang C, Peng S, Zhang L, Chang G, et al. Clinical analysis of 10 neonates born to mothers with 2019-nCoV pneumonia. *Transl Pediatr.* 2020; 9: 51–60.
 34. WAPM (World Association of Perinatal Medicine) Working Group on COVID-19. Maternal and perinatal outcomes of pregnant women with SARS-CoV-2 infection. *Ultrasound Obstet Gynecol.* 2021; 57 (2): 232–41.